Spatial and temporal variability of surface energy fluxes in an alpine catchment

A thesis
submitted in fulfilment
of the requirements for the degree
of
Doctor of Philosophy
in the
University of Canterbury

by

Andrew J. Oliphant

University of Canterbury
2000

To the memory of my father, James Oliphant

(November 6th, 1927 to September 10th, 2000)

Table of Contents

Chapter Four: Seasonal and synoptic controls of surface radiation and energy fluxes

Chapter Five: Surface controls of radiation and energy fluxes

Chapter Six: Spatial modelling of surface radiation components

List of Figures

List of Tables

Acknowledgements

This thesis has been produced with the support and assistance of many people. The nature of this support has varied greatly, including technical, financial, intellectual, moral, social and emotional support. First and foremost, my sincere gratitude is extended to my supervisor Associate Professor Andy Sturman and associate supervisor Dr Rachel Spronken-Smith who have continued to provide all of the facets of support listed above. Their energy and intellect has been inspirational to me throughout my Ph.D. experience. I would also like to thank Dr Ian Owens, Dr Meinolf Kossmann, Dr David Whiteman, Dr Burn Hockey, Peyman Zawar-Reza, Dr Hamish McGowan, Dr Paul Gudikson and Dr David Campbell for useful and interesting discussions and editorial comments. Financial assistance for this research was provided under the project 'Local and Regional Wind Systems', funded by Marsden fund contract UOC602. I'd like to thank all the participants in this project for their assistance in fieldwork (particularly Rachel) and for a positive collaborative research experience.

The Geography Department has also provided considerable technical and infrastructural support for this research and I would particularly like to thank John Thyne, Gary Smith and Tim Nolan for their excellent technical assistance, as well as Steven Sykes, Graham Furniss, Janet Bray, Marney Brosnan and Walter Gallager. Final thesis production could not have been completed without with the invaluable help of Peter Mayell and Chandra Harrison. I'd also like to thank the Geography Department as a whole for its strong support of a positive research environment for its graduate students. For moral and social support, many thanks to my fellow graduate students, whose unity and positive spirit kept my head above water, particularly during difficult periods. In particular, thanks Peyman for the laughs and coffees. My gratitude also goes to the members of the Geography Giants, the finest basketball team ever to emerge from the department.

I would like to acknowledge the enormous importance to me of my family's unconditional support, especially my father, who never faltered for a second in his belief in me. Thanks Jim, Jenny, Fiona, Jeannie and Lesley for everything. To my son Dylan, four months old as this goes to print, who solves all with a single smile. And finally, to Monique, my champion, to whom I owe it all.

Abstract

One of the most important issues facing mesoscale modelling and atmospheric energy budget studies in complex terrain, is addressing the complicated pattern of energy fluxes that occur at the boundary of the Earth's surface. This study was designed to improve understanding of the characteristics and mechanisms of spatial and temporal variability in surface energy fluxes within a large alpine catchment. An observational dataset of time series and space series of surface radiation and energy fluxes in a 2500 km^{-2} catchment in the Southern Alps of New Zealand was generated. Observations were made for a period of fourteen months at a single site in the MacKenzie Basin and at nine locations in the Tekapo catchment on clear-sky summer days, during a month-long intensive observation period. The seasonal range in Q^* was found to be 14.2 MJ m^{-2} dy^{-1}, resulting primarily from the annual cycle of K^*, which provided greater variability than L^* by a factor of three. The range in Q^* due to synoptic influences was of a similar magnitude and was found to be most significantly a function of cloudiness, which was seen to vary significantly from one end of the study area to the other. Daily Bowen ratio (β) values ranged from 6.85 during the 1997/98 summer to –0.13 for the 1998 winter and 9.38 for the 1998/99 summer. A consistent logarithmic relationship was found between β and soil moisture content for all data, irrespective of season or synoptic situation. Overall, the largest impact on surface energy fluxes on the temporal scale was found to result from synoptic controls on the magnitude of net radiation, and secondly from seasonal control on the partitioning of turbulent fluxes.

Spatial series of observations focused on the five dominant surface classes in the catchment including, rock, lake water and three classes of vegetation. From this dataset, energy balances were derived for each surface class, to assess the spatial variability associated with heterogeneity of surface properties. A large range in surface flux density was found, related to radiative, thermal, hydrological and vegetative properties of the surface. The lake surface recorded the highest daily total Q^* values of the five surface types, rock surfaces recorded the lowest and the three vegetated surfaces recorded very similar flux densities. The most significant influences were the mean diurnal albedo and the ratio between $L\uparrow$ and absorbed allwave radiation. Significant differences also existed between the surface types in the diurnal range of albedo. Modelling of surface radiation flux components was conducted using SRAD, a topographically based radiation model. Output from the model compared well with observations, with closer agreement found for daily mean than instantaneous fluxes. In both observational and modelled results, $K\downarrow$ was found to contribute most significantly to the radiation budget both in terms of the mean and variability of flux magnitudes. By contrast, longwave radiation fluxes contributed little variability to the spatial distribution of Q^*. The variability in $K\downarrow$ was associated most strongly with slope aspect, secondly with slope angle, thirdly with shading, and lastly with elevation. The largest range associated with slope throughout the year was found during at the equinox when a range of 20.3 MJ m^{-2} dy^{-1} existed between south-facing 60° slopes and north-facing 40° slopes. Turbulent heat flux maps were constructed using modelled Q^* maps and observed turbulent flux densities non-dimensionalised by Q^*. Maps of the latter were derived from observations over each surface type and surface cover maps,

generated using supervised classification of IRS-1C imagery. Large spatial variability in surface energy flux density was found to exist at any given time, although these were greatest near mid-day. Spatial variability was found to be controlled equally by spatial variability of Q^* and surface heterogeneity. The role of topographic complexity on the spatial distribution of fluxes was investigated by comparing three sub-areas of the Tekapo catchment that showed strongly contrasting topographical properties. Increase in topographic complexity was associated with decrease in mean Q^*, but a large increase in spatial variability. Similar, but less extreme results were found for turbulent fluxes. However, despite the large ranges in flux densities found throughout the catchment, spatial averages of turbulent fluxes for the three sub-areas were relatively consistent, providing some confidence for the use of spatial averaging for sub-grid areas of numerical models. It is hoped that future research can build on the evidence, methodologies and hypotheses generated by this research. In particular, it is envisioned that future observations in other mountain settings will help determine the extent to which the findings of this study can be applied generally to areas of complex terrain.

Chapter One:

Introduction

Energy fluxes that occur across the boundary of the Earth's surface provide the fundamental driving force for many atmospheric, hydrological and biological processes. In complex terrain the variability of topography and physical properties of the surface combine to generate complicated spatial and temporal patterns of surface energy fluxes. Improving the understanding of the mechanisms for variability of surface fluxes is a necessary goal for improved modelling of boundary layer behaviour and airflow in complex terrain. This study examines the controls on the spatial and temporal variability of surface energy fluxes within a mid-latitude alpine catchment. The purpose of the present chapter is to outline the nature of the research, the objectives of the study and how they are to be addressed in the course of this thesis.

1.1 Background

This section outlines the background to the objectives of this study, including the nature of the problem within the context of standard meteorological scales, the rationale for the investigation, and the research foundation on which the present study is based.

1.1.1 Defining the boundary processes

The nature of surface-atmosphere energetics at a given time can be defined by the budget of incoming and outgoing radiative, conductive and convective energy fluxes near the boundary of the Earth's surface. On time scales of minutes to thousands of years, the surface radiation budget is rarely balanced and, in order to satisfy the First Law of Thermodynamics, the surplus or deficit is balanced predominantly by heat and moisture transfer from or to the surface, respectively. Spatial variability in surface energy fluxes exists in response to changes in the location, topography and physical properties of the surface as well as heterogeneity of thermal and hydrological properties in the overlying airmass. The Earth's spin and solar orbit, changes in the physical properties of the surface and broader-scale meteorological controls govern temporal variability. The incident angle of the solar beam to the surface is important for locational, topographical, diurnal and seasonal controls. The physical properties of the surface that are relevant to surface energy fluxes are the radiative, thermal and

hydrological properties of the surface material, including albedo, thermal conductivity and water content. The nature of the overlying airmass is governed most strongly by synoptic pressure gradients, although the behaviour of any airflow in complex terrain can produce significant heterogeneity of airmass properties. Some of these influences are uni-directional (*e.g.* solar position) while others produce feedbacks that alter the boundary conditions that govern the fluxes (*e.g.* soil moisture content). In the remainder of this thesis, the term *surface radiation budget* is used to define the budget of incoming (positive) and outgoing (negative) radiative components relative to the surface, typically represented by *net radiation* (Q^*). The term *surface energy balance* is then used to define the resulting balance of heat fluxes, typically *sensible heat*, *latent heat* and *ground heat*, where positive values represent fluxes away from the surface (both down and up) and negative values represent fluxes toward the surface.

1.1.2 Scale definition

The study of surface energy fluxes over a 2700 km^2 catchment is difficult to locate within the traditional framework of atmospheric scales. The horizontal and temporal scales of most meteorological phenomena can be found within the scale ranges shown in Figure 1.1. A selection of meteorological phenomena is located within the logarithmic axes of the scale model. An attempt has been made to approximate the range of scales that provide the focus for this study (dark grey) as well as those which have less direct, but still important influence (light grey). The use of logarithmic scales on each axis appropriately illustrates the importance of processes operating close to the surface and at smaller scales of time and space.

On the vertical scale, the planetary boundary layer is generally recognised as the depth of the atmosphere that is influenced by the Earth's surface and responds to surface forcings on timescales of less than an hour (Stull 1988). The depth of this layer is variable in time and space, ranging from a few hundred to a few thousand metres above ground level. The turbulent surface layer is located in the lower 10% of the boundary layer and is characterised by intense small-scale turbulence, where fluxes are approximately constant throughout the layer (varying by less than 10%). In this study, direct attention is paid to the turbulent surface layer and sub-surface layer because they are the active layers in surface energy fluxes, although links can be made between these and all other layers discussed above.

From the early work of Wagner (1938) and Ekhart (1944, 1948), translated in Whiteman and Dreiseitl (1984), it became clear that complex terrain greatly complicates the structure of the planetary boundary layer. Ekhart (1948) proposed sub-units to the boundary layer, which he termed the *mountain atmosphere*, to include *valley atmospheres* and *slope atmospheres*. The idea of grouping climatic variables within scales set by the landscape was taken further by Yoshino (1975), who integrated meteorological scales over time to produce a topoclimatological model. This was adapted further by Barry (1992), whose conceptual model is presented in Figure 1.2. This model describes divisions at three different scales, regional climates, topoclimates and microclimates. Regional climates include divisions of broader scale topography such as mountains and plains and influence a relatively deep layer of the troposphere. Topoclimates are associated with sub-features of the mountain region, including valleys, basins and broader scale divisions of surface cover such as lakes, ice, and urban areas as well as broader vegetative divisions. Microclimates are associated with small-scale variability of surface characteristics including slope properties, elevation and

surface cover which varies at the species level of vegetative divisions as well as urban, rock and ice surfaces.

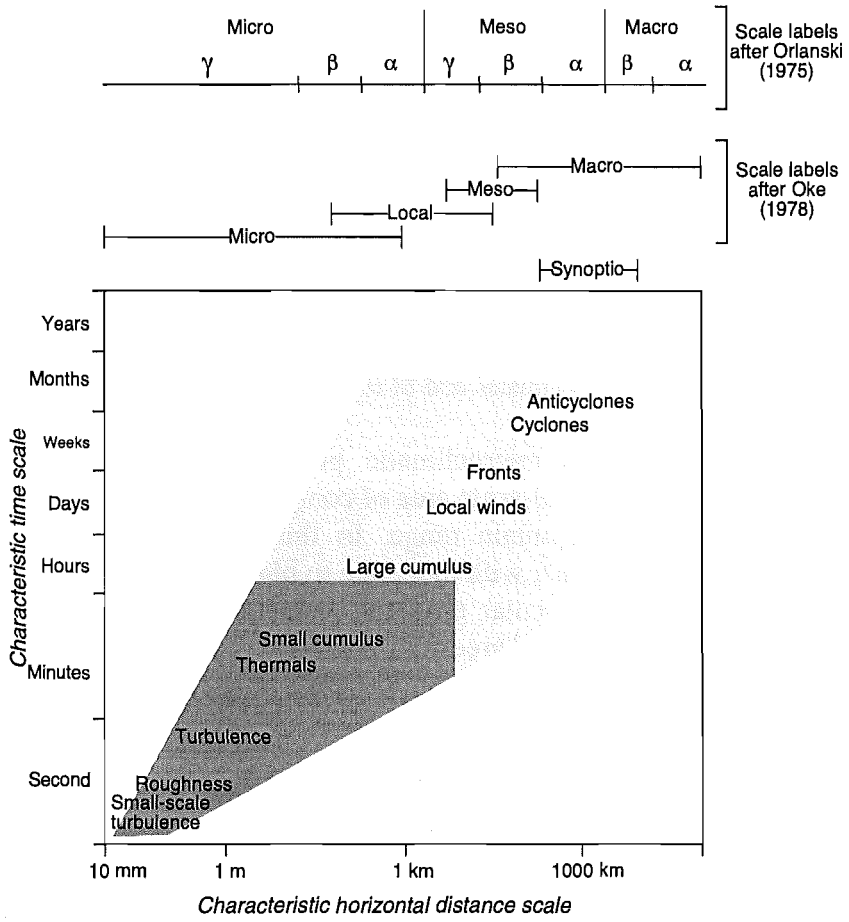

Figure 1.1 Characteristic horizontal and temporal scales of meteorological phenomena, including those examined directly (dark grey) and indirectly (light grey) in this study (after Oke 1987).

Despite the convenience of such subdivision, the gradation of effects such as altitude and relief means divisions like these will remain speculative. Furthermore, the degree to which each scale dominates atmospheric conditions at a given site is largely dependent on the behaviour of the largest scale. For example, in calm, clear-sky conditions, topoclimates and regional climates will be controlled most strongly by surface energy fluxes rather than advective effects. Conversely, when ambient conditions produce strong winds, the surface effects are recognised only through mechanical wind shear generated by the complex terrain.

A further issue related to scale is the relativity of the definition of *complexity*. Complex terrain has been the focus of many recent boundary layer studies, which consider comparatively quite different landscapes (Konzelmann *et al.* 1997, Wenzel *et al.* 1997, Whiteman *et al.* (1989b), Huntingford *et al.* 1998). The complexity of terrain determines, in part, the nature of processes that are likely to dominate. For example, Whiteman (1982) demonstrated the importance of the cross-sectional valley shape on inversion breakup. There is therefore a need to define not just the scales with regard to distance and time, but the complexity of terrain through relief, shape and surface cover information.

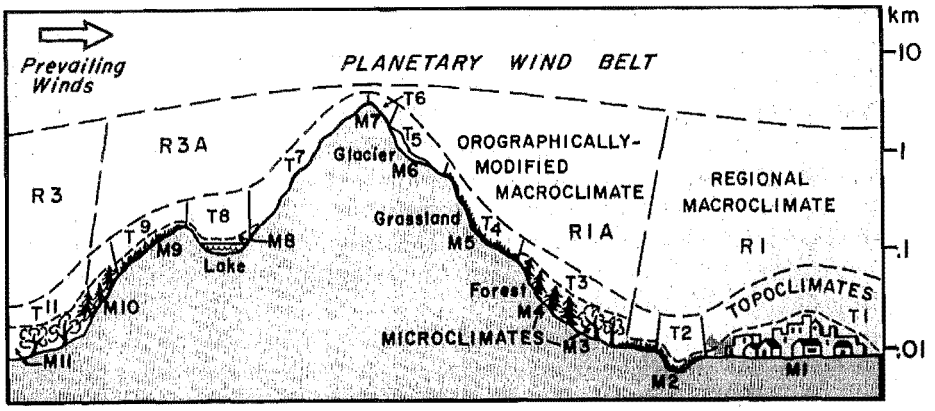

Figure 1.2 Characteristic delineation of climatological scales in complex terrain, where R refers to regional climates, T refers to topoclimates and M refers to Microclimates (from Barry 1992).

In summary, this study covers microclimatic processes that occur over various topoclimatic divisions within a local-scale area of complex terrain. This is set within the regional division of a large mountain range. In this situation, *complex terrain* is represented by an area of 2700 km^{-2}, with moderate to high relief and an elevation range of 2300 m. Definition of the particular physical characteristics of this study area are provided in greater detail in Chapter Three.

1.1.3 Rationale

Spatial variability in surface energy fluxes is responsible for spatial patterns of meteorological variables and phenomena at a range of scales. In complex terrain, heterogeneous atmospheric heating and cooling rates at the surface have a large influence on the mean diurnal wind fields in the lower troposphere (Sturman 1987, Kondo 1990, Whiteman 1990), and the concentration of pollutants (Tyson 1969, Tangirala *et al.* 1992, Tinarelli *et al.*1994). Whiteman (1990) pointed out that there was growing recognition among researchers that the valley meteorology problem is a continuum problem, since the relative importance of different processes varies from valley to valley, time to time in the same valley and even site to site within a valley, ensuring that generalisations are difficult. One important source of variability at all these scales is surface energy fluxes. Relatively few observations of surface energy fluxes are yet available in valleys and areas of complex terrain due to the difficulties inherent in making the measurements (Whiteman 1990, Barry 1992).

The operational resolution of atmospheric models that contain surface layer processes is typically insufficient to resolve the detail inherent in complex terrain. For example, the alpine catchment considered in this study is the approximate area represented by a single grid point in a regional scale model, 0.1 of a gridpoint in a forecasting model and 0.01 of a gridpoint in a general circulation model. Models have been run at finer resolution, although, as a compromise, these have tended to ignore detail in surface processes (van den Assem 1997, de Wekker *et al.* 1998).

The most important meteorological implications that result from a better understanding of surface energy fluxes in complex terrain, are the role fluxes play in boundary layer processes and phenomena. For example, there is currently a need to better understand the transport and dispersion of air pollution in complex terrain, which is strongly governed by boundary layer structure and airflow. This can be extended to the behaviour of other atmospheric aerosols such as dust, seeds, pollen or agricultural

sprays, as well as the behaviour of wild fire. Although this research is approached as a meteorological problem, a better understanding of surface energy fluxes in complex terrain is important in hydrological, ecological and agricultural applications. This is because surface energy fluxes are critical to diurnal and seasonal changes in ground and near surface air temperature, evaporation, dewfall and frost. This information is also important for land management since the effect of land-use change on the microclimate can be significant.

The rationale for this study stems from a weakness in the understanding of surface energy fluxes in complex environments. These fluxes are a critical component of boundary layer processes that directly impact on the lives of people who live there. This is compounded by increasing population density in mountain environments, where problems such as air pollution and contamination and wildfire pose serious threats to health and property. In addition to meteorological applications, information yielded from research on variability of surface fluxes in complex terrain can be usefully applied to hydrological, ecological and agricultural problems and can be influential in land management decisions.

1.1.4 Research background

The foundations of research for the present study began with the recognition that winds generated on sloping surfaces, in large valleys and across coastlines was often associated with atmospheric heating and cooling of the surface (Bemmelen 1922, Wagner 1938, Defant 1951). A considerable amount of research on local circulations in complex terrain was undertaken in the latter half of the 20th Century, as reviewed by Atkinson (1981), Whiteman (1990) and Barry (1992). This research paid increasing attention to stable nocturnal flows, which coincide with high air pollutant concentrations near the surface (Gudiksen and Shearer 1989, Doran *et al.* 1990). Large field programmes have been run in Europe, including DISCUS (Hacker 1982), MESOKLIP, MERKER (Freytag 1985), TRACT; in North America, including ASCOT (Orgill and Schroek 1985), IMADA-AVER (Doran *et al.* 1998); and Asia, including HEIFE (Mitsuta and Tamagawa 1993). These were designed specifically to study boundary layer phenomena in complex terrain, and particularly their role in dispersion of air pollutants and contaminants. In order to better isolate particular processes, study sites with reasonably simple topography and homogeneous surface cover were typically selected. Furthermore, spatial variability of surface energy fluxes received relatively minor consideration, although Hennemuth (1987) Whiteman *et al.* (1989b), Whiteman 1990 and Kalthoff *et al.* (1999) provide notable exceptions. These authors found considerable spatial variability in surface fluxes within relatively homogeneous settings. At the same time, numerical studies were showing the influence of heterogeneous land surface cover in generating mesoscale atmospheric circulations when surface fluxes were parameterised in appropriate detail (Avissar and Pielke 1989), and these circulations were also found in observational data (Doran *et al.* 1995).

Contributions to the understanding of variability of surface energy exchanges in complex terrain has been approached in several ways, including surface layer schemes in numerical models, observational studies using point measurement, observational studies using remotely sensed data, surface modelling using radiation and hydrological schemes, and tools for spatial and statistical modelling such as GIS and neural networks.

Numerical work

Atmospheric models rely on parameterisation of the radiative, thermal and hydrological properties of the surface and the spatial patterns of these properties are typically assigned using land-use classification. Significant improvement in parameterisation has been made recently with the inclusion of additional processes (Naot and Mahrer 1989, de Ridder and Schayes 1997, Acs and Hantel 1998, Best 1998). These surface schemes have focussed on the importance of radiative transfer (Nunez 1980, de Ridder 1997, Saunders *et al.* 1999a), energy partitioning (Saunders *et al.* 1999b) and water budgets (Famiglietti and Wood 1994a, b, 1995). Attention has also been paid to transfer schemes (Kalma 1989, Mikami *et al.* 1996, Lee 1997, Guilloteau 1998). As surface parameterisations include more processes, they have moved from being subroutines of atmospheric models to independent schemes with increasing detail applied to the interface (Polcher *et al.* 1998). Because of the difficulty of spatial resolution, there is a growing interest in atmospheric modelling for obtaining spatial-mean values of surface fluxes through aggregation schemes (Pielke *et al.* 1993, Raupach 1993, Hasager and Jensen 1999).

Liang *et al.* 1998 compared sixteen soil-vegetation-atmosphere transfer schemes for predicting surface energy fluxes, using 10 years of meteorological and radiative forcing data from the Red-Arkansas River Basin. Of the components of the surface energy budget, prediction of annual mean net radiation was most consistent among the schemes. This was followed by latent and sensible heat fluxes respectively. Ground heat fluxes showed greatest relative variability (including opposite signs) although values were an order of magnitude lower. Generally, less variability was found between schemes when averaged over longer time intervals. In a review of the same dataset, Wood *et al.* (1998) found the mean annual Bowen ratio of sensible to latent heat flux (β) varied from 0.53 to 1.73 between the schemes as compared with 0.92, estimated from meteorological variables observed at the site. They also noted that those surface schemes that didn't undertake calibration runs using observed data didn't perform as well as those that calibrated. These valuable inter-comparisons show that there remains significant progress to be made in order to converge on accurate parameterisation of surface processes and particularly, to be able to apply such schemes to locations where observational data are not available.

Modelling topographic variation in radiation in a GIS environment has been a recent focus (Orvis 1997), considering both solar radiation (Kumar *et al.* 1997, Dubayah and Rich 1995) and longwave radiation components (Marks and Dozier 1979). Hydrological models that focus on surface processes have been applied to individual catchments with promising results (Familigetti *et al.* 1994a,b, 1995). The weakness in such models is the lack of attention paid to 3-dimensional atmospheric effects and non-hydrological processes. Use of remote sensing data to estimate surface energy fluxes has yielded valuable spatial information (Lhomme and Monteny 1993, Sun and Mahrt 1994, Humes *et al.* 1997, Laymon *et al.* 1998, McKeown and Leighton 1999) and has been combined with digital elevation data to improve determination of both radiation and heat fluxes in complex terrain (Duguay 1995, Schneider *et al.* 1996, Dubayah and Loechel 1997). The potential of remotely sensed data to characterise surface properties and variables is considerable, although either spatial or temporal compromises must be made. For example, currently, spatial resolution from satellite platforms in many spectral bands is as low as 20m, but has return frequencies of days to weeks. Conversely, geostationary satellites provide data at temporal resolution of minutes to hours, but with spatial resolution of several kilometres. Furthermore, estimation of

energy balances often relies on extrapolation of very few points of meteorological data to augment image data. The same problem applies when estimating sensible heat flux using neural networks, based on links to net radiation, wind speed, air temperature, surface temperature and time (Abareshi and Schuepp 1997). In general, considerably greater spatial resolution is possible with surface modelling than with 3-dimensional atmospheric modelling and more detail can be given to key processes. However, the shortfall of the lack of atmospheric feedback remains considerable.

Observational work

Observational methods of estimating surface fluxes have developed rapidly in recent decades, with fast response instruments able to resolve the timescale of turbulent eddies. These methods have been well tested, and are particularly suited to examining changes over time, although they are limited to points in space. Most investigations carried out in mountainous areas in the past have focussed on ice and snow covered surfaces (Pluss and Mazzoni 1994). Investigations focussing on vegetated surfaces in alpine regions include Rott (1979), Hennemuth and Kohler (1984) and Konzelmann *et al.* (1997). In these latter studies, emphasis was given to the hydrological aspects of local to regional scale catchment basins in Europe. The results from these studies have provided valuable information for modelling purposes (Gurtz *et al.* 1997, cited in Konzelmann *et al.* 1997). However, the generalisation of such models to the whole alpine domain is still uncertain. Longer-term records of surface energy fluxes in complex terrain have been examined with regard to radiation budgets and energy balances in the Southern Alps of New Zealand (Greenland 1973, Greenland and Clothier 1975), evaporation over a tussock grassland (Campbell and Murray 1990), radiation budgets over different surface types in Germany (Kessler and Jaeger 1999) and energy balances in the Rhine Valley (Wenzel *et al.* 1997, Kalthoff *et al.* 1999) and the Sahel (Verhoef *et al.* 1999). These studies have illustrated the importance of solar declination, as well as changing surface properties and synoptic controls for temporal variability.

The problems associated with making observations of spatial variability of surface energy exchanges in complex terrain using instrumented towers have limited such studies. These problems include accessibility, sensitivity of instruments to rain, snow, wind blown dust and animal vandalism, large uniform fetch requirements, difficulty in making observations over sloping terrain and the difficulty of extrapolating from point measurements. Topographically complex areas are often associated with all these issues, particularly the problems of complicated flow structure, which generates turbulent situations that defy the theory of measurement techniques such as surface-parallel flow regimes and zero mean vertical wind velocity. For example, the problems of making measurements of energy fluxes on sloping surfaces have been discussed by Fritschen and Qian (1990) and Oliver (1992). A discussion of the issues associated with the particular measurement techniques used in this study is provided in Chapter Three. The development of fast response instruments, including accurate GPS, has allowed the use of aircraft for turbulent flux measurement (Frech and Jochum 1999, Sun *et al.*1997). This removes many of the difficulties associated with instrumented towers, although is limited by cost to short term sampling frequencies and aircraft height restrictions typically limit the spatial detail of fluxes that can be observed.

Whiteman *et al.* (1989b), Assouline and Mahrer (1996), Konzelmann *et al.* (1997), Wenzel *et al.* (1997) Kalthoff *et al.* (1999), Sugita *et al.* (1993) and Beyrich *et al.* (2000) used concurrent measurements of surface energy fluxes at multiple sites to

examine spatial variability in surface climates. Oue and Tgashina (1993) and Boyer and Feldhake (1994) derived estimates using standard meteorological observations at several sites. These studies yielded valuable information on the role of particular surface characteristics on energy flux behaviour. Additionally, single point measurements of surface energy fluxes have been made over a great deal of surfaces. Although these studies tend to be site and time-specific, they have provided a great deal of information on the relevant processes and a large database for purposes of comparison. These studies are too numerous to list here, although many are cited in the following chapters.

In summary, the past several decades have witnessed rapid progress in the measurement and modelling techniques, and consequent understanding, of surface energy fluxes. However, these studies have tended to focus on relatively simple landscapes with homogeneous surface cover and at broader scales than are appropriate for local areas. This section has highlighted the need for observations of surface energy fluxes in complex terrain and for examination of the key parameters that control spatial and temporal variability at a spatial scale appropriate to the complexity of the landscape.

1.2 Research Aims

The research goal of this study is to investigate the spatial and temporal variability of surface energy fluxes in an area of complex terrain. This general aim can be broken into three specific objectives:

1. Evaluate temporal variability of the magnitude of surface radiation and energy fluxes in response to seasonal and synoptic controls.

2. Evaluate spatial variability of the magnitude of surface radiation and energy fluxes within a complex alpine catchment during clear-sky summer days and determine the major controlling factors with regard to topographic characteristics and physical properties of the surface.

3. Map the spatial pattern of surface radiation and energy fluxes throughout the catchment on a scale appropriate to the complexity of the landscape, and evaluate the role of surface complexity on their spatial variability.

This study sets out to achieve these objectives using a combination of point measurements, spatial modelling of surface characteristics and mathematical modelling of surface radiative fluxes. Temporal variability is investigated through fourteen months of observations at a single station in an alpine basin as well as seasonal modelling of radiation components. Concurrent measurement over a number of surfaces during a summer intensive observation period provide data for analysis of the role of surface properties on spatial heterogeneity of surface energy fluxes. A topographical surface radiation model is built for the entire study area at a spatial resolution of 100 m and spatial models of energy balance components are produced in a GIS environment through amalgamation of observations, radiation model output and surface cover classification. These techniques provide the materials by which the objectives of this research are tackled.

1.3 Thesis outline

The structure of this thesis broadly follows the outline of the objectives. The second chapter provides a theoretical background to the physical processes relevant to this research, while the third chapter provides study-specific information, both in terms of the nature of the study area and detail of the methods used to obtain results. The four chapters that follow present the main findings of the study. Chapter Four is concerned with the first objective. Fourteen months of observations at a single site are examined with the purpose of evaluating the variability of energy fluxes found over the synoptic to seasonal timescales. Chapter Five presents comparisons of surface flux observations from nine locations in an alpine catchment, including five major surface types during weak gradient, clear-sky summer conditions. Chapter Six presents results from a modelling study designed to investigate the role of topography and surface type on the surface radiation budget. The results of energy partitioning over the major surface types reported in Chapter Five are then applied to the modelled net radiation output in Chapter Six in order to map the spatial variability of surface fluxes of heat and moisture which is presented and discussed in Chapter Seven. The results, their implications and suggestions for future research are then summarised in the final chapter.

1.4 Summary

The purpose of the first chapter has been to outline the nature of the research, the objectives of the study and the order in which they are to be addressed in the remainder of this report. In attempting to locate the scale of the research problem, it is defined as a set of micrometeorological processes in the surface layer of a local-scale area of high-relief terrain. However, indirect influences exist in all scales relevant to meteorology. The rationale for this study is the need to better understand spatial heterogeneity in surface energy fluxes in complex terrain as a critical component of boundary layer structure and airflow. The research background reveals the need for observations of surface fluxes in complex terrain, particularly those designed to observe spatial variability. It also reveals the need for greater detail required in assessing heterogeneity of surface fluxes in complex terrain. Hence, this research examines the spatial and temporal variability of surface energy fluxes in an alpine catchment. This is achieved through both an observational programme and mathematical and spatial modelling.

Chapter Two:

Theoretical background

2.1 Introduction

The Earth's surface presents a fundamentally important boundary to the domain of the atmosphere. This boundary interacts with the lower portion of the overlying atmosphere through forcings of frictional drag, heat and moisture transfer and surface induced flow modification. The vertical extent of influence of these forcings defines the depth of the planetary boundary layer, which is strongly dependent on their magnitude. The magnitudes of heat and moisture transfer are most strongly controlled temporally at the diurnal and seasonal timescales in response to solar cycles, and spatially by the physical properties of the surface and its location in space. These factors influence both the availability of energy at the surface in the form of radiative fluxes and the partitioning of this energy through conductive and convective fluxes.

The purpose of this chapter is to outline current knowledge of the causes and behaviour of surface energy fluxes and how they vary over space and time in complex terrain. Since the radiation budget is considered the initial input into the surface energy balance, the first section considers the role of radiative transfer at the Earth's surface and how it varies with respect to astronomic controls, radiative properties of the surface and broader scale atmospheric controls. This is followed by an examination of the partitioning of this energy into fluxes of heat and moisture. Discussion then shifts from idealised processes to the nature of surface energy exchanges in complex terrain. Following this, links between surface energy exchanges and the generation and modification of airflow in complex terrain, are considered. Since numerical methods of estimating the surface radiation budget are used in the present study, emphasis is placed on the application of such methods in complex terrain in Section 2.2. In contrast, the surface energy balance components are estimated from observations in this study, so the emphasis in Section 2.3 is on measurement techniques and observational reports.

2.2 The surface radiation budget in complex terrain

Evaluation of the surface radiation budget involves quantification of the processes of absorption, reflection, transmittance emittance, and scattering of radiation. The fundamental laws of radiation are not covered in depth here except where they are of direct relevance to this study. Such background can be found in the comprehensive reviews of Kondratyev (1969), Gates (1980) and Geiger (1965). Each of the above processes is controlled by the wavelength of radiation and the properties of both the Earth's surface and the atmosphere along the length of the radiant path. Since the influence of the state of the atmosphere on radiation fluctuates with such irregularly variable quantities as cloud amount, water vapour content and atmospheric particulates, precise quantification of atmospheric radiation is extremely difficult. For the purposes of evaluating the transfer of radiant energy into fluxes of heat and moisture, two broad wavebands of radiation are generally considered discretely. The sun may be regarded as a black body whose surface radiates at about 6000 K. It follows from the laws of Planck and Wien that the maximum intensity in solar radiation occurs at about 0.5 μm, and almost the entire solar emission is contained between 0.15 and 4 μm. The surface of the earth is approximately a black body at 300 K, and the maximum intensity is in radiation of wavelength about 10 μm, with the outer limits for most applications being set at 3 and 80 μm (Sutton 1953). The virtual non-overlapping of the two spectral bands enables an effective distinction to be made between shortwave (solar) radiation and longwave (terrestrial or infrared) radiation.

A simplistic representation of radiative fluxes at the Earth's surface is presented in Figure 2.1. The radiation budget for any point on the Earth's surface can be expressed as:

$$Q^* = K^* + L^* = K\downarrow + K\uparrow + L\downarrow + L\uparrow \qquad (2.1)$$

where Q^*, K^* and L^* are net allwave, shortwave and longwave radiation respectively. $K\downarrow$ is incident shortwave radiation, while $K\uparrow$ is reflected shortwave radiation and is governed by the magnitude of $K\downarrow$ and the proportion of reflected $K\downarrow$, which is determined by the surface albedo (α). $L\downarrow$ is incident longwave radiation and $L\uparrow$ is longwave radiation made up of thermal radiation emitted from the surface and the portion of $L\downarrow$ that is reflected, determined by the surface emissivity (ε). The sign convention used here is that downward fluxes are positive while upward fluxes are negative. The following sections consider each term of this equation and how they are characterised in complex terrain.

2.2.1 Shortwave radiation

At the top of the atmosphere, the intensity of solar radiation on a plane perpendicular to the sun's rays is relatively constant at approximately 1360 Wm^{-2} (Gates 1980). Incident at the surface, shortwave radiation is somewhat less and made up of direct beam (K_S), diffuse beam (K_D) and, in complex terrain, reflected beam (K_r) components. Solar radiation is not widely measured, but the fact that it is strongly governed by K_S and that the apparent solar path relative to any location can be simply and easily calculated with great accuracy suggests radiation indices can be usefully used to compare sites (Fleming 1987). This is significantly truer of clear-sky days than overcast days, since clouds have a strongly negative influence on the ratio of K_S to K_D. This section considers the

governing parameters in the surface shortwave radiation budget and methods used to estimate them. These estimates are valuable because the surface radiation budget exerts a strong influence on surface energy fluxes.

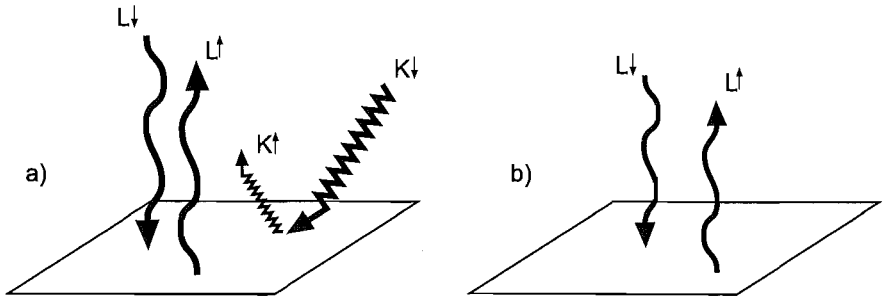

Figure 2.1 Schematic representation of the radiation budget at a simple ground surface a) by day, b) at night (after Oke 1987).

Extraterrestrial solar radiation

The amount of sunlight incident on a horizontal surface just outside the Earth's atmosphere (K_{oh}) can be determined by combining a series of fundamental angles as defined in astronomy and related to one another by means of spherical trigonometry, with the solar constant. The magnitude of K_{oh} is a function of the time of year, time of day, and geographical latitude as follows:

$$K_{oh} = (I / r^2) \cos z \qquad (2.2)$$

where I is the solar constant (~1360 Wm^{-2}), r is the ratio of the Earth-Sun distance to its mean, and z is the zenith angle (Gates 1980, Fleming 1987). The magnitude of r^2 varies continuously throughout the year but never deviates more than 3.5% from 1 (Gates 1980). The zenith angle is the angle of the solar beam relative to surface-normal and can be estimated from:

$$\cos z = \sin \Phi \sin \delta + \cos \Phi \cos \delta \cos h \qquad (2.3)$$

where Φ is the latitude of the observer (degrees), δ is the declination of the sun (ranging to 23.5° either side of the equator), and h is the hour angle of the sun from solar noon (Wilson and Gallant 2000). Figure 2.2 illustrates the daily magnitudes of shortwave irradiance on a horizontal surface at the top of the atmosphere as a function of latitude and month. It is clear from this figure that northern and southern hemispheres have opposing solar seasons and that the relative importance of solar seasonality increases with distance from the equator.

Shortwave radiation on a horizontal surface

Since the atmosphere is only partly transparent to solar radiation, the amount reaching the surface is reduced from that calculated above. Some of this radiation is attenuated by scattering, absorption and reflection due to the gaseous and particulate constituents of the atmosphere. Also influencing this attenuation is the path length through the atmosphere, a function of the solar elevation angle and altitude (Lowry 1980). The molecular constituents of the atmosphere, along with water droplets, dust and other particulate matter, scatter the direct solar beam and create a hemispherical (diffuse) source of radiant energy. In addition, the direct and diffuse irradiance are both reduced

as a result of direct absorption and reflectance to space along the radiant beam's path through the atmosphere to the ground (Linacre 1992). The most common approach to estimating the transmission properties of a homogeneous and cloudless atmosphere is through Beers law:

$$K_{Sh} = K_{oh}\tau^{m} \tag{2.4}$$

where K_{Sh} is the direct beam shortwave irradiance incident on a flat surface under clear skies, τ is the transmission coefficient or fraction of radiation incident at the top of the atmosphere which reaches the ground along the vertical path and m is the ratio of the path length in the direction of the sun at zenith angle z to the path length in the vertical direction and is given by $m = \sec z = 1/\cos z$ (Gates 1980, Linacre 1992). However, m is only accurately calculated this way when the zenith angle is less than about 60°. When the sun is lower in the sky, the curvature of the Earth reduces the solar path length relative to the depth of the atmosphere in the zenith direction (Gates 1980). Over changing surface elevations, a lapse rate of attenuation also applies to surface irradiance and this has been commonly observed (*e.g.* Whiteman 1989a, Hastenrath 1997). However, the local transmission coefficient (at zenith) also varies spatially depending on the properties of the atmosphere, particularly atmospheric aerosols. For example, Greenland and Clothier (1975) found lower incident solar radiation in the New Zealand Southern Alps than in Christchurch (780 m lower) during spring and early summer in clear sky conditions. This was related to much higher atmospheric humidity in the mountains during these months.

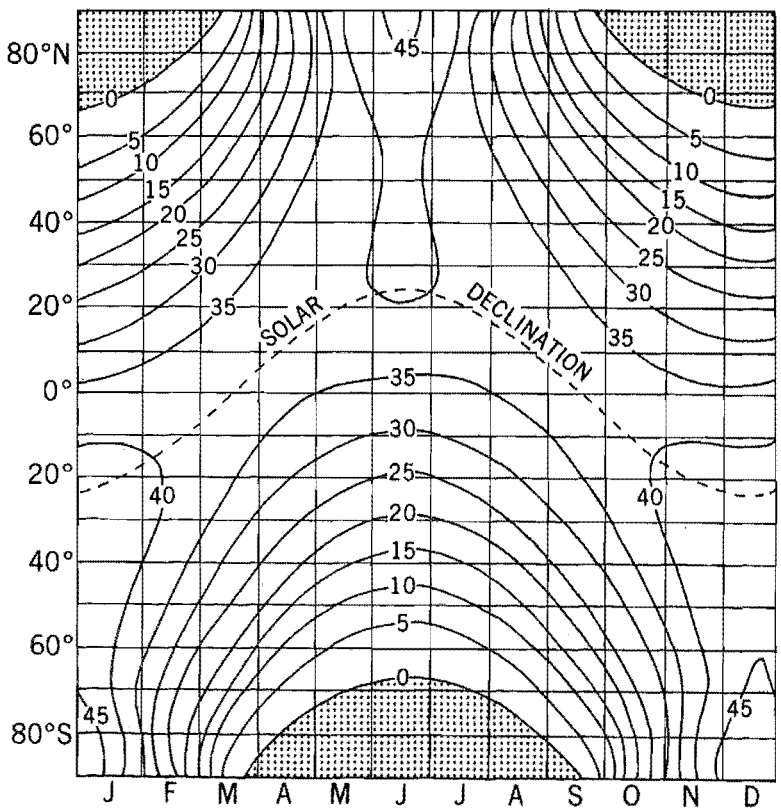

Figure 2.2 Daily total solar radiation incident on a unit horizontal surface at the top of the atmosphere as a function of latitude and date in 10^6 MJ m^{-2}. Shaded areas represent no solar illumination (from Peixoto and Oort 1992).

Diffuse shortwave radiation

Diffuse shortwave radiation is generated when direct beam radiation is scattered on its path through the atmosphere. It is therefore, a function of the scattering properties of the atmosphere and the path length and is defined by Liu and Jordan (1963) as:

$$K_D = (0.271 - 0.294\tau^m)K_{oh} \tag{2.5}$$

which shows that diffuse radiation transmittance decreases as direct beam transmittance increases (Gates 1980). Linacre (1992) distinguished between 'skylight' diffuse radiant energy, which is isotropic and circumsolar diffuse radiation, which comes from within approximately 5° of the direct solar beam. This distinction becomes important when evaluating irradiance on sloping surfaces as discussed in the following section. Linacre (1992) estimated that models which don't incorporate a circumsolar component, may generate errors as large as 40% when used to estimate irradiance on sloping sites.

Shortwave irradiance on sloping surfaces

Solar radiation received on a slope is comprised of three components; direct beam (K_S), diffuse beam (K_D) and that reflected from surrounding terrain (K_r). Direct beam radiation on surfaces of any orientation (K_S) can be defined as:

$$K_S = K_{Sh} \cos i \tag{2.6}$$

where i is the angle between the solar beam and normal to the sloping surface. This can be derived from:

$$\cos i = \cos s \cos z + \sin s \sin z \cos(A - A_s) \tag{2.7}$$

where s is the slope angle z the zenith angle, A is the solar azimuth angle and A_s the azimuth angle of the slope. These angles are illustrated in Figure 2.3. Slope and aspect effects are greatest during winter in middle latitudes and they tend to become smaller toward the equator and poles (Kondratyev 1977). Not included in the above calculation is the effect of shadowing caused by surrounding terrain. Equations 2.6 and 2.7 alone would derive a direct beam shortwave irradiance on a sunward facing slope, even if the sun were obstructed by a nearby mountain peak. If this was the case, direct beam irradiance would be removed so that $K{\downarrow}=K_D+K_r$. To determine the occurrence of this situation the sunward horizon angle relative to the solar elevation angle must be known. The circumsolar portion of diffuse beam radiation is similarly subjected to shadowing effects while the remaining skylight component of diffuse radiation will remain unmodified by the sloping surface since its direction is isotropic.

Complex terrain maintains a further influence on diffuse radiation through the effect that sloping surfaces and surrounding terrain have of reducing the sky view from hemispherical. This reduces the skylight component of diffuse beam radiation by the fraction of visible terrain in the overlying hemisphere. At the same time, this visible terrain provides the observation point with reflected shortwave radiation. The exact quantity of this depends on the albedo of the surrounding surfaces (which may be variable), the fraction of the hemisphere covered by terrain and the geometric relationships between each point of the visible terrain, the sun and the point of

observation. The complexity of evaluating this is clearly proportional to the complexity of the landscape, in terms of both shape and albedo. Given the relatively small magnitudes involved, this component is generally considered isotropic and calculated based on a mean albedo and fractional coverage (*e.g.* Fleming 1987). This is probably sufficient in many situations although significant errors might result, for example, when the observer is on a steep slope facing away from the sun but facing another steep slope with high albedo (*e.g.* fresh snow), which is facing towards the sun.

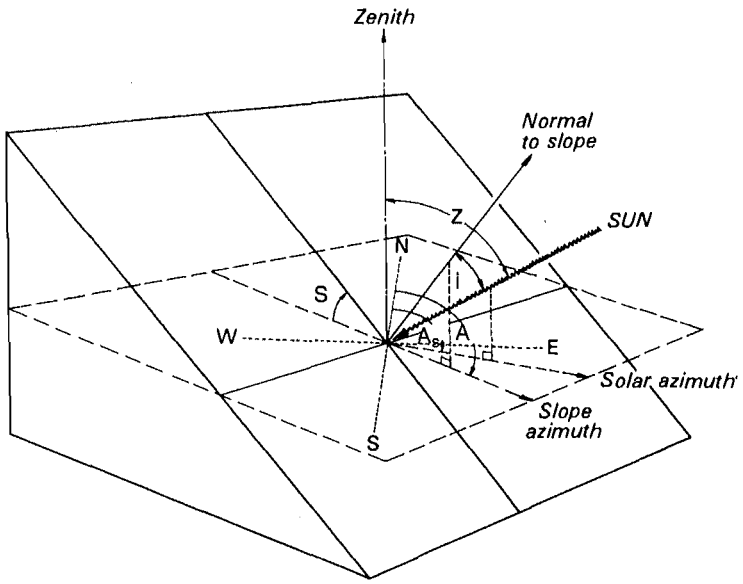

Figure 2.3 Schematic of solar beam irradiance on a sloping plane (from Oke 1987)

Sky-view factors can be estimated using photography or through radial measurements of horizon angles. The latter technique is typically used in complex topography, since it can be computed easily from accurate digital elevation data. The number of measurements taken is also proportional to the accuracy. The sky view factor (v) can be computed by averaging the cosine of the horizon angles (H_ϕ):

$$v = \frac{1}{n}\sum_{i=1}^{n} \cos H_\phi \qquad (2.8)$$

Clouds

The flux of direct and diffuse shortwave solar radiation incident at the Earth's surface is highly variable and difficult to predict when the sky is partially or totally obscured by clouds. Clouds are variable in form, size, composition, density, height, duration and location. Optically thin, transparent cirrus clouds have little influence on shortwave irradiance at the surface, whereas deep cumulonimbus clouds may reduce radiation to 1% of its clear sky value (Gates 1980). The most common approach to evaluating the effect of clouds on the surface radiation budget uses statistical averages of observational data collected over long periods of time. Kasten and Czeplak (1979, cited in Gates 1980) used 10 years of continuous records of global radiation and cloud observations to derive an empirical relationship between these variables. They found the ratio of global radiation as a function of cloud cover in oktas $G(N)$ to global radiation under clear skies $G(0)$ to be mostly independent of solar elevation angle and able to be parameterised by:

$$G(N)/G(0) = 1 - 0.75(N/8)^{3.4} \quad (2.9)$$

Clouds in complex terrain may display some spatial consistency where adiabatic cooling is sufficient to induce saturation and cloud formation as air rises over a topographic feature, due either to forced or thermal convection. This will have spatial implications (and temporal in the case of thermal convection) for incident short and longwave radiation over ridges and hills.

Albedo

Albedo has so far been evaluated as a static variable in these discussions. In reality, the albedo of a surface may display significant changes over space and time. This variability can impact significantly on the overall surface radiation budget. In the diurnal cycle, the albedo of most surfaces changes as a function of solar angle, although for many surfaces this is negligible. This effect is most strongly evident in water where greater portions of incident radiation are transmitted down into the water column at lower zenith angles. Kondratyev (1969) presented albedo data ranging from 0.05 to 0.65 as a function of zenith angle in seawater. A similar effect is found in grasses due to the vertically oriented canopy structure. For New Zealand snow tussock, Brown and Fitzharris (1993) presented diurnal albedo ranges from 0.15 to 0.35.

Additional changes over time result from alteration of the structure of the surface due to the presence of water (after rain or dew fall), wind (*e.g.* in water or vegetation) or melting (*e.g.* in snow or ice). Where the surface changes shape due to the force of the wind, complex patterns may result, related to the timescale of individual eddies, but they tend to average out over longer time intervals. This effect diminishes that of solar angles due to the continually changing incident angles that may occur on wind blown waves or canopy structure. Where snow and ice surfaces show a diurnal pattern of melt and freeze, albedo is diminished by the rougher melt-affected surface. This may produce a hysteresis effect in diurnal albedo traces over snow or ice. Surface albedo can be altered dramatically by changes in the surface cover due to frost, snowfall or leaf fall in deciduous trees, or it may be subtler due to changes in the growing season or soil moisture.

Since the incident angle of solar radiation influences the albedo of many surfaces, complex topography introduces a spatial dimension to this effect. In order to account for this, the relationship between incident angle and albedo must be established and applied to all surfaces for independent times through the day. Of greater consequence to spatial variability of albedo is the large range in spectral properties of different surfaces that are found in the natural landscape. These alone can create differences of an order of magnitude over small spatial scales. Observed albedos for many different surfaces are presented in Oke (1987) and Kondratyev (1969), and range from 0.05 for water bodies to 0.9 for fresh snow (Oke 1987). Even in a relatively uniform ecosystem, Goodin and Isard (1989) found that the albedo of alpine tundra surfaces showed considerable temporal and spatial variability (of the order of 25% of mean values). Temporal variability was caused particularly by varying moisture conditions and spatial variations by surface heterogeneity.

2.2.2 Longwave radiation

Longwave radiative fluxes at the Earth's surface are controlled primarily by the temperatures of the surface and the atmosphere and their respective emissivities. This is defined in the Stefan-Boltzmann equation:

$$L = \varepsilon \sigma T^4 \tag{2.10}$$

where ε is the emissivity coefficient, σ is the Stefan-Boltzmann constant (5.67×10^{-8} Wm^{-2} K^{-4}) and T is the surface temperature of the radiating body (K). For most Earth surfaces it is reasonably simple to derive $L\uparrow$, since surface temperature is reasonably easy to measure and emissivity values vary by relatively small amounts over natural surfaces and have been tabulated in many standard texts (*e.g.* Geiger 1965, Oke 1987). However, the surface longwave radiation emittance also includes the portion of reflected incoming longwave radiation, which is partly a function of surface emissivity (ε_0) so that:

$$L\uparrow = \varepsilon_0 \sigma T_0^4 + (1-\varepsilon_0) L\downarrow \tag{2.11}$$

By contrast the process of longwave radiative transfer in the atmosphere is very complex. At all levels, the atmosphere absorbs radiation emitted from the surface below and all other levels through the atmospheric column. Absorption and emission of longwave radiation in the atmosphere occurs primarily through its constituents; water vapour, carbon dioxide and ozone. Each of these molecules absorb differentially in different wavelengths (Oke 1987, Geiger 1965), with water vapour most important and becoming significantly greater if liquid or solid water (clouds) is present. The atmosphere at all heights emits longwave radiation consistent with its temperature and emissivity, in accordance with the Stefan-Boltzmann equation. The processes of absorption and re-emission take place on a continuous basis throughout the atmosphere, but quantitatively they are most important in the lowest layers where the concentrations of water vapour and carbon dioxide are greatest. For this reason, atmospheric variables measured near the surface are often used to quantify the downward flux of longwave radiation. Longwave irradiance at the surface is also typically assumed to be isotropic but in reality increases away from zenith towards the horizon. Although this might have negligible effects in open areas, when the observer is surrounded by terrain it is the portion of sky from which the greatest radiant energy is received that is obstructed. However, since the surrounding terrain is also continuously emitting longwave radiation, and since it will typically be warmer than the lower atmosphere and with a larger emissivity, longwave irradiance is enhanced. In order to determine the magnitude of this effect, the fraction of the sky hemisphere obstructed by terrain requires calculation, as well as the relative emission of longwave radiation from both sky and terrain. Longwave irradiance at the surface then can be calculated by:

$$L\downarrow = \varepsilon_a \sigma T_a^4 v + (1-v) L\uparrow \tag{2.12}$$

where T_a is the air temperature, v is the skyview fraction and ε_a is atmospheric emissivity, defined empirically by Idso (1981) for cloudless skies as:

$$\varepsilon_a = 0.7 + 5.95 \times 10^{-5} e_a \exp(1500/T_a) \quad (2.13)$$

where e is the vapour pressure (hPa) and the subscript $_a$ refers to the atmosphere.

The range of radiation components important to net radiation in complex terrain is summarised schematically in Figure 2.4. Given the large range of flux densities expected for the individual components of the surface radiation budget in complex terrain, it is not surprising that observations of net radiation in complex terrain have yielded strongly contrasting and sometimes contradictory results. The following section provides some examples.

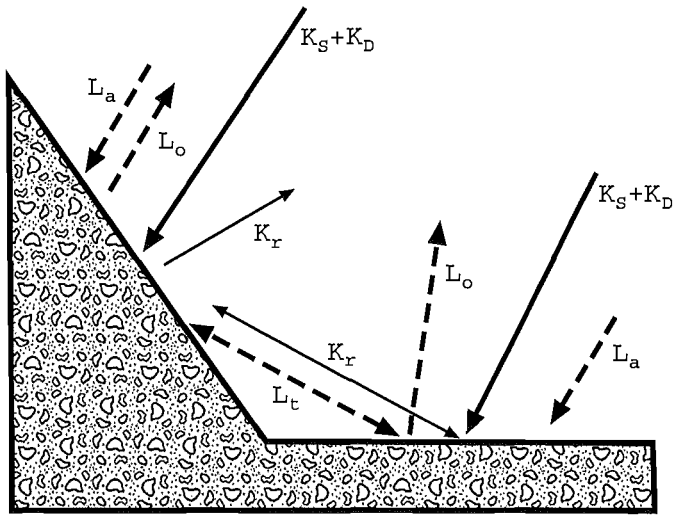

Figure 2.4 Schematic representation of short and longwave components of the surface radiation budget in complex topography, where L_a is incident longwave radiation from the atmosphere, L_t is incident longwave radiation from surrounding terrain and L_o is outgoing longwave radiation (adapted from Barry 1992).

2.2.3 Net radiation observed in complex terrain

Both temporal and spatial variability of Q^* in complex terrain is well revealed in field measurements. Even at the catchment scale, Whiteman *et al.* (1989a) showed large inter-site differences between five radiation budget stations in daily totals of net radiation associated with topographic effects. This range was found to be larger than standard deviations of the daily totals from a single site computed over a 16-day period of variable weather. The topographic effects included elevation, slope angle and aspect, surface cover and sky view factor.

In the Austrian Alps using long-term data, Rott (1979) found solar and net radiation to be 10% and 15% greater respectively at 2560 m than 1960 m. This was concluded to be a combined result of lower horizon screening and lower atmospheric extinction of shortwave radiation at the higher station. Similarly in the Dischma valley, Switzerland, Konzelmann *et al.* (1997) reported Q^* to be 25% greater at a station at 2220 m than one at 1680 m. Since the albedo and longwave radiation budget did not differ significantly, Q^* was estimated to be linearly dependant on global radiation. Conversely, in an investigation using five energy balance stations on the east slope of the Rhine Valley, Wenzel *et al.* (1997) found a slight decrease in net radiation with increasing altitude (100 – 1200 m). This was attributed to a decrease in net longwave radiation, because air temperature decreased faster than the surface temperature with height.

Also working in the Rhine Valley, Kalthoff *et al* (1999) found a similar altitudinal result to Wenzel *et al.* (1997) when integrating 36 stations over 3 years. However, they noted considerable spatial and temporal variability (the coefficient of determination (R^2) of this relationship was only 0.4), related primarily to two factors. The first was the effect of spatially varying landuse on albedo and seasonally varying snow cover. The second was the increased clouds at both low levels in winter due to fog, and higher in the mountains in summer, due to convective activity. The overall decrease in Q^* with height by approximately 18 W m^2 km^{-1} was found to be the sum of somewhat smaller decreases in K^* (~11 W m^{-2} km^{-1}) and L^* (~7 W m^{-2} km^{-1}) with height. The former was seen to be a function of the higher snow induced albedo in winter and convective activity in summer in the mountains while the latter was thought to be the result of vertical decreases in temperature and humidity in the atmosphere. Kalthoff *et al* (1999) also considered the spatial variability of net radiation as a function of precipitation. Despite a 590 mm variation in annual precipitation in the study area, they found deviations of only 4% from the mean value of the radiation balance. Lower radiation balances were found to occur with both low and high precipitation. The former is dependant on the higher albedo of dry soil and the latter is associated with the cloudiness that is concurrent with precipitation.

2.3 The surface energy balance in complex terrain

Since the First Law of Thermodynamics states that energy cannot be created or destroyed, only converted from one form to another, the imbalance of the radiation budget at any given time must be accounted for. This section examines the forms and behaviour of energy fluxes that occur to balance the net surplus or deficit that results from the radiation budget. In this way, Q^* is not only the end result of the radiation budget but the basic input to the surface energy balance. This balance is achieved by a combination of turbulent exchange to or from the atmosphere, either as sensible (Q_H) or latent heat (Q_E) and conduction to or from the underlying substrate (Q_G). Thus, the surface energy balance for a simple, non-vegetated surface is:

$$Q^* = Q_H + Q_E + Q_G \qquad (2.14)$$

The sign convention employed in this study is that fluxes directed away from the surface are positive into both the atmosphere and the substrate, while those directed toward the surface are negative. Figure 2.5 presents typical energy balances for a simple bare surface under clear skies. By day surplus net radiation is offset by conduction of heat into the ground and convection of heat and moisture into the atmosphere. By night, the radiative deficit is offset by a return of heat from the substrate and turbulent fluxes directed toward the surface.

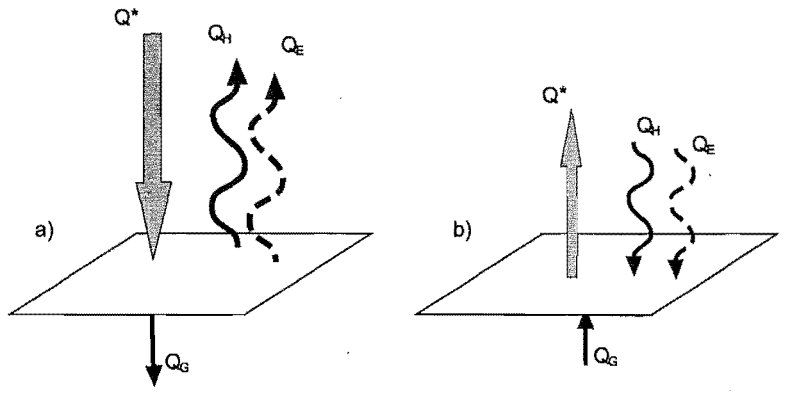

Figure 2.5 Schematic representation of the energy balance of a simple ground surface under clear skies a) by day and b) by night (after Oke 1987).

In the case of many natural and human-made surfaces, it is not possible to consider the surface to be 2-dimensional, since the 3-dimensional structure of the surface means energy fluxes occur within a volume. Such surfaces include vegetation, water (liquid and solid) and urban areas. Although the nature of fluxes for these surface types varies considerably, a common feature is the storage of energy within the volume (ΔQ_S) and the advection of energy through the sidewalls of the volume (ΔQ_A) (Figure 2.6). Thus the surface energy balance for a given volume is:

$$Q^* = Q_H + Q_E + Q_G + \Delta Q_S + \Delta Q_A \,. \tag{2.15}$$

2.3.1 Deriving surface heat fluxes

The spatial flux of any entity can generally be derived by multiplying the gradient of that entity by its ability to be transported (conductivity and diffusivity). Thus, despite the fact that the forms of energy and their methods of transport differ, the fluxes on the right hand side of Eq. 2.14 have analogous derivations. The large differences typically found in magnitudes between these fluxes, relate to the different strengths of both their gradients and conductivities/diffusivities. This section will expand on these derivations, considering first, the role of conduction and second, the role of turbulent transport.

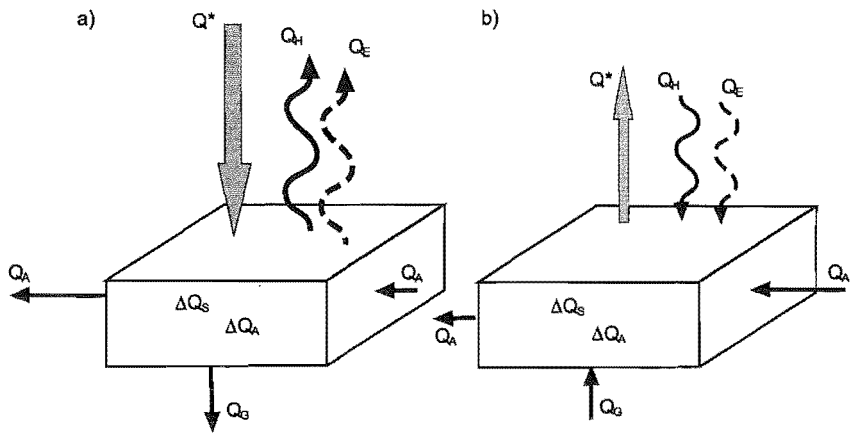

Figure 2.6 Schematic representation of the energy balance of a volume under clear skies a) by day and b) by night (after Oke 1987).

Conductive sensible heat flux

Conduction of energy away from and toward the surface dominates both in the surface substrate and in the very thin layer of air adjacent to the surface known as the laminar boundary layer. Above the laminar boundary layer, at a height governed by speed of flow, distance and viscosity, airflow changes from laminar to turbulent and transport changes from molecular conduction to turbulent diffusion. However, energy fluxes are roughly equivalent through both the laminar and turbulent parts of the surface layer because the lower efficiency of molecular transport is made up for by larger energy concentration gradients. Since it is easier to measure energy fluxes higher in the surface layer where they are also spatially representative of larger areas, turbulent fluxes have received considerably larger attention than conductive fluxes in the atmosphere. Therefore, with regard to conductive energy transport, this section concentrates on the flow of energy through the sub-surface layers.

The sensible heat flux density through sub-surface layers (Q_G) can be expressed as Fourier's law:

$$Q_G = -k_s \frac{\partial \overline{T}_s}{\partial z} \tag{2.16}$$

where k_s is thermal conductivity ($Wm^{-1} K^{-1}$), $\partial \overline{T}_s / \partial z$ is the change in soil temperature (°C or K) over the change in depth (m) into the substrate. The negative sign indicates that the flux is in the direction of decreasing temperature so that when $\partial \overline{T}_s / \partial z$ is negative, the flux is away from the surface and consequently positive.

Thermal conductivity is defined as the quantity of heat (J) flowing through a unit cross-sectional area (m^2) of the substance in unit time (s), when there exists a temperature gradient of $1° m^{-1}$ perpendicular to it. In soils, k_s depends on the conductivity of the soil particles and the relative amounts of air (porosity) and water that is contained in the soil volume, since each substance has very different magnitudes of k_s. Soil moisture content has the greatest impact at smaller temporal and spatial scales. Moisture added to the soil increases the magnitude of k_s through the dual effects of increasing the thermal contact between individual soil grains and replacing pore air with water, which has a much higher k_s.

Turbulent sensible heat flux

The flux of sensible heat (Q_H) in the turbulent surface layer is given by:

$$Q_H = -C_a K_H \left(\frac{\partial \overline{\theta}}{\partial z} \right) \tag{2.17}$$

where C_a is the heat capacity of air ($J m^{-3} K^{-1}$), K_H is eddy conductivity for heat ($m^2 s^{-1}$) and $\partial \overline{\theta} / \partial z$ is the vertical gradient in potential temperature (°C or $K m^{-1}$). Thus z refers to distance away from the surface. The form of this equation is directly analogous to Eq. 2.16, where a negative potential temperature gradient (lapse) produces a positive Q_H. Heat capacity of air is temperature dependent since $C_a = \rho c_p$ where ρ is air density (kg

m^{-3}), which is temperature dependent, and c_p is the specific heat at constant pressure (J kg^{-1} K^{-1}). This variable is dependent on the water vapour content through the relationship $c_p = c_{p(dry)}(1+0.84r)$, where r is the mixing ratio of water vapour to air (g g^{-1}). The value of K_H is a measure of the ability of turbulent eddies to transport heat and is dependent on the aerodynamic properties of the surface such as the roughness length (z_0) and zero plane displacement (z_d), as well as wind speed, atmospheric stability and height above ground.

The relative partitioning of sensible heat flux at the surface into the substrate and into the atmosphere is a function of the ratio of the thermal admittance of the substrate (μ_s) to that of the atmosphere (μ_a). Thermal admittance is a measure of the ability of a surface to accept or release heat and is expressed as a temperature change produced by a given heat flux change (J m^{-2} $s^{-1/2}$ K^{-1}). Thus:

$$\frac{Q_G}{Q_H} = \frac{\mu_s}{\mu_a} = \frac{C_s \kappa_{Hs}^{1/2}}{C_a K_H^{1/2}} \qquad (2.18)$$

where C_s is the specific heat of the soil and κ_{Hs} is the molecular diffusion coefficient for heat in the substrate. Since K_H reaches much higher magnitudes than κ_{Hs} in the natural environment, the ratio Q_G/Q_H is most strongly determined by the state of turbulence. It is for this reason that turbulent exchange tends to dominate daytime fluxes, when surface heating generates convection. In more stable nocturnal conditions, turbulent fluxes are purely mechanically generated and hence much smaller in general. Consequently, conductive transport plays a more important role during the night. The secondary determinant of Q_G/Q_H is soil moisture content since it affects both κ_{Hs} and C_s, producing a positive relationship with μ_s.

Latent heat flux

Latent heat (Q_E) is released or stored when water phase changes occur. The most important forms of latent heat flux in the surface energy balance are evaporation and transpiration, which involve a mass flux from the surface into the atmosphere and results from a vapour gradient in the surface layer. An opposite gradient exists when dewfall or frost occur at night, although this is minimal by comparison to evaporative fluxes. The latent heat flux can be derived from:

$$Q_E = -L_v K_V \left(\frac{\partial \overline{\rho}_v}{\partial z} \right) \qquad (2.19)$$

where, L_v is the latent heat of vaporisation (J kg^{-1}), K_V is the eddy diffusivity for water vapour (m^2 s^{-1}) and $\partial \overline{\rho}_v / \partial z$ is the vertical gradient in vapour density (kg m^{-3} m^{-1}). This process depends on the availability of water, as well as the availability of energy for phase change and a turbulent atmosphere for transport.

In addition, plants yield significant physical control on water vapour flux and the processes of photosynthesis and respiration can play an active role in determining the climate near the surface (Oke 1987). Although it is also species-dependent, a positive relationship exists between biomass and the strength of this role. The dominant control is transpiration, which occurs as a consequence of respiration. This is because

respiration requires the opening of stomata, which allows the evaporation of internal plant moisture (transpiration). The climatic significance of stomata is their ability to open and shut, so that they act as regulatory 'valves' in the transfer of water vapour.

This control is frequently considered analogous to resistance in an electric circuit. Using the relationship given by Ohms Law, the conductance of an entity between the leaf and adjacent atmosphere is a function of the concentration difference and the resistance to flow. The total resistance for any surface is the sum of canopy (or surface) resistance and aerodynamic (or boundary layer) resistance. Stomatal resistance plays a critical role in canopy resistance, and magnitudes for various vegetated surfaces can be found in Oke (1987) and Monteith and Unsworth (1990).

At night, the stomata are typically closed, but with sunlight the guard cells controlling the stomatal aperture operate to open the pore. The degree of opening is related to light intensity, the ambient temperature, vapour density and CO_2 concentration (Gates 1980). Furthermore plant water stress caused by excessive transpiration losses or depletion of soil moisture will decrease stomatal aperture size (increase stomatal resistance). Because of this mechanism, plant species have adapted to a range of light and moisture environments and it can be expected that stomatal resistance, as well as other physiological controls such as leaf roll, will be greater in drier environments.

Similarity principle and the Bowen ratio

It has often been assumed that eddies are approximately non-discriminatory with respect to the property being transported. This similarity principle holds that the diffusion coefficients for heat, water vapour, momentum and carbon dioxide are equivalent (Stull 1988). In recent years however, this assumption has been critically assessed and found to be invalid under certain conditions.

Bink (1996) showed that diffusivity was non-similar when temperature and vapour fluctuations were not highly, positively correlated and either temperature or humidity variations dominated the buoyant production of vertical motion. K_H / K_V was found to depart from unity to as high as 3 when temperature dominated (high β) and decreased to as low as 0.5 when vapour dominated (low β). McNaughton and Laubach (1998) examined advective influences on K_H / K_V over an irrigated crop downwind of a dry area and found non-similarity to result due to lack of full adjustment of turbulent transport processes to the new surface. This showed that the fetch to height requirement for similarity of diffusivities must be a great deal larger than is generally recognised. This effect was also noted by Bink (1996).

Since the magnitudes of turbulent exchanges tend to be much larger than conductive transfer through the substrate, the relative importance of sensible versus latent heat fluxes is key to characterising variability in surface climates. This has resulted in the formulation of the Bowen ratio (β) to describe energy partitioning:

$$\beta = \frac{Q_H}{Q_E}. \qquad (2.20)$$

At most times, β is most strongly controlled by the availability of water for evaporation. For this reason, typical diurnal β values for the ocean are on the order of 0.1 while for deserts they are greater than 10 (Oke 1987). Also important is the relative strength of

the atmospheric heat and water sinks. Thus for a given surface temperature and moisture content, a cold moist atmosphere will strengthen the surface-air temperature gradient, and diminish the vapour gradient. Inspection of Eq. 2.17 and 2.19 illustrates that this favours Q_H rather than Q_E (assuming K_H and K_V are similar) and in turn, increases β (Eq. 2.20).

Considerable spatial variability in Q_H, Q_E and Q_G is clearly likely to result where large differences in surface and atmospheric properties exist. These include different thermal properties of the substrate such as thermal conductivity and admittance, different aerodynamic properties such as roughness length, different quantities of available moisture and different vegetative controls. In complex terrain, geomorphological, biogeographical and hydrological controls serve to generate considerable spatial variability in such properties. Many of these properties also vary over time, especially those governed by biological and hydrological processes. The dominant driver of temporal variability however, is regional to synoptic scale meteorological effects. Examples of energy balances observed over surfaces similar to those in this study are provided in Chapter Five. The following sections discuss the dominant controls and characteristics of temporal and spatial variability of energy balances in complex terrain.

2.3.2 Temporal variability

The strongest influence on the temporal variability of the surface energy budget comes from diurnal, seasonal and synoptic controls on the amounts of available energy in the form of net radiation (Section 2.2). However, these controls also exert significant influence on the relative partitioning of this energy. This comes from changes most strongly associated with surface hydrology and biology and the changes in the properties of the overlying airmass. In these ways both the gradients and transport capabilities for each energy flux are affected. The processes and characteristics associated with these changes are assessed with regard to climate (diurnal and seasonal) and meteorology respectively.

Climatological controls

Diurnal changes in the surface energy balance, assuming advective effects to be minimal (Section 2.3.4), are influenced most strongly by the diurnal movement of water to and from the surface. For this reason, the Bowen ratio has often been found to be relatively lower in the early morning as initial net radiation surplus is utilised in favour of evaporating dew or melting frost that has formed on the surface during the night. β increases as the supply of moisture diminishes through the morning until it is replenished at night. This effect only occurs if the surface and the atmosphere are favourable to dew or frost occurrence. This requires a relatively moist and shallow boundary layer atmosphere with enough turbulence to transport the moisture but not enough that substantial mixing with the drier atmosphere above occurs. Furthermore, it requires an increase in specific humidity with height, which seldom occurs over water or other saturated surfaces. Finally, the surface must be cool enough for condensation (dew) or freezing (frost) to occur. In a different process, localised convection may lead to precipitation occurrence in the afternoon or evening, enhancing soil moisture content and subsequently increasing Q_E relative to Q_H.

The requirement of solar radiation for photosynthesis means that transpiration is also linked with $K\downarrow$. Furthermore, as the air temperature increases so does the saturation deficit (D) increasing the water vapour gradient near the surface. However, vegetation

may respond by increasing stomatal resistance (Campbell 1989). Combined, these controls have been found to produce a positive correlation between Q^* and Q_E but with a plateau effect occurring during the hottest part of the day in response to higher D.

Seasonal change in the surface energy balance similarly occurs as a result of changes in soil moisture and biophysical changes to plant/atmosphere interactions through the growing season. The former is dominated by seasonal changes in the water balance which, assuming percolation doesn't remove water from the active substrate layer, can be expressed from the point of view of soil moisture content by:

$$\Delta S = p - E - \Delta r \tag{2.21}$$

where ΔS is the net change in soil moisture content, p is precipitation, E is evapotranspiration and Δr is the net runoff. E is proportional to Q_E and related by the latent heat of vaporisation, which is temperature-dependent. Seasonal controls on precipitation are typically governed by synoptic weather patterns (at least in the mid-latitudes). Synoptic patterns will therefore have downstream effects on seasonal β through precipitation. This was found to be the case in observations made over two surfaces in the Sahel (Verhoef *et al.* 1999). Net runoff (Δr) presents a negative feedback to soil moisture content since greater runoff tends to occur once a soil has become saturated. Furthermore, the intensity of the precipitation event has a strong positive correlation with runoff. A negative feedback mechanism exists between soil moisture and Q_E, since greater soil moisture content results in larger Q_E, which then diminishes the supply of soil moisture.

Physiological changes to vegetation in response to season vary widely with plant species. However most species share seasonal controls in growth rates, which affect transpiration. This results largely from the influence of solar radiation, in terms of both intensity due to changes in declination angle and duration due to length of day. Seasonal changes in canopy structure may influence surface roughness. This in turn, will change the eddy diffusivity of the surface layer over the course of the year. For a tussock grassland in the South Island of New Zealand, Campbell and Murray (1990) showed strong vegetative controls on transpiration with a consistent seasonal pattern in Q_E, which reached a peak in summer and a trough in winter. Soil moisture content also impacts on plant water stress and consequently on transpiration through the response of stomata. For example, water stress during the summer growing season over an alpine tundra site was considered to account for a decrease observed in the latent heat flux (Le Drew and Weller 1978).

Some of these parameters may also be controlled by human activity. Lyons *et al.* (1996) found a large reduction in sensible heat flux as a result of the replacement of native vegetation with agriculture in Western Australia. Kalthoff *et al.* (1999) found that within any one year the behaviour of crop areas in the Rhine Valley was characterised by elevated latent heat fluxes in the spring due to rapid growth and after harvest due to the exposure of bare soil. For boreal forest, Sun *et al.* (1997) found a summer maximum in latent heat flux, which they related to enhanced transpiration.

In conclusion, both diurnal and seasonal climatic controls on the surface energy balance may yield significant ranges of magnitudes. The annual total as well as the ratio of diurnal to seasonal controls depends on the latitude and is higher at lower latitudes.

Other influences include continentality, elevation and dominant synoptic meteorology of the location as well as the characteristics of vegetation cover.

Meteorological controls

The difference in airmass properties that are associated with different synoptic systems provide considerable variability in the surface energy balance for a given site. Synoptic systems may influence almost every aspect of the surface energy budget. The primary control is on the radiation budget through radiative properties of clouds. Furthermore, the nature of the surface may be affected in terms of soil moisture or snow cover. The latter, for example, influences radiative properties as well as surface temperature, water content, roughness and atmospheric stability. With regard to Eq. 2.18 and 2.20, the transport of synoptic-specific airmass characteristics could affect both the gradients in terms of the thermal and humidity properties of the broader scale flow and the eddy diffusivity through both wind speed and atmospheric stability. Greenland (1973) noted marked variability of responses of the surface energy balance to different synoptic situations in a study in the Southern Alps of New Zealand. Furthermore, he found variability between seasons with the same synoptic pattern and variability within a single synoptic event (the passage of a cold front). He also observed surface fluxes to be influenced by the mesoscale effect of foehn wind. Here, very low β were associated with the warm, dry and gusty conditions produced by the foehn 'Nor'wester'. Negative Bowen ratios were also found on occasions due to the reversal of temperature gradients toward the surface. Higher occurrence of this has been found in studies of the same wind type, to the east of the Southern Alps on the Canterbury Plains near sea level where the foehn effect is greater (Lamb 1970). Overall, Greenland (1973) recorded daily mean Bowen ratios associated with different synoptic situations ranging from 0.15 to 6.1 with negative values associated with foehn conditions down to –0.18.

2.3.3.Spatial variability

It was emphasised in Section 2.2 that variability in radiative fluxes can be considerable over small spatial scales in complex terrain. This is due to geometric complexity in the sun-surface relationship, elevation effects and the differing radiative properties of varying surface types. Since Q^* is the basic input to the energy balance, it is clear that the magnitudes of Q_H, Q_E and Q_G will vary considerably in complex terrain as a consequence of variability in the radiation budget. Further to this however, is the influence that complex terrain yields on the partitioning of Q^*. This is considered in the following sections with regard firstly, to topography and secondly, to surface heterogeneity.

Topographic controls

Topography perturbs practically every process and variable relevant to the surface energy balance including air temperature, saturation deficit, wind (both mean and turbulent fields), cloudiness and precipitation, and properties of the surface. An exhaustive review of all the possible combinations of these is beyond the scope of this section. However, it is important to isolate the key generalisations that can be made about topographic controls, in order to assess their relevance to surface energy exchanges. These will be considered with respect to elevation and topographic shape. Following this, evaluation of the response of surface energy balances will be discussed with reference to observational and modelling studies.

In the free troposphere, temperature lapses with height due to the decrease of pressure in accordance with the equation of state and the hydrostatic equation. This yields a dry adiabatic lapse rate with a mean value of about 9.8° C km^{-1}. Further, moister and warmer atmospheres have a slower lapse rate since condensation releases latent heat. The saturated adiabatic lapse rate ranges from about 4.0° C km^{-1} in warm moist air close to sea level to 7.0° C km^{-1} in cool dry air at high altitudes. (Sturman and Tapper 1996). In the boundary layers of complex terrain these approximations become difficult due to the influence of the terrain on boundary layer structure. This structure shows significant change on the diurnal time scale, particularly when synoptic pressure gradients are weak.

By comparison with the surrounding atmosphere, the air adjacent to a mountain slope is affected by radiative and turbulent heat exchanges that modify the temperature structure over small spatial and temporal scales. This includes near adiabatic conditions by day and nocturnal inversions at night. This may also be affected seasonally by airmass types. For example, continental polar air in Japan in winter produces stronger lapses over mountainous areas than warm subtropical airmasses in summer (Yoshino 1966). Airmasses may be influenced by the topography itself in generating foehn conditions or cold air drainage and ponding, thus affecting the vertical temperature structure. In contrast to Yoshino's findings, in the Austrian Alps, von Hann (1906, cited in Barry 1992) found the lapses between stations at 1600 and 3106 m to be stronger in summer and during the day than in winter and during the night. Considerable differences may occur in vertical lapses due to location, mountain size and configuration. Tabony (1985) presented significantly different temperature profiles from three idealised mountain sizes. He related the differences to the amount of mixing that could occur with the free tropospheric air. This may be extended to the location of the profile within a mountain range. The mass-elevation effect, introduced by de Quervain (1904, cited in Barry 1992) accounts for the observed tendency for temperature related parameters such as tree line and snowline to occur at higher elevations in the central Alps than on their outer margins.

The exponential decrease of water vapour with height in the free troposphere is also significantly perturbed by mountainous terrain. In general, greater amounts of atmospheric moisture are present in mountain atmospheres than in the free troposphere at the same elevation as well as orographic effects. As with temperature this is due to the additional sources provided by evapotranspiration at the surface. Atmospheric moisture is important to surface energy balances by influencing the saturation deficit which partially controls rates of latent heat flux.

Wind velocity is strongly influenced by complex terrain in association with both topographic shape and altitude effects. In the mid-latitudes wind speed on average increases with height due to the characteristics of the global westerly wind belts (Barry 1992). When these westerlies meet mountains they are influenced by forces of compression and friction, which have opposing effects on wind speed. Isolated peaks and exposed ridges experience high average and extreme speeds as a result of the limited frictional effect of the terrain on the motion of the free air. This can be compared with sheltered valleys where relatively weak average winds can occur. The effects of exposure are also strongly influenced by atmospheric boundary layer structure. In unstable conditions turbulent eddies transport momentum easily and stronger wind speeds are experienced in typically sheltered locations. Conversely, stable atmospheres reduce downward flux of momentum to the point where entire valley atmospheres may become decoupled from the overlying airflow. According to Hunt and

Richards (1984) the threshold between ventilation and stagnation in a valley depends on the ratio between the separation distance, the lee wavelength and the ratio of separation length to valley width.

The role of relief in modifying the wind velocity over complex terrain has been the focus of numerous studies (*e.g.* Hunt *et al.* 1978, Carlson and Foster 1986, Eckman *et al.* 1992). Surface fluxes are a consequence of complex interactions between variations in the flow (themselves complex and including flow separation) and the surface energy balance. The accentuated vertical wind profile near the ground that results in areas of terrain with stronger wind speeds increases the vertical fluxes of heat and moisture from the mechanical generation of turbulence. Isard (1987) also considered a single hill in an observational study to determine the impact of local convergence and divergence of airflow on turbulent transfer. He found strong linear relationships between wind speed and friction velocity and subsequently transfer of momentum. Thus an important term in surface energy budgets was found to vary systematically in relation to topographic controls on wind speed. In addition to relief and elevation, McCutchan and Fox (1986) showed that the effect of aspect (acting to generate slope winds) exceeded that of elevation on wind velocity and, to a lesser degree, on temperature on a conical-shaped mountain. They also showed that ambient wind speeds in excess of 5 m s^{-1} eliminated any differences associated with slope, aspect or elevation.

In addition to atmospheric variables, topography has strong controls on surface properties through geomorphological, ecological and hydrological processes. Soils are typically shallower, coarser textured and less nutrient-rich on hillcrests than in valleys. Slope angles also influence soil depth through the frequency of disturbance by mass movement. Soil water content is often strongly, but not simply correlated with topography. These factors act together with modulations in the microclimate to create ecological changes with topography. The changes in surface properties are typically much more severe over vertical than horizontal distances. For example, Raupach and Finnegan (1997) pointed out that vertical ecological variations on a 3000 m mountain range in Arizona are similar to horizontal variations along a 2000 km north-south transect from Mexico to Canada. The effect of surface heterogeneity is considered in more detail in the following sections.

A very simplified schematic of the combined surface and atmospheric influences on the latent heat flux over idealised sinusoidal ridges in non-stratified flow is presented in Figure 2.7. Both the solar and net irradiances are greatest on sunny slopes and therefore quadrature with the elevation. The near surface air temperature varies largely through adiabatic heating and cooling, and so is in antiphase with the elevation. Saturation deficit, responding mainly to air temperature, is also in antiphase. Since the flow is non-stratified, the perturbations in near surface wind speed and surface stress are both nearly in phase with the elevation (maxima occur slightly upwind of the crests). Assuming the surface to be uniformly vegetated by a single species, the surface resistance is likely to vary in phase with the elevation because soil water deficits and plant water stresses are likely to be lowest in the valleys and highest on the crests. Even in this simplified illustration, the effect of all these differentially phased perturbations on the latent heat flux is clearly complex, and depends on which of the perturbations in forcing variables dominates the evaporation perturbation.

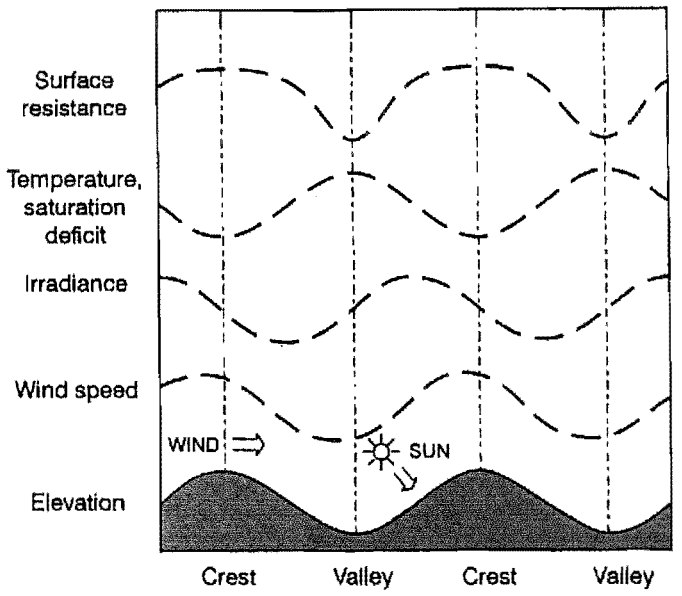

Figure 2.7 Typical topographically induced perturbations in net irradiance, near surface air temperature, saturation deficit, wind speed and surface resistance, for non-stratified flow over a series of ridges normal to the wind, with the sun shining on upslopes (from Raupach and Finnigan 1997).

The effect of topography on the surface energy balance is likely to be significant given the variability found in the parameters discussed above. However, relatively few studies have been conducted that focus specifically on the energy balance. Two studies used Budkyo's (1958) methods for calculating annual values of turbulent heat fluxes with respect to altitude from measured meteorological parameters and produced contrasting results. The first (Borzenkova 1965, cited in Barry 1992), for both the Greater Caucuses and Armyanski Mountains found a consistent decrease in the Bowen ratio with altitude. This was thought to be associated with the increase in available moisture and the decrease in air temperature relative to surface temperature with height. The second study (Plesko and Sinik 1978), found the opposite to occur in Croatia. In winter, both turbulent fluxes as well as net radiation were found to vary little with altitude. However in summer, the Bowen ratio was constant to about 600 m and then increased steadily. This was due to a consistent increase in sensible heat flux in response to increased advection effects and an initial increase in latent heat flux followed by a decrease above about 600 m. The behaviour of the latent heat flux was considered to be the result of increased precipitation initially, but with larger longwave radiative cooling above 600 m leading to lower surface temperatures. This effect would also result in lowering of sensible heat flux, although this is not evident in the data.

In the Austrian Alps, Rott (1979) provided comparative data at two elevations. For a clear summers day the higher station (2560 m) estimated lower latent heat but greater sensible and ground heat fluxes than at the lower station (1960 m). In the Dischma Valley, Switzerland, Konzelmann *et al.*(1997) compared energy partitioning at two locations above and below the tree line. Despite similar magnitudes of evapotranspiration, the Bowen ratio was higher at the upper site due to 25% higher net radiation totals. The reason for this difference was not noted, although the vegetation types were different and the vegetation density and soil depth were greater at the lower site.

In a long-term investigation using five energy balance stations on the east slope of the Rhine Valley ranging from 100 to 1200 m, Wenzel *et al* (1997) found a large increase in the Bowen ratio (0.2 to 0.9) with increasing elevation. This was created by a 45% decrease in latent heat (despite a 50% increase in precipitation), which equated to 0.3mm m^{-1} day^{-1} (or 8.16 Wm^{-2} m^{-1}) and an increase of sensible heat flux by a similar magnitude. Seasonal analysis showed that the sign of the Bowen ratio was consistent in all months except February. Theoretical evaluation of the Bowen ratio over horizontal surfaces at different altitudes resulted in the same sign of Bowen ratio gradient (i.e. positive) as the experimental data. Sensitivity analysis of the contributing factors revealed that realistic variations in pressure, stomatal resistance and the magnitude of the Bowen ratio had negligible effect on the vertical gradient of the Bowen ratio, while it increased moderately with increasing temperature and decreased strongly with an increasing ratio between the vertical gradient of specific humidity and the vertical gradient of air temperature. It is these two variables then, which are likely to cause the greatest locational variability in the altitudinal gradients of the Bowen ratio when all other variables such as surface type, aspect and soil moisture content are consistent. Also in the Rhine Valley, Kalthoff *et al* (1999) used data from 36 stations over 4 years. This somewhat larger and more spatially variable dataset yielded similar results to Wenzel *et al* (1997) (*i.e.* a latent heat decrease of 17 W m^{-2} m^{-1}) but with considerable variability between stations (the R^2 for latent heat flux was 0.327 and for sensible heat flux was not reported). The reason for the trend was not specifically examined by Kalthoff *et al.* (1999), although seasonal analysis showed that the altitude dependant decrease of annual mean latent heat flux almost exclusively resulted from its pronounced reduction during the summer months.

The results of these studies indicate that altitude has some influence on the surface energy balance. However, the differences between these sites were often better explained by the differences in the nature of the surface than purely altitude effects. This point is fundamentally important to the question of variability of fluxes in complex terrain. It is clear that the nature of the surface plays a critical role in the magnitudes of surface fluxes and the ratios between them. Altitude therefore, may provide variability in less direct ways, including changes in the surface characteristics (*e.g.* tree lines, snow lines and precipitation gradients). It is nearly impossible to find a location where surface characteristics do not change with altitude and results from such a study would not be representative of most areas.

Other studies considered spatial variability of surface energy exchanges in complex terrain more holistically. For example, comparison of surface energy balances between a valley floor and mountain peak by Scheaffer and Reiter (1987), revealed the critical effects of terrain setting and surface cover. In the Dischma Valley, a study by Hennemuth and Kohler (1984) using observations at three stations as well as aircraft observations of surface temperature and digital vegetation and elevation models, found net radiation to be determined mainly by topographic exposure and latent heat flux by vegetation cover. Both Wenzel *et al* (1997) and Kalthoff *et al* (1999) also showed a strong dependence of the Bowen ratio on precipitation. The former examined the spatial variability of precipitation versus latent heat flux and found a consistent ratio of evapotranspiration to precipitation at various sites along the Rhine Valley of approximately 0.8 arising for the range of precipitation between 700 and 900 mm yr^{-1}. The latter considered the data temporally and presented a negative curvilinear relationship between precipitation and the Bowen ratio at one station (Figure 2.8). The Bowen ratio ranged from 0.45 in a year with approximately 500 mm precipitation to

0.23 in a year with 1050 mm. These studies imply that in the Rhine Valley the distribution of precipitation sets the pattern for evapotranspiration.

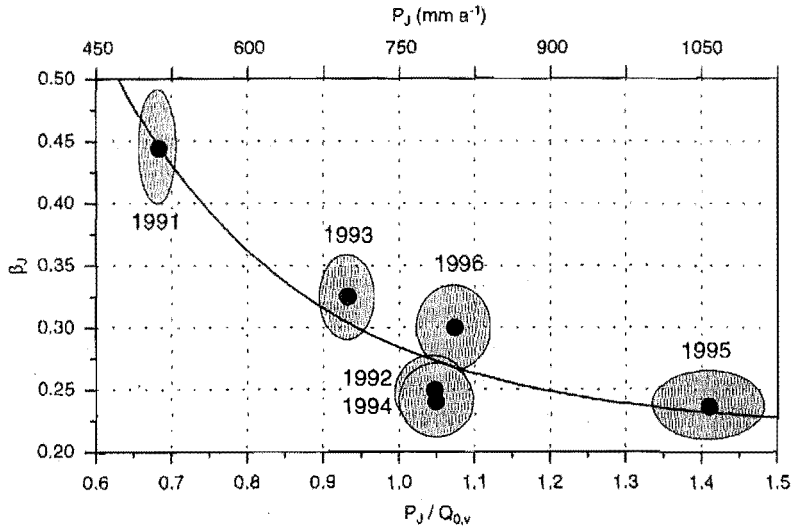

Figure 2.8 Annual Bowen ratio as a function of precipitation collected from a station in the Rhine Valley where β_J is the Bowen ratio, P_J is precipitation and $P_J / Q_{0,v}$ is precipitation normalised by the six-year mean equivalent radiation balance (from Kalthoff *et al.* 1999).

In a numerical investigation of spatial variation of evaporation over idealised hills of 100 and 200 m, Huntingford *et al* (1998) demonstrated that it was possible to extend horizontal surface concepts to a hill situation. First, they considered a case with uniform surface resistance over the hill. In this simulation they found evaporation increased on the slopes of the hill due to the increase in surface area and decreased on the top of the hill due to the adiabatic decrease in temperature. The feedbacks of the topographically effected airflow and turbulent mixing at the surface were smaller in magnitude and nearly cancelled when averaged over the hill. Second, they adjusted surface resistance to allow for soil drainage effects, with lower moisture levels (higher surface resistance) near hilltops. This provided a greater influence on evaporation than those noted above, where simply the presence of the hill was accounted for. This study identified important processes and relationships with regard to evaporation in complex terrain, although generalisation of these results to other thermodynamic regimes, hill configurations and wind conditions requires further numerical investigation as well as observational data.

Using five energy balance stations in a 650 m deep Colorado valley (Brush Creek Valley), Whiteman *et al* (1989b) compared energy balances over different slopes, surface types and elevations for a single clear-sky day (Figure 2.9). Mean daytime Bowen ratios were found to vary from 0.86 at a valley floor meadow site to 7.6 on a southwest facing sidewall with sparse vegetation and dry soil. The significant differences in instantaneous heat fluxes between the five sites throughout the day were attributed primarily to the radiation balance and secondly to site characteristics, including vegetation and soil moisture.

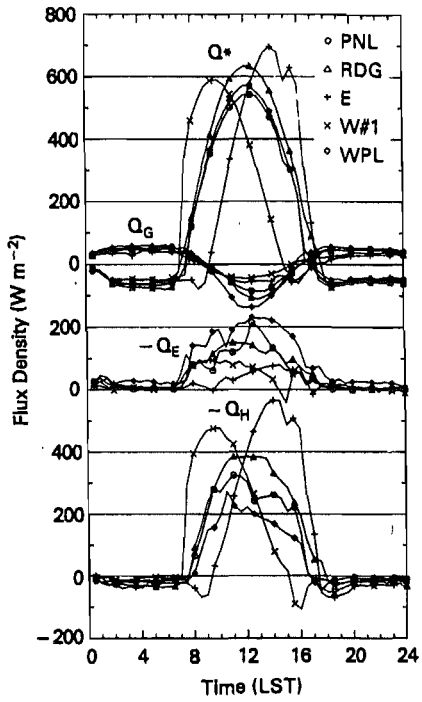

Figure 2.9 Net radiation and energy balance components at five sites in the Brush Creek Valley, 25 September 1984. PNL was located on the lower valley floor, RDG on the ridge top, E on the east sidewall, W#1 on the west sidewall and WPL on the upper valley floor (from Whiteman *et al.* 1989b). Note that the sign convention for non-radiative fluxes is opposite to that used in the present study.

It is clear from these studies that the variability in the surface energy balance results from a range of parameters including altitude, aspect, slope, surface type and physiological control by vegetation. Due to the large spatial variability found in these parameters, it is difficult to generalise surface energy flux characteristics from one site to another. Careful consideration must be made therefore, of the unique surface and climatological parameters of the location in question. The following section discusses in more detail the range of surface fluxes that might be expected due to heterogeneity of surface characteristics.

Surface heterogeneity

From the derivations of surface energy exchanges (Section 2.3.1), it is clear that the natural range of surface types that exist in an alpine catchment such as Tekapo, will generate a similarly large range in surface energy balances. Observations from surfaces similar to those considered in this study are presented in Chapter Five. Ground heat flux is governed strongly by the thermal properties of the substrate material and the ratio between the conductive flux and turbulent fluxes in the overlying air depends, in part, on the roughness characteristics of the surface. Furthermore, the Bowen ratio, which is governed most strongly by the availability of moisture, displays ranges from 0.1 for water to over 10 for arid surfaces (Oke 1987). This makes it clear that even a flat surface with heterogeneous surface cover will generate large spatial disparities in the surface energy balance. It also implies that the scale of variability relates directly to the scale of surface heterogeneity, while the magnitude of variability is dependent on the surface types.

Kalthoff *et al* (1999) showed a large range in energy partitioning in response to land use patterns within the Rhine Valley. Humes *et al* (1997) found spatial variability in surface fluxes as a result of soil moisture variations caused by highly localised precipitation events. Even within a single ecosystem Rott (1979) observed Bowen ratios across an alpine meadow to range from 0.2 to 0.6. Land use patterns may generate artificially large variability in fluxes across small spatial scales. Surface energy balances were measured at 5 locations on a semi-arid grassland steppe and 5 locations on an adjacent irrigated cropping farm (Doran *et al.* 1995). Sensible heat fluxes were found to be up to 4 times greater on the steppe and to vary considerably within the farm as a function of crop type.

2.3.4 Advection

The interaction that occurs near the boundaries between two surface types further complicates the spatial variability in surface fluxes, since each energy balance generates a unique near surface climate. As air flows from one surface to another, the airmass being transported must adjust to the new set of boundary conditions. This occurs initially at the surface and diffuses upward in the downwind direction at a rate dependent on roughness length and atmospheric stability (Stull 1988). The affected layer is referred to as the internal boundary layer (Figure 2.10). The air above this layer remains completely influenced by the upwind surface and only the lowest 10% of the internal boundary layer is adjusted to the properties of the new surface (Oke 1987). The remaining depth of the internal boundary layer is known as the transition zone. Where heterogeneity of surface characteristics exist, multiple internal boundary layers may exist in a single vertical profile (Figure 2.10b).

Advection of airmasses generated over a different set of boundary conditions is an important determinant of the surface energy balance. In volumetric studies, ΔQ_A is the net amount of energy that is transported through the sidewalls of the volume (Eq. 2.15, Figure 2.11). Assuming no crosswind influence, the advective flux (Q_A) of a scalar (ξ) can be estimated by:

$$Q_{A\xi} = -u\frac{\partial \xi}{\partial x} \qquad (2.22)$$

where ξ denotes the scalar being transported (such as heat, moisture or momentum), u is windspeed in the along-wind direction (x). The effect of the boundary between two surface types on the downwind surface energy balance then, depends on the magnitude of the horizontal gradients of temperature and humidity that are generated as well as the change in roughness.

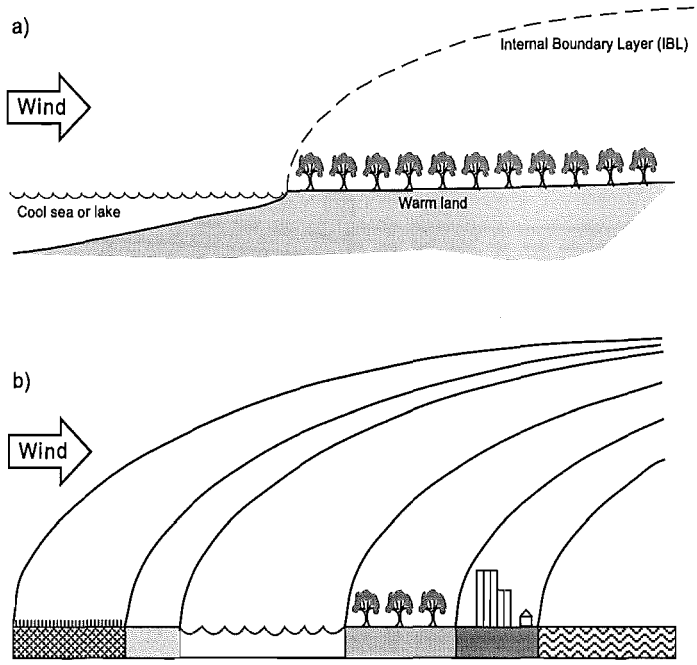

Figure 2.10 The downwind development of a) a single internal boundary layer and b) multiple internal boundary layers over heterogeneous surfaces (after Sturman and Tapper 1996 and Stull 1988).

Advection plays an important role in determining surface heat fluxes since it alters the nature of the airmass above the surface and thus the gradients used to derive the fluxes. Figure 2.11 considers schematically 2 hypothetical situations of the influence of advection on the surface energy balance. The first considers airflow from a hot, dry and rough surface to a cool, moist and smooth surface (Figure 2.11a), while the second reverses the direction of flow (Figure 2.11b). It is clear that, using these parameters, there are 6 other possible combinations, although they should be easily conceived based on these two contrasting examples. In the first example wind speed ($\overline{u}$) accelerates due to reduced friction, resulting in horizontal divergence, which causes subsidence and decreased surface shearing stress (τ_0). The decrease in τ_0 reduces eddy diffusivity, decreasing turbulent transfer of Q_H and Q_E. Sensible heat flux drops significantly as the advection of warm air reduces (or even reverses) the vertical temperature gradient. As the air cools with distance downwind of the boundary, sensible heat flux converges toward an equilibrium with the new surface boundary climate. The transport of dry air across the boundary results in an increase in Q_E relative to Q_H. Latent heat flux similarly approaches equilibrium with distance downwind although its total change in magnitude depends on the balance between the altered vapour gradient and the altered eddy diffusivity. A good example of this was observed in an urban park (Spronken-Smith *et al.* 2000), when warm, dry air from the built-up surroundings flowed across the cool moist park surface. In the second example (Figure 2.11b), flow onto the rougher surface enhances τ_0, increasing eddy diffusivity. This increased transport mechanism will favour Q_H relative to Q_E , and hence β, due to the increased vertical temperature gradient relative to humidity.

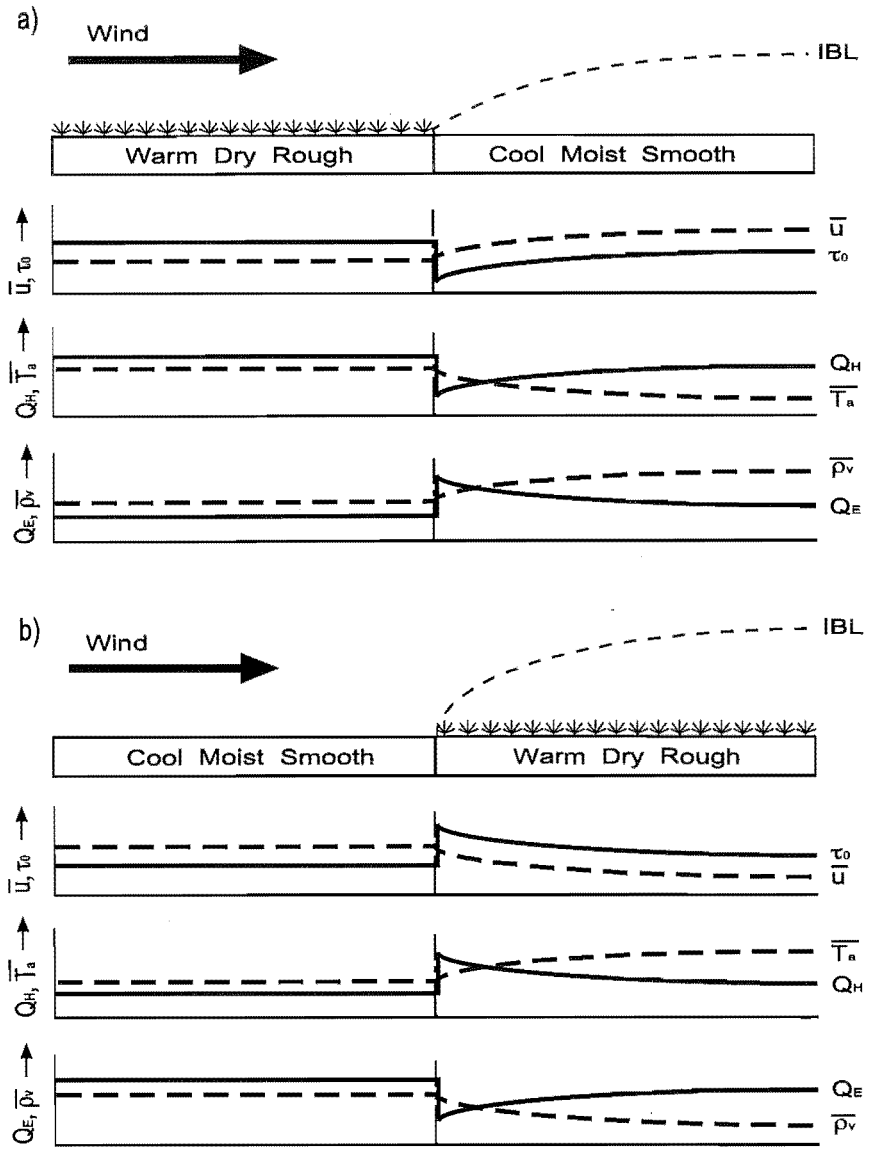

Figure 2.11 Schematic representation of the influence of advection on surface fluxes and meteorological parameters in a) warm, dry air advection and b) cool moist air advection (after Oke 1987).

The importance of advection to surface energy fluxes links atmospheric processes at a wide range of scales. Advection may occur in response to synoptic scale pressure gradients, regionally perturbed airflow (such as foehn effects), local to meso-scale thermal circulations with smaller scales represented as air flows across patchwork surface cover. The following section considers the relationship between surface energy fluxes and local winds in complex terrain, which are best expressed during anticyclonic conditions.

2.4 Surface energy fluxes and local winds in complex terrain

2.4.1 Slope winds

Slope winds, which include anabatic (upslope) and katabatic (downslope) flows are driven by buoyancy and horizontal pressure gradient forces which are governed by

temperature differences between the slope and the adjacent air. From this it is clear that surface energy exchanges are the primary controller of slope flows and Whiteman *et al.* (1989) found the onset of slope winds to be closely related to the time of sign reversal of sensible heat flux at several individual sites on a valley side wall. The surface energy balance typically becomes positive soon after local sunrise, due to the flux of energy provided by solar radiation. This initiates the development of a very shallow layer with a superadiabatic lapse rate, which in turn causes the air near the slope surface to rise. The stable atmosphere immediately above this layer provides an upper boundary to further vertical ascent and the air moves upslope. When the surface energy budget becomes negative, usually as a response to radiative cooling after local sunset, a shallow stable layer is formed and the air begins to sink. The slope surface this time provides the boundary for further vertical movement and air drains downslope. For the purpose of maintaining local air mass conservation, a compensating return circulation develops in both situations. Idealised schematics of slope flows in valley cross-sections are presented in Figure 2.12.

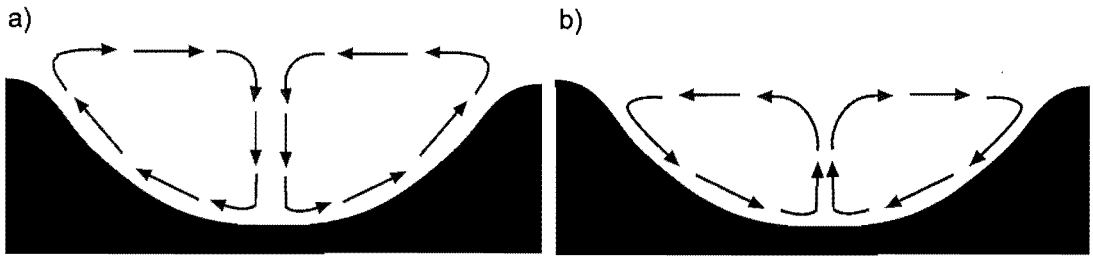

Figure 2.12 Idealised depiction of slope flows in the cross-section of a steep sided valley, a) in the daytime and b) at night.

The theory of slope flows is such that, provided external forces are absent, they may occur over almost any scale. Katabatic flows are commonly observed operating over the entire Antarctic continent, reaching velocities on the order of 18 m s^{-1} near the coast (Parish and Bromwich 1990). The present study however, is concerned with flows that occur on the slopes of an alpine valley and basin. Such slope flows are subject to local terrain, surface characteristics and soil moisture influences, are intermittent in time and may change over short distances (Vergeiner 1982, cited in Whiteman 1990). In the past, katabatic flows have received considerably more attention than anabatic flows as a consequence of their importance to suppressing pollutant dispersion. (Mahrt 1982, Horst and Doran 1988, Doran *et al.* 1989, 1990, Hennemuth and Schmidt 1985, Lee *et al.* 1995, Leone and Lee 1989, Clements *et al.* 1989). It is important to note that most studies have considered the energy balance of the slope surfaces to be uniform in slope flow studies. In fact, spatial variability of fluxes can impact on the flow structure due to such factors as variability in soil moisture (Banta and Prantley 1987).

Very few studies have dealt with the feedback processes that occur as a result of the effect that advection of upwind airmass characteristics has on the surface energy balance, although it is included in most analytical slope wind models and has been considered as a control on boundary layer development (Kossmann *et al.* 1998). In the morning transition period when the energy balance becomes positive on a slope and a slope wind develops, a temperature inversion typically exists in the valley atmosphere as a result of nocturnal drainage flow. Within this inversion layer upslope winds will result in cold air advection. This should result in an increase of sensible heat flux. Furthermore, Kossmann *et al.* (1998) point out that when a non-horizontal (terrain following) convective boundary layer (CBL) top exists, the stable stratification of the

atmosphere above the CBL can also lead to a gradient in potential temperature along the slope. This process would therefore, contribute to cold air advection in anabatic flow, enhancing sensible heat flux. As the CBL grows and slope wind circulations help to mix the valley air, advection from slope winds will have a decreasing impact on the surface energy balance. Furthermore, as a consequence of this heating, larger scale (along-valley) thermal circulations are likely to develop (following section) over-riding, or at least greatly complicating, the influence of the slope wind on the surface energy balance.

In the nocturnal katabatic flow, stable stratification of the valley atmosphere results in warm air advection. However, initially a well-mixed air mass will be likely to exist over the entire slope layer from daytime heating. The warm air advection leads to an increase in the sensible heat flux toward the surface, although katabatic flows have been found to have very low turbulence (Clements and Nappo 1983), suggesting that net radiation deficits may be preferentially offset by ground heat flux. As the valley inversion strengthens and deepens through the night, the influence of warm air advection is likely to increase, except that, again, broader scale flows are likely to develop in the valley situation (following section).

It is clear that in both anabatic and katabatic cases, the stratification of the valley atmosphere would have a strong control on the magnitude of advection. This would result in an increase of warm air advection in katabatic flows and a decrease of cold air advection in anabatic flows. This effect is suggested in plots of diurnal potential temperature along a slope presented by Kossmann *et al.* (1998), although it is yet to be confirmed in direct treatment.

2.4.2 Along valley flows

Since slope flows often have a compensating return circulation, sensible heat fluxes at the surface are effectively transported into the surrounding atmosphere. In this way, over time the air is heated or cooled primarily near the surface but also secondly in the adjacent atmosphere. In the case of a valley with slope flows occurring on opposing side walls, the return circulations are theorised to meet somewhere in the centre of the valley. For anabatic flows, this leads to flow convergence aloft near the centre of the valley with flow divergence near the valley floor (Figure 2.12a). Similar, but opposite, mechanisms exist for katabatic flows (Figure 2.12b). This provides an efficient method for heating or cooling the entire valley cross section. The rate at which this occurs (ignoring along valley advection and dynamic exchange with the overlying atmosphere) depends on the magnitude of the sensible heat flux density at the surface, the efficiency of the slope wind circulation to transport this through the valley atmosphere and the ratio of valley width to cross-sectional area (McKee and O'Neal 1989). The smaller this ratio is, the more effectively the heating and cooling of the cross-sectional area can take place. Since this ratio tends to decrease further up valley due to a typical narrowing and steepening of valley geometries, the air in the upper valley volume tends to heat and cool more efficiently than further down valley, or in an adjacent basin or plain. Because of this, the mountain valley atmosphere has a larger diurnal temperature amplitude than the basin or plain. This geometric control is known as the Topographic Amplification Factor (TAF) and can be defined for a vertical valley cross-section as:

$$TAF = \frac{\left[\frac{W}{A_{yz(valley)}}\right]}{\left[\frac{W}{A_{yz(plain)}}\right]} \qquad (2.23)$$

where the TAF in this case is for a valley to plains ratio, W is the width at the top of the two cross sections and A_{yz} is the area of the vertical cross-section. From this it is evident that the cross-sectional shape of the valley will be important in determining the TAF as well as the width of the valley floor. From u-shaped to v-shaped to convex valley cross-sections the width to area ratio increases as it does with widening valley floors. By day this effect generates an upvalley temperature gradient, which is expressed at the surface as a negative pressure gradient and results in upvalley airflow (valley wind). By night the opposite occurs and a downvalley (mountain) wind develops.

The TAF has been successfully related to along valley flows and inversion destruction in several studies (Steinacker 1984, Whiteman and McKee 1982, Bohm 1985, Muller and Whiteman 1988, McKee and Oneil 1989). However, the extent to which the TAF is responsible for differential heating and cooling of valley atmospheres is influenced by several other considerations. First, energy flux may occur through the 'ceiling' of this volume in exchanges with the atmosphere above. This is governed most strongly by the airmass characteristics of the broader scale flow aloft, especially wind speed. Under weak to moderate gradient wind conditions Maki and Harimaya (1988) show that one of the effects of valley geometry is to limit the dynamic exchange between the air above the valley and the air within the valley. Second, the TAF method of evaluating along valley winds assumes an efficient means of transport of heated or cooled air from the surface to the entire atmospheric volume. This is more valid in deeper valley atmospheres where slope circulations act more closely to the ideal depicted in Figure 2.12. However, stability factors may confine energy input to certain altitudes in the valley.

The factor that has been least considered, yet is arguably very relevant, is the along valley variability that may exist in surface energy exchanges. For example, a decrease in the valley width to cross-sectional area ratio at one point in the valley relative to another, could be offset by a decrease in sensible heat flux. This might be related to a decrease in the absorption of solar radiation or a decrease in either Q_H/Q_E or Q_H/Q_G. Lower solar radiation absorption could result from a less favourable aspect or an increase in albedo or shadowing, while decreases in the flux ratios above are governed by surface thermal, hydrological and vegetative characteristics. This includes differences in soil moisture content (which may additionally be controlled by topographical characteristics) or differences in land cover including lakes, glaciers, snow cover, urban areas, sediment deposits or changes in vegetation type including agricultural. All of these surface types are relatively common in alpine catchments and may vary over small spatial scales. Thus to accurately determine the TAF influence, it is necessary to either, select a region of uniform surface cover and radiation regime, or account for the variability found in surface energy exchanges.

Advection influences the heating and cooling directly, but may also play a role in changing the magnitudes of sensible heat flux along the valley, which presents a feedback mechanism to the energy source that is initially responsible for generating the flow. This process has received little attention in the past, particularly in observational

studies. However, since both mountain and valley winds are driven by pressure gradients that develop through temperature gradients along the valley, the horizontal flow is from cool to warm air masses, resulting in cold air advection. By day, this should increase the rate of sensible heat flux. Further, Hennemuth and Neureither (1986, cited in Whiteman 1990) found consistent advection of moist air in along-valley winds. This would decrease the vapour density gradient near the surface and the increase in Q_H would be offset by a reduction in Q_E. By night the cold air advection would decrease the sensible heat flux toward the surface as the cooling air diminishes the near surface temperature gradient and enhances any latent heat flux directed toward the ground in the form of dew or frost. Halbsguth *et al* (1984) recorded Bowen ratios greater than 1 for the mountain wind and less than 0.7 for the valley wind, although it is difficult to isolate the feedbacks associated with advection from differences between daytime and nocturnal micrometeorological processes.

In north-oriented valleys (looking upvalley) Whiteman (1989), Whiteman *et al* (1989b) and Hennemuth (1985) observed cross valley circulations in relation to preferential heating of west and east valley sidewalls in the morning and evening respectively. The transitions from upslope to upvalley to downslope to downvalley produced clockwise rotating diurnal hodographs for the west side wall and anticlockwise for the east. The valley floor sites showed clockwise rotation in response to cross-valley circulations. This effect was found to diminish in winter through reduced differences in surface heat flux (Bader and Whiteman 1989).

2.4.3 Thermal circulations generated by heterogeneous surfaces

The juxtaposition of surfaces with different thermal characteristics can also lead to the development of local thermal circulations. The most commonly observed and studied of such winds is the sea or lake breeze where the contrasting nature of surface energy balances between water and land surfaces generates differential boundary layer heating horizontal pressure gradients across the coastline. In the absence of strong broader-scale flows, the pressure gradient generates flow across the coastline once the retarding influence of friction is overcome. The relatively greater heating and cooling of land surfaces compared to water surfaces is dominated by the large heat capacity and molecular conductivity of water bodies, which minimise diurnal temperature changes. Furthermore, the little energy available at the surface for turbulent transport is dominated by latent heat flux, given the small Bowen ratios observed over water surfaces. Again, conservation of mass requires that a compensating flow develops.

Thermal circulations driven by contrasting surface energy fluxes are not restricted to the land/water interface. Analogous processes may generate airflow between urban and rural areas, areas with different vegetation or different soil moisture regimes, edges of snow fields or glaciated regions. Doran *et al.* (1995) observed thermal circulations over the boundary between semi-arid grassland and irrigated farmland over a spatial scale of <10 km.

Local to mesoscale cold air advection generally occurs in surface airflow of circulations generated by heterogeneous surfaces, since the climate of the upwind air mass is typically cooler and moister than the equilibrium climate for the downwind surface. This induces an increase in sensible heat flux and decrease in latent heat flux as the vertical temperature and water vapour gradient increase and decrease respectively. Using Q_H data collected from a network of energy balance stations in the urban area of St Louis, Missouri, Ching *et al.* (1983) clearly showed that advection can strongly

modulate and even dominate the vertical heat flux above surfaces in areas, which maintain large horizontal temperature gradients. The advective flux generally decreases away from the upwind surface in response to a slackening of the temperature gradient. This effect has been demonstrated in observational data from the Sendai Plain (Kuwagata *et al.* 1993). At the horizontal extent of the circulation this generalisation is greatly complicated by processes of frontogenesis resulting from convergence, where turbulent and mean vertical airflow is greatly increased.

Interacting multi-scale airflow in complex terrain

It is important to note that only an idealised and generalised depiction of thermal circulations has been discussed in the previous sections. The reality in complex terrain is likely to be significantly more complicated (Sturman 1987). Firstly, these flows are usually much weaker than those driven by the ambient atmospheric motion, and when this is itself weak, thermally forced winds typically interact with ambient flows in subtle ways (Barr and Orgill 1989, Raupach and Finnigan 1997). Secondly, the structure of thermal circulations can deviate significantly from the classic conceptual model. For example, Vergeiner and Dreiseitl (1987) hypothesised that two slope circulations may exist within a valley at separate heights divided by a stable layer. Thirdly, interaction is likely to exist between different types of local wind systems. Kondo (1990) reproduced observations well in a numerical study of wind flow on the Kanto Plain, Japan, where he illustrated the extension of the sea breeze inland and vertically through interaction with valley winds and similar results were found in a numerical study of sea breeze and slope wind interaction (Asai and Mitsumoto 1978).

Further advective influences corresponding with a regional or gradient flow may occur in the afternoon when convective mixing occurs between the valley atmosphere and the free atmosphere above in the deep afternoon boundary layer (Banta and Cotton 1981). Assouline and Mahrer (1996) describe a situation where an afternoon westerly sea breeze arrives at Lake Kinnerat, Israel after passage over a hot and dry surface. Latent heat fluxes estimated over the lake surface on the western side were occasionally twice the corresponding fluxes on the eastern side after the airmass had passed over the lake surface. McGowan and Sturman (1995) presented observations of multi-scale wind systems within the Tekapo catchment, New Zealand, where a lake breeze from a small lake interacted with along-valley flows as well as regional scale foehn effects. These systems were also found to produce pronounced diurnal effects on the meteorology of a single site.

2.5 Summary

The purpose of the second chapter has been to define the causes and behaviour of surface fluxes and how they vary over space and time in complex terrain. The conceptual understanding and derivations of individual components of the surface radiation budget and surface energy balance were outlined. These highlighted the governing variables and the potential for both spatial and temporal changes in these variables to alter the surface energy balance. The temporal variability of surface fluxes was then discussed more generally, considering diurnal, seasonal and meteorological controls and how they influence the surface hydrology and biology as well as properties of the overlying air mass. The magnitude and patterns of temporal variability are strongly linked to locational controls that govern local climates and meteorology.

Attention was then turned to spatial variability in surface fluxes considering firstly, topographic controls and secondly surface heterogeneity. These controls are based on a range of parameters including, altitude, aspect, slope angle, surface radiative, thermal and hydrological properties and physiological controls of vegetation. Air flowing across spatially variable surface fluxes results in the influence of advection of air, which can occur on a range of scales. Finally the links between surface fluxes and local winds in complex terrain was assessed where surface fluxes contribute the energy for the generation of flow, a consequence being the advection of different, usually cooler air and the feedbacks to the surface energy balance.

Chapter Three:

Physical setting and methodology

3.1 Introduction

It is critical for any field based observational study to provide details of the location and techniques used so that results and conclusions can be considered in light of the context that these provide. This is particularly relevant in this study because of the site-dependent variability of surface energy fluxes in complex terrain, as outlined in Chapter Two. The purpose of this chapter is therefore to provide this context. Initially, the physical setting is described in relation to the topography and other surface characteristics as well as its climatology and meteorology. Secondly, the field methodology is outlined with details of instrumentation and their deployment, including site characteristics, calibration and comparison procedures, and error assessment.

3.2 Physical landscape

The Tekapo catchment is situated in the central South Island of New Zealand at approximately 170°30'E, 44°S (Figure 3.1). The catchment is comprised of 3 large valleys (Cass, Godley and Macaulay), which drain via Lake Tekapo into an inner montane basin (MacKenzie Basin). The catchment is bounded to the north and west by the Southern Alps and to the east by the eastern front ranges (Two Thumb Range). Several such large alpine catchments feed into MacKenzie Basin, which then drains from its southeastern corner via the Waitaki River to the Pacific Ocean. This section considers the dominant physiography, climatology and meteorology of the Tekapo catchment.

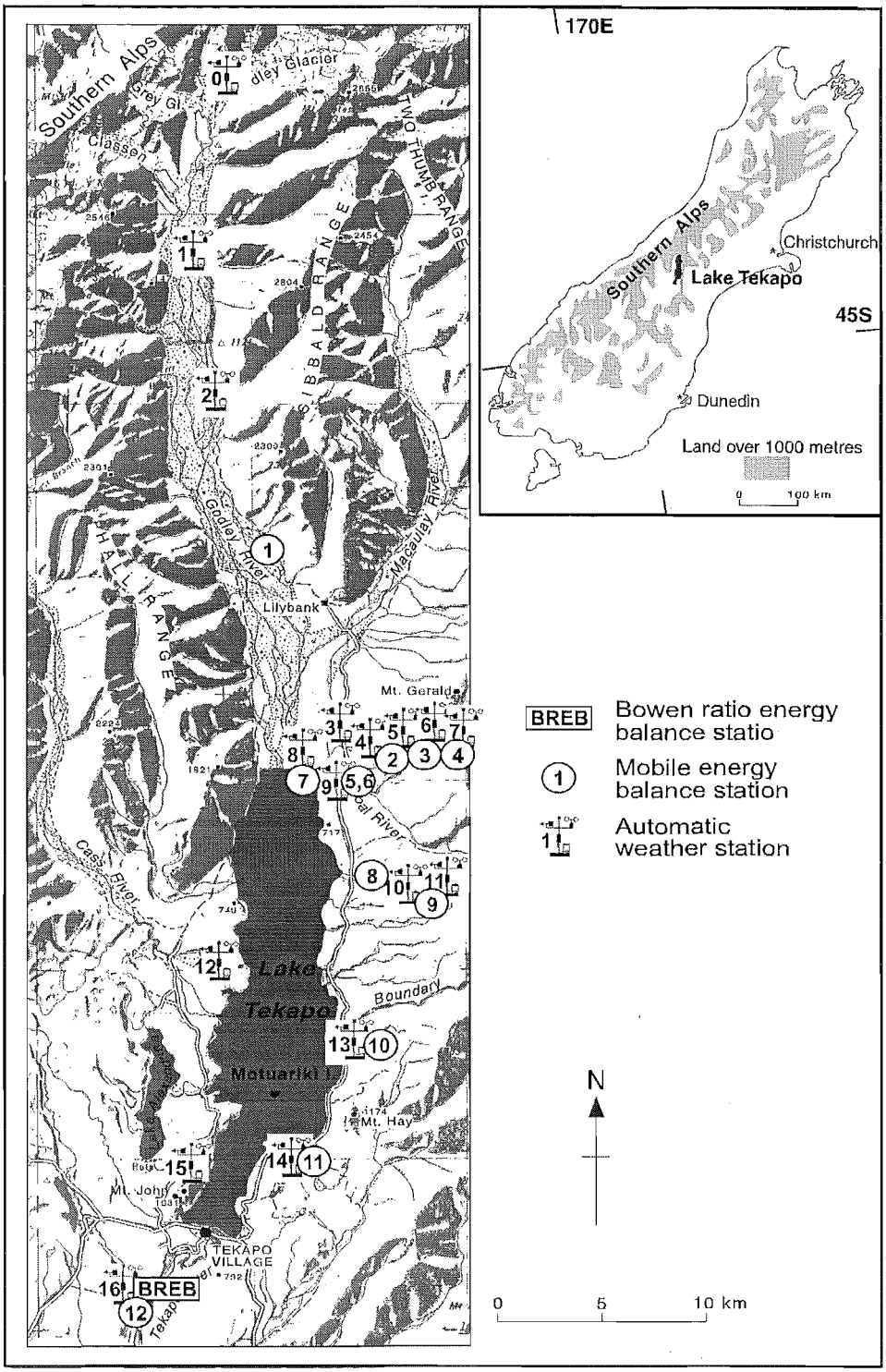

Figure 3.1 Site map of part of the Tekapo catchment showing locations of data collection systems.

3.2.1 Topography

Geomorphic control of the shape of the Southern Alps is dominated by rapid tectonic uplift and equally rapid erosion. These processes are not mutually exclusive but correspond to relationships between uplift, rainfall, relief and erosion, which combine to produce an equilibrium height and shape of the alpine barrier (Adams 1980). The magnitude of relief and associated processes diminish in the study area with distance from the Alpine divide. The elevation ranges from the 600 m basin floor at the southern

to frequent and intense flooding, valley floors are typically flat in cross-section with terraced flood plains and deep layers of alluvial sediment ranging from large boulders to glacial silts.

Elevation and slope angles derived from a digital elevation model (DEM) with a 100 m resolution are mapped in Figure 3.2. There appears to be three broad divisions to the topographic structure of the study area. The northwest section is comprised of very complex terrain, with high relief and greatest elevation (2000-2500 m). Furthermore, large ranges of elevation and slope angle can be seen to occur over horizontal distances of less that 1 km. The southeast boundary of the catchment is composed of moderate slope angles and elevations ranging between 1000 and 2000 m. Between these two features and to the south is the gently sloping lake basin area. Figure 3.3 provides oblique aerial views of these dominant topographic divisions.

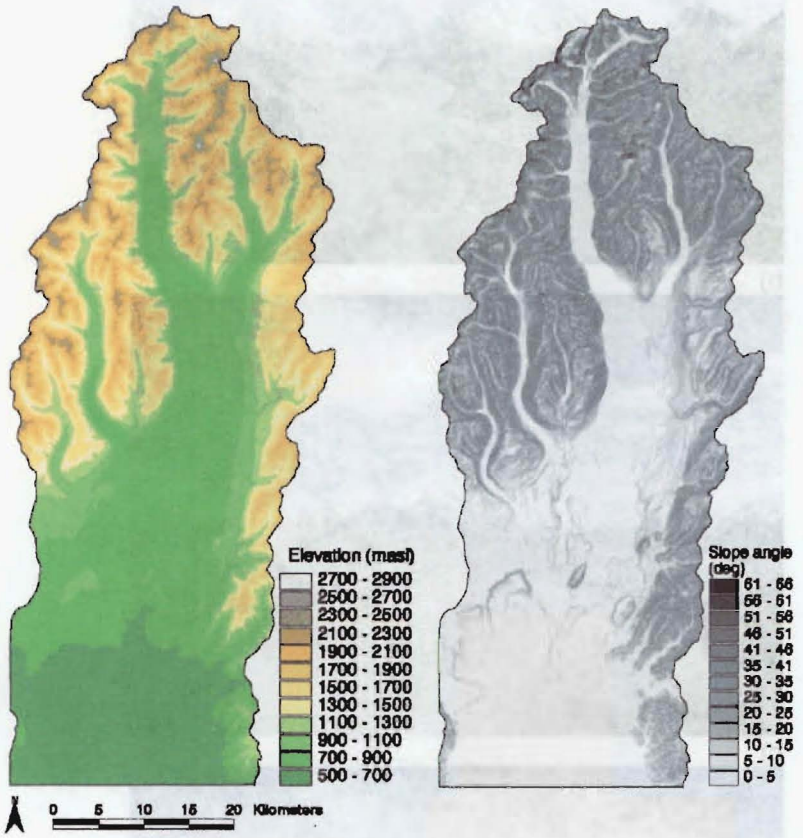

Figure 3.2 Maps of the Tekapo catchment showing a) elevation and b) slope angle.

Erosion rates on the steep alpine slopes of the Southern Alps are extreme by world standards (Whitehouse and Pearce 1992) and inhibit the formation of soils and consequently vegetated surfaces in many areas. These areas are dominated by greywacke bedrock and scree slopes with periodic snow cover (Figure 3.3a). Permanent snow and ice is present only on the upper slopes above about 2500 m, except for several glaciers, which transport ice to the valley floor at the northern end of the catchment. However, at any time of year, but particularly in winter months, snowfalls can occur over the entire study region. Valley floors are covered by large alluvial gravel flats, with soils and vegetation developing only over older river floodplains, covering a proportionately small area of the valley floor (Figure 3.3b). Relic terminal moraines near Lake Tekapo Village have dammed the major catchment rivers to form Lake Tekapo, which is 87 km^2 in area and approximately 707 masl (Figure 3.3c). Smaller

Tekapo, which is 87 km^2 in area and approximately 707 masl (Figure 3.3c). Smaller lakes have formed behind more recent terminal moraines of the Godley, Maude, Grey and Classen glaciers at the head of the Godley valley (Figure 3.3a). Other small, shallow lakes have formed in glacial hollows to the west of Lake Tekapo. The soils of the catchment are classified as upland yellow-brown earths and are predominantly shallow (<50 cm), stony, well-drained, sandy loams with low fertility (Espie 1997). There is large variation in soil age and depth throughout the catchment related primarily to the local climate and disturbance history.

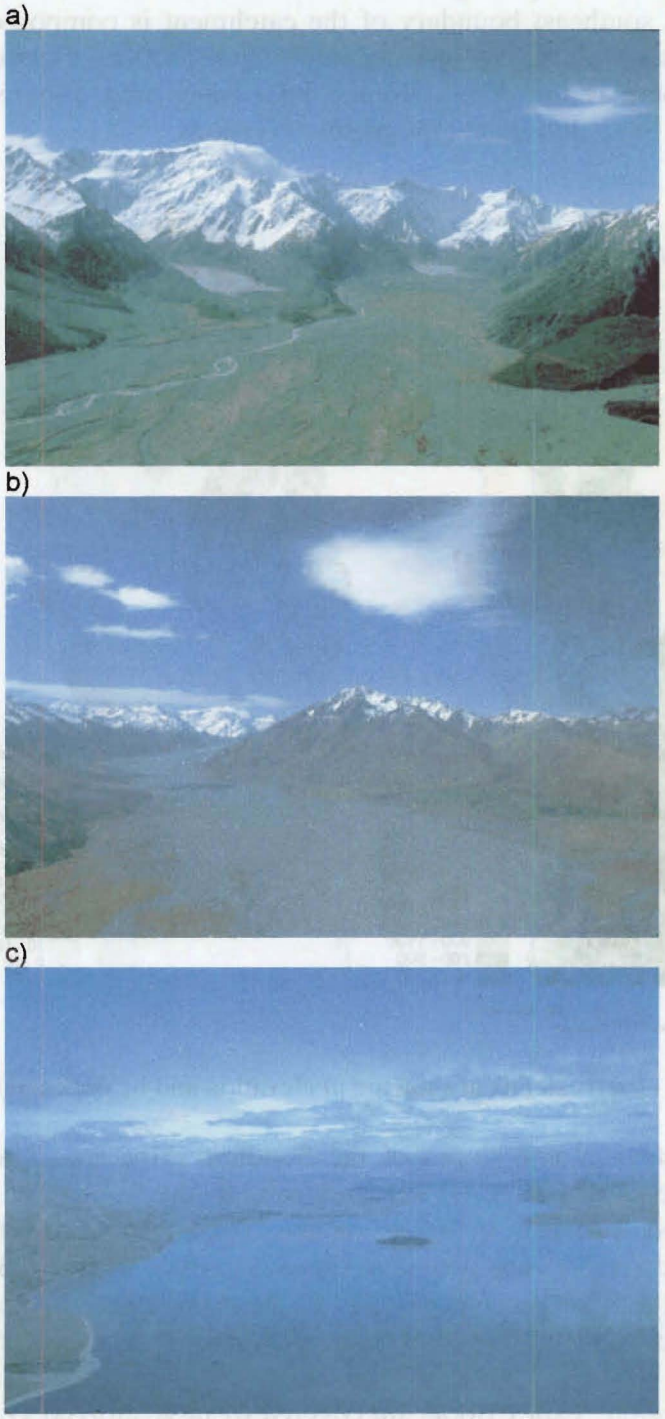

Figure 3.3 Oblique aerial views of the study area looking, a) north at the headwaters of the Godley Valley and the alpine divide, b) north from the northern margin of Lake Tekapo at the confluence of the Godley (left) and Macauley valleys, and c) south from the middle of Lake Tekapo to the MacKenzie Basin.

3.2.2 Surface cover

An understanding of spatial variability in the physical properties of the surface is critical to a study of surface energy fluxes in complex terrain. This section discusses the nature of the surface in the Tekapo catchment and the major controls on its variability. A selection of major classes of surface cover for the Tekapo catchment is mapped in Figure 3.4. This map was derived from supervised classification of Indian Remote Sensing Satellite (IRS-1C) imagery. An outline of the classification procedure is provided in Appendix A.

Surface cover is dominated by tussock grasslands of varying type and bare rock with much smaller coverage of water, snow and ice. The catchment can be broadly divided into three sections; snow and rock to the northwest, tussock over the central region and degraded tussock to the south. This resembles divisions in topographical characteristics and emphasises the role of slope, elevation and precipitation on surface cover. This is an important relationship because it illustrates that topographical characteristics indirectly play a significant role in surface energy budgets through the controls they have on surface cover.

Vegetation is predominantly composed of native tussock grasses. These include short tussock species, predominantly Fescue tussock (*Festuca novae-zealandiae*) and tall tussock species, predominantly snow tussock (*Chionochloa rigada*). These are interspersed in places with scrub species including matagouri (*Discaria toumatou*) and spear grass (*Aciphylla colensoi*). Generally, the size and density of tussock decreases toward the southeast in response to a strong precipitation gradient (discussed subsequently in Section 3.2). This degradation has been compounded by historic burning, overgrazing and rabbit infestation (McKendry and O'Connor 1990). As a result, much of MacKenzie Basin is covered in severely degraded tussock with a large portion of bare, frost-heaved soil and invasion by exotic groundcover species, predominantly mouse ear hawkweed (*Hieracium pilosella*). Some small areas of oversown or cultivated pasture exist in the area, although land-use is predominantly extensive sheep, cattle and deer farming. Some small plantations of exotics, mostly *Pinus* species exist near the southeast corner of Lake Tekapo, on the southern slope of Mt John and on the small island, Motuariki, near the centre of Lake Tekapo.

The area of the three-dimensional topographic surface ($A_{3\text{-}D}$) is larger than the two-dimensional surface ($A_{2\text{-}D}$) grid, as described by digital elevation models (*e.g.* Figure 3.2a), by an amount dependent on slope angles. For each grid point:

$$A = \sqrt{\frac{100}{\cos\omega(x)} \times \frac{100}{\cos\omega(y)}} \qquad (3.1)$$

where $\omega(x)$ and $\omega(y)$ are slope angles in the x and y directions. By this estimation, the 3-D area of the catchment is approximately 11% larger than the 2-D area. Furthermore, this does not affect all surface classes evenly since, for example, rock surfaces are commonly associated with steeper slopes and lake surfaces are horizontal as is evident in Table 3.1. Using Eq. (3.1), a map of the ratio $A_{3\text{-}D}$:$A_{2\text{-}D}$ was generated and applied to model output. Areal distributions documented in subsequent discussion refer to the 3-D area unless otherwise stated.

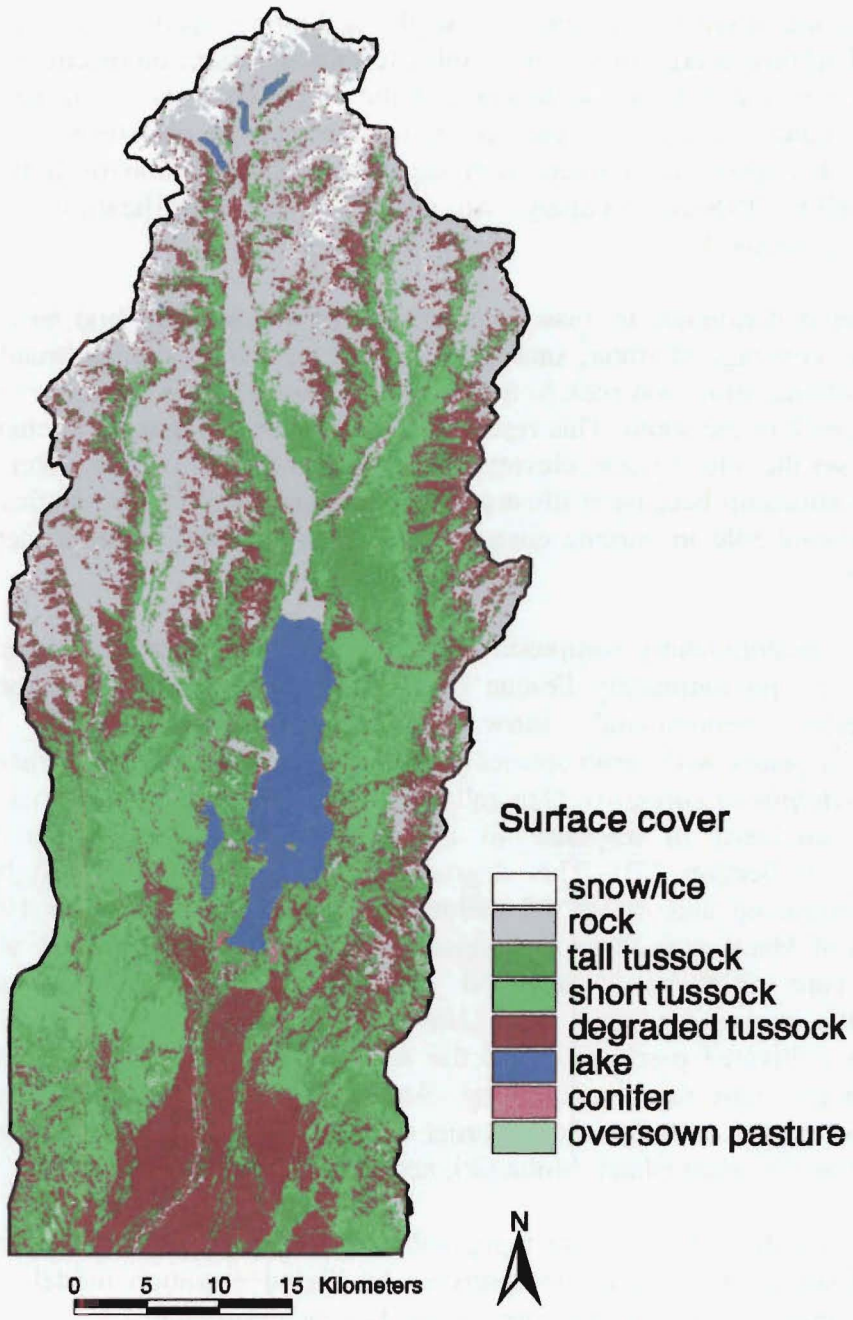

Figure 3.4 Surface cover map based on supervised classification of IRS-1C images.

3.3 Climatological setting

This section considers the climatic setting of the Tekapo catchment with regard to seasonal climatology and dominant meteorological controls. Unless otherwise stated, mean values cited in this section were taken from the long-term record (1925-1980) for Lake Tekapo Village compiled by the New Zealand Meteorological Service (1986).

The climate of the Tekapo catchment is set within the broader framework of the maritime setting of New Zealand, so typically shows a smaller range of extremes than mountains at mid-latitudes in the northern hemisphere. Within this context however, the catchment is situated in the climatological region that has the least maritime influence

with the largest average daily range of temperatures in New Zealand (Garr and Fitzharris 1991). The monthly mean and average daily maximum and minimum temperatures are plotted in Figure 3.5. The mean daily range is greatest in late summer and the diurnal and seasonal ranges are of similar magnitudes (11.6 and 13.2 °C respectively).

Table 3.1 Classified image 2-D area and calculated 3-D area of surface cover classes for the Tekapo catchment.

	$A_{2\text{-}D}$ (km^2)	$A_{3\text{-}D}$ (km^2)	Difference (%)
snow/ice	57.0	65.0	+14
rock	665.7	805.5	+21
tall tussock	405.2	478.1	+18
short tussock	637.6	656.7	+3
degraded tussock	389.3	397.1	+2
water	97.7	97.7	+0
conifer	0.6	0.7	+13
pasture	6.1	6.2	+2
total	2259.1	2506.9	+11

The region is typically dominated by a reasonably regular procession of eastward moving anticyclones across New Zealand with a periodicity of approximately 7 days (Greenland 1973). Between each pair of anticyclones there is a trough of low pressure containing one or more (usually cold) fronts (Greenland 1973). The passage of a front is typically prefaced by moderate to strong west to northwest flow, with orographic rainfall and downstream foehn conditions resulting from interaction with the mountain barrier. The front itself is usually associated with deep, precipitating cumuli and colder south to southwest flow (Ryan 1984). However, frontal splitting around the Southern Alps has also been observed, leaving the MacKenzie Basin comparatively clear.

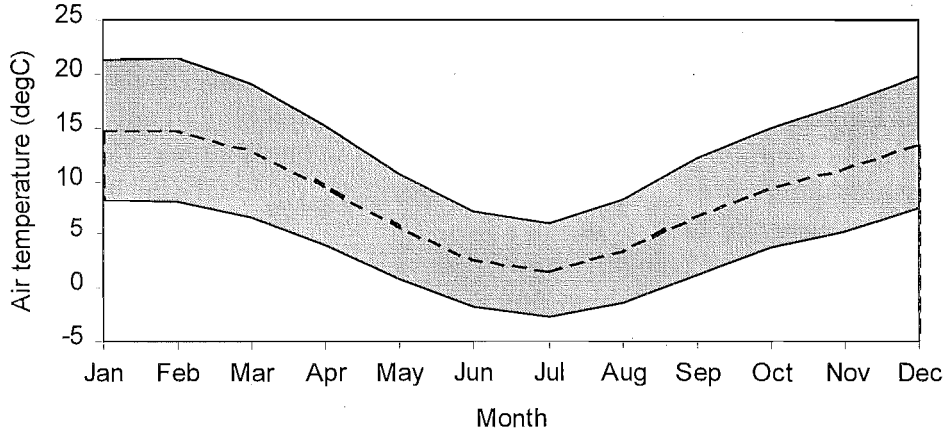

Figure 3.5 Monthly means of daily minimum, maximum and mean temperatures for Lake Tekapo Village between 1925 and 1980 (data from New Zealand Meteorological Service 1986).

The broader setting of airflow over the South Island is a reflection of the prevailing westerly quarter winds and their interaction with the 2000 to 3000 m alpine barrier. This results in the development of upstream blocking (McCauley and Sturman 1999), downstream foehn conditions (Lamb 1974, Brenstrum 1989), and forced and pressure driven channeling of airflow within mountain valleys (Revell *et al.* 1996). Orographic disturbance of the regional pressure field also results in the generation of a lee-side

trough, which has a significant effect on the wind field of the eastern side of the South Island (McKendry *et al.* 1987). Foehn west to northwest airflow is the most prevalent surface wind observed in the catchment, although it varies spatially in strength and direction due to local topographic influences. Under clear anticyclonic conditions, light, diurnally reversing thermal circulations operate in response to thermal forcing by the local topography and the presence of the lake (McGowan *et al.* 1995, McGowan and Sturman 1996). In addition, on such days, regional-scale easterly plain-to-mountain flow commonly enters the basin in the afternoon through low points in the eastern ranges.

Classification of daily synoptic situations by Watts (1947) showed that, for most of the South Island, four types of synoptic situation prevail for a total of 76 percent of the time. These are: anticyclones (20%); moderate to strong northwest airflow (15%); cold fronts (10%); and weather at the rear of cold fronts (31%). Sturman *et al.* (1984) derived synoptic circulation statistics from 20 years of daily mean sea level (msl) pressure analyses for New Zealand. They found circulations to be anticyclonic 49% of days, cyclonic 32% of days and unspecified 19% of days. Seasonal analyses showed cyclonicity to be greatest in winter and spring and lowest in late summer. In the present study, daily msl pressure maps for the New Zealand region from December 1997 to February 1999 were classified subjectively to generate monthly statistics of the synoptic situation over the study area. The classes selected were anticyclonic (weak pressure gradients), cyclonic northwest gradient flow and cyclonic southwest gradient flow. The selection of these classes is based on the significantly different climates produced by each situation in the Tekapo catchment, as discussed above. The mean statistics for 1998 showed an anticyclonic situation (ANT) on 51% of days, cyclonic northwesterlies (CNW) on 20% of days, cyclonic southwesterlies (CSW) on 19% of days and unspecified situations on 10% of days. Monthly statistics from this record are provided in Appendix B.

Precipitation is extremely variable throughout the catchment, due to rain shadow effects. The main divide receives up to 12 m yr^{-1} declining rapidly to below 1 m yr^{-1} on the eastern edge of the alps (Griffiths and McSaveney 1983). Average rainfall for Lake Tekapo Village is 0.597 m yr^{-1} resulting from an average of only 72 days with rainfall greater than 1 mm. Seasonal variability in both monthly total rainfall and number of rain days is minimal except for a small decrease (~ 15 %) in late summer. Correspondingly, annual sunshine hours are in excess of 52 percent of potential sunshine hours with greatest percentages occurring in summer. Ground frosts can be expected on approximately 170 days yr^{-1} ranging from 1.1 days in January to 27.6 days in July. As a result of low rainfall, high sunshine hours and prevailing dry northwest winds, soil water mean annual deficits of 400 to 450 mm exist (Webb 1992).

3.4 Methodology

There are four methodological steps taken in this study to address the three main objectives outlined in Chapter One. Firstly, longer-term radiation budget and energy balance data were collected at a single site in MacKenzie Basin. Secondly, three mobile energy balance stations were deployed over nine different surfaces in the course of a month in summer to observe spatial patterns, particularly those associated with surface cover. Thirdly, surface radiation budget modelling was conducted for the Tekapo catchment surface, in order to examine the spatial variability of radiation components, primarily as a function of topography. Finally, the surface classification presented

earlier, in collaboration with radiation model output and observed flux ratios is used to map the spatial variability of individual components of the surface energy balance. A schematic flow diagram is presented in Figure 3.6 to describe this general procedure.

The following sections provide an outline of the observational methods used in this study including the instruments, techniques and sampling strategies. The theoretical and instrumental limitations of the techniques used are discussed and results of inter-comparisons are presented. The physical basis and computational procedures for the surface radiation model SRAD are discussed at the outset of Chapter Six. The model relies on a digital elevation model to define such spatially varying parameters as slope angle, aspect and elevation. The surface cover map was also used in conjunction with observations to provide the model with spatial patterns of parameters that are related to surface cover, such as albedo and leaf area index. Additional inputs included air and surface temperature statistics from a reference station, an optical transmissivity coefficient and latitudinal range. Radiation components measured at a variety of locations were used for comparisons against radiation components from model output.

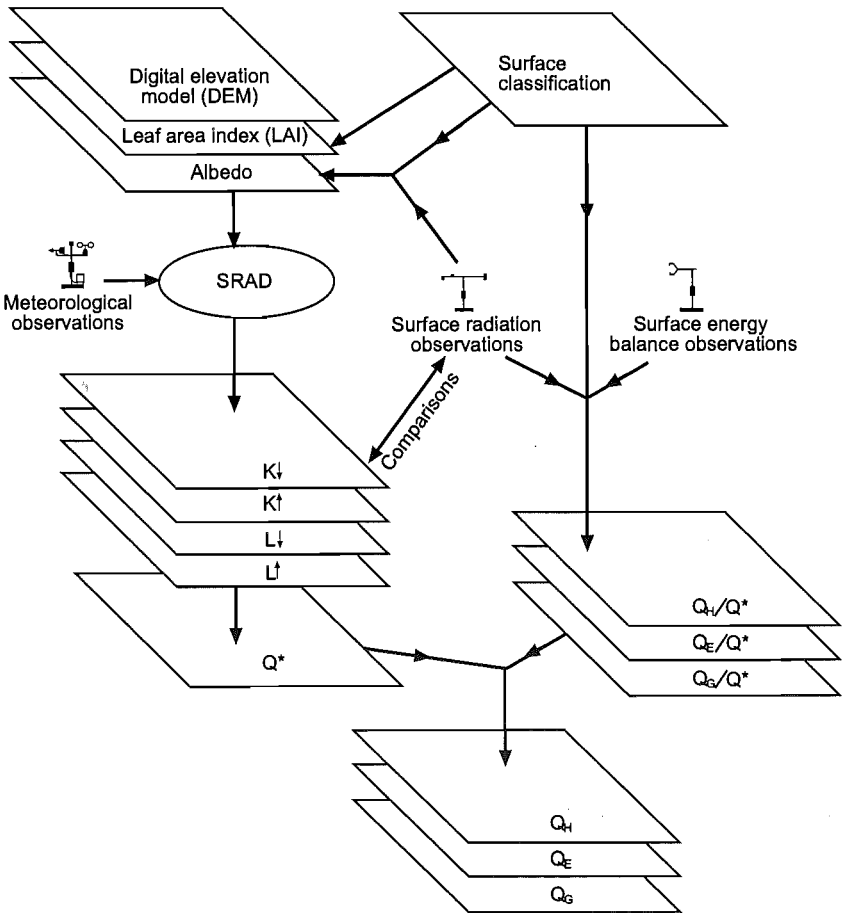

Figure 3.6 Schematic flow diagram representing the procedure in producing maps of energy balance components.

3.4.1 AWS network

The surface meteorological data used in this study were derived from a network of automatic weather stations (AWS). The locations of these can be found in Figure 3.1. In general, the AWS measured wind speed and direction, air temperature and relative humidity at about 3m. Soil temperature, atmospheric pressure and rainfall were also

typically measured. A list of relevant information pertaining to each station can be found in Table 3.2 and manufacturers, models and the estimated error of each instrument is provided in Table 3.3.

All instruments were calibrated prior to deployment in the field and routine checks were made using handheld instruments throughout their deployment. Data were collected by Campbell Scientific Inc (CSI) CR21X and CR10 dataloggers at sampling intervals of 5 seconds. During the bulk of deployment when site visits were restricted to 6 weekly intervals, data were stored as hourly averages with daily means, maximums and minimums also recorded. This was reduced to 10-minute averages during two field experiments in November/December, 1997 and January/February, 1999.

Table 3.2 Summary of surface meteorological stations, where Ta and RH are screen level air temperature and relative humidity respectively, U and dir are wind speed and direction respectively, P is air pressure, K↓ is incoming solar radiation and T_{surf} is surface temperature.

Name	Location	Parameters	Observation period
AWS0	Panorama Ridge	Ta, U, dir, rain, snow depth	Nov97 – Apr 99
AWS1	North end of Godley Valley	Ta, RH (0.2,2.4m) U, dir (2.5), K↓, Ts (0.1m)	Nov 97 – Apr 99
AWS2	Godley Valley between North Branch & Weka Stream	Ta, RH (0.2, 2m), U, dir (2.1m), P, K↓, Q*, Q_G	Jan/Feb 99
AWS3	Roadside near Mt Gerald station house	Ta, RH (1.6m), U, dir (3.2m), P	Jan 28 – Feb 15 99
AWS4	Lower first paddock	Ta, RH (1.6m), U, dir (3.2m), P	Feb 1 – Feb 2 99
AWS5	Upper first paddock	Ta, RH (1.6m), U, dir (3.2m), P	Jan 24 – Feb 2 99
AWS6	Midway up Mt Gerald slope	Ta, RH (1.6m), U, dir (3.2m), P	Jan 24 – Feb 8
AWS7	Top of Mt Gerald slope	Ta RH (1.6m), U, dir (3.2m), P	Jan 30 – Feb 15
AWS8	Godley Delta north of lake	Ta, RH, U (1.03, 3.9, 9.05m), U (6.09m), dir (9.05m), Ts (0.1m), P	Nov 97 – Feb 99
AWS9	Northeast corner of lake Tekapo	Ta, RH (1.6m), U, dir (3.2m), P	Feb 1 – Feb 6 99
AWS10	Midway up the ski road	Ta, RH (1.6m), U, dir (3.2m), P	Jan 25 – Feb 1 99
AWS11	Top of the ski road	Ta, RH (1.6m), U, dir (3.2m), P	Jan 25 – Feb 1 99
AWS12	Cass Stream delta	Ta (0.6, 3.13m), RH (3.13m), U, dir (3.4m) Ts (0.1m), K↓	Nov 97 – Apr 99
AWS13	Lake edge near Boundary Stream	Ta, RH (3.12m), U, dir (3.37m), Ts (0.1m), P	Nov 97 – Apr 99
AWS14	Lake edge near Mt Hay	Ta, RH (1.4m) U, dir (1.55m), Q_G	Jan/Feb 99
AWS15	Mt John	Ta, RH (3.14m), U, dir (3.34m), Ts (0.1m)	Nov 97 – Apr 99
AWS16	4 km south of airport	Ta, RH (3.2m), U, dir (10m), Ts (0.1m), P, K↓, Tsurf.	Nov 97 – Apr 99

3.4.2 Radiation

Observations of various radiation components were made at several locations. Long-term radiation budget data were collected at the location of AWS 16. This included Q^*, $K\downarrow$ (both total and diffuse beam), $K\uparrow$, and surface temperature, from which $L\uparrow$ was calculated using Eq. 2.11. Incoming longwave radiation was calculated as a residual by rearranging Eq. 2.1 so that,

$$L\downarrow = Q^* - (K\downarrow - K\uparrow) + L\uparrow \qquad (3.2)$$

Additionally, $K\downarrow$ was recorded at AWS1, 2 and 12 (Figure 3.1, Table 3.2). A mobile radiation station, measuring all components of Eq. 2.1 was deployed over various surfaces in the 1999 experiment in conjunction with mobile energy balance equipment. The locations and observation periods for this station can be found in Table 3.4. In addition, hand held instruments were used to make observations over a variety of surfaces during the two experiments.

Instrument details are provided in Table 3.3. Prior to deployment, pyranometers and pyrradiometers used in this study were calibrated in a uniform environment over a period of 4 days. Due to the linear response of voltage to radiation flux density in these instruments, linear regression was used to compare instruments and calibration coefficients were altered so that their output converged on a mean value. In this way inter-instrument errors were negligible, which is critical when they are utilised for inter-site comparison. As with the AWS, CSI dataloggers were used and output was averaged at intervals ranging from 10 minutes to one hour.

Table 3.3 Instruments used to measure meteorological and radiation parameters and the expected margins of error based on factory calibration where available.

Parameter	Make and model	Accuracy
Air temp and RH	CSI 207 thermistor	+/- 0.5 °C, 10%
	Vaisala HMP35D	+/- 0.2 °C, 5%
Soil temp	CSI. 107 probe	+/- 0.5 °C
Wind speed	Vector A101M-LI cup anemometer	
	Young wind sentry 03002	+/- 2%
Wind direction	W200P wind vane	
	Young wind sentry 03002	+/- 5°
Atmospheric pressure	Sen Sym SCX pressure transducer	
K↓ and K↑	Licor LI-200SZ pyranometer	+/-3%
K↓(diffuse)	Kipp & Zonen CM5 pyran + shadow band	
Surface temperature	Everest 4000A infrared transducer	+/- 0.5 °C
	Omegascope OS2000A infrared pyrometer	+/- 1 °C
L↓	Kipp & Zonen CG1 pyrgeometer	+/- 10%
Q*	REBS Pyrradiometer	+/-3%

3.4.3 Ground heat flux

In order to estimate ground heat flux, Radiation and Energy Balance Systems (REBS) heat flow transducers (flux plates) were used, as well as additional transducers that were manufactured in the University of Canterbury Geography Department (Moran 1971). All of these sensors were calibrated in a sand bath, using a new (factory calibrated)

REBS transducer as a benchmark. Since, like the pyranometers and pyrradiometers, these sensors produce a linear voltage response to changes in heat flow, linear regression was used to adjust the calibration coefficients of all other sensors. With this adjustment, relative errors of +/- <2% could be expected.

The field deployment of sensors is likely to cause greater accuracy problems than those noted above. Ground heat flux measurement theory and practise are discussed by Massman (1992). Currently, two techniques are commonly used. The first, the 'storage' technique, is to bury heat flux plates at 5–10 cm below the surface. Since a portion of heat flux is stored in the overlying column of soil before reaching the flux plate, it is necessary to determine the magnitude of this using:

$$\Delta S = \frac{\Delta T_S}{\Delta t} \times D \times BD \times (C_S + W \times C_W) \tag{3.3}$$

where ΔS is the change in heat storage, ΔT_S is the bulk average change in temperature of the soil layer over a given time period (Δt) , D is the measurement depth to the flux plate, BD is the bulk density of the soil, C_S and C_W are the specific heat of dry soil and water respectively and W is the soil water content by mass. This calculation requires the measurement of temperature through the overlying column, as well as site-specific inputs for bulk density, water content and the specific heat of dry soil. Estimation of each of these parameters is subject to small errors depending on the techniques or assumptions. Furthermore, this approach neglects the role of air in the soil on heat capacity, although the specific heat of air is relatively close to that of dry soil. It also assumes no horizontal flow of heat through the soil column, an assumption reliant on the homogeneity of the soil.

The second technique (non-storage) is to place the flux plates as near to the surface as is practically possible, and assume heat storage to be zero. This approach greatly reduces the number of contributing parameters to the measurement, although its accuracy is subject to the amount of storage actually occurring in the thin column above the plate. Another source of error is the impediment of moisture migration by the flux plate, which may cause the soil layer to dry more quickly than adjacent soil. However, this study was conducted in a semi-arid environment, so that this effect is expected to be minimal. In this study, longer-term measurements at the BREB site used the storage technique, while MEB stations used the non-storage method for ease of relocation. A comparison was made between the two techniques at the BREB site. The results of this comparison can be reviewed in Appendix C. The storage technique produced a higher over-all range in Q_G than the non-storage method, which also showed more temporal detail. Differences were generally less than 25 W m^{-2}.

3.4.4 Estimating turbulent fluxes

Of the four terms in the surface energy balance equation, the turbulent fluxes (Q_H and Q_E) are the most difficult to determine due to the complicated behaviour of turbulence and limitations of similarity principles (Oke 1987). There are a growing number of methods by which turbulent fluxes can be estimated, each with a set of assumptions or limitations. The two techniques employed in this study were the eddy covariance (EC) method and the Bowen ratio energy balance (BREB) method. In this section, the theory and limitations of these two techniques are discussed, followed by an evaluation of the extent to which outcomes of the two systems can be compared. The BREB station was

located at a fixed site throughout the study period, while three EC systems were used as mobile energy balance (MEB) stations over a variety of surfaces. A list of the instruments, locations and timing of all energy balance observations made in this study is provided in Table 3.4. In addition, Figure 3.7 illustrates the BREB and EC systems used as well as some of the site characteristics.

Table 3.4 Summary of site details for surface flux stations. Description of instrument notation can be found in Tables 3.2 and 3.3.

Station	Site description	Instruments/parameters and heights	Obs. period
MEB1	Valley floor, flat flood plain, river gravel sediment, very uniform	CSAT3, KH20, Ta, RH (1.8m), P, Q_G, Q* K↓, K↑, L↓, L↑	Feb 10-13 99
MEB2	5deg west facing slope, dense tussock grassland, 50 cm veg.	CSAT3, KH20, Ta, RH (2m), P, Q_G, Q*, K↓, K↑, L↓, L↑	Feb 1-2 99
MEB3	8deg west facing slope, dense tussock grassland, 50 cm veg.	CSAT3, KH20, Ta, RH (1.8m), P, Q_G, Q*, K↓, K↑, L↓, L↑	Feb 2-3 99
MEB4	11deg west facing slope, dense snow tussock, 60 cm veg.	CA27, KH20, Ta, RH (1.8m), U, dir (2m), P, Q*, Q_G	Feb 2-4 99 (night only)
MEB5	3deg west facing alluvial fan, 300m from lake. 60% tussock (15cm), 30%Hieracium, 10%bare	CSAT3, KH20, Ta, RH (1.7m), P, Q_G, Q*, K↓, K↑, L↓, L↑	Jan 25-29 99
MEB6	3deg west facing alluvial fan, 300m from lake. 60% tussock (15cm), 30%Hieracium, 10%bare	CSAT3, KH20, Ta, RH (1.7m), P, Q_G, Q*, K↓, K↑, L↓, L↑	Feb 5-9 99
MEB7	Lake surface, northeast corner, 0.8m deep turbid water, deepening gradually offshore	CA27, KH20, Ta, RH (2m), U, dir (2.05m), P, Q*, Q_G	Feb 4-13 99
MEB8	2.5deg west facing slope, 70% tussock (25cm), 30%Hieracium	CA27, KH20, Ta, RH (1.6m), U, dir (2m), P, Q*, Q_G	Feb 13-16 99
MEB9	10deg west facing slope, patchy snow tussock (60cm) with some Spaniards	CSAT3, KH20, Ta, RH (1.9m), P, Q_G, Q*, K↓, K↑, L↓, L↑	Feb 13-16 99
MEB10	3deg west facing alluvial fan, 300m from lake. 30%degraded tussock, 40%Hieracium, 30%bare	CA27, Ta, RH (1.65m), U, dir (2m), P, Q*, Q_G	Jan 25-31 99
MEB11	Lake surface, north oriented shore, 1m deep water, deepening rapidly offshore	CA27, KH20, Ta, RH (1.4m), U, dir (1.6m), P, Q*, Q_G	Jan 24-25 99
MEB12	Degraded tussock grassland. 40% bare soil, 40% Hieracium, 20% tussock	CA27, Ta, RH (1.8m), P, Q*, Q_G	Jan 24-26 99
BREB	Degraded tussock grassland. 40% bare soil, 40% Hieracium, 20% tussock	Ta, Vap P (0.8, 2.6m), Q*, Q_G, K↑, Kdif	Nov97-Apr98, Jun-Aug98, Oct 98–Feb 99

Eddy Covariance

The EC method estimates turbulent fluxes directly by examining the relationship between the convective transport mechanism (vertical wind speed) and fluctuations of the scalars that are being transported. This method has developed significantly since its

instrument capabilities, and is currently the most widely used technique. The EC approach, coupled with measurements of net radiation and ground heat flux, offers the advantage of being able to determine all the terms in Equation 2.1 directly, and subsequently use closure of the surface energy budget as a valuable, but not absolute, check on the flux measurements.

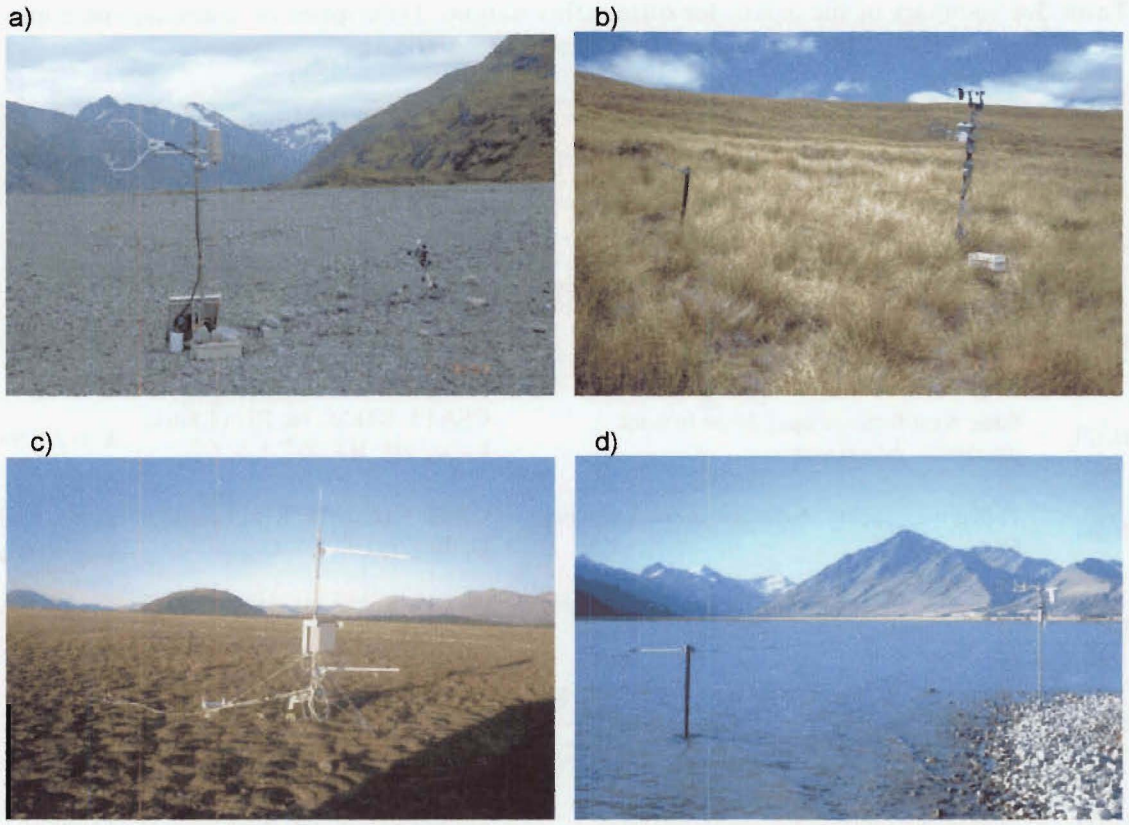

Figure 3.7 Plates showing the main energy balance stations; a) CSAT3 over the Godley Valley river gravels at MEB1, b)CA27a on the slope of Mt Gerald at MEB4, c) BREB in MacKenzie Basin and d) CA27bon the edge of Lake Tekapo at MEB7.

The physical basis for EC estimations of surface fluxes is that atmospheric transport involves both a mean and fluctuating component as a result of turbulence. The properties transported by turbulent eddies are mass (given for a unit volume by density (ρ)), vertical velocity (w) and the volumetric content of any scalar it possesses (s). Since each one can be broken into a mean and a fluctuating part, the mean vertical flux density of a scalar (S) can therefore be written:

$$S = \overline{(\overline{\rho} + \rho')(\overline{w} + w')(\overline{s} + s')}. \qquad (3.4)$$

This can be simplified since all single primed quantities can be averaged to zero, the density prime term can be neglected because it is virtually constant in the lower atmosphere and by measuring over uniform terrain, the mean vertical velocity term can be neglected (Oke 1987). With these assumptions, Equation 3.4 can be reduced to the form of the relation underlying the EC approach:

$$S = \overline{\rho w' s'}. \qquad (3.5)$$

The overbar denotes the time averaged instantaneous covariances of w and s. Inserting the scalars of heat and moisture, sensible and latent heat can be derived respectively so that:

$$Q_H = C_a \overline{w'T'}, \tag{3.6}$$

$$Q_E = L_v \overline{w'\rho_v'} \tag{3.7}$$

where C_a is specific heat of air, L_v latent heat of vapourisation and ρ_v is vapour density. To obtain time averaged instantaneous fluxes by the above formulations, CSI sonic anemometer thermometers (CA27 and CSAT3) and krypton hygrometers (KH20) were used to obtain measurements of w, T and v respectively with a sampling frequency of 10 Hz (Table 3.4). To measure fluctuations in temperature the CA27 uses a 12.7 μm copper-constantan thermocouple while the CSAT3 has the capacity to determine sonically measured virtual temperature by relating variation in the speed of sound (determined by averaging the 3 sonic axes) to temperature.

The estimated noise equivalent wind measured by the CA27 and CSAT3 is +/-0.5 mm s^{-1} in the vertical and +/-1 mm s^{-1} in the horizontal (for CSAT3), which equates to a 0.002 °C error in virtual temperature. Further error has been found to occur as a result of shadowing effects by the sonic transducer heads. Some corrections have been suggested (*e.g.* Massman *et al.* 1990) using algorithms derived empirically from wind tunnel experiments (*e.g.* Conklin 1988). However, significant variability has been found to occur as a result of environmental factors (*e.g.* wind speed, stability and temperature) as well as instrument factors (*e.g.* sensor size, shape and orientation relative to wind direction) making the shadowing effect difficult to quantify and no correction was used in this study. On a broader scale, the mast and instruments produce a strong influence on turbulent characteristics of airflow immediately downwind of them. To limit this problem, instruments were oriented into the prevailing winds and data that were collected when the wind direction was from a 70-degree angle centred behind the instruments were discarded.

The KH20 measures the absorption of ultraviolet radiation by water molecules to determine atmospheric vapour density. Since oxygen also absorbs UV radiation, a correction was applied for the density of oxygen based on the work of Tanner and Green (1989) and Massman *et al.* (1990). Variation in density associated with heat and moisture fluxes also affects Q_H and Q_E values, which are measured initially using a constant density coefficient. This influence was corrected for in post processing, based on the formula of Webb *et al.* (1980). The configuration of instruments used in each station and individual site details are listed in Table 3.4, while the site locations can be found in Figure 3.1 and Figure 3.7 illustrates several MEB sites.

Bowen ratio method

The theory for this method was first established by Bowen (1926) and uses the similarity assumption that K_H and K_V are equal (Section 2.3.1). In this case, K_H and K_V need not be estimated since they are cancelled out in the Bowen ratio equation, which can then be defined:

$$\beta = \frac{Q_H}{Q_E} = \frac{C_a \Delta \overline{T}}{L_v \Delta \overline{\rho}_v} \tag{3.8}$$

where $\Delta \overline{T}$ is the vertical temperature gradient and $\Delta \overline{\rho}_v$ the vertical gradient in vapour density. Calculating the Bowen ratio (β) in this way requires accurate observations of temperature and vapour density at two heights within the surface layer. The energy balance approach then relies on accurate measurements of Q^* and Q_G so that $Q_H + Q_E$ is known (*i.e.* $Q^* - Q_G$). The individual turbulent fluxes can be calculated from the surface energy balance in terms of β from:

$$Q_H = \beta \frac{(Q^* - Q_G)}{(1+\beta)} \tag{3.9}$$

and

$$Q_E = \frac{(Q^* - Q_G)}{1+\beta} \tag{3.10}$$

The system used to estimate vertical gradients in temperature and water vapour in this study was a CSI Bowen ratio energy balance system. Temperature was measured at two heights using 25μm diameter chromel-constantan thermocouples. These were found by the manufacturer to experience less than 0.2 °C and 0.1 °C heating at 0.1 ms^{-1} and 1 ms^{-1} for 1000 Wm^{-2} radiation. Vapour pressure was measured with a single General Eastern Corp. Dew-10 cooled mirror dewpoint hygrometer. Air was drawn in from two heights and alternately sampled by the hygrometer at two-minute intervals with 40 seconds allowed for the mirror to stabilize on the new dewpoint. Vapour pressure was calculated using the equation described by Lowe (1977), illustrating that the limiting stability of the Dew-10 of 0.05°C yields better than +/-0.01 kPa vapour pressure resolution over most of the environmental range. The site details, measurement heights and additional measurements are provided in Table 3.4, the location can be found in Figure 3.1 and Figure 3.7(d) provides a perspective of the system with the nature of its surrounding surface.

Errors in the gradient measurements affect the accuracy of β directly, so that 1% error in a measurement results in 1% error in β. However, errors in β do not affect the flux estimates linearly. The relationship between Q_H, Q_E and β is plotted in Figure 3.8 using Equations 3.8 and 3.9. The turbulent fluxes are relatively insensitive to error in β when $\beta > 1$ than when $\beta < 1$. Furthermore, as β approaches –1, the fluxes diverge unrealistically until Equations 3.8 and 3.9 are indefinable when β is –1. For this reason, when $-0.3 > \beta < -1.7$ data were discarded and fluxes were extrapolated by fitting a sine curve to the existing data. Fortunately, this occurred relatively infrequently and only for brief periods, typically around sunrise and sunset.

The limitation of the diffusivity similarity assumption is another source of error using this approach, as discussed in Section 2.3.1. This has been found to be most strongly violated over patchy surfaces or when measurement height was near the top of an internal boundary layer (Motha *et al.* 1979, Lang *et al.* 1983, Bink 1996). However, McNaughton and Laubach (1998) concluded that typical ranges of non-similarity in K_H and K_V will usually incur only minor error in the BREB method. The impact of 25%

deviation from similarity on turbulent flux magnitudes as estimated by the BREB approach is added to Figure 3.8. This illustrates the relatively small magnitude of error that violation of this principal presents, especially during the day when β is typically positive and the magnitude of $Q^* - Q_G$ is significant.

Additional considerations

The source area for surface fluxes has been the focus of numerous studies (Gash 1986, Horst and Weil 1992, Leclerk and Thurtell 1990, Schmid 1994), which show that the size and shape of the surface source area of scalar fluxes, as observed by the instruments, are controlled by the instrument height, surface roughness, wind speed (both downwind and crosswind components) and surface layer stability. This places limitations on the siting of instruments because the well-established surface layer relationships used to describe turbulent exchange of heat, mass and momentum collapses in regions of surface heterogeneity. In absence of source area data, this area covers a distance of 100 to 300 times the measurement height in the upwind direction since 1:100-300 is the approximate range of vertical growth rate of the surface layer downwind from a change in surface (Tanner 1976). Furthermore, different scales of surface heterogeneity may influence measurements in different ways (Mahrt 1996). For example, it is possible to locate sensors where local plumes preferentially occur, thereby failing to properly account for the spatial dispersive flux and causing overestimation of turbulent fluxes (Barr *et al.* 1994). In this study, detailed analysis of source area was not made because the fetch requirements were easily met on most occasions. In some situations this was not true for all wind directions, so data collected from wind directions with inadequate fetch were discarded from calculations. Furthermore, surfaces were generally homogenous within the source areas, with heterogeneity occurring only on scales of the order of 0.1 m.

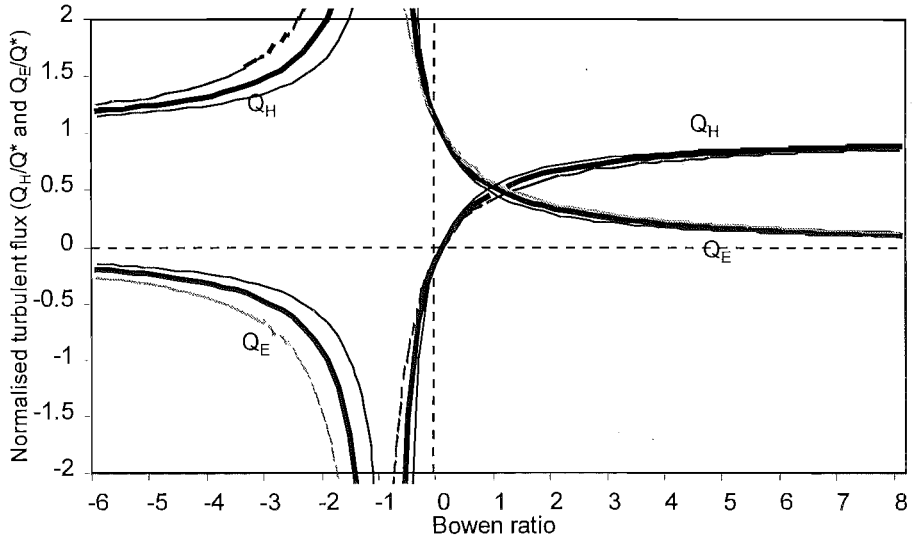

Figure 3.8 Dependence of Q_H (black) and Q_E (grey) on the Bowen ratio using Eq. 3.9 and 3.10, when K_H/K_V =1 (thick lines), 0.8 (thin dashed lines) and 1.25 (thin solid lines).

Cross comparisons and error assessment

The calibration of many meteorological instruments is relatively simple, since they typically derive variables through a linear relationship with resistance or voltage output. The calibration of radiation sensors for this study provides a good example. However,

since energy balance estimation involves the measurement of multiple variables and relies, in this study, on entirely different estimation theories, it is very unlikely that linear adjustment of output in this way would be appropriate. It is also likely that the adjustment required would differ for different surface types and meteorological conditions. Furthermore, the surface characteristics and airflow of each site usually requires different deployment configurations such as the height, orientation and angle of the instruments. Nevertheless, a comparison of the performance of energy balance systems used in this study is important since inter-site variability is an important component of the research.

The comparison of EC and BREB systems has been assessed in several studies over different surfaces. Kolle (1997) compared these systems over an agricultural field on a small hillock. Long-term data (421 days) produced close agreement for Q_H with small discrepancies in Q_E over the diurnal cycle. These discrepancies were concluded to be a function of the shape of the humidity profiles, which often showed a maximum at heights between 1 m and 4 m. Subsequently, BREB estimation using temperature and water vapour data from different pairs of heights and using Q_H derived from the EC system, also yielded different Q_E values. Above forests, Barr *et al.* (1994) and McNeill and Shuttleworth (1975) found EC to underestimate daytime turbulent fluxes, which was thought to result from loss of low frequency data due to short averaging periods. Differences between EC and BREB energy partitioning have also been concluded to result from the invalidity of the BREB similarity assumption when variations in temperature and humidity were not highly correlated (Barr *et al.* 1994). Close agreement between EC and BREB methods have been found when estimating evaporation for a lake surface (Stannard and Rosenberry 1991) and for a raised peat bog (Thompson *et al.* 1999). In the latter study, β was consistently higher in the BREB system, although the difference in Q_E averaged less than 10%.

Prior to deployment, the two KH20s were calibrated using a dew point generator. A third KH20 was used to replace a damaged instrument mid-experiment and this was calibrated post experiment. On two occasions prior to the main field experiment, comparisons were made at the BREB site between the MEB stations and the BREB station. The first study compared the two EC systems, CA27A and CSAT3, which use 1 dimensional and 3 dimensional sonic anemometers respectively. In addition, sonically derived temperature fluctuations from CSAT3 were used in Q_H estimation and compared with those derived from the fine wire thermocouple of CA27A. This study was conducted on October 23/24 1998 in clear, anticyclonic conditions with moist soil, following a period of rain several days earlier. Figure 3.9 shows the diurnal sequence of Q_H and Q_E estimated by the two systems. Q_H from the two stations was almost identical (Figure 3.9a). This provides confidence in the performance of the instruments, as well as the technique and siting since the statistical information derived from the turbulence measurements was very similar at both sites, yet obtained from different turbulent eddies (since the stations were ~10 m apart). Q_E also showed good agreement, although with less consistency in the afternoon (Figure 3.9b). Closure of the energy balance for the two stations is also plotted (Figure 3.9c). It is interesting to note that the two systems deviate in closure at the same times as they deviate in Q_E. Furthermore, the higher CSAT3 closure in the morning seems to compensate for the lower CA27A Q_E values, while the reverse is true of the afternoon. Since the same Q^* and Q_G data were used for the calculation of closure for both stations and Q_H, Q_E and closure corresponded between the two stations, evidence suggests that the energy imbalance is generated by either an underestimation of Q^* or an over estimation of Q_G (or a combination). This

could indicate the difficulty in obtaining Q^* and Q_G data that are representative of the same source area as the turbulent fluxes.

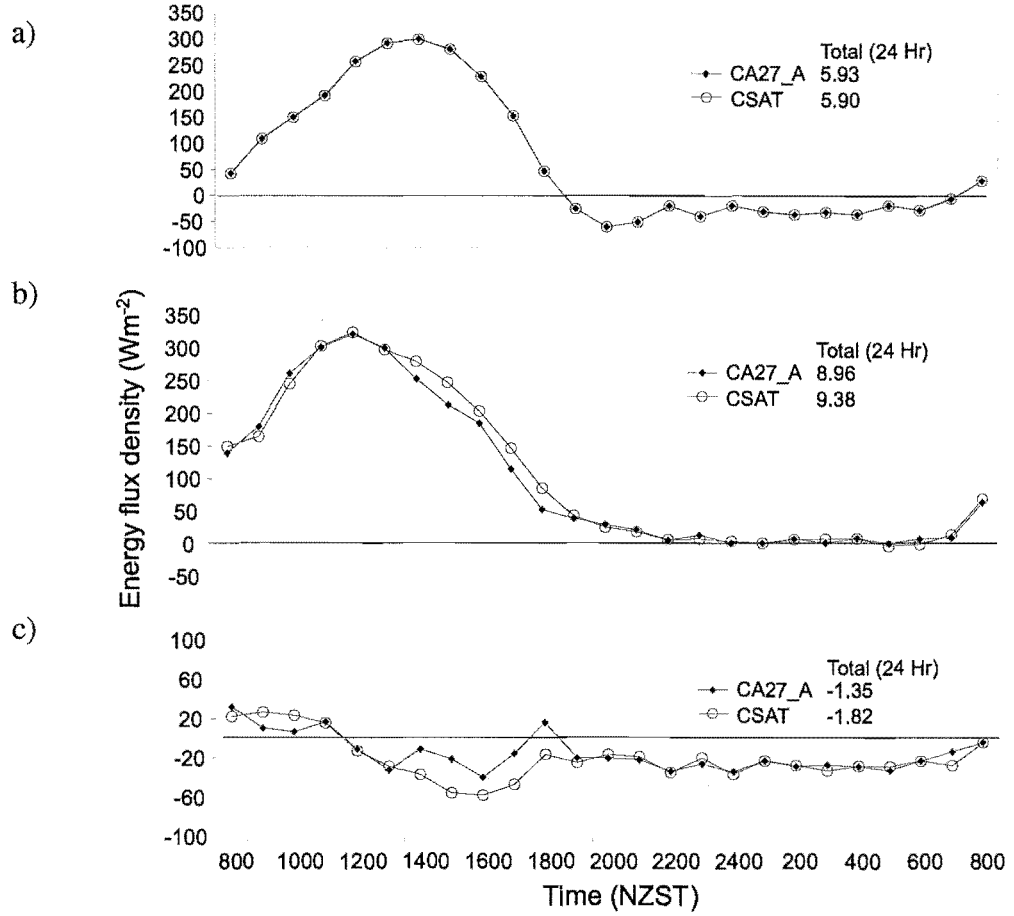

Figure 3.9 Comparisons between CA27A and CSAT3 for (a) Q_H, (b) Q_E and (c) energy balance closure for October 23/24 1998 at the BREB site.

The second comparative study was conducted at the same location on December 15/16 1998 in similar conditions but with considerably dryer soil. In this study, flux data are presented from stations CA27A, CA27B and BREB (Figure 3.10). With Q_H, again the two EC stations show favourable agreement, although with larger point-to-point variability, especially during the middle of the day. In comparison, Q_H estimated by BREB was generally larger than by the EC stations and with less point to point variability. Q^* has been included in this figure to illustrate the mid morning peak in energy, which is reflected in both the EC Q_H traces but less so by BREB. Unfortunately, the low magnitude of Q_E on this day prevents detailed comparisons, although the fluxes compare reasonably well. It is important to note that CA27B did not use a KH20 and so Q_E was calculated as a residual. Consequently, this value contains the sum of errors associated with the other three components. The larger range of Q_E estimated by CA27B than by the other two systems, is most likely a result of underestimation of Q_G or overestimation of Q^*, given the conclusions from the first study and the similarity of Q_H.

Since CA27A was the only station common to both studies, it was used as the independent variable in regression analyses to compare the estimation of Q_H and Q_E for the four stations. Descriptive and comparative statistics are provided in Table 3.5 and the scatter plots of all data are compared to CA27A in Figure 3.11. In general, good

agreement was found between these stations for the two comparison studies. The weakest agreement was found in CA27B's estimation of Q_E, which was calculated as a residual of the energy balance. This is not surprising since this estimation incurs the net error in measurement of the other energy components. In particular, concern was raised earlier over the representativeness of point measures of Q^* and Q_G of the source area of fluxes. In order to completely assess station comparability for this study, it would be necessary to undertake these same tests over each of the different surfaces examined. Nevertheless, evidence presented here provides confidence for the inter-site comparisons made in Chapter Five and a useful context for the conclusions that are subsequently drawn.

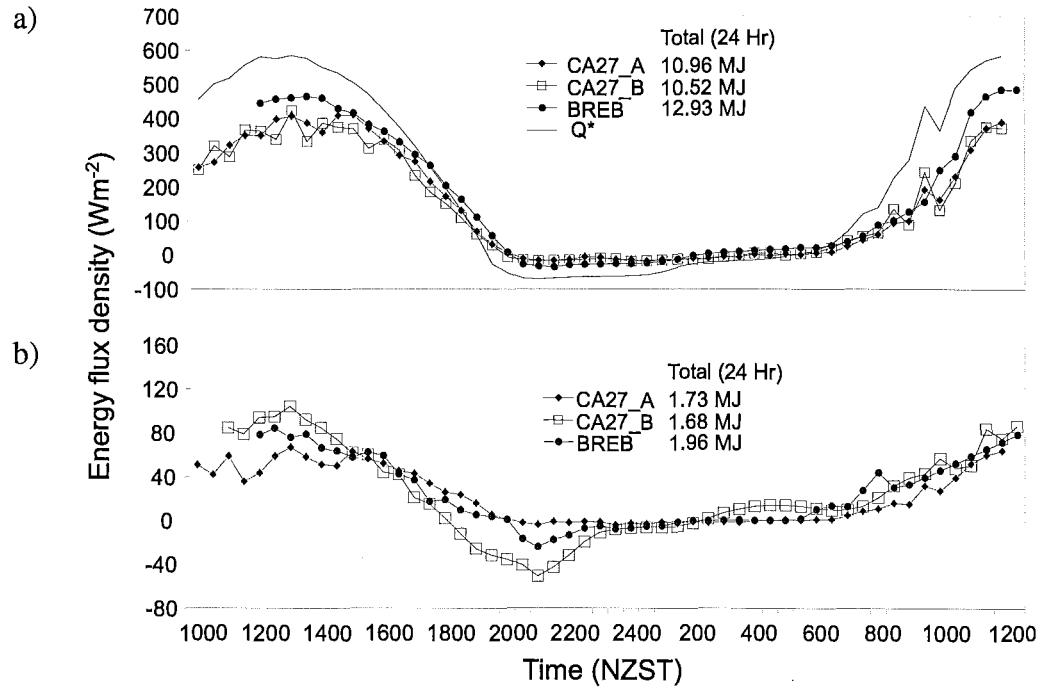

Figure 3.10 Comparisons between CA27A, CA27B and BREB for (a) Q_H and (b) Q_E for December15/16 1998 at the BREB site.

3.4.5 Soil water and organic content

Periodic observations of the volumetric soil water content ($S_{(v)}$) were made at several locations in the study area. These were derived from gravimetric measurements of water content. Soil samples were extracted and weighed ($S_{T(w)}$), dried at 105 °C for 24 hours and re-weighed to determine the weight of water content ($S_{W(w)}$) as a ratio of dry soil weight. Volumetric soil water content ($m^3\ m^{-3}$) was then determined by converting the water weight to a volume so that:

$$S_{(v)} = \frac{S_{W(v)}}{S_{T(v)}} \quad \frac{(m^3)}{(m^3)} \tag{3.11}$$

Since the volume of the sample was not always known, soil bulk density (BD, $g\ m^{-3}$) for each site was determined by taking the ratio of dry soil weight ($S_{D(w)}$) to a known soil volume ($S_{T(v)}$):

$$BD = \frac{S_{D(w)}}{S_{T(v)}} \tag{3.12}$$

Volumetric water content was then determined by,

$$S_{(v)} = BD \times \frac{S_{W(w)}}{S_{D(w)}} \tag{3.13}$$

Since typically only 2-5 samples were taken from each site at each time, the magnitude of error associated with methodological inconsistencies or heterogeneity of soil moisture at a given site was evaluated. For this, 20 samples were taken on two occasions for two different locations, yielding a mean of 6.4% and 10.3% volumetric water content with a standard error of 0.23 and 0.26 respectively. The organic content was also derived on one occasion for all sites. Dried soil samples were placed in a 1200° C oven for 24 hours, and the loss of mass due to burning of organic matter was derived by the difference in weight before and after firing. Soil organic content was then calculated by the same method as soil water content.

Table 3.5 Statistical comparison of Q_H and Q_E determined by a) CA27A and CSAT3 on October 23/24 1998 and b) CA27A, CA27B and BREB on December 15/16 1998 at the BREB site.

A) Comparison 1

Q_H (n = 49)	CA27A	CSAT3
Mean (Wm^{-2})	65.6	65.2
Standard deviation (Wm^{-2})	118.7	118.4
Coefficient of determination (R^2)		1
Intercept linear regression(Wm^{-2})		0
Slope linear regression		1
Standard error of estimation (Wm^{-2})		0.3
Q_E (n = 49)		
Mean (Wm^{-2})	103	107.1
Standard deviation (Wm^{-2})	110.5	112.9
Coefficient of determination (R^2)		0.986
Intercept linear regression (Wm^{-2})		2.87
Slope linear regression		1.01
Standard error of estimation (Wm^{-2})		13.8

B) Comparison 2

Q_H (n = 48)	CA27A	CA27B	BREB
Mean (Wm^{-2})	131.5	126.8	155.7
Standard deviation (Wm^{-2})	161.6	155.5	187.6
Coefficient of determination (R^2)		0.955	0.98
Intercept linear regression (Wm^{-2})		3.17	1.15
Slope linear regression		0.94	1.18
Standard error of estimation (Wm^{-2})		33.3	26.5
Q_E (n = 48)			
Mean (Wm^{-2})	20.5	21.0	23.8
Standard deviation (Wm^{-2})	24.6	40.4	31.3
Coefficient of determination (R^2)		0.727	0.869
Intercept linear regression (Wm^{-2})		-7.66	-0.47
Slope linear regression		1.39	1.18
Standard error of estimation (Wm^{-2})		21.3	11.4

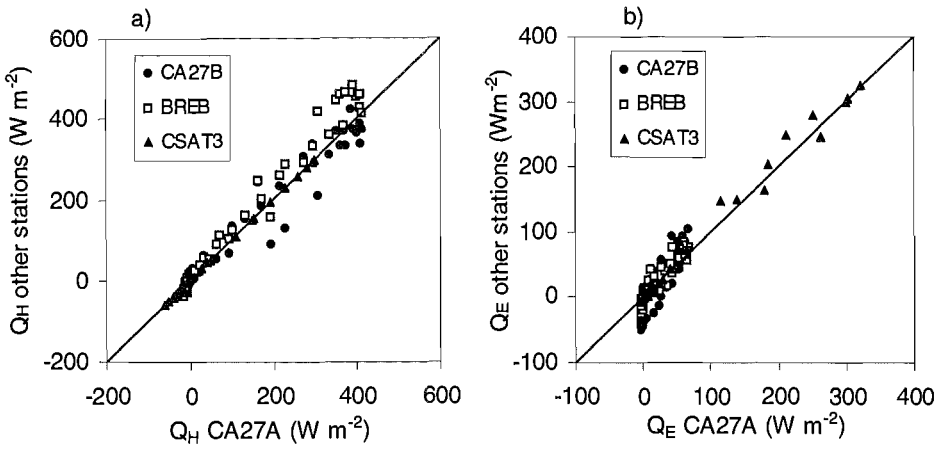

Figure 3.11 Scatter plots comparing a) Q_H and b) Q_E determined by the four energy balance stations during the two experiments at the BREB site in October and December 1998.

3.5 Summary

The purpose of this chapter has been to outline the physical characteristics of the environment in which this study was conducted and the methods that were used. The Tekapo catchment provides a range of topographic complexity, from the gently sloped lake basin area to deeply incised alpine terrain, with an elevation range of over 2000 m. The complexity of surface cover was considered to correspond approximately to topography, emphasising the links between uplift, rainfall, erosion, relief and surface cover in landscape development. The climatological setting of the catchment is dominated by the maritime setting of New Zealand, with the regular eastward passage of anticyclones punctuated by troughs of low pressure containing fronts. Within this setting, the catchment experiences relatively large diurnal and seasonal ranges in temperature, rain shadow effects and strong modification of prevailing westerly airflow.

The observational techniques used in this study were outlined, including theoretical considerations of the Bowen ratio energy balance and eddy covariance methods to estimate surface energy exchange. Measurement details for automatic weather stations, radiation sensors and energy balance systems were also provided. These included site locations and descriptions, as well as instrument models and error assessment. System limitations were discussed and the results of inter-system comparisons were reported so that conclusions of inter-site comparisons in subsequent chapters can be assessed in light of these limitations.

Chapter Four

Seasonal and synoptic controls of surface radiation and energy fluxes

4.1 Introduction

Surface energy exchanges are governed by the amount of available energy, vertical gradients of heat and moisture and the ability to transport energy through both the atmospheric surface layer and a shallow layer of the substrate (Section 2.3.1). Changes in all of these governing factors due to influences of the changing declination of the sun on week to month timescales, and to synoptic patterns on day to week timescales, leads to considerable temporal variability in the magnitude and partitioning of surface fluxes. This can be attributed to both direct and indirect effects. For example, the magnitude of Q^* is influenced most strongly by the solar declination angle. However, seasonal variability in cloudiness will also influence Q^*, as will changes in albedo due to frost or snow cover or soil colour change as a result of moisture content. Air temperature and humidity are governed by seasonal controls of Q_H and Q_E, as well as airmass properties that are advected into the region by regional and synoptic scale pressure gradients. Surface temperature is also affected in this way in combination with the surface radiation budget and changes in surface properties such as frost, soil moisture and vegetative changes. On the same timescales, transport mechanisms are also affected. For example, thermal conductance in the substrate is influenced by soil moisture content and eddy diffusivity is affected by changes in roughness due to vegetative changes or snow cover, as well as both seasonal and synoptic influences on wind speed. Combined, these properties (and others described in Chapter Two) potentially provide large and complex variability in surface energy exchanges over timescales from days to seasons.

The influences of seasonal and synoptic controls are not independent, since synoptic patterns vary in frequency and intensity during different seasons. Such influence is further complicated by the circularity of links between surface energy exchanges and

both seasonal and synoptic controls. Seasonal climates are most strongly driven by surface energy exchanges, which reflect changes in the Sun-Earth geometric relationship. Synoptic patterns are strongly governed, particularly in their genesis, by spatial variability in surface energy exchanges, which result in advection of airmasses with different properties of temperature and humidity. As these spatial and temporal changes in surface fluxes influence the local climate, the boundary conditions are altered, resulting in adjustment to the behaviour of the surface fluxes. These feedbacks generate a complex relationship that is itself in a constant state of flux. This circularity is evident in this research with regard to seasonal climatology and local scale advection, but feedbacks associated with synoptic controls are not evident, since the spatial focus is restricted to a single catchment.

The purpose of this chapter is to assess the magnitude of variability in surface energy exchanges in the Tekapo catchment that is associated with seasonal and synoptic patterns and to evaluate the causes for this variability. For this purpose, data are presented from the AWS16 and BREB site. From this dataset, 15 months of nearly continuous radiation and standard meteorological data are used in conjunction with 8 months of energy balance data, including one winter and two summer periods. Daily synoptic classification statistics (Section 3.2) are used in conjunction with this data set. Although this chapter focuses predominantly on temporal changes at a single site, implications for other locations in the catchment are evaluated through comparable data and modelling. The nature of the surface in the flux source area at the BREB site is described in Table 3.4. Since it is predominantly bare soil with some patchy evergreen ground cover, changes related to vegetative controls are thought to be minimal and not assessed directly in this chapter.

Initially, radiation fluxes are considered using both observed and modelled data. The impact of seasonal patterns on the radiation budget is assessed from longer-term data trends, and synoptic controls are evaluated through statistical analysis based on synoptic classification. Secondly, variability in the partitioning of Q^* into Q_H, Q_E and Q_G is examined. In this case, winter and summer seasons are considered separately. Within these seasons, case studies and statistical evidence are presented to isolate the influence of dominant synoptic controls. This is followed by an assessment of the influence of soil moisture on energy partitioning.

4.2 Surface radiation budget

This section presents longer-term observational data from the BREB site, as well as modelled $K\downarrow$ data. Initially the net short, long and allwave components are assessed and these are broken down in subsequent sections, focussing predominantly on $K\downarrow$ with respect to its importance for Q^*.

The daily mean Q^*, K^* and L^* for the entire study period is presented in Figure 4.1(a) as well as the breakdown into shortwave (b) and longwave (c) components. Missing longwave radiation component data in the winter of 1998 is due to instrument failure. As indicated in Chapter Two, the sign convention employed here assigns positive values to downward directed fluxes and negative values to upward directed fluxes. Relative to their means, large ranges can be seen to operate in all radiation components on timescales related to both seasonal and synoptic (day to week) timescales.

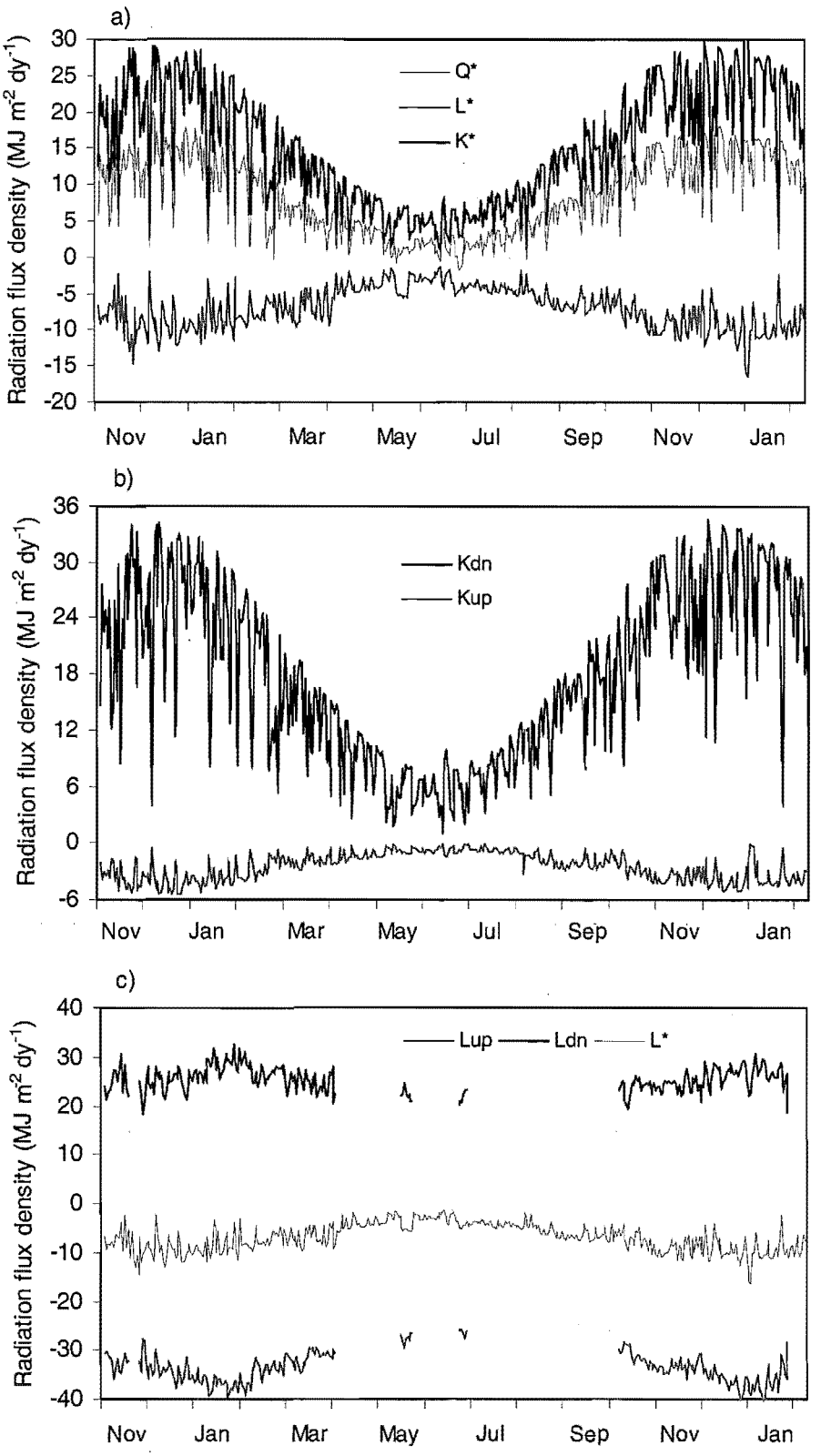

Figure 4.1 Daily total radiation flux densities for a) Q^*, K^* and L^*, b) $K\downarrow$ and $K\uparrow$ and c) $L\downarrow$, $L\uparrow$ and L^* recorded at the BREB site between November 1997 and February 1999. Winter gaps in $L\downarrow$ and $L\uparrow$ resulted from instrument failure. Note that $K_{dn} = K\downarrow$, $L_{up} = L\uparrow$ *etc.*

The maximum seasonal range of K^* was 21.1 MJ m^{-2} dy^{-1} while the maximum found within any seven day period was 22.2 MJ m^{-2} dy^{-1}. This compared with ranges in L^* of 6.3 MJ m^{-2} dy^{-1} over the seasonal timescale, with 10.6 MJ m^{-2} dy^{-1} within the course of a week. This comparison illustrates that K^* has the greater control of variability in Q^*.

For both Q^* and K^* the maximum synoptically influenced range was of a similar magnitude to the maximum seasonal range, although the latter was somewhat larger for L^*. This shows that synoptic and seasonal influences provide similar magnitudes of variability, but over different scales of time. However, the pattern of daily radiation totals associated with seasons produces an easily identifiable sine wave, which is considerably more uniform and predictable than the episodic and chaotic pattern of daily radiation associated with synoptic controls.

In Figure 4.1b it is clear that $K\downarrow$ dominated K^*, since $K\uparrow$ varies little. This is because the mean daily albedo of 0.14 reduces $K\uparrow$ to almost an order of magnitude lower than $K\downarrow$, and mean daily albedo does not vary significantly through the course of the study period (standard deviation = 0.05). The low variability of albedo is due to the very sparse vegetation, which changes little over the seasonal cycle, and large coverage of bare soil. Of the longwave components, $L\uparrow$ varied more than $L\downarrow$ on the seasonal timescale, illustrating that mean daily surface temperature had a larger range than atmospheric temperature (Figure 4.1c). By contrast, day-to-day variability in $L\downarrow$ was greater than $L\uparrow$. This accounts for the larger short-term variability in cloudiness and may also be indicative of the role of air temperature and humidity advection. While clouds reduce surface heating, their impact is more significant on $L\downarrow$ by reflecting or absorbing and re-emitting energy emitted from the surface. The resulting trend in L^* can be seen to correspond more closely to $L\uparrow$ on the seasonal timescale and more closely to $L\downarrow$ on a day to week timescale.

4.2.1 Seasonal influence on $K\downarrow$

The previous section has illustrated that, of the four components of the surface radiation budget, $K\downarrow$ has the most significant influence on Q^*. Therefore, it is useful to parameterise Q^* by $K\downarrow$ since it is possible to model $K\downarrow$ using Earth-Sun geometry relationships and characteristics (slope, aspect) of the terrain. Linear regression was used to find the relationship between $K\downarrow$ and Q^* for daylight hourly average fluxes (Figure 4.2a) and daily total fluxes (Figure 4.2b). In both cases, this relationship is strong, although it is evident that the relationship is stronger when assessed over a longer time period. The multiplier in both cases is similar and the offset difference simply recognises the inclusion of nocturnal net radiative losses with the absence of $K\downarrow$ in Figure 4.2b.

In order to assess the importance of cloudiness on $K\downarrow$ at the BREB site, observed fluxes were compared with those modelled for clear sky days. Direct beam and diffuse beam $K\downarrow$ ($K_S\downarrow$ and $K_D\downarrow$ respectively) were calculated for hourly instantaneous fluxes using Eq. (2.2 – 2.5) and integrated into daily totals. Figure 4.3a compares daily $K\downarrow$ observations with modelled results for the entire dataset. The modelled daily totals of $K\downarrow$ show good agreement with the seasonal pattern of maximum observed totals (clear-sky days), although with slight overestimation in winter and underestimation in summer. This might result from seasonal departure from the mean optical depth of 0.77 that was used in these calculations or from surrounding topography. For the former, this would imply that there was a generally dustier or more humid atmosphere in winter than in summer. Although suitable data to quantify this relationship are unavailable, it is doubtful, since long term data show neither windier nor significantly more humid records for winter (NZ Met. Service 1986). More likely to be the cause of the winter decrease is topography. Since this site is located in an extensive, nearly-flat basin with

distant mountains providing topographical obstructions at low elevation angles, fluxes were modelled under the assumption that the horizon was unobstructed. This assumption is more valid in summer than winter since the elevation of topographical obstructions increase toward the north (see Figure 3.1). This has the effect of obstructing high zenith angle $K_S\downarrow$ more significantly in winter. This effect does not account for the propensity for $K\downarrow_{(measured)}/K\downarrow_{(modelled)}$ to be greater than unity in summer (Figure 4.3a). This is likely to result from the inability of the model to account for days when atmospheric transmissivity was greater than 0.77.

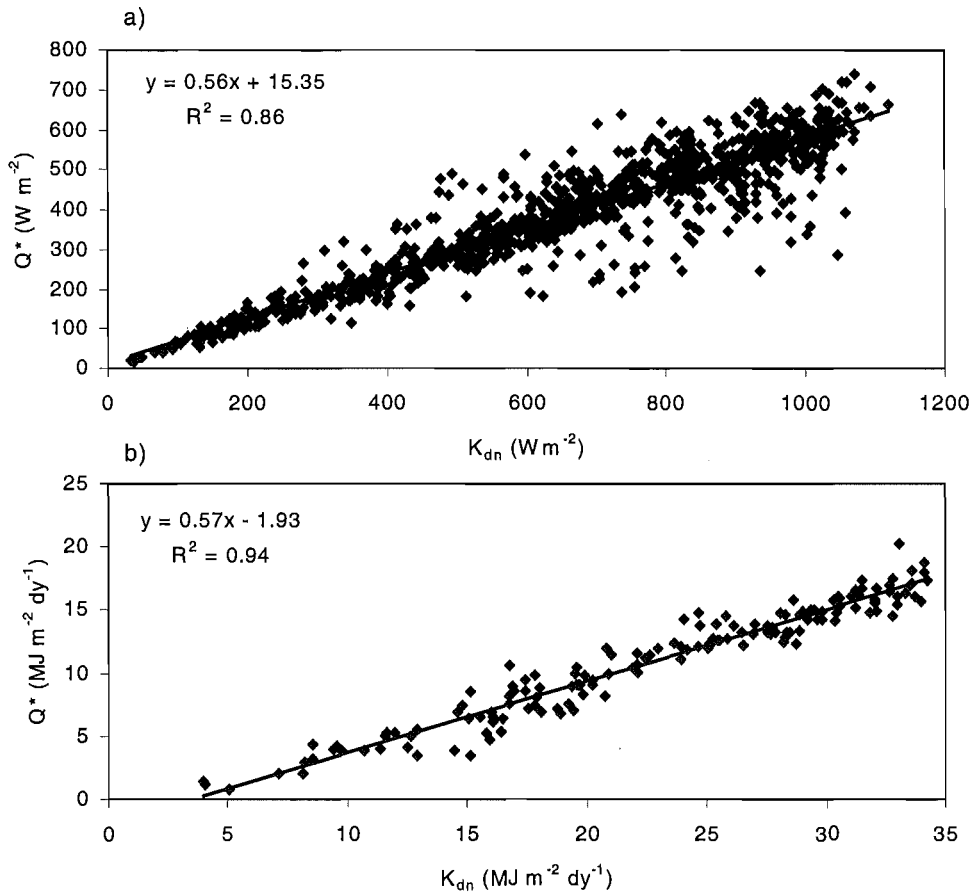

Figure 4.2 Linear regression analysis of the relationship between radiation flux densities of a) daylight mean hourly instantaneous $K\downarrow$ and Q^* and b) daily total $K\downarrow$ and Q^*, from concurrent data recorded at the BREB site between November 1997 and February 1999.

The agreement between the observed and modelled seasonal trends clearly illustrates the predictability of the role of the Sun-Earth geometric relationship in $K\downarrow$. The day to day variability, which is absent in the clear-sky modelled values but reaches a similar magnitude to the seasonal range, is likely to be a function of cloudiness. Monthly mean daily $K\downarrow$ values were compared with proportions of the clear sky potential to assess the magnitude of radiation depletion due to cloudiness (Figure 4.3b). This illustrates that only 8 of the 14 months reached greater than 80% of the clear-sky potential and none reached 90%. Although the largest depletion appeared to occur in winter with the least in late summer, a well-defined seasonal pattern is not evident, although significant month to month variability existed, as does variability between the same months of different years. Figure 4.3 illustrates that, while the seasonal trend in $K\downarrow$ as a function of Earth-Sun geometry is clear, day to day, month to month and even year to year

variability as a function of cloudiness is more complex and daily values of 50% depletion can occur in any given month.

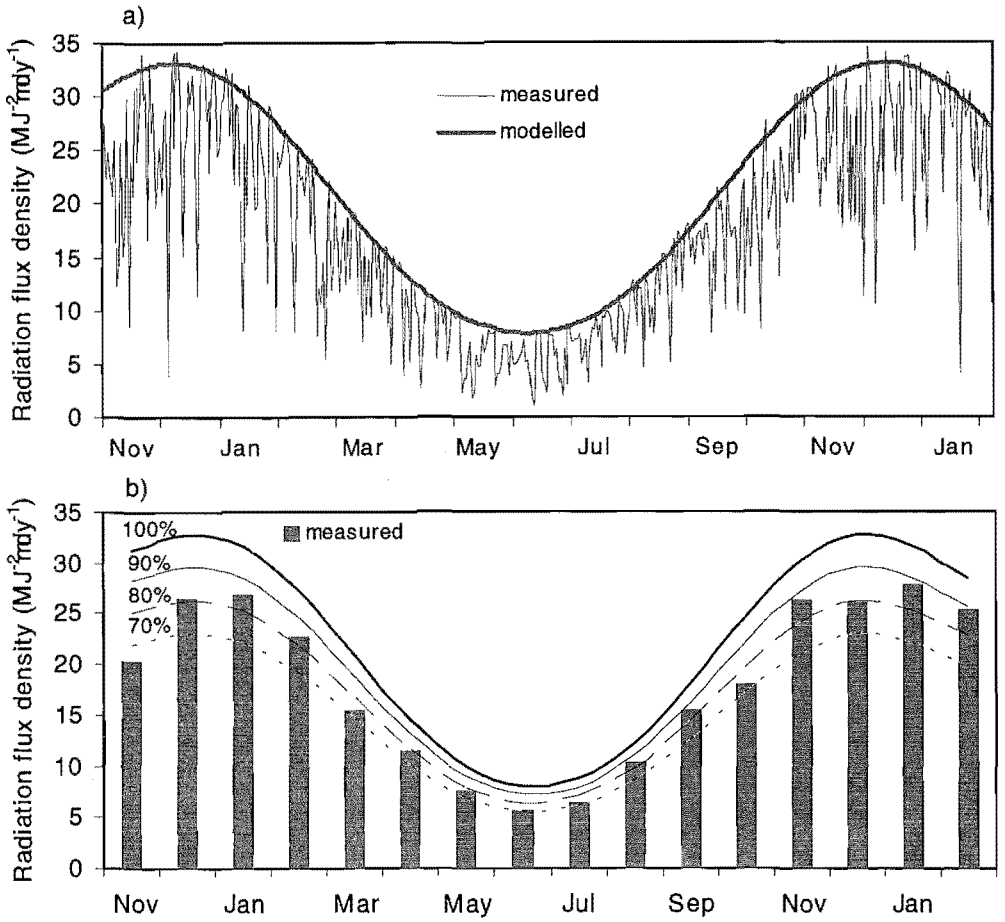

Figure 4.3 Comparison of $K\downarrow$ recorded at the BREB site and modelled for clear-sky days from November 1997 to February 1999, including a) daily totals and b) monthly average daily totals. Curves in (b) represent proportions of modelled values.

Variability in atmospheric transmissivity

The value for atmospheric transmissivity used in the model (0.77) was obtained from a multi-year periodic record of atmospheric extinction data from the nearby Mt John Observatory (see Figure 3.1 for location). For a review of the method used and atmospheric extinction values recorded, the reader is directed to Forbes *et al.* (1995). Atmospheric transmissivity values calculated from the extinction data are plotted in Figure 4.4. Prior to June 1991, values were relatively closely bunched and averaged 0.77. Following this point in time, data can be seen to fluctuate considerably more and with a generally lower average of 0.69. This change in pattern corresponds with the June 15 1991 eruption of Mt Pinatubo, which was found to influence atmospheric extinction at many sites (Forbes *et al.* 1995). This resulted in a potential decrease of at least 10% of $K\downarrow$ (higher for higher solar zenith angles), as well as a great deal of day to day variability in the Tekapo catchment. Using the relationship between $K\downarrow$ and Q^* described earlier, this translates to a reduction in available energy (*i.e.* Q^*) for surface fluxes of >9%. It is clear that the record is insufficiently complete to consider day to day or even season to season variability. Nevertheless, it is likely that significant variability does exist as a result of changes in atmospheric turbidity from water vapour and dust. Furthermore, it is likely that a spatial component to this variability exists due

does exist as a result of changes in atmospheric turbidity from water vapour and dust. Furthermore, it is likely that a spatial component to this variability exists due to the preferential location of dust storm genesis and transport within the catchment (McGowan *et al.* 1996).

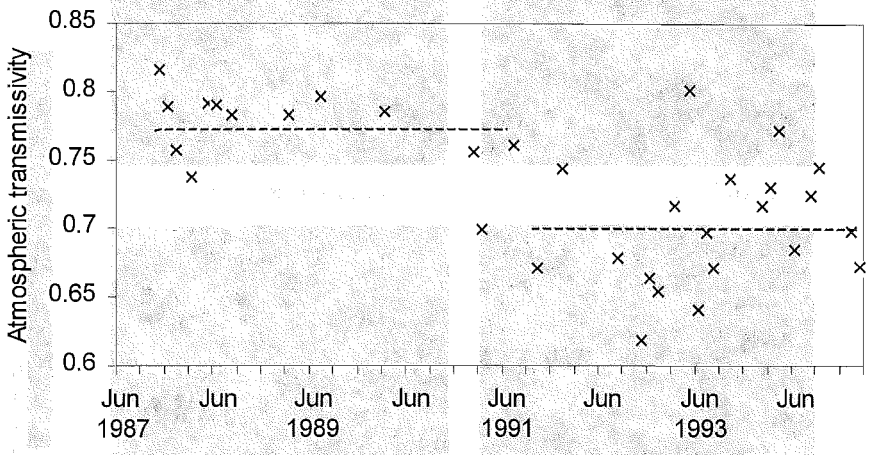

Figure 4.4 Atmospheric transmissivity calculated from atmospheric extinction data recorded at Mt John Observatory between June 1987 and March 1995.

4.2.2 Modelling $K\downarrow$ for different sloping surfaces

Previous sections have concluded that the clear sky modelled fluxes correspond favourably with observed clear sky fluxes of $K\downarrow$ at the BREB site and that $K\downarrow$ is a useful analogue for Q^* at this site. Using these assumptions, it is possible to consider the role of complex topography on the surface radiation budget by modelling $K_S\downarrow$ on the seasonal timescale for various sloping surfaces typical of the Tekapo catchment.

A contour plot of annual mean daily $K_S\downarrow$ totals, as well as those for the summer and winter solstices and spring equinox, for a range of slope angles and aspects is provided in Figure 4.5. On an annual timescale, the most favoured slopes are north facing between approximately 25° and 45°. This decreases away from north and toward both steeper and gentler slopes. Horizontal surfaces receive equivalent densities to west/east surfaces at low angles and to steeper more north-facing slopes. From this level, radiation flux density decreases rapidly toward the south and steeper slopes. The contours of the winter solstice (Figure 4.5b) are approximately orthogonal to the summer solstice (Figure 4.5d), illustrating that, for this mid-latitude, Southern Hemisphere location in winter, slope aspect is the more important control on $K\downarrow$ while in summer, slope angle dominates. This is because, in winter, the solar path above the horizon occurs across a relatively small azimuth range (approximately 105°) and zenith angle range (summit approximately 60°) compared with large summer ranges of both azimuth angle (approximately 246°) and zenith angles (summit approximately 21°). Consequently in winter, $K_S\downarrow$ variability is dominated by the inability of solar radiation to reach southerly facing slopes compared with the north, while in summer $K_S\downarrow$ is able to reach even vertical south facing slopes, allowing more consistency in aspect, with greater variability related to slope angle.

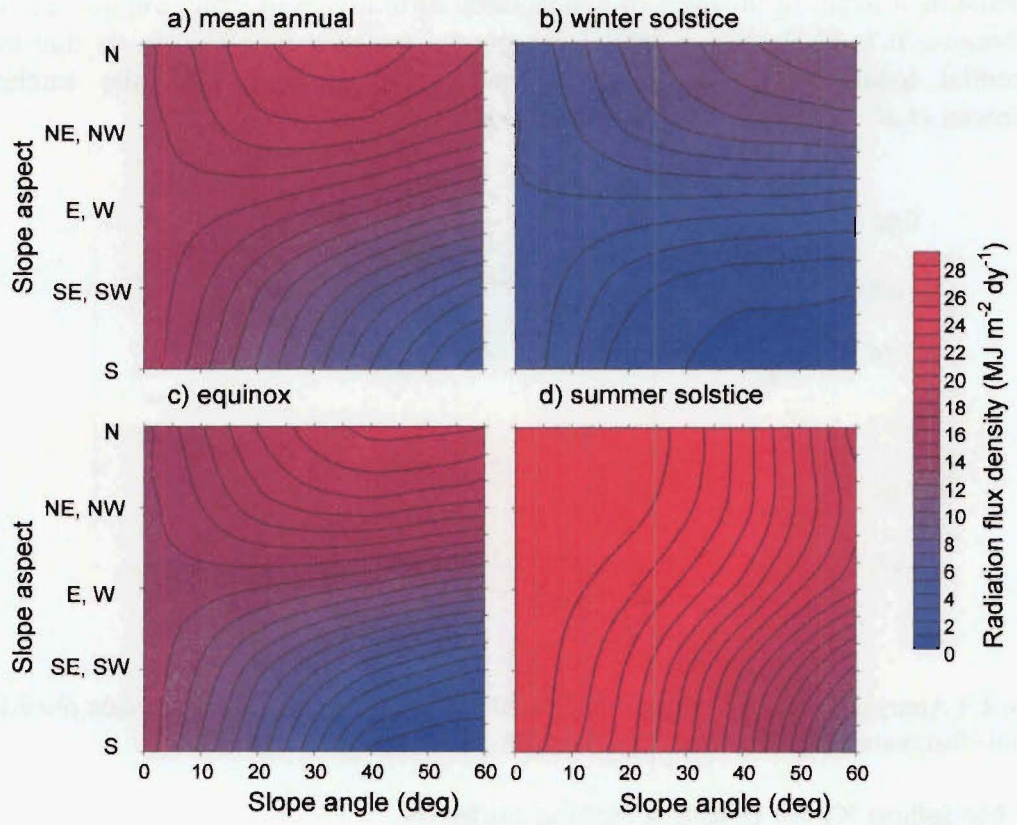

Figure 4.5 Modelled $K_S\downarrow$ for the BREB site for a) mean annual, b) winter solstice, c) equinox and d) summer solstice radiation flux densities for all slope aspects and slope angles from 0 to 60°.

The pattern that emerges at the spring equinox more closely resembles the winter than the summer pattern and contains the largest overall range in $K_S\downarrow$ (Figure 4.5c). This illustrates that temporal and spatial variability in the surface radiation balance are inter-dependent and that, in this location, spatial variability in $K_S\downarrow$ is greatest during the equinox and is greater during summer than winter. This latter point is influenced by the difference in total available energy, which is strongly a function of daylength (8.42 hours at the winter solstice compared with 15.19 hours at the summer solstice). It is also for this reason that the annual mean pattern is not equivalent to the equinox pattern, but is obviously slightly skewed toward the summer pattern.

4.2.3 Synoptic influence on surface radiation fluxes

In order to assess the influence of synoptic systems on the radiation balance, daily radiation totals were sorted by synoptic class. Mean daily total and standard deviation of fluxes for the BREB site for days classified as anticyclonic (ANT), cyclonic northwest gradient flow (CNW) and cyclonic southwest gradient flow (CSW) are presented in Figure 4.6. The derivation of this classification and the influence of these three synoptic situations on the local weather are described in Section 3.3. The mean values of K^* are highest in anticyclonic conditions followed by CSW, with smallest values during CNW flow. These results confirm the regular occurrence of lee side alto-cumulus lenticularis during CNW flow and the somewhat less consistent cumulus shower cloud associated with the interaction of frontal cloud with the mountain region. The high anticyclonic values are indicative of the typically clear-sky, subsiding airmasses associated with these systems. Since the BREB site is located near the centre

of a basin, it is relatively unobstructed by cumulus associated with convection over mountain slopes and ridges during these conditions. This site therefore, is not necessarily characteristic of other locations in the catchment during this synoptic situation.

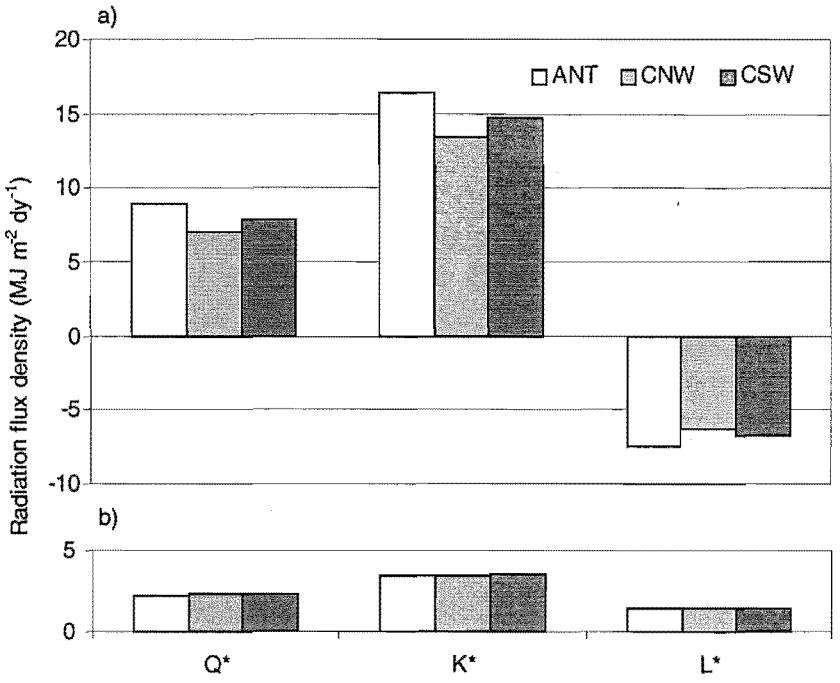

Figure 4.6 Mean (a) and standard deviation (b) daily total radiation flux densities for Q^*, K^* and L^* under three synoptic situations; a) ANT, b) CNW and c) CSW.

The mean variability in L^* between the three synoptic classes suggests the same influences as K^*. Increased cloudiness in CNW and, to a lesser extent CSW flow decreases the net longwave loss to the atmosphere due to absorption and re-emission of longwave radiation by clouds. Complementing this is the generally lower $L\uparrow$ in cloudy conditions associated with cooler surface temperatures resulting from decreased K^*.

The result for mean Q^* variability is clearly a combination of the above. This suggests that in a broad statistical approach such as this, cloudiness associated with synoptic situations appears to have a significant control on the radiation budget. Thus Q^* is greatest under anticyclonic flow and smallest under northwest flow. Other influences on Q^*, such as airmass temperature and moisture characteristics, are not easily resolved using this approach.

The standard deviation of daily radiation densities are consistently high for each of the synoptic classes, being up to three times the range found between classes in mean values (Figure 4.6). Therefore, while these results suggest that synoptic controls have a significant impact on the radiation budget, they also highlight the large variability within individual synoptic classes at this site. With regard to anticyclonic conditions, this variability could result from afternoon convective cloud development in summer or persistence of fogs in winter. In northwest flow, the location and persistence of wave clouds is likely to generate significant variability. The complex interaction between southwest post-frontal flow and the mountain region means that some of these events result in dense cumulus cloud, while others split to the east and west of the mountains leaving cool but clear conditions.

4.2.4 Inter-site variability

In order to assess longer-term spatial variability in cloudiness in the catchment, $K\downarrow$ from the BREB site was compared with values recorded at the AWS1 site (see Figure 3.1 for locations). These sites were chosen because they represent opposite extremes of topographical complexity within the catchment, as well as distance from the alpine divide. Figure 4.7 illustrates the generally higher $K\downarrow$ recorded at the BREB site. This is not entirely due to the effect of clouds, since AWS1 site was located on the floor of a steep sided valley where the mean elevation angle of topographic obstruction was 14° compared with 3° at BREB. The pattern of daily $K\downarrow$ totals that is associated with cloudiness shows a similar trend at both sites, although periods of cloudiness seem to have reduced $K\downarrow$ at AWS1 more significantly than at BREB. This indicates that generally, when it was cloudy at BREB, it was cloudier at AWS1. On the whole, there are few exceptions to this generalisation, although if the dataset was complete, winter months may have revealed further exceptions when stable anticyclonic conditions result in fog formation in the basin. Other exceptions occurred during some of the peaks that followed cloudy periods, when AWS1 often had values closer to BREB than average. This is likely to reflect post-snowfall periods in the upper catchment, when the reflected component of $K\downarrow$ from surrounding terrain would provide a significant additional contribution.

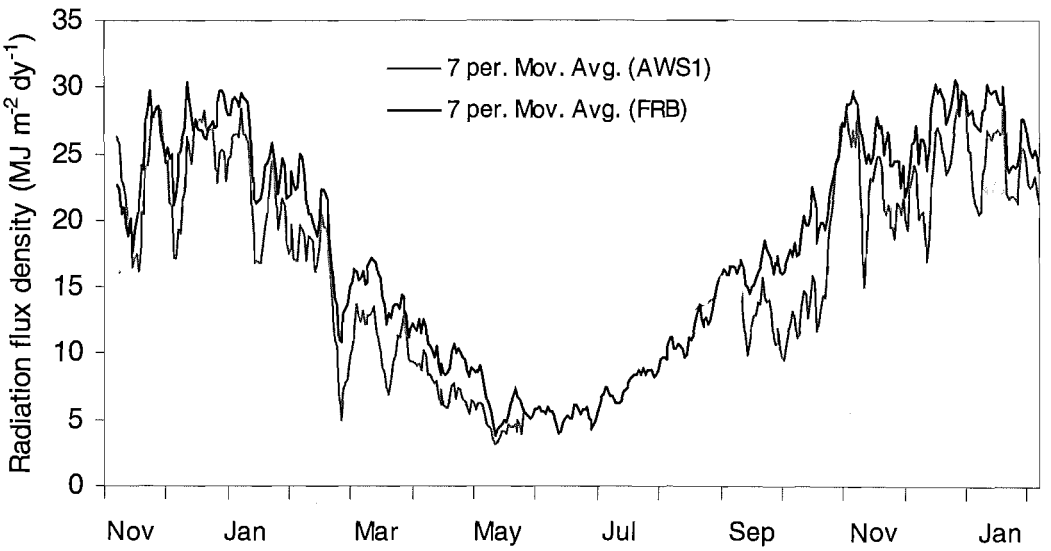

Figure 4.7 Seven day running means for $K\downarrow$ recorded at AWS1 and BREB sites between November 1997 and February 1999. Missing data at AWS1 are due to instrument failure.

The breakdown of $K\downarrow$ totals into the three synoptic classes for both BREB and AWS1 for all concurrent data is presented in Table 4.1. The reduction in $K\downarrow$ associated with synoptic situations was particularly significant during northwest flow when $K\downarrow$ at AWS1 decreased by double the amount of that during either anticyclonic or southwest flow. These findings reflect the site's proximity to the alpine divide, which is strongly influenced by orographic cloud due to its perpendicular orientation to the northwest flow. This influence decreases with distance southeast of the mountain barrier. Furthermore, AWS1 has a consistently higher standard deviation and range than BREB over all synoptic classes. This illustrates enhanced variability in cloudiness associated with the more complex topography.

Table 4.1 Mean, standard deviation and range of daily total $K\downarrow$ at BREB and AWS1 for synoptic classes of anticyclonic (ANT), cyclonic northwest (CNW), cyclonic southwest (CSW) and all days (T), using all concurrent data from November 1997 to February 1999. The difference between the sites (BREB-AWS1) is also given (%).

Mean (MJ m^{-2} dy^{-1})			
	BREB	AWS1	% Diff.
ANT	22.4	19.3	-14
CNW	18.2	12.1	-33
CSW	20.5	17.3	-16
T	20.5	16.6	-19
Standard	deviation (MJ m^{-2} dy^{-1})		
	BREB	AWS1	% Diff.
ANT	8.7	10.3	+19
CNW	7.4	9.1	+24
CSW	8.4	9.0	+6
T	8.6	10.3	+19
Range (MJ m^{-2} dy^{-1})			
	BREB	AWS1	% Diff.
ANT	31.8	39.5	+24
CNW	30.4	38.8	+28
CSW	32.1	34.9	+9
T	33.0	35.4	+8

Used as an analogue for Q^*, the mean $K\downarrow$ magnitudes observed at both stations through out the study equate to a mean Q^* of 9.8 MJ m^{-2} dy^{-1} at BREB and 7.5 MJ m^{-2} dy^{-1} at AWS1, with a maximum range of 16.9 and 22.9 MJ m^{-2} dy^{-1} respectively. This comparison assumes that the same statistical relationship exists between $K\downarrow$ and Q^* at AWS1 as at BREB (Figure 4.2), which is unlikely to be the case. Nevertheless, the potential error associated with this assumption would not alter the conclusion that overall, less energy was available for partitioning into Q_H, Q_E and Q_G at AWS1 than BREB, while significantly more variability was found at the AWS1 site.

4.3 Surface energy balance

The previous section has provided an assessment of the seasonal and synoptic controls on the surface radiation budget and the magnitude of variability that is found in Q^*. This section is concerned with variability associated with the partitioning of Q^* into the turbulent and ground heat fluxes in response to seasonal change, as well as synoptic influences. For this purpose, data collected during two summer periods and one winter period at the BREB site are evaluated with regard to seasonality, synoptic influence and soil moisture content. Data for the two summer periods included the full months of December, January and February, but for winter included June 22 to August 26. The mean temporal variability in energy partitioning is assessed by longer-term statistical analyses, while case studies provide closer inspection of the mechanisms involved.

Background data are provided for each season examined (Table 4.2). A large seasonal range in daily mean air and soil temperature existed, as well as diurnal air temperature range. Specific humidity reveals smaller seasonal variability with the difference between the two summers greater than the difference between winter and summer 1997/98. This inter-annual difference probably reflects the large difference in the Southern Oscillation Index (SOI), between the two years. The SOI here is defined by:

$$SOI = 10\frac{\Delta p - \overline{\Delta p}}{\sigma \Delta p} \qquad (4.1)$$

where $\bullet p$ is the mean monthly pressure difference between Tahiti and Darwin (hPa), the overbar is the long term monthly average difference, while $\bullet$ represents the standard deviation (Australian Bureau of Meteorology 2000). The summer of 1997/98 was influenced by a strong El Nino event (SOI was –23.5 in Jan 1998), which produced stronger and more consistent westerly airflow than usual. Due to depletion of moisture through orographic processes as they cross the mountain barrier, air masses from this direction are typically dry in the Tekapo catchment. The La Nina summer of 1998/99 (SOI was 15.6 in Jan 1999) produced more anticyclonic and easterly flow than usual. These are typical relationships for the New Zealand region (Gordon 1986). In all other aspects, the two summers produced similar mean values.

Table 4.2 Mean background data recorded at the BREB/AWS16 site during three seasons.

	Summer 1997/98	Winter 1998	Summer 1998/99
Mean air temp. (°C)	17.6	1.1	16.5
Mean daily air temp. range (°C)	14.4	7.5	14.2
Mean soil temp (°C)	20.1	2.1	21.2
Mean specific humidity (g kg^{-1})	5.2	3.8	7.7
Mean volumetric soil moisture content (%)	6.75	14.7	5.7

4.3.1 Synoptic classification of surface energy balance data

The purpose of this section is to ascertain the statistical differences in energy flux magnitude and partitioning as a function of seasonality and synoptic weather patterns. Daily energy flux totals were calculated for all BREB data from the two summer and one winter periods. These were sorted by the three dominant synoptic classes and averaged to provide mean daily total energy fluxes for each synoptic class, as well as the mean for each season. Mean daily partitioning of Q* into Q_H, Q_E and Q_G are presented for each class and each season in Figure 4.8

The first point to note is the extreme difference in the partitioning between sensible and latent heat fluxes (β) between summer and winter seasons. For both summer seasons, Q_H dominated Q_E as a sink for available surface energy, while the reverse occurred during the winter period. This is likely to be a consequence of the difference in soil moisture content, and to a lesser extent differences in mean specific humidity between the seasons (Table 4.2). The soil moisture content remained consistently higher during the winter, probably due to a higher occurrence of rainfall events and a relatively low rate of evaporative loss due to the low magnitude of available energy, despite the high Q_E /Q^* ratio. The difference between the two summer seasons is also reflected in the

mean difference in soil moisture (Table 4.2). Further analysis of the role of soil moisture is provided in Section 4.3.5.

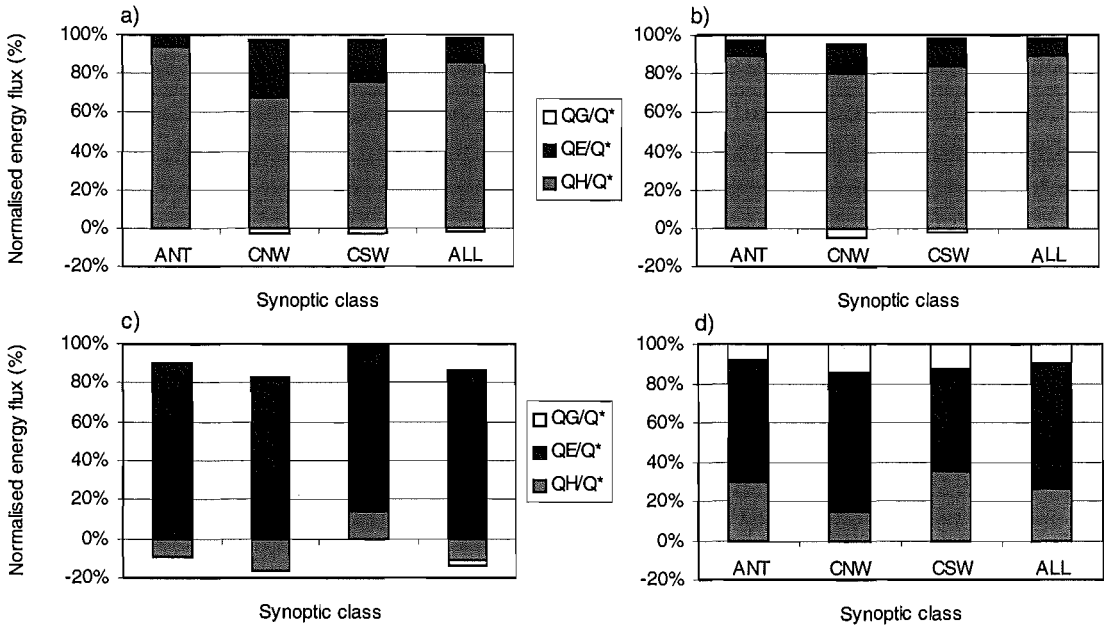

Figure 4.8 Daily energy partitioning ratios under different synoptic patterns during a) summer 1997/98, b) summer 1998/99, c) winter 1998 and d) winter 1998 daylight hours. ANT = anticyclonic, CNW = cyclonic northwesterly and CSW = cyclonic southwesterly.

During the 1998 winter, Q_H showed a net loss of energy from the atmosphere to the surface when integrated over the 24-hour cycle (Figure 4.8c). This is due to the long winter nights when Q_H predominantly compensated the large net radiative losses with strong temperature inversions and due to the dominance of Q_E in transferring available daytime energy. Consequently, daytime energy partitioning has been plotted in addition for the winter season for ease in interpreting flux behaviour (Figure 4.8d).

The difference in total available energy and its partitioning between the three synoptic classes was considerable. The two summer periods show a consistent pattern whereby the smallest amounts of energy were available during northwest flow (as found earlier) and β was lowest during northwest and southwest flow. This could result from two mechanisms. The first is that advected air associated particularly with northwest flow, but also southwest flow, was relatively dry. This would provide a larger saturation deficit to enhance evaporation during these conditions, provided moisture was available at the surface. This is examined in the case studies, which follow. The second reason is that rainfall is more likely to occur during northwest spill over conditions or southwest frontal situations (Section 3.2), thereby providing more moisture for evaporation during these conditions. The seasonal mean of β in the summer of 1997/98 is lower than the average of the three classes, while in the summer of 1998/99 it is higher. This finding recognises the greater number of northwest days that occurred during the first summer and the greater number of anticyclones during the second, as discussed previously. This point is important, because it shows that the difference in frequency of synoptic situations from year to year due to controls such as ENSO, or other causes of change in synoptic patterns, results in significant differences in seasonal surface energy balances.

During the winter, the smallest β again occurred during northwest flow (Figure 4.8c and d), although during this season β was higher during southwest flow than anticyclonic flow, in contrast to summer. The reason for this contrast with summer appears to result from the relative importance of moisture supply and advection as a control on β. For the summer datasets, it was suggested that south west flow had a positive influence on evaporation due its contribution of surface moisture from rainfall. In a season with low overall soil moisture content this would be likely to dominate changes in β. However, during winter, when it appears a ready supply of moisture was available, the advection of cold air, which would enhance Q_H, might be the more important control on β. These points are not proven by this dataset but remain hypotheses for larger datasets or modelling studies to test. Nevertheless, Figure 4.8 clearly illustrates the large range in both available energy and partitioning of this energy as a function of seasons within a year, synoptic situations within a season and the inter-annual variability that can result from different frequencies of occurrence of synoptic situations within a season.

As a summary, the ranges of surface energy exchange associated with seasonal and synoptic controls at the BREB site found in this study are presented in Table 4.3. Ranges of Q^* were extracted from Section 4.2 and Q_H and Q_E values were determined from the data presented in Figure 4.8.

Table 4.3 Estimated ranges of daily total surface energy exchange (MJ m^{-2} dy^{-1}) associated with seasonal and synoptic controls.

	Q^*	Q_H	Q_E
Seasonal	14.2	11.5	3.2
Synoptic	22.2	7.1	1.97

The largest impact on surface energy fluxes in this analysis results from controls on the amount of available energy provided by the radiation budget. In particular, the synoptic controls on the radiation budget produced the largest range of magnitudes. The second strongest variability results from seasonal control on the partitioning of turbulent fluxes. With the purpose of further investigating the reasons for these findings, the following sections present case studies of diurnal radiation and energy budgets under the different synoptic and seasonal conditions used in statistical analysis above.

4.3.2 Summer surface energy balance case studies

The purpose of this section is to compare the surface energy balance and meteorological parameters associated with strongly contrasting synoptic situations in summer. Three case studies are presented; anticyclonic, cyclonic northwest and cyclonic southwest flow.

Case I: Summer anticyclone

The first case illustrates a clear-sky anticyclonic situation in early summer (Figure 4.9). The low values of Q_E were typical of summer days at this site, resulting from the low moisture availability (Table 4.2). Consequently, available energy was partitioned most substantially between Q_H and Q_G. The partitioning between these two variables however, shows an asymmetric pattern, whereby Q_G peaked in late morning and Q_H peaked in late afternoon. The reason for this appears to be associated with local diurnal meteorology during anticyclonic situations, as explained below.

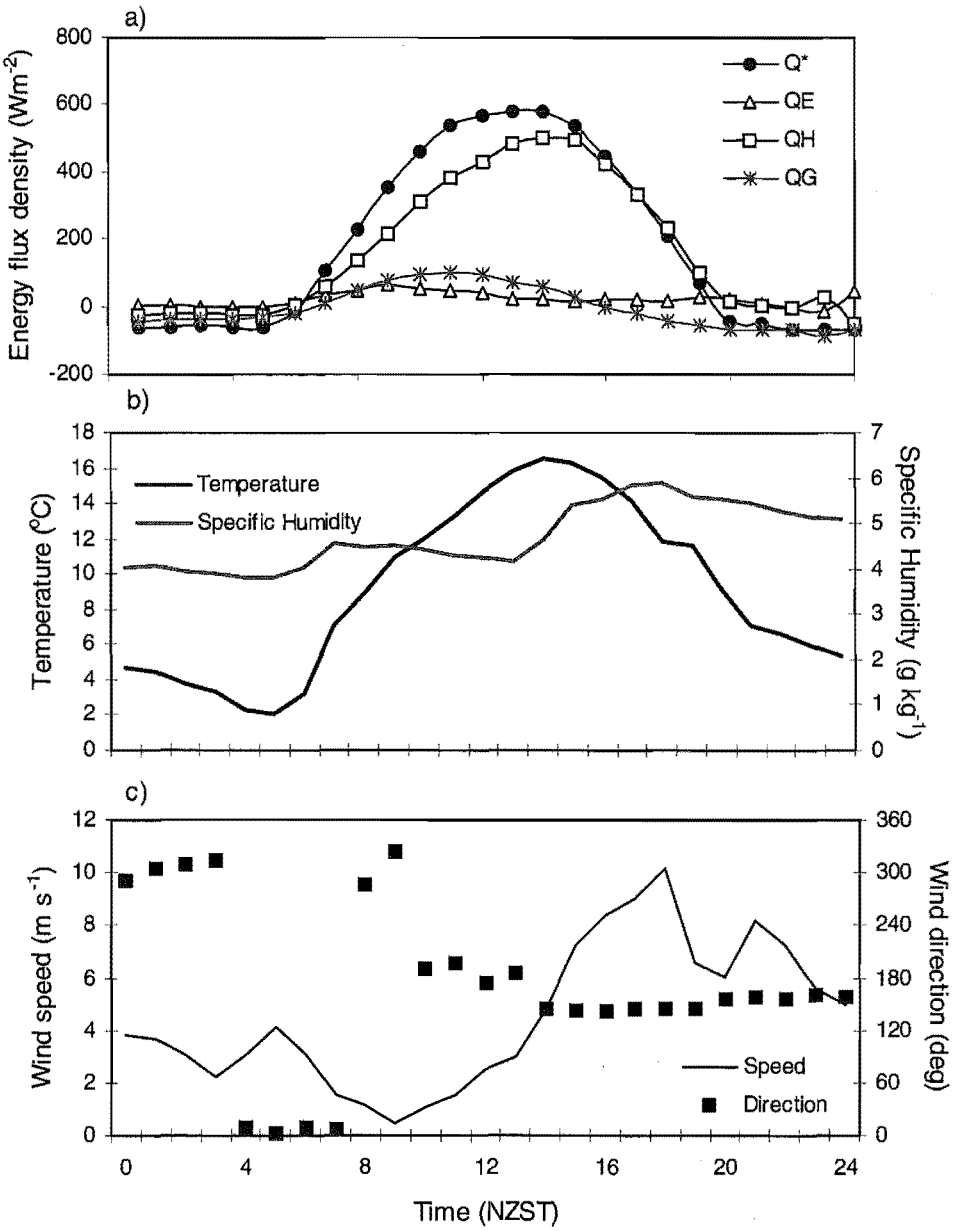

Figure 4.9 Hourly mean a) energy flux densities, b) temperature and specific humidity and c) wind speed and direction recorded at the BREB site on December 7 1997.

The early morning period was governed by cool katabatic flows draining off the slopes to the north and northwest associated with a net radiative loss, partly compensated by a surface layer temperature inversion. Sunrise was followed by a rapid increase in temperature and a smaller jump in specific humidity, associated with positive sensible and latent heat fluxes respectively. Q_E quickly reached the diurnal peak, starved of moisture and unable to increase above about 50 W m^{-2}. At around 1000 NZST, airflow reversed to a general southerly upvalley flow and slowly increased in speed to 3 m s^{-1} by 1300 NZST. During this period, temperature increased in response to the large Q_H, while specific humidity gradually declined in association with the decline of Q_E.

At 1300 NZST, a regional scale coastal plain-to-basin flow entered the basin and reached the BREB site, resulting in the advection of cool moist air. Wind direction swung to the SSE and wind speed increased steadily to 10 m s^{-1} by 1800 NZST. The influence of this advection on surface fluxes was to diminish Q_E further and to

strengthen Q_H as the surface layer gradients of heat and moisture increased and decreased respectively. Furthermore, the influence of the stronger wind speed was to increase the thermal admittance of Q_H relative to Q_G so that Q_G decreased rapidly to become negative by 1500 NZST. This, coupled with the near zero Q_E, allowed Q_H to become greater than Q^*. The continuation of this regional scale airflow regime into the night prevented a strong temperature inversion from developing and the net radiative loss was accounted for by Q_G.

This case illustrates the complicated relationship between local meteorology and surface fluxes during anticyclonic situations. In these conditions, the fluxes are responsible for driving local and regional circulations, which result in advection of airmasses from surrounding regions, which then act as a feedback mechanism by altering the boundary conditions. In this case, the plain-to-basin flow provided a positive feedback for Q_H at this site, although this enhanced Q_H was unable to offset the cool air advection and a net temperature decrease resulted.

Case II: Summer cyclonic northwest flow

The second case study represents another nearly clear-sky day in early summer, recorded 8 days before the previous case (Figure 4.10). This time the local meteorology was dominated by strong foehn northwest conditions, although cloud cover was less influential than inferred in longer-term mean data (Section 4.2). At the local scale, these conditions produced nearly consistent north-northwest wind direction and speed, with only 4 hours of the day recording less than 5 m s^{-1}. The main break in this consistency occurred between 0300 and 0500 NZST, when it appears northwest flow was briefly terminated and replaced by cool, moist drainage flow. The range in temperature was much lower than the summer mean and the peak occurred significantly later in the day. The northwest case also produced a generally dryer atmosphere. In contrast to the previous case, the partitioning of fluxes produces a symmetric pattern, with considerably lower Q_G and more consistent Q_E, despite a similar maximum value. During the early morning break in northwest flow, Q_H and Q_E fluxes can be seen to converge somewhat with the decrease in Q_E and increase in Q_H associated with the advection of cool, moist air. If a larger supply of moisture were available at the surface, it could be expected that this situation would favour Q_E due to the relatively warm, dry airmass with high wind speeds.

Case III: Summer cyclonic southwest flow

This case illustrates the influence of the passage of a front on surface energy exchanges (Figure 4.11). Prior to 0900 NZST, the local meteorology is dominated by weak to moderate, damp and warm northerly flow, except between 0500 and 0700 when wind turned southerly with light rainfall. The low Q^* loss in the early morning hours and the low Q^* gain during daylight hours indicates cloud cover throughout the day. At 1000 NZST, the main frontal passage occurred with strong southwest wind and a rapid drop in temperature and a smaller drop in specific humidity (although relative humidity increased to near saturation). Shortly after this, Q^* dropped significantly in response to denser cloud cover and 18 mm rainfall occurred in the following four hours. During this time Q_E, which had until now represented a significant portion of available energy, decreased to negative values. This, coupled with the consistently negative Q_G, and in response to cold air advection, produced a relatively high Q_H, which remained greater than Q^* in the following hours. This case illustrates the role of cloud cover, rainfall and

cold air advection associated with an extreme example of cyclonic southwest influence on surface energy exchanges.

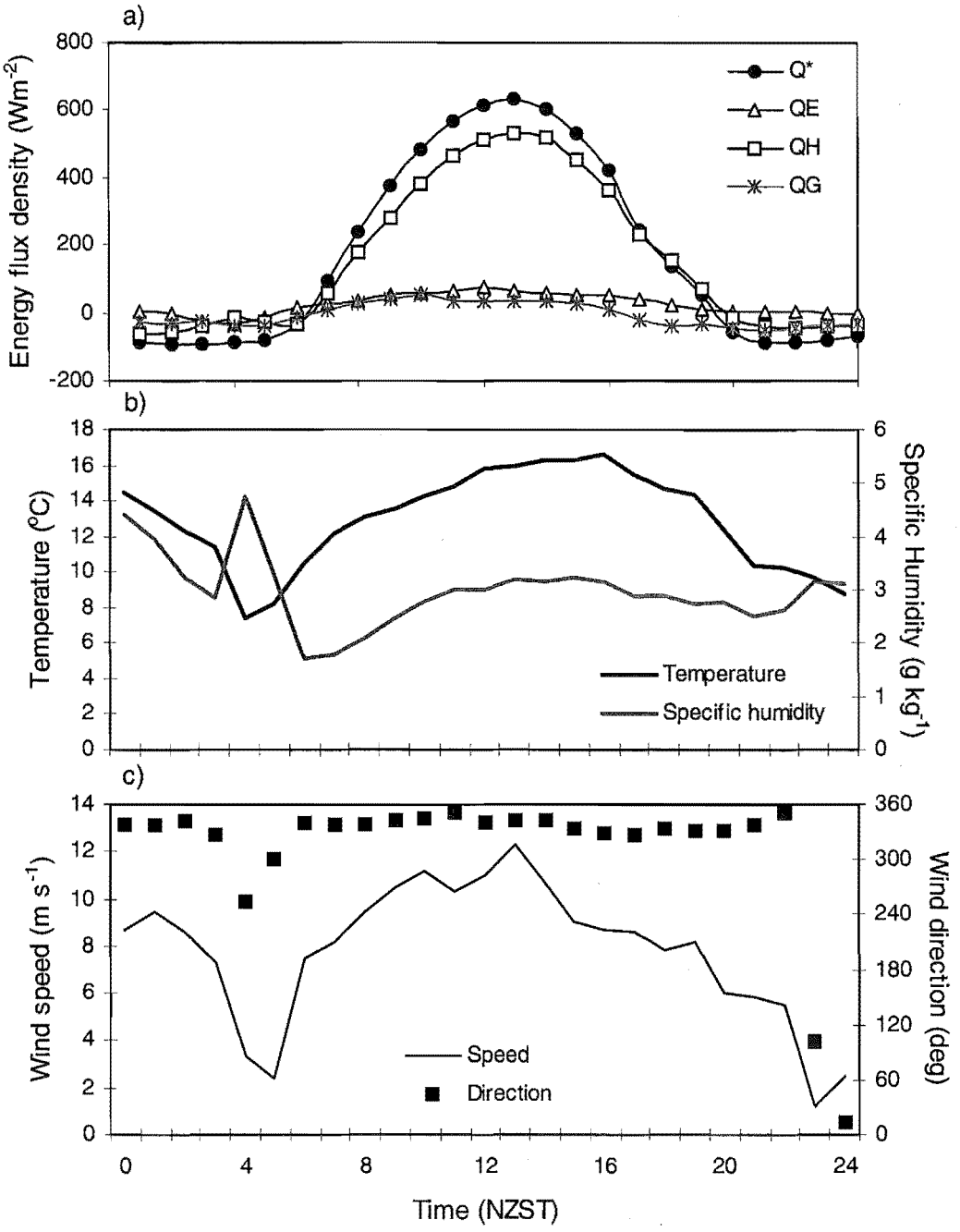

Figure 4.10 Hourly mean a) energy flux densities, b) temperature and specific humidity and c) wind speed and direction recorded at the BREB site on November 29 1997.

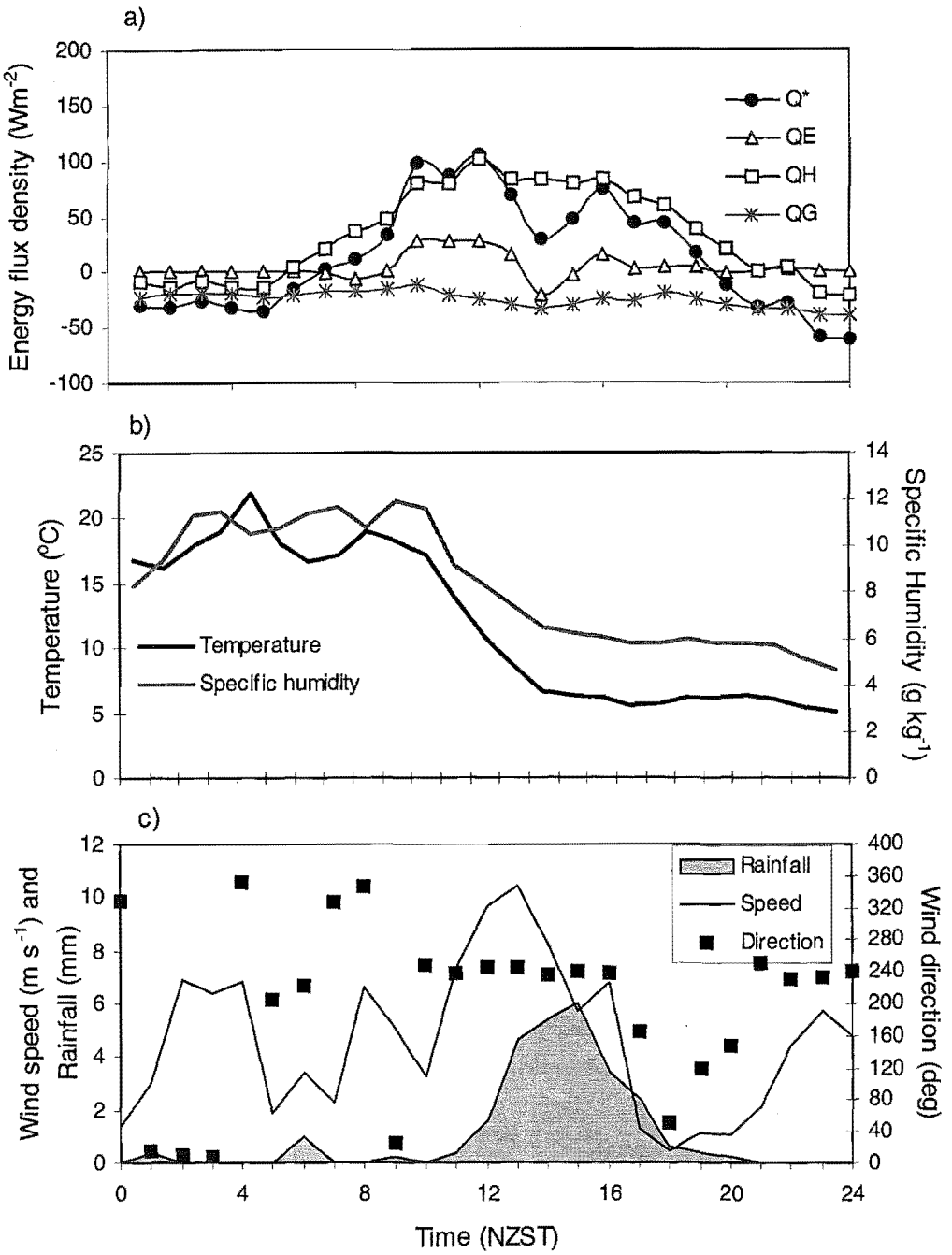

Figure 4.11 Hourly mean a) energy flux densities, b) temperature and specific humidity and c) wind speed and direction and rainfall recorded at the BREB site on January 31 1999. Note difference in y-axis scale compared with previous two figures.

4.3.3 Winter surface energy balance case studies

For the winter period, three cases are presented for similar synoptic patterns to the summer cases. Unfortunately, during this period the wind sensors at BREB were not operational. Although data from neighbouring stations were used in conjunction with MSL analyses to identify the dominant wind conditions for each case, they are not presented in conjunction with energy balance data due to the differences found between sites.

Case IV: Winter anticyclone

The first case presented is a clear-sky, anticyclonic day in mid winter (Figure 4.12). Both the diurnal mean temperature and range were above average for the winter period. At night, the net radiative loss was most strongly accounted for by Q_H, with a strong surface temperature inversion. Conversely, once the radiation budget became positive, energy use was dominated by Q_E. The relatively low specific humidity through both day and night would enhance this behaviour. During daylight hours, Q_H was small and, integrated over the diurnal cycle, amounted to a net loss. As with the summer case, the remaining energy produced an asymmetrical balance between the conductive and convective transport of energy. This balance resulted in Q_G peaking around noon, while Q_E peaked at 1400 NZST.

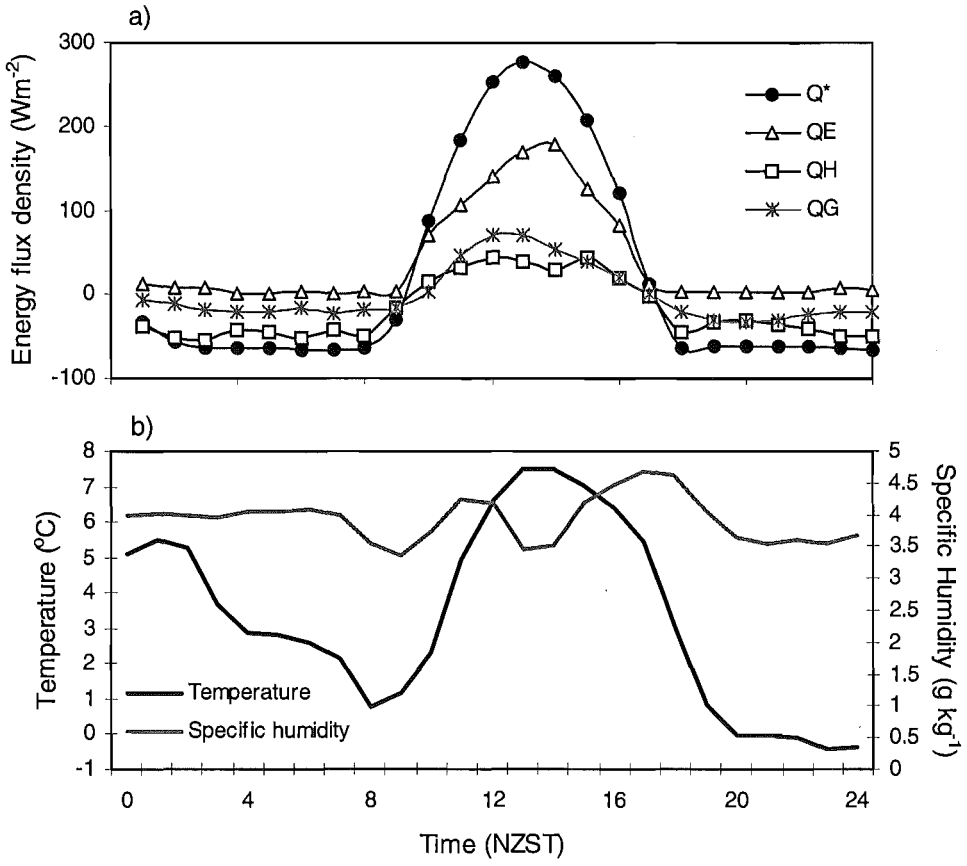

Figure 4.12 Hourly mean a) energy flux densities and b) temperature and specific humidity recorded at the BREB site on July 24 1998.

It is likely that the diurnal wind speed curve peaked later in the afternoon in response to decreased thermal stability, although wind data were unavailable to confirm this. However, the strong nocturnal temperature inversion and daytime temperature lapse in the surface layer would lend itself to this pattern of variability. The near surface substrate was likely to be quite moist on this occasion, since no apparent nocturnal surface layer humidity inversion existed, while turbulent fluxes were dominated by Q_E during daylight hours. Further evidence is provided by the mean seasonal soil moisture data, which shows higher soil moisture content in winter (Table 4.2). Apart from the much lower magnitudes involved, this case is similar to the summer anticyclonic case with regard to the diurnal pattern of convective relative to conductive fluxes, except the relative dominance of Q_H and Q_E are reversed.

Case V: Winter cyclonic northwest flow

The second winter case was a partly cloudy day with strong northwest winds (as assessed from neighbouring sites), which resulted in dry and warm air advection (Figure 4.13). The diurnal temperature trace shows a significantly higher mean temperature with a much lower range than the wintertime mean. Very little radiative cooling occurred in the early morning period, probably due to the presence of clouds and possibly contributed to by higher wind speeds. During daylight hours, a very weak temperature lapse existed as the weak radiative flux struggled to raise surface temperature above the relatively warm advected airmass. The warmth and strength of wind combined to enhance evaporation so that Q_E completely dominated the daytime energy balance. This dominance over Q_H is likely to be a function of the warmth of the airmass and the ready availability of moisture at the surface, while dominance over Q_G is likely to be a function of the wind speed, greatly increasing turbulent transport of energy. Again, the comparative summer synoptic situation produced a similar pattern of convective versus conductive fluxes, except that the relative dominance of Q_H and Q_E was reversed.

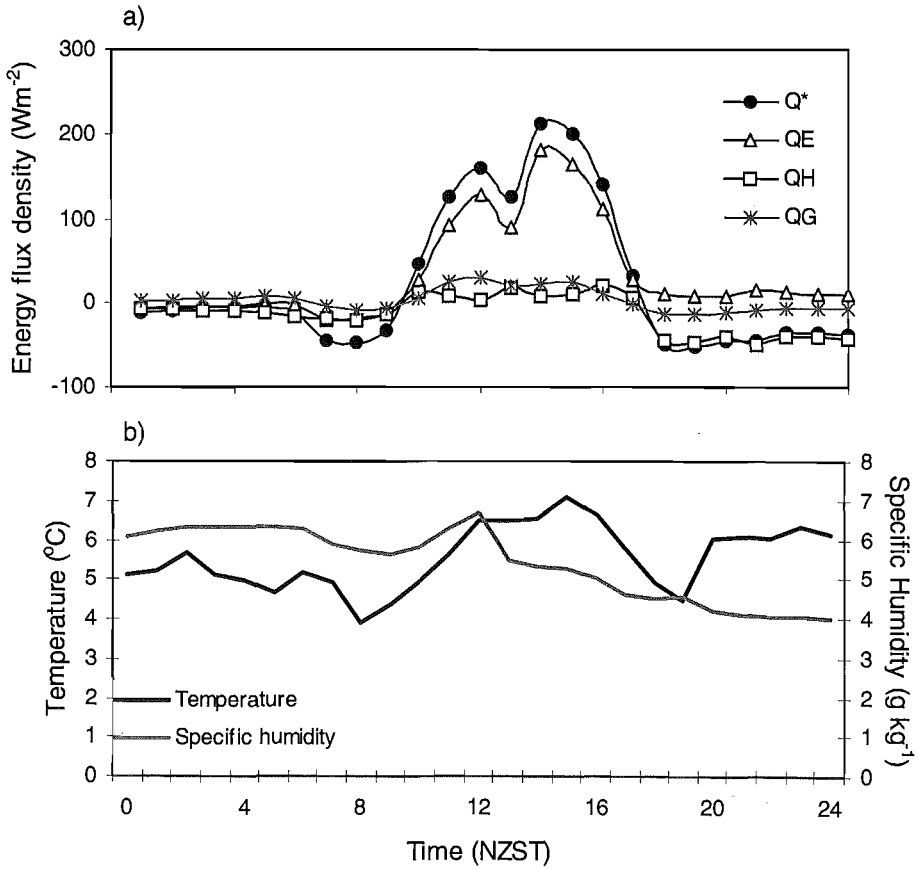

Figure 4.13 Hourly mean a) energy flux densities and b) temperature and specific humidity recorded at the BREB site on July 23 1998.

Case VI: Winter cyclonic southwest flow

The third winter case is a clear-sky day during southwest airflow following the passage of a front (Figure 4.14). This case differed from the summer southwest case because there was no cloud and no precipitation involved. Instead, the most significant control of the synoptic situation was on temperature. Air temperature was lower than average

but had an average range for winter. On this occasion, clear-sky early morning hours produced a large net radiative loss, which was accounted for most dominantly by Q_E and Q_H. The negative Q_E values and below zero air temperature are indicative of frost formation during these hours. Following sunrise, Q_G remained below zero for several hours, while the positive radiation budget was completely dominated by Q_E. This suggests that frost melt and subsequent evaporation dominated these hours, with very little surface warming occurring. Following 1200 NZST, Q_G rapidly increased above zero, indicating that frost had been removed sufficiently for surface heating to result in increased Q_G. The decrease in Q_E from late morning was balanced by an increase in both Q_H and Q_G once the surface was warmed.

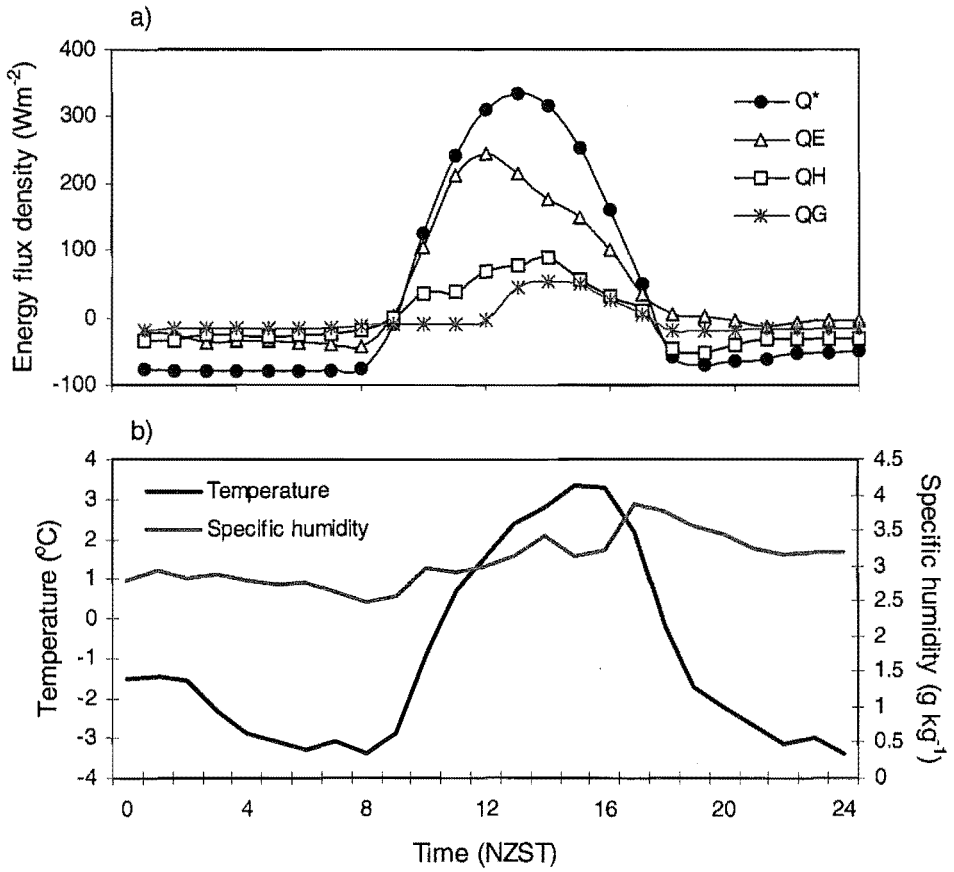

Figure 4.14 Hourly mean a) energy flux densities and b) temperature and specific humidity recorded at the BREB site on August 8 1998.

4.3.4 Discussion of summer and winter case studies

The three cases presented for summer days reflect the large differences in surface energy exchanges associated with the three most commonly experienced synoptic situations in the study area. The differences in temperature, humidity and wind speed in advected airmasses, as well as cloudiness and precipitation, accounts for this large variability. The daily total fluxes and partitions for each case are provided in Table 4.4.

The smaller β (Q_H/Q_E) during the northwest case compared with the anticyclonic case in summer appears to be related to the warm, dry air advection associated with northwest flow. If more moisture was available at the surface, it is likely that Q_E would be significantly greater during northwest flow than anticyclonic conditions, and thus daily energy totals would be significantly different. The relatively high β during

southwest flow in summer was due to the low and sometimes negative Q_E values found during rainfall, as well as the influence of cold air advection on Q_H. This case also illustrates the role of cloud in determining total flux magnitudes, regardless of partitioning.

Table 4.4 Daily total Q^* (MJ m^{-2} dy^{-1}) and energy partitioning ratios for six case study days. Values in brackets are for daylight hours only.

	Q^*(MJ m^{-2} dy^{-1})	Q_H/Q^*	Q_E/Q^*	Q_G/Q^*	Q_H/Q_E
Summer					
ANT	15.70	0.91	0.11	-0.02	8.27
CNW	14.96	0.88	0.16	-0.04	5.50
CSW	1.10	2.67	0.32	-1.99	8.26
Winter					
ANT	1.63	-1.02	2.11	-0.09	-0.48
(daylight)	(4.93)	(0.14)	(0.65)	(0.21)	(0.23)
CNW	2.02	-0.60	1.46	0.14	-0.41
(daylight)	(3.61)	(0.07)	(0.80)	(0.13)	(0.09)
CSW	2.70	-1.10	1.25	-0.15	-0.08
(daylight)	(6.40)	(0.23)	(0.70)	(0.07)	(0.33)

As with summer, the winter case studies illustrate large variability in surface energy fluxes associated with synoptic controls. Again, the role of advection was important in determining the diurnal pattern of fluxes. Daily total Q^* and energy partitioning is provided for each case in Table 4.4. The effect of cloudiness on Q^* is again evident, this time associated with northwest flow. The greater importance of evaporation is clearly evident in these cases due to the much larger supply of surface moisture. The third winter case (CSW) introduced the role of frost, which results when Q_E is directed toward the surface at sub-zero temperatures. This subsequently impacts on the surface energy partitioning after sunrise by providing ice, which requires a large supply of energy for melt and evaporative processes. In this case, the enhancement of Q_H through cold air advection was offset by the requirement for available energy to remove the frost, thereby enhancing Q_E.

Soil moisture difference clearly plays a key role when comparing all the winter with summer cases and this is likely to be enhanced by the generally dryer winter atmosphere. Apart from this difference, similar processes can be seen to operate in both the summer and winter cases for each synoptic situation. In both cases, the anticyclonic conditions produce an asymmetrical balance between convective and conductive fluxes due to the relatively lower morning and higher afternoon wind speeds. Also, in both cases, strong northwest winds produce a much more consistent and high rate of convective compared with conductive heat flux.

4.3.5 Role of soil moisture content

The differences between summer and winter case studies above illustrate graphically the role of soil moisture content in the partitioning of fluxes, particularly by comparing β values in Table 4.4. Most summers in the MacKenzie Basin (location of the BREB site) are very dry, and the two summers when data were recorded for this study were not exceptions to this. By contrast, the winter period is associated with higher frequency

of frontal events and lower total evaporation, providing a larger moisture supply at the surface. The role of soil moisture is considered initially using a case study to illustrate the effect of a single rainfall event on surface moisture. This is followed by evaluation of the relationship between soil moisture content and β using all available concurrent data.

Figure 4.15 presents surface energy balance and rainfall data over a period of five days from January 31 to February 4 1999 to illustrate the impact of a single rainfall event on surface moisture during a dry summer period. The purpose of this is to isolate soil moisture influences from other seasonal or synoptic controls. The advantage of this case was that soil samples were taken on January 31, February 2 and February 4, allowing comparison between rainfall, soil moisture and Q_E. The rainfall event followed a period of very dry weather, where volumetric soil moisture levels reached close to the minimum values recorded at this site (4.9%) and Q_E was negligible. Following the rainfall event, Q_E re-established itself as a sink for net radiation, although this decreased rapidly in the following days (Figure 4.15).

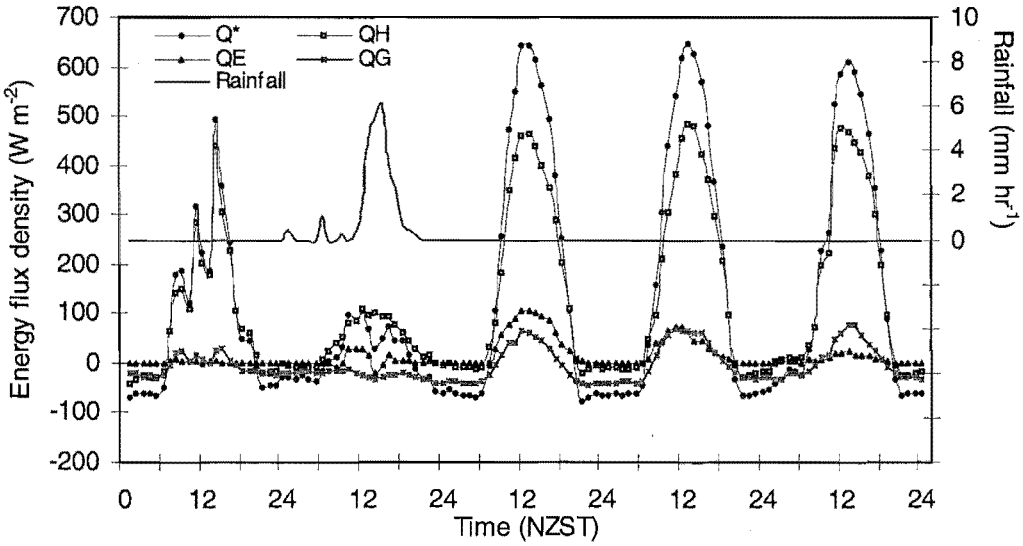

Figure 4.15 Hourly mean energy flux densities and precipitation recorded at the BREB site from January 30 to February 3 1999.

A mass balance approach was used to equate the input of precipitation to the output of evaporation by calculating the daily total evaporation from Q_E and L_v (Table 4.5). The balance at the end of the four-day period including and following the rainfall event shows that 8.5% of water contributed by rainfall was lost by evaporation. Since runoff can be assumed to be zero due to the flatness of the site, the large proportion of water input is likely to have been lost to lower levels by infiltration. This illustrates the weak capacity of the soil to retain water, which would greatly contribute to its aridity. Since β is strongly governed by the availability of moisture for evaporation, Q_H was also influenced by default. The daily total β dropped significantly following the rainfall event before climbing back toward the very high pre-rainfall level. It is relevant to note that, when Q_E is so low, β can become unrealistically inflated and the difference between changes in Q_E and changes in β become very large. For example, if the value of Q_E on Jan 31 were increased by just 0.5 MJ m^{-2} dy^{-1}, β would decrease from 80 to 13.

Table 4.5 Daily totals of precipitation and evaporation, as well as daily-integrated Bowen ratios for the period January 30 to February 3 1999 including observations of soil moisture on three of the days.

	Jan 30	Jan 31	Feb 1	Feb 2	Feb 3	Total (Jan 31–Feb 3)
Precipitation (mm)	0	26.6	0	0	0	26.6
Evaporation (mm)	0.04	0.14	1.28	0.76	0.24	2.27
β	80	10	4	7	23.	
Soil moisture (%)	5.3		12.3		6.2	

Since soil moisture observations were restricted to site visits and the BREB was not operational throughout the entire study period, relatively few data exist to examine the statistical relationship between β and soil moisture content. Furthermore, due to the unrealistic inflation of β at low Q_E levels as discussed above, days where β was greater than 20 have been omitted. The remaining data are plotted in Figure 4.16 where β was found to correspond well to the natural logarithm of volumetric soil moisture content. These data were not filtered for season or synoptic situation, which illustrates that soil moisture appears to play a significant role in determining the partitioning of turbulent fluxes under varying weather conditions at this site. The control of soil moisture on spatial variability of surface fluxes is considered in the following chapter.

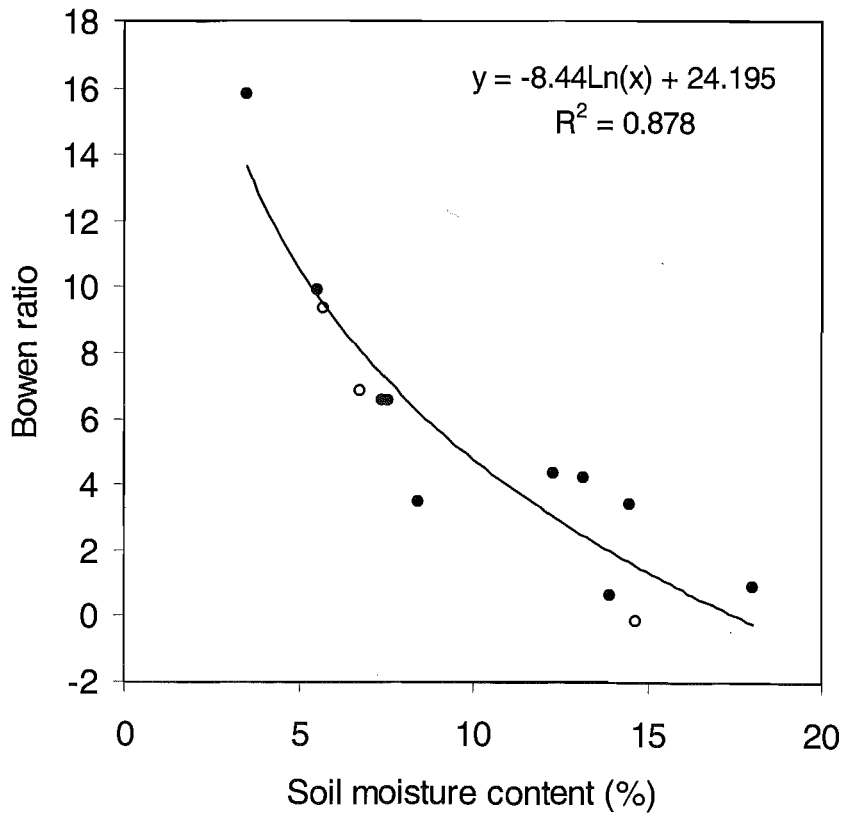

Figure 4.16 Regression analysis between volumetric soil moisture content and daily integrated β from all concurrent data recorded at the BREB site between November 1997 and February 1999. Open circles represent summer 1997/98 and 1998/99 and winter 1998 means.

4.4 Summary

The aim of this chapter has been to evaluate the variability in surface energy exchanges that is associated with seasonal and synoptic influences in an alpine basin setting. This included quantifying the magnitude of variability associated with different controls, as well as to make some progress in understanding the mechanisms that generate this variability.

Initially radiation flux densities were considered. The seasonal range in Q^* (14.2 MJ m^{-2} dy^{-1}) resulted primarily from variability in K^* (21.1 MJ m^{-2} dy^{-1}) and secondly from L^* (6.3 MJ m^{-2} dy^{-1}). Day to day variability for both Q* and K* values was approximately equal to seasonal ranges, while L* reached significantly greater ranges in weekly flux densities (10.6 MJ m^{-2} dy^{-1}). Daily to weekly variability was seen to be most significantly a function of cloudiness. Cloudiness was found to vary significantly from one end of the study area to the other as a function of topography and proximity to the alpine divide. This produced ranges in $K\downarrow$ at AWS1 of 35.4 MJ m^{-2} dy^{-1} compared with 33.0 MJ m^{-2} dy^{-1} at BREB, despite a 20% lower mean $K\downarrow$ resulting from generally greater cloudiness, as well as topographic shading at the former site. $K\downarrow$ at AWS1 was at its lowest relative to BREB during northwest flow (33% lower). By using the analogue of $K\downarrow$ for Q^* at BREB, mean Q^* at AWS1 was 23% lower than BREB, but ranged by 26% more. Variability in the radiation budget was found to reflect processes associated with synoptic situations, although longer-term statistics found significant variability within synoptic classes (as much as 3 times the difference between mean values).

The radiation budget is controlled most significantly by $K\downarrow$. Modelling $K\downarrow$ for clear-sky days agreed closely with observed values. The seasonal impact of $K_S\downarrow$ was modelled for the range of sloping surfaces found within the study area. The mean annual flux densities for all slopes produced a range of 17.3 MJ m^{-2} dy^{-1}, with a maximum of 28.8 MJ m^{-2} dy^{-1}. The largest range associated with slopes at any one time was found during the equinox, when a range from south facing 60° slopes to north facing 40° slopes of 20.3 MJ m^{-2} dy^{-1} was found. This was reduced somewhat at the summer equinox (18.7 MJ m^{-2} dy^{-1}), but was significantly less at the winter equinox (11.2 MJ m^{-2} dy^{-1}) due to the shortness of daylight hours.

The partitioning of energy available from the radiation budget also showed large ranges. The most extreme variability was found in the partitioning between Q_H and Q_E, which was found to vary significantly between summer and winter. Daily β values ranged from 6.85 during the 1997/98 summer to –0.13 for the 1998 winter and 9.38 for the 1998/99 summer. This was found to primarily be a function of soil moisture and a reasonably consistent logarithmic relationship was found between β and soil moisture content for all data, irrespective of season or synoptic situation. The daily net loss of Q_H from the atmosphere to the surface in winter was found to be the result of very strong nocturnal surface layer temperature inversions and the low β values during daylight hours.

Variability in energy partitioning associated with synoptic situation was also found to be significant. Lower β values were found during northwest airflow and southwest airflow. The reason for lower β during northwest flow was thought to be a function of the relatively warm and dry air advection that occurs during this condition. The lower β associated with southwest flow in summer was considered to result from the potential

for soil moisture to be higher following the passage of a front, particularly in a season dominated by very low soil moisture, where an input in moisture leads to a significant jump in Q_E. In winter, southwest winds produced higher β values, which were thought to be primarily a result of cold air advection.

Isolation of all individual influences on the variability of surface fluxes is difficult to achieve in observational data, since surface energy flux values typically express a combination of these influences. Furthermore, this dataset is not comprehensive enough to quantify the influence of all mechanisms, which would require longer-term data as well as modelling efforts. Processes associated with vegetative controls were ignored in this analysis due to the very low density of vegetation at this site. Nevertheless, responses by vegetation may help explain some of the variability found in these results.

Despite these shortcomings, large variability has been found in this dataset associated with both seasonal and synoptic controls. The largest impact on surface fluxes was found to result from controls of the amount of available energy from the radiation budget. In this, seasonal and daily variability associated with cloudiness was found to provide similar magnitudes of variability, although seasonal variability was significantly easier to predict. The second strongest control was found to be seasonal control on the partitioning of turbulent fluxes and this in turn, was found to be controlled most significantly by soil moisture content. Thirdly, advection of airmasses associated with particular synoptic situations was found to provide the smallest, yet still significant, influence on the partitioning of fluxes.

Chapter Five:

Surface controls of radiation and energy fluxes

5.1 Introduction

The purpose of this chapter is to evaluate the spatial variability of surface energy exchanges in the Tekapo catchment as a function primarily of heterogeneous surface cover. In contrast to the previous chapter, which considered temporal variability by comparing fluxes from a single site over different seasons and synoptic situations, this chapter focuses on fluxes from different locations during the same season and synoptic situation. In order to observe spatial variability, concurrency of multi-locational sampling is necessary to ensure that the differences observed depend on space and not time. However, since the number of surface types in the catchment (Figure 3.3) is greater than the number of energy balance systems used in the study, three mobile eddy covariance stations and radiation sensors were deployed at multiple sites during the period of a month in mid summer. From this data set, clear-sky anticyclonic days were selected so that diurnal energy balances could be ascertained for nine separate locations in the catchment, either concurrently or at least under similar conditions. The temporal consistency of surface energy balance data used in this chapter was assessed by referencing them to continuous measurements made at the stationary BREB station throughout the study period.

The nine sites selected, represent the five most extensive surface classes in the catchment; degraded tussock, short tussock, tall tussock, rock and lake surfaces. Description of the location and timing of these observations is provided in Table 5.1. The diurnal surface radiation and energy balances of each of these five surface classes in clear-sky, summer anticyclonic conditions are examined individually in the following sections. The variability between surfaces is then examined with respect to the magnitude of heterogeneity and the mechanisms responsible. Finally, the role of soil moisture is assessed through the comparison of summer locations and a case study rainfall event at the BREB site.

Table 5.1 Energy balance stations used, surface types covered and dates selected for analysis in Chapter Five (see Figure 3.1 for locations).

Station name	Surface type	Selected days
MEB1	Rock (floodplain gravels)	Feb 11, 12, 13
MEB2	Tall tussock	Feb 1, 2
MEB5	Short tussock	Jan 25, 28, 29
MEB6	Short tussock	Feb 7, 8, 9
MEB7	Lake	Feb 5, 6, 7, 8, 9
MEB9	Tall tussock	Feb 13, 14, 15
MEB10	Degraded tussock	Jan 27, 28, 29
MEB11	Lake	Jan 24, 25
BREB	Degraded tussock	All of above

5.2 Vegetated surfaces

By far the largest extent of vegetated surface in the Tekapo catchment is comprised of tussock grasslands. The surface cover classification for the catchment (Figure 3.3, Table 3.) estimated that of the 2259 Km^2 catchment, 17 % was degraded tussock, 28 % was short tussock and 18 % was tall tussock. Further details of the plant species are provided in Section 3.1.2. By comparing energy balance observations made over similarly vegetated surfaces in other mountainous regions, considerable variability in energy flux partitioning can be found (Campbell 1989, Whiteman *et al.* 1989, Halbsguth *et al.* 1984, Saunders and Baily 1996, Konzelmann *et al.* 1997). Furthermore, large differences can be found, not only between study areas, but also between sites within a study area. These differences implicate the role of spatially varying local climate, soil moisture and plant species on energy partitioning. The findings of these studies are compared to the results of the current study more directly at the conclusion of this section.

The influence of different types, sizes and density of tussock grasses on surface energy fluxes results from their radiative properties, roughness characteristics, ability to store heat in the canopy volume and control on water movement through interception, root uptake and stomatal resistance. The flux of energy due to photosynthesis is typically very small in comparison to the other energy balance terms (Oke 1987) and is neglected in this study.

The surface roughness of tussock grassland in the catchment varies considerably due to the differences in size and density of tussock. Tussock height ranges between 0.15 and 0.65 m, with plant diameters of similar magnitudes. Degraded tussock however, contained very sparse coverage of tussock plants and was dominated by flat Hawkweed species and bare soil. Surface roughness is governed most significantly by frost heave landforms of the order of 0.1 to 0.2 m. Furthermore, the density of tussock vegetation varied considerably throughout the catchment from areas with near-continuous canopy to areas with only a few plants in 10 m^2. Finally, taller species bend easily in moderate to strong winds significantly smoothing the effective surface relative to the direction of flow, particularly in densely vegetated areas. This produces a variation in surface roughness with wind speed.

The influence of heat storage within the canopy is likely to be of smaller concern since vegetation structure is oriented vertically allowing radiation and airflow to penetrate well into the canopy. The storage term in other studies over grasses is typically very small and often neglected, with ΔQ_S estimation based only on measurement of Q_G (e.g. Monteith *et al.* 1965, Campbell 1989). In these studies, Q_G was found to be typically less than 10% of Q^*. In the present study, Q_G was measured using heat flux plates inserted in the soil close to the surface and ΔQ_S was assumed to be negligible. The validity of this approach was questioned by examining the residual of $Q^* - Q_H - Q_E - Q_G$. Residual values ranged between 0% and 8% of Q^*, within the margins of error of the estimation technique.

The influence of bulk stomatal resistance (r_{st}) on Q_E and the relationship between r_{st} and saturation vapour pressure deficit (D) in tall tussock (*Chionochloa rigida*) in another South Island region was evaluated by Campbell (1989). Water use by tussock was conservative with a relatively high r_{st}. The lowest β occurred when D was high and higher values occurred when D was small. r_{st} was calculated using the Penman-Monteith equation and found to have a statistically significant linear relationship with D. Stomata are found only inside the tightly rolled tussock leaf in deep furrows and are covered by a thick waxy encrustation and Pollock (1977, cited in Campbell 1989) showed that the degree of leaf roll increased with moisture stress. The apparent direct dependence of r_{st} on the size of D could therefore be caused by changes in both r_{st} and relative leaf roll (Campbell 1989, Jarvis and McNaughton 1986). This hydrologically conservative behaviour of tussock was confirmed in a comparative review of evaporation over grasslands (Kelliher *et al.* 1993), where Campbell's (1989) findings were located at the lower end of maximum hourly and daily evaporation rates, despite a high aerodynamic conductance, due to the large roughness length. However, these were found at a site with a mean annual rainfall of 1270 mm yr^{-1}, more than double that of most of the Tekapo catchment. The relationship between D, r_{st} and Q_E is likely to be less pronounced when moisture stress is greater. An additional consideration is that the hydrologically conservative behaviour of tussock would result in soil moisture levels being less readily depleted, thereby allowing evapotranspiration to continue, albeit at low magnitudes, in drier areas.

5.2.1 Degraded tussock

'Degraded tussock', as outlined in Section 3.1.2, is made up of sporadic short tussock species, invasive ground cover species and bare soil. The radiation and energy balance of degraded tussock was evaluated at two sites. The BREB station ran continuously throughout the intensive observation period and all anticyclonic days were used in this analysis. The second site (MEB10) was located on the eastern side of Lake Tekapo. The locations of these sites can be found in Figure 3.1, measurement details in Tables 3.3 and 3.4 and data used for analysis in Table 5.1.

Surface radiation budget

The radiation budget for the BREB site on February 12, 1999 is presented in Figure 5.1. The pattern of Q^* was offset slightly from K^* with lower values in the afternoon than morning. This results from larger $L\uparrow$ in the afternoon as a function of surface heating (Figure 5.1a) and changes in albedo throughout the day. Figure 5.1b plots albedo as a function of solar zenith angle. The trend lines generated for these data suggest that zenith angle had a consistent but small influence on albedo. The values on the lower

trend line were morning observations, while those on the upper were observed in the afternoon, with a mean difference of approximately 0.02. Given that a large portion of this surface is soil, the most likely cause of this offset is diurnal change in soil colour as a function of moisture near the surface. In the morning, the slightly damp soil had a darker complexion and smaller albedo. As the surface began to heat, moisture available at the surface was removed by evaporation, thereby lightening the soil colour and raising albedo. The diurnal range in albedo as a function of changes in both solar angle and surface colour in this case is 0.04. With reference to daylight mean $K\downarrow$, this equates to a range in $K\uparrow$ of approximately 14 W m^{-2}, which constitutes a very small contribution to the overall radiation budget. Despite this, a very strong linear relationship existed between $K\downarrow$ and Q^* illustrating the dominance of $K\downarrow$ in the energy balance of degraded tussock (Figure 5.1c).

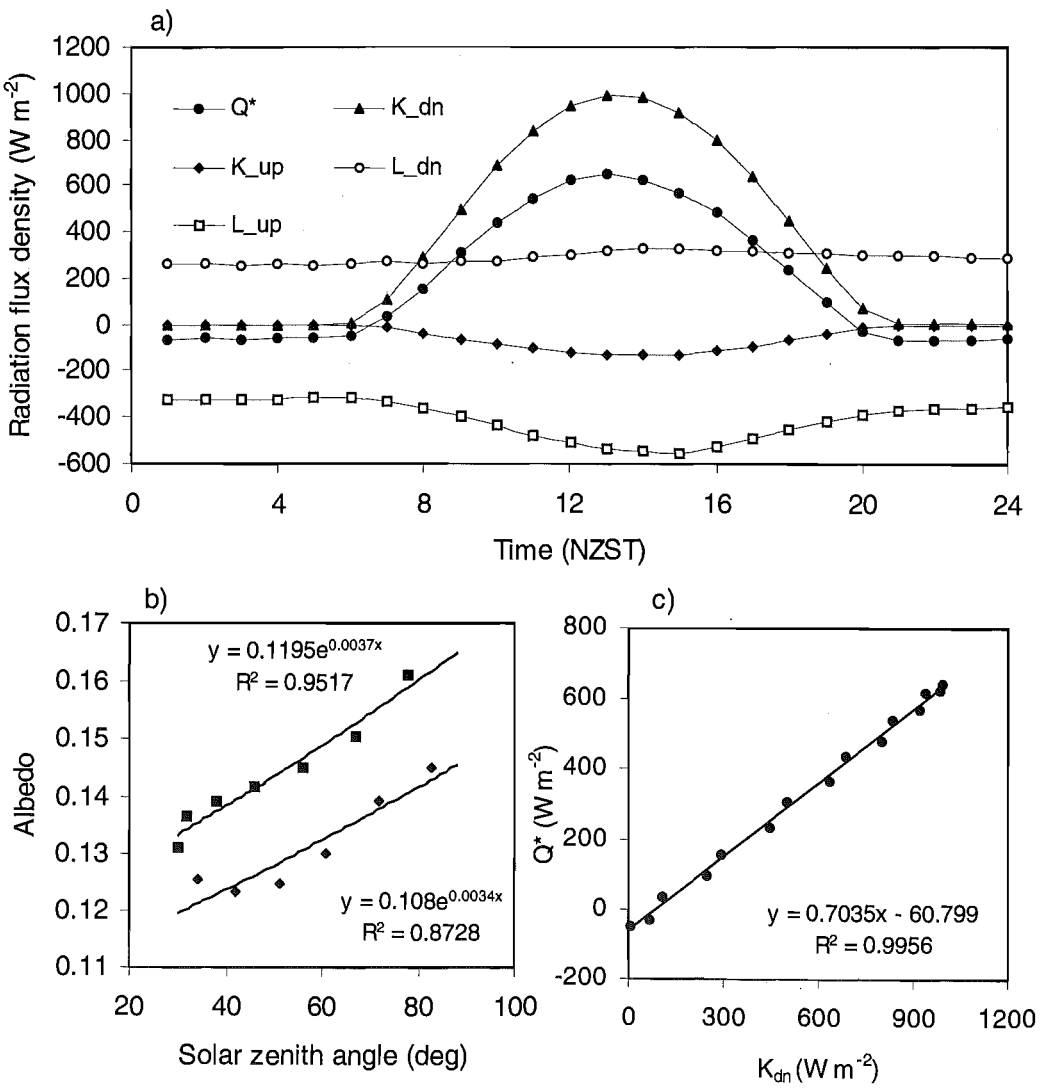

Figure 5.1 Mean hourly surface radiation budget components (a) and relationships between albedo and solar zenith angle (b) and Q^* and $K\downarrow$ (c) at BREB, February 12, 1999. (Note: K_dn = $K\downarrow$, L_up = $L\uparrow$ *etc.*)

Surface energy balance

The surface energy balance for February 12, 1999 at the BREB site, presented in Figure 5.2, compares closely with the summer anticyclonic case presented for this site in the previous chapter (Figure 4.9). Q^* surplus was converted most significantly into Q_H, associated with an increase in temperature (Figure 5.2b), and secondly by Q_G. Q_E peaked soon after sunrise as near surface moisture was evaporated, but this moisture was clearly not replenished due to low overall moisture content in the soil column. Again local airflow played an important role in the diurnal partitioning between Q_H and Q_G. Firstly, wind speed increased in the afternoon (Figure 5.2c), which increased the ratio of thermal admittance between Q_H and Q_G, allowing an asymmetrical balance between the two in relation to Q^*. Secondly, the role of the afternoon easterly intrusion, was to further enhance Q_H and reduce Q_E, due to cool, moist air advection as well as to enhance Q_H relative to Q_G as a result of increased wind speed.

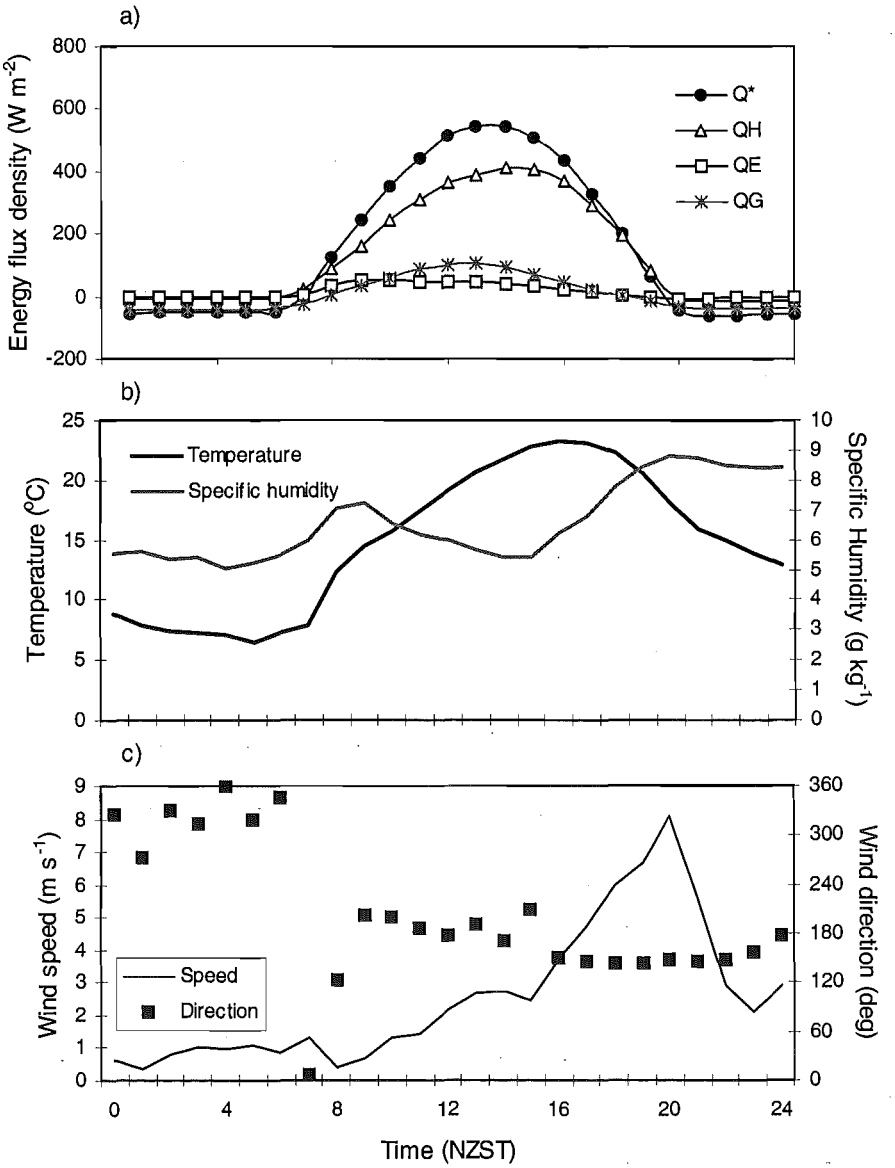

Figure 5.2 Mean hourly surface energy balance components (a) temperature and specific humidity (b) and wind speed and direction (c) at BREB, February 12, 1999.

The relationship between Q^* and energy partitioning is presented in Figure 5.3. Both Q_H and Q_G show a close dependence on Q^*. They also both show a hysteresis effect, with differences between morning and afternoon values for the same Q^* magnitude. This is due to the positive influence of wind speed on Q_H and negative influence on Q_G. Because of this, the pattern of data points for Q_G follows a clockwise rotation about the linear trendline, while Q_H rotates anticlockwise. Q_E has a much weaker dependence on Q^*, also with a clockwise rotation about the trendline. This is not likely to be related to wind speed, since this should produce a similar pattern to Q_H because the influence of turbulent transport is similar for both scalars. Instead it is most likely related to availability of moisture at the surface for evaporation, which is greater during morning.

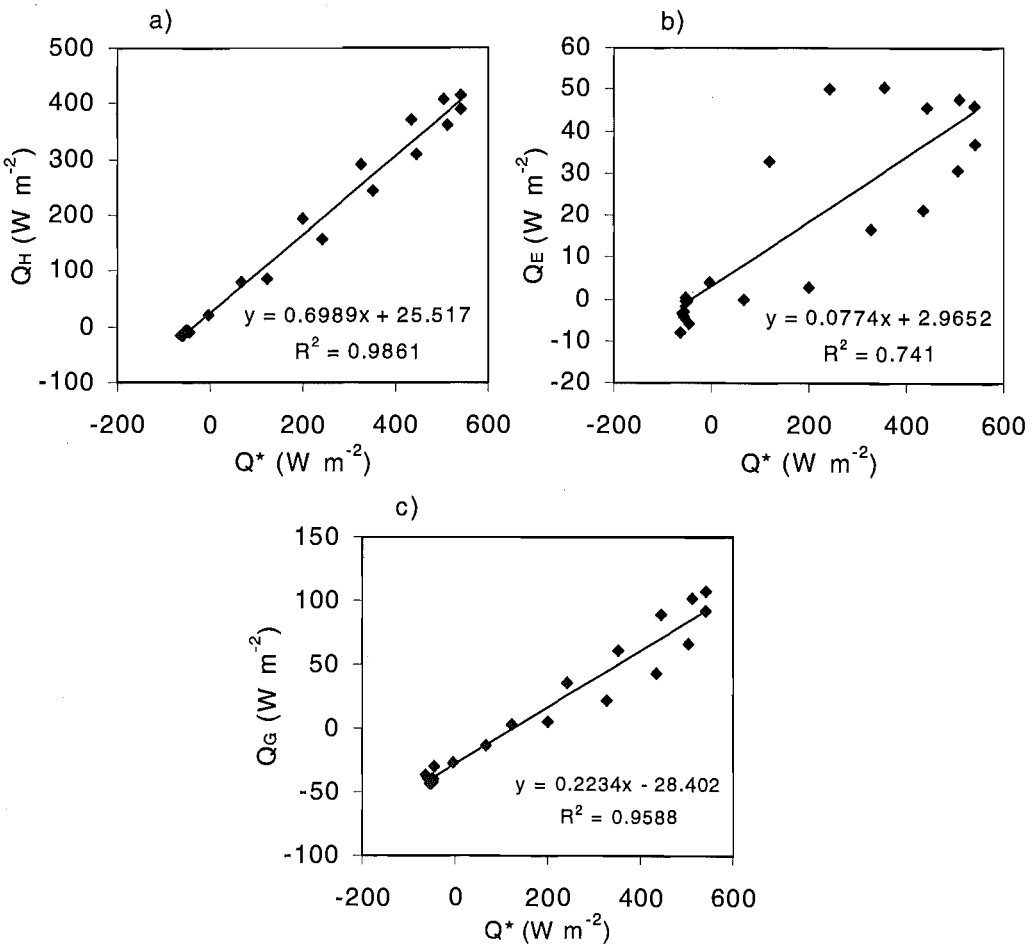

Figure 5.3 Relationship between mean hourly Q^* and energy balance components at BREB, February 12, 1999.

Degraded tussock mean statistics

The case presented above describes the nature of diurnal surface energy exchange patterns in terms of the characteristics of the surface and its interaction with the overlying atmosphere. The daily total Q^* and energy partitioning into Q_H, Q_E and Q_G for this case is provided in Table 5.2 as well as the mean values for the BREB site, MEB10 site and for all degraded tussock as a surface class. Standard deviation values provide information on the scale of variability found within this class as derived from these observations. Although the two locations recorded comparable daily energy partitioning, the MEB10 site showed an overall higher Q_E and lower Q_H. The reason for this is likely to be exposure to the afternoon easterly intrusion, since soil moisture was

similar at both sites. The MEB10 site was completely sheltered by high ridgelines on the Two Thumb Range from the regional scale afternoon easterly airflow, thereby diminishing the role of cool, moist air advection at this site, as well as higher wind speed. The spatial variability of β is therefore likely to depend on exposure to such advective influences, given identical surface conditions. The main region exposed to the easterly intrusion is the central Mackenzie Basin area, as well as in the vicinity of Tekapo Saddle (see Figure 3.1). Energy partitioning is likely to vary by at least as much as 4% of Q^* for both Q_H and Q_E as a result of this.

Table 5.2 Mean statistics for energy balance observations over degraded tussock surfaces.

	Q^* (MJ m^{-2} dy^{-1})	Q_H/Q^*	Q_E/Q^*	Q_G/Q^*	n (days)
BREB 12-2-99	13.2	0.87	0.10	0.03	1
BREB mean	14.5	0.79	0.16	0.05	15
BREB σ	0.90	0.05	0.03	0.01	15
MEB10 mean	13.4	0.74	0.21	0.05	3
Class mean	14.2	0.78	0.17	0.05	18
Class σ	1.28	0.09	0.05	0.03	18

The mean β for degraded tussock was therefore 4.6, which is generally higher than those found in previous studies over grass surfaces in mountainous terrain (these comparisons are provided at the conclusion of this section). This illustrates the dryness of the area as well as the low capacity of the degraded tussock surface to conserve moisture.

The standard deviation for the BREB mean is also provided in Table 5.2. This illustrates the relatively small variability found in energy partitioning over all days covered by stations in this data set. This finding is important because it provides confidence in making comparisons between sites when data were recorded on different days. Furthermore, the mean values from the observation period used in this chapter compare well with the summer, anticyclonic mean values reported in Chapter Four. The magnitude of potential error associated with day to day variability, based on these data, equates to 5%, 3% and 1% of Q^* for Q_H, Q_E and Q_G respectively.

5.2.2 Short Tussock

Observations were made using a mobile energy and radiation balance station on two separate occasions for 3-day periods near the northeastern corner of lake Tekapo (MEB5 and MEB6). The locations of the station in the two periods were slightly different, although within 100 m of each other with no change in the nature of the surface for about 400 m in any direction.

Surface radiation budget

The complete surface radiation budget for February 8, 1999 is plotted in Figure 5.4a. As with degraded tussock, Q^* was strongly a function of $K\downarrow$ (Figure 5.4c), although, a relative dip in surface temperature between 1000 and 1400 NZST also appeared to account for some of the variability found in Q^*. The diurnal change in albedo followed a very consistent second order polynomial fit to solar zenith angle with a range of 0.15.

Using the diurnal mean $K\downarrow$, this equates to a range in $K\uparrow$ of 60 Wm^{-2}. The reason for the apparent change in $L\uparrow$ is discussed in the following section where diurnal meteorological parameters are presented.

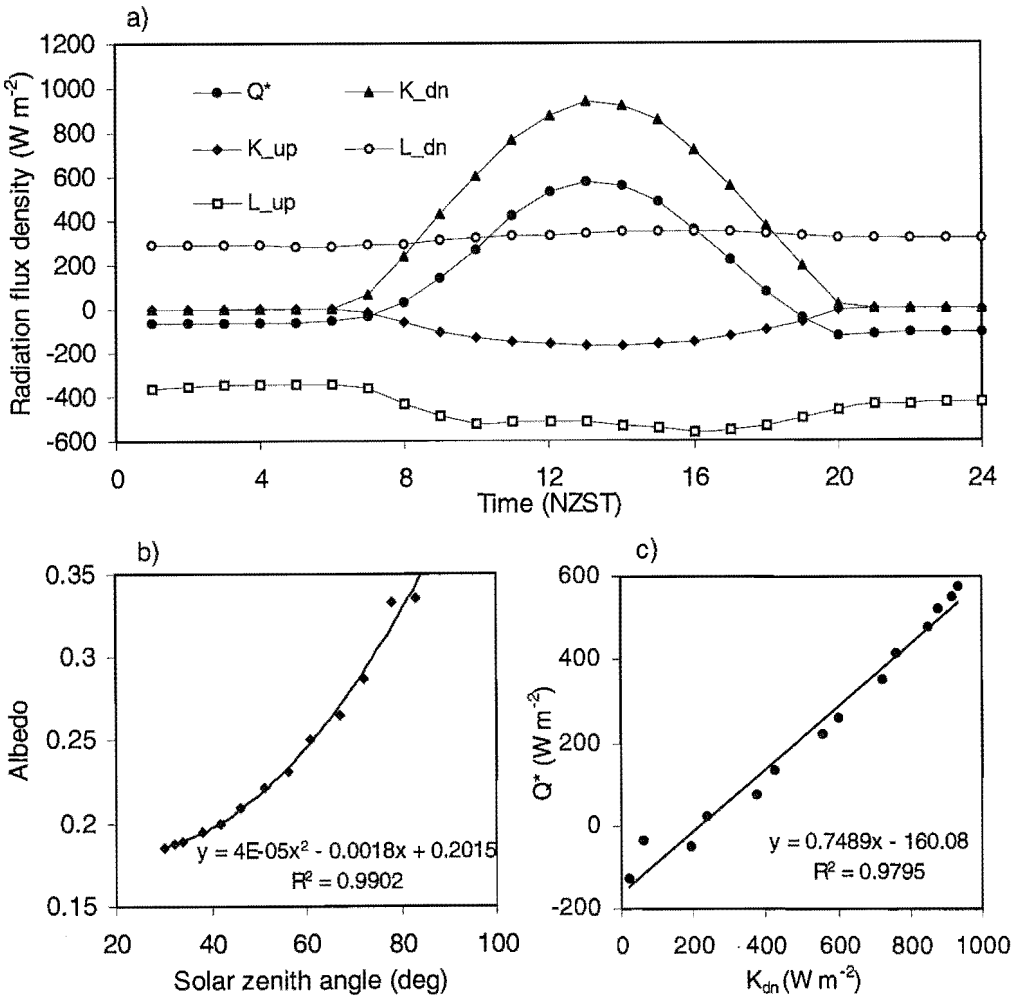

Figure 5.4 Mean hourly surface radiation budget components (a) and relationships between albedo and solar zenith angle (b) and Q^* and $K\downarrow$ (c) at MEB6, February 8, 1999.

Surface energy balance

The surface energy balance for February 8 (Figure 5.5a) showed the dominance of Q_H as an energy sink, although not to the same extent as over degraded tussock. Both Q_E and Q_G reached a plateau at about 150 W m^{-2} from 1000 to 1500 NZST. Other studies have found a plateau effect in Q_E, when evaporation is slowed by stomatal resistance, reacting to increases in saturation deficit (Campbell 1989). As with the BREB site, this can also be linked to local diurnal meteorology. Figure 5.5 (b and c) illustrates three distinct meteorological patterns for the day (meteorological data were taken from MEB7, located about 400m away on the lake edge). Initially, cool nocturnal drainage flow dominated from the two large valleys to the north. At about 0900, this was replaced by an onshore lake breeze, which gradually increased in velocity to 3 m s^{-1} by 1400 NZST. Cool and moist advection associated with this airflow is clearly illustrated in the diurnal temperature and humidity traces. The morning increase in wind speed coincided with a halt in the increase of Q_G at 1100 NZST, while the increase in humidity and relative decrease in temperature corresponded to a relative drop in Q_E and peak in Q_H respectively. The cool airmass also appears to have had an impact on surface

temperature and consequently $L\uparrow$, as noted in the previous section. From 1600 NZST, the lake breeze was replaced by a down valley incursion of warm dry air with wind speeds up to 8 m s^{-1}. The origins of this airflow during anticyclonic conditions is the subject of ongoing research, although it appears to be topographically channelled flow, which was found to occur consistently to the north of Lake Tekapo (McGowan and Sturman 1995). The advective influence of this airflow is surprisingly minimal, although Q_E increased slightly. The reason this was not more pronounced could be due to the response of stomata to the increased saturation deficit, as well as the generally low soil moisture content, particularly later in the day.

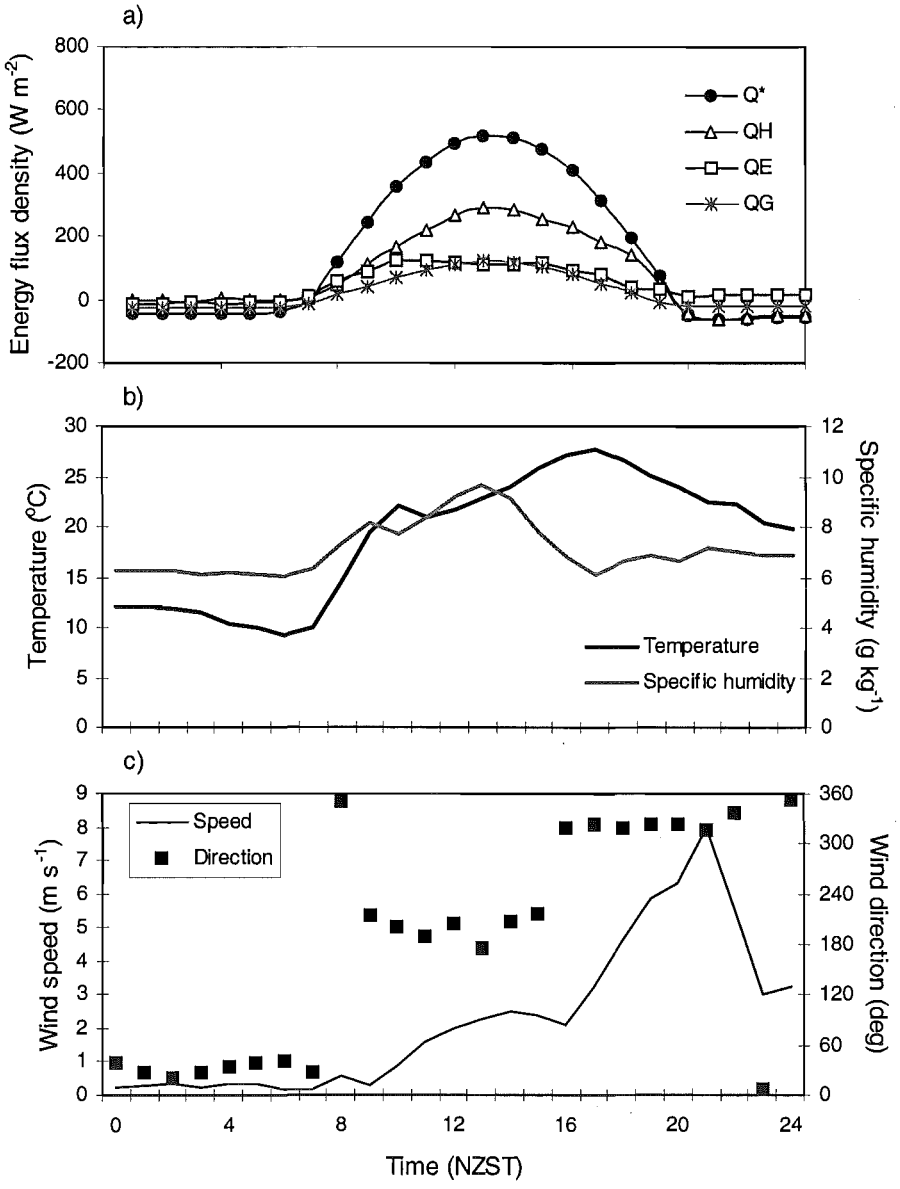

Figure 5.5 Mean hourly surface energy balance components (a) temperature and specific humidity (b) and wind speed and direction (c) at MEB6, February 8, 1999.

The dependence of all three heat fluxes on Q^* was found to be more significant than the degraded tussock case, with generally more symmetrical diurnal traces (Figure 5.6). This is likely to be largely the control of vegetation on regulating Q_E through stomatal control, as well as Q_G through biomass. Furthermore, the longer roughness length means that the ratio of convective to conductive fluxes would be less dependent on wind speed.

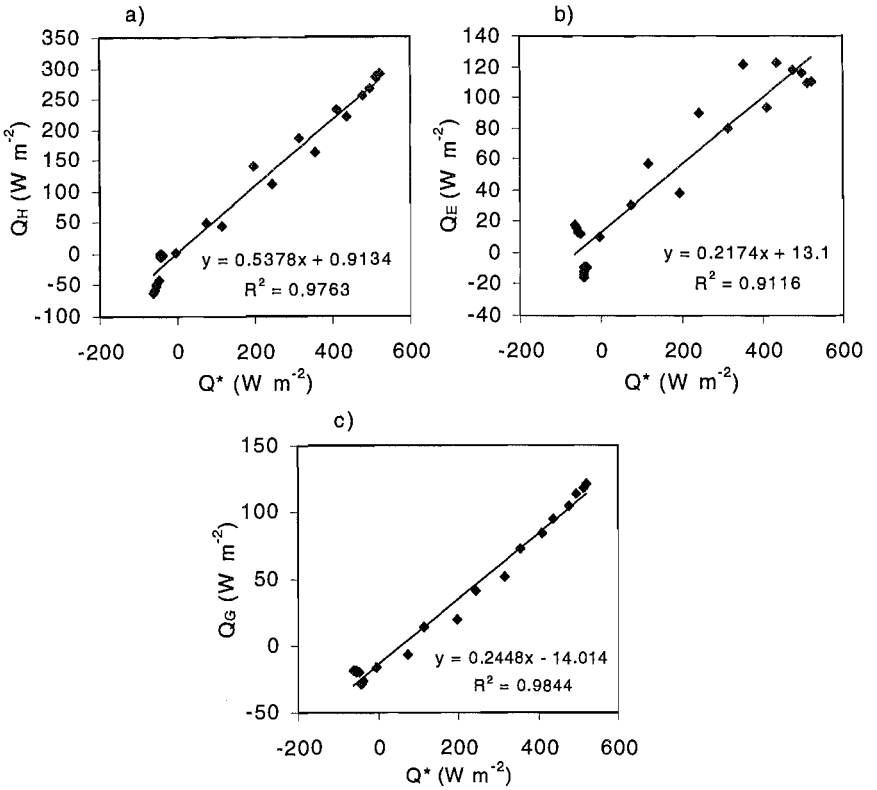

Figure 5.6 Relationship between mean hourly Q^* and energy balance components at MEB6, February 8, 1999.

Short tussock mean statistics

The case presented above, as well as the individual site and overall surface class mean Q^* and energy partitioning ratios are presented in Table 5.3. Despite the similarity of the site for the two periods, the balance between Q_H and Q_E is significantly different. The volumetric soil moisture content at this site was 10% on January 24 (one day before MEB5 observation period) and was 18% on February 2 (five days before MEB6 observation period). The reason for this difference was the rainfall event described in Section 4.3.5. This was likely to be the cause of the relative decrease in β in the second observation period, confirming the influence of soil moisture levels on the energy balance.

Table 5.3 Mean statistics for energy balance observations over short tussock surfaces.

	Q^* (MJ m^{-2} dy^{-1})	Q_H/Q^*	Q_E/Q^*	Q_G/Q^*	n (days)
MEB6 8-2-99	12.9	0.56	0.31	0.15	1
MEB5 mean	13.4	0.73	0.14	0.12	3
MEB6 mean	13.0	0.53	0.33	0.12	3
Class mean	13.2	0.64	0.23	0.12	6
Class σ	0.43	0.10	0.10	0.02	6

The mean β for this site was 2.8, which is still somewhat higher than observed in other mid-latitude studies in mountain areas (comparisons provided at the conclusion to this section). Q_G played a more dominant role in the energy balance than might be expected. Typically, daily total Q_G is low due to the re-transfer of stored energy by night, although above-zero values are common for summer. It could be expected that higher values

would occur during clear-sky days and lower values during cloudy days, when the surface is cool and energy is transferred up from the underlying soil. The reason for the higher value for this surface compared to degraded tussock however, is unknown but could be related to soil type. It is unlikely to be the poor placement of a heat flux transducer, since three sensors observed approximately the same magnitudes, and similar Q_G/Q^* values were observed at both MEB5 and MEB6.

5.2.3 Tall tussock

The best example of clear-sky anticyclonic observations over tall tussock came from a 24-hour period covering two days at MEB2, although observations were also made at MEB9, covering a total period of 4 days. The two sites were both located on the eastern slope of the lake basin. Site location and details can be found in Figure 3.1 and Table 3.4, with observation dates in Table 5.1.

Surface radiation budget

The surface radiation balance for February 1, 1300 NZST to February 2, 1200 NZST, 1999 is presented in Figure 5.7.

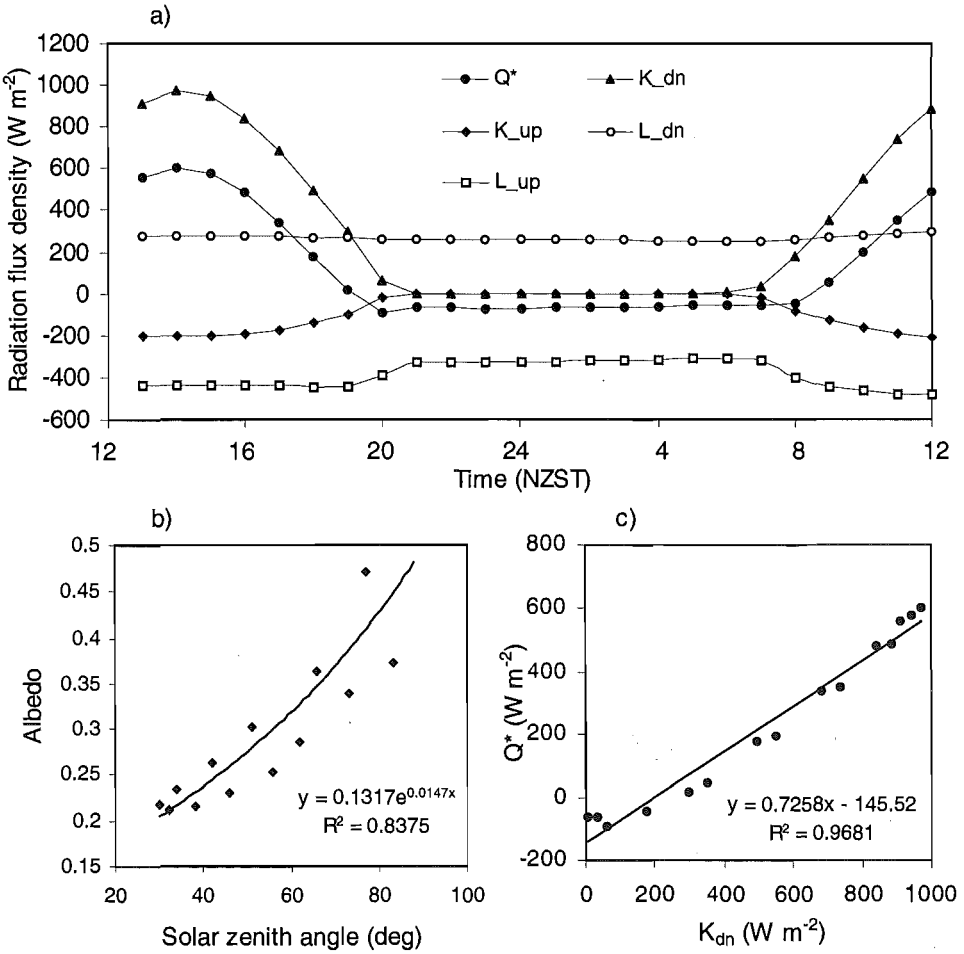

Figure 5.7 Mean hourly surface radiation budget components (a) and relationships between albedo and solar zenith angle (b) and Q^* and $K\downarrow$ (c) at MEB2, February 1 1300 NZST to February 2 1200 NZST, 1999.

The diurnal trace of $K\downarrow$ peaked relatively high and late due to the WNW orientation of the 5° slope. $L\downarrow$ varied little due to the relatively cool air (see following section) and $L\uparrow$ changed rapidly in the transition between night and day but not significantly in response

to changing flux densities of $K\downarrow$. This is probably due to the regulatory effect of the dense, vertically oriented vegetation on canopy temperature. The comparison of albedo with solar zenith angle (corrected for slope angle) revealed a reasonably significant exponential relationship (Figure 5.7b), although with generally lower albedo values recorded in the afternoon than morning. The reason for this is not entirely clear, although could be related to the direction of lean of the 60 cm tall tussock, which may alter the effective surface reflectance relative to the direction of $K\downarrow$. This could be a local effect, since the downward pointing radiometer had a field of view on the order of only a few individual tussock plants. Alternately, mean winds would have a broader scale effect on plant orientation, as would gravity for plants on steeper sloping surfaces. Relatively lower morning albedos could also be related to the presence of dew on the canopy. Diurnal range of albedo was 0.18, which equates to a range in $K\uparrow$ of 60 W m^{-2} based on the diurnal mean $K\downarrow$. However, the diurnal change of albedo did not impact significantly on Q^*, which maintained a strong dependence on $K\downarrow$ (Figure 5.7c).

Surface energy balance

The surface energy balance components for February 1 and 2, 1999, as well as general meteorological parameters, are plotted in Figure 5.8.

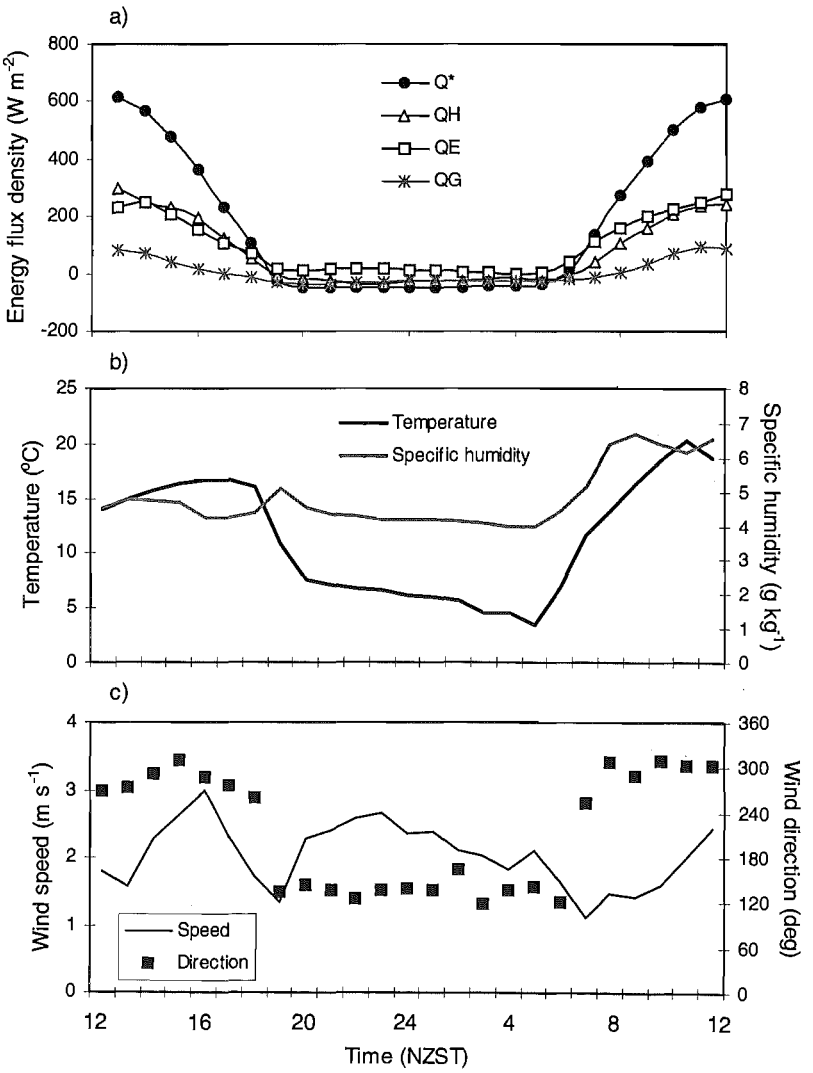

Figure 5.8 Mean hourly surface energy balance components (a) temperature and specific humidity (b) and wind speed and direction (c) at MEB2, February 1 1300 NZST to February 2 1200 NZST, 1999.

The diurnal local airflow was relatively simply divided into upslope flow by day and downslope flow at night. This observation period occurred two days after a significant rainfall event so that soil moisture values (28%) were higher than average (18%). At the BREB site for example, it was shown that excess moisture provided by rainfall lasted for about 3 days before being evaporated (Section 4.3.5). Given the more hydrologically conservative nature of tall tussock than degraded tussock, the impact of the rainfall event at the MEB2 site would be smaller but longer lasting than at the BREB site. Available energy during this case was fairly uniformly partitioned between Q_H and Q_E, with much smaller flux directed into the ground.

All three partitioned energy components were found to correspond closely with Q* (Figure 5.9). In contrast with the previous cases, wind speed was more consistent throughout the 24-hour period, diminishing the diurnal asymmetry between convective and conductive fluxes. The taller tussock would also produce a longer roughness length, thereby reducing the need for significant wind speed to generate turbulence. Furthermore, with the larger moisture supply, stomatal resistance was probably lower, allowing energy components to correlate more strongly with Q^*.

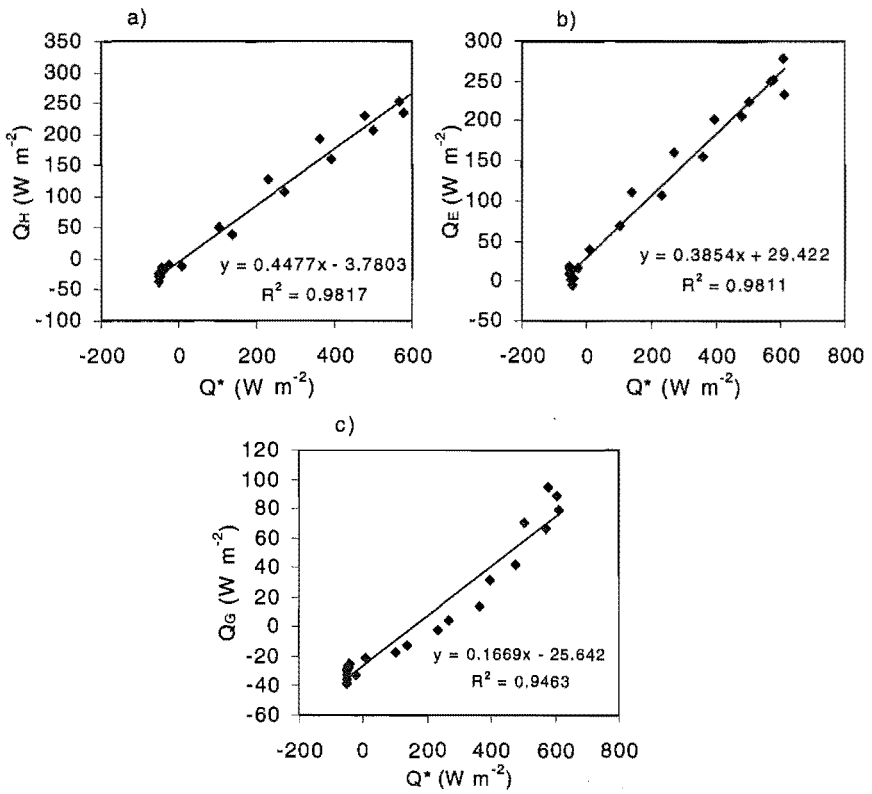

Figure 5.9 Relationship between mean hourly Q^* and energy balance components at MEB2, February 1, 1300 NZST to February 2, 1200 NZST, 1999.

Tall tussock mean statistics

The case study presented above was the only full day of observations at MEB2, although 3 days of observations during partly cloudy conditions were available from MEB9. The daily total Q^* and energy partitioning for both sites is presented in Table 5.4. The relative partitioning between Q_H and Q_E at the two sites was significantly different. Soil moisture data were not collected at MEB9, although no rain fell between the two study periods, suggesting it was lower during the latter period. The surface class mean values were obviously closer to MEB9 than MEB2 means due to the larger

sample from the latter site. This is probably a realistic statistical skew however, given the unusually high soil moisture levels during the observation period at MEB2. The mean β recorded for this surface type was 1.53, which is very similar to that found by Campbell (1989) for the same plant species in Otago.

Table 5.4 Mean statistics for energy balance observations over tall tussock surfaces.

	Q^* (MJ m^{-2} dy^{-1})	Q_H/Q^*	Q_E/Q^*	Q_G/Q^*	n (days)
MEB2 1-2-99	15.5	0.43	0.55	0.02	1
MEB2 mean	15.5	0.43	0.55	0.02	1
MEB9 mean	12.2	0.65	0.30	0.06	3
Class mean	12.9	0.58	0.38	0.05	4
Class σ	1.97	0.10	0.12	0.02	4

5.2.4 Comparison with similar vegetated study areas

Table 5.5 presents β observed over similar vegetated surfaces in other mountainous mid-latitude areas in comparison to those found in this study. This comparison shows that the surface energy fluxes observed in the Tekapo catchment show a generally dryer microclimate than other similar study areas, illustrating the significance of rain shadowing from the alpine divide located upwind relative to the prevailing airflow. It also illustrates that a significant range in surface energy partitioning can be found within individual study areas as well as between different study areas. The mean β for degraded tussock was the highest of all observations tabulated here, while tall tussock surfaces provided the most comparable data to studies in other regions.

Table 5.5 A selection of Bowen ratios found in mid-latitude studies in mountain regions over grass and shrub surfaces as well as those found in this study (~ indicates estimates based on published graphs, not cited values).

Reference	Location, vegetation	Season	β
Halbsguth *et al.* (1984)	Dischma Valley floor, Switzerland, meadow	clear summer day	~0.37
Whiteman *et al.* (1989)	Brush Creek Valley floor, USA, wheat grass	clear autumn day	0.55
	Brush Creek Valley ridge top plateau, sagebrush	clear autumn day	1.94
Konzelmann *et al.* (1997)	Dischma Valley floor, meadow	summer range	0.2-0.6
	Dischma Valley N-facing sidewall, dwarf shrubs	summer range	0.6-0.8
Saunders and Baily (1996)	Scout Mtn, Canada, dry alpine tundra	clear spring day	~1.8
Campbell (1989)	Otago hill country, New Zealand, tall tussock	summer	1.58
Present study...	Tekapo catchment, New Zealand, tall tussock	clear summer days	1.53
	Tekapo catchment, short tussock	clear summer days	2.13
	Tekapo catchment, degraded tussock	clear summer days	4.56

5.3 Rock surface

In the northern part of the Tekapo catchment, rock surfaces dominate the steep slopes and valley floors in the form of rock scree slopes and active river floodplain. This surface makes up a significant portion of the entire study area (30%). Observations were made for a three-day period (Table 5.1) over an extensive gravel floodplain on the Godley Valley floor at MEB1 (Figure 3.1).

Surface radiation budget

The diurnal surface radiation budget for February 12 1999 (Figure 5.10) illustrates the very strong control that $K\downarrow$ had on the radiation budget at this site, particularly since mean albedo was relatively low. It also illustrates the role of topography. Although topography was relatively low toward the rising sun (southeast), the local sunset can be seen to have occurred between 1800 and 1900 NZST, approximately 2 hours before the BREB site due to the high ridgeline to the southwest. $L\uparrow$ was high due to the warm rock surface, although surface temperature reached a plateau from about 1100 NZST and remained high long after sunset due to the large heat capacity of the rock. Albedo changed relatively little as a function of solar zenith angle (Figure 5.10b), equating to a range of only 9 W m^{-2} when albedo range was multiplied by mean $K\downarrow$. Given this low range, the dependence of Q^* on $K\downarrow$ was very strongly significant (Figure 5.10c).

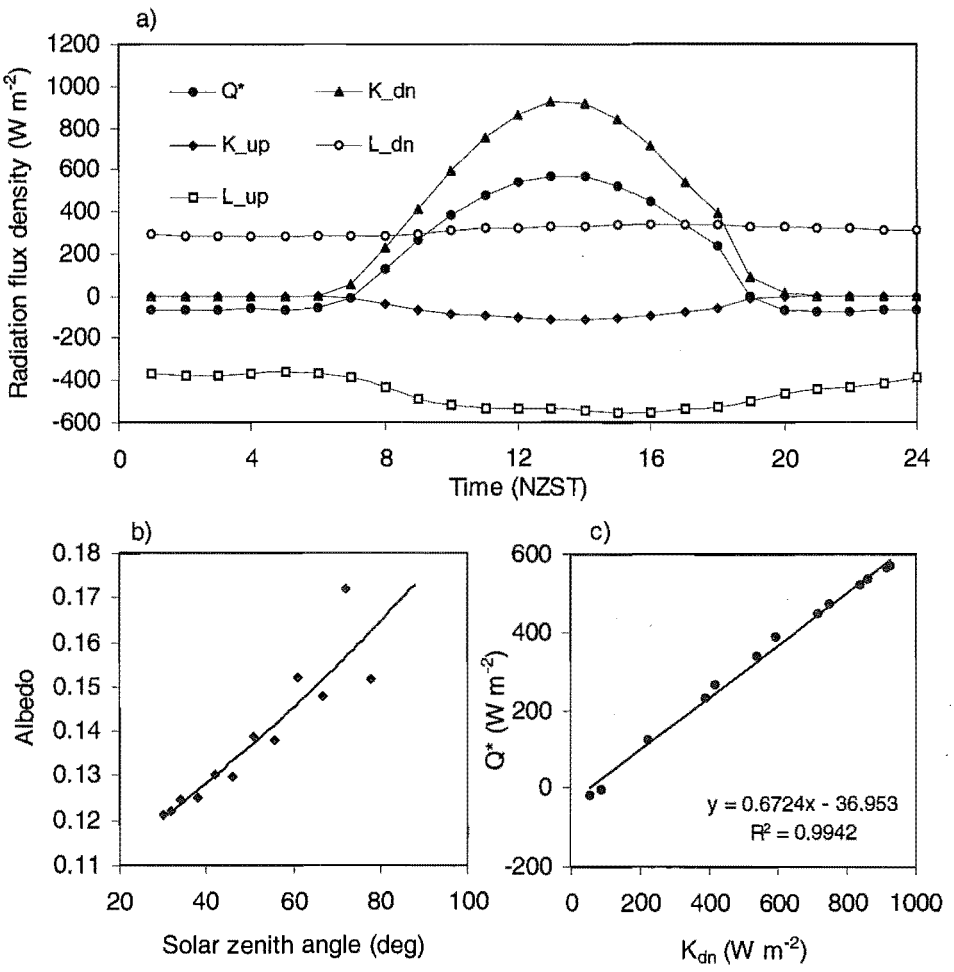

Figure 5.10 Mean hourly surface radiation budget components (a) and relationships between albedo and solar zenith angle (b) and Q^* and $K\downarrow$ (c) at MEB1, February 12, 1999.

Surface energy balance

Over the rock surface, Q^* was most strongly partitioned into Q_H and Q_G, with Q_G reaching the highest values of the land surfaces (Figure 5.11). Consequently, the Q^* loss at night was most strongly compensated by the return of Q_G stored in the sub-surface volume by day, preventing strong nocturnal cooling from occurring. The local meteorology was dominated by weak down-valley flow by night with moderate up-valley flow by day. As with the degraded tussock sites, the relative partitioning of Q_H and Q_G formed an asymmetrical pattern in relation to Q^*, with Q_G dominating in the morning, during weaker wind speeds and Q_H dominating in the afternoon valley wind.

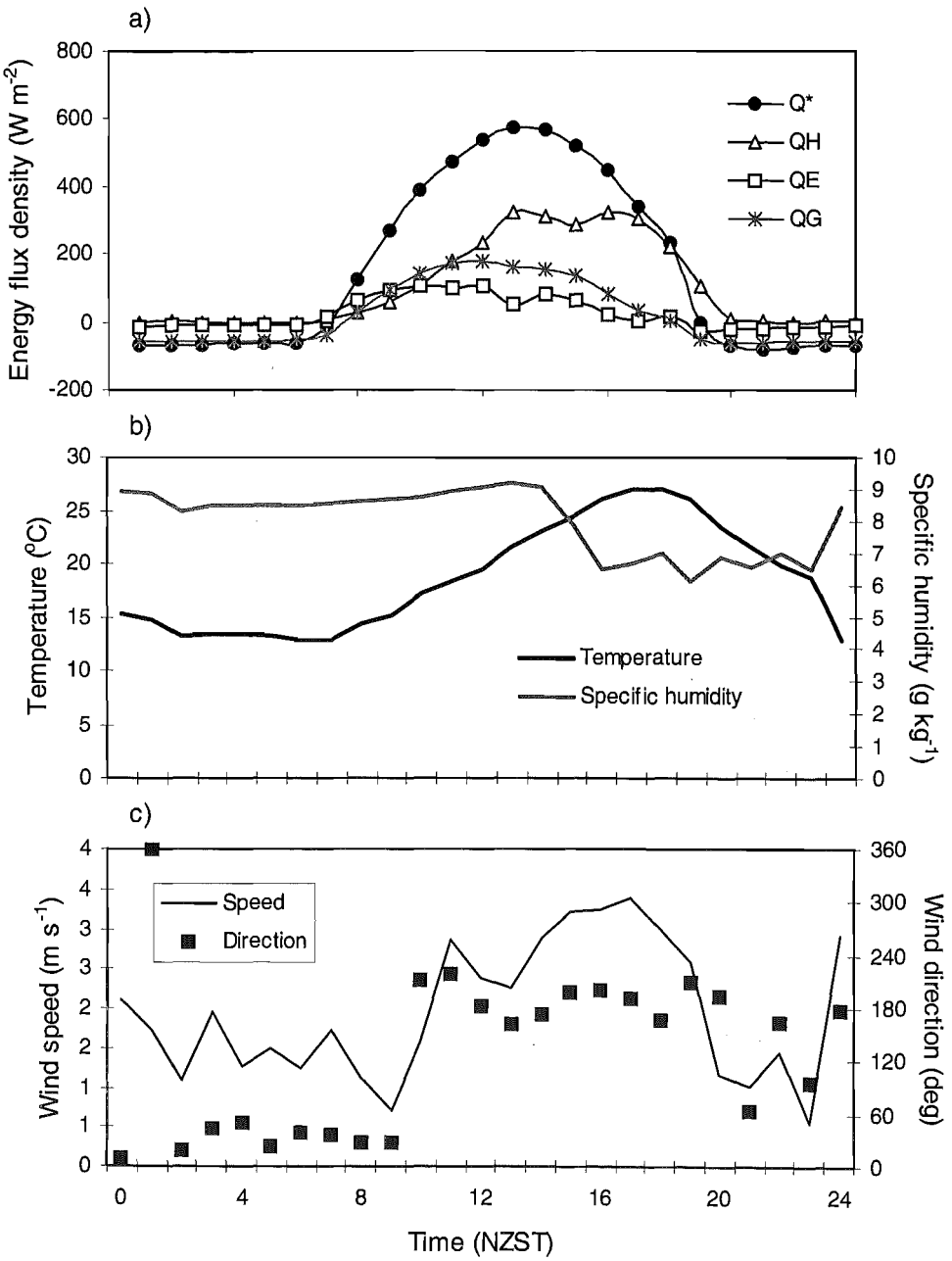

Figure 5.11 Mean hourly surface energy balance components (a) temperature and specific humidity (b) and wind speed and direction (c) at MEB1, February 12, 1999.

Consequent to the strong diurnal counter asymmetry in Q_H and Q_G, the dependence of these two components on Q^* was not as strong as the more densely vegetated cases (Figure 5.12). Hysteresis patterns were evident with the same rotational pattern as was found in the degraded tussock case. Q_E was correlated to Q^* with similar r^2 values as the degraded tussock case, and likewise peaked early in the day, suggesting that most available surface moisture was removed in the hours after sunrise.

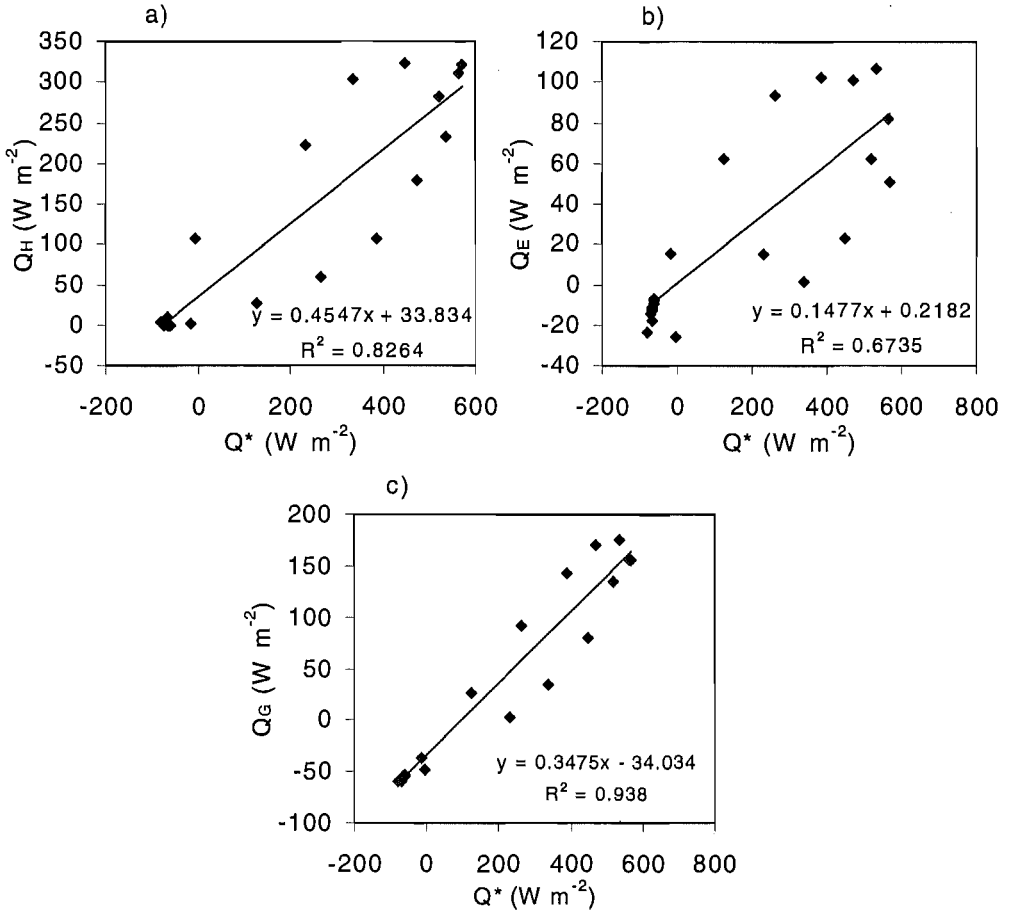

Figure 5.12 Relationship between mean hourly Q^* and energy balance components at MEB1, February 12, 1999.

Rock surface mean statistics

The rock surface class was represented by the smallest sample making up the class statistic, with only three days of data collected at one location (Table 5.6). Nevertheless, Q^* surplus was clearly dominated by Q_H with the remaining energy partitioned equally between Q_E and Q_G. Compared with most land surfaces, this represents a very small Q_E and very large Q_G. The low Q_E was due to the low moisture supply for evaporation. The reason for the large Q_G is likely to be due to the high thermal conductivity of rock and also the low surface roughness, which weakens turbulent transport, particularly in light winds. Q_E was not as negligible as might be expected from a very porous, soil-free rock surface. However, in the case of the floodplains, moisture is available at the water table, which is likely to be within several metres of the surface in this case. This is unlikely to be true for many scree slopes in the catchment, beneath which the depth to water would be likely to be significantly larger and extremely difficult to predict. Nevertheless, over these drier surfaces it could be expected that β would be higher.

Table 5.6 Mean statistics for energy balance observations over the floodplain gravel surface.

	Q^* (MJ m^{-2} dy^{-1})	Q_H/Q^*	Q_E/Q^*	Q_G/Q^*	n (days)
MEB1 12-2-99	13.2	0.76	0.15	0.12	1
Class mean	13.2	0.80	0.11	0.11	3
Class σ	0.03	0.05	0.04	0.03	3

5.4 Lake surface

The area of lake surface in the study area is approximately 4 % of the total. However, lake surfaces have been found to have considerable impact on the local meteorology (Burba *et al.* 1999, Assouline and Mahrer 1996, McGowan *et al.* 1995, Sun *et al.* 1997). Studies of diurnal energy balances over water surfaces have generally found large Q^* magnitudes, due to small albedos and small L^* losses, as well as typically the largest portion of Q^* to be stored in the water volume (*e.g.* Burba *et al.* 1999). The remaining energy is used in evaporation, while Q_H is typically very small and often negative (Assouline and Mahrer 1996, Burba et al 1999). The energy balance of the lake surface was observed at two locations, MEB7 and MEB11 (Figure 3.1). Just 24 hours of data were available from MEB11, while five days of data were collected at MEB7, although approximately 30% of data were rejected from the latter site due to fetch limitations. Q^*, Q_H and Q_E were all estimated directly using an eddy covariance system, while ΔQs was determined as a residual from $\Delta Qs = Q^* - Q_H - Q_E$. The surface radiation budget presented in this section was observed on December 7, 1997, through hourly observations using handheld instruments to measure $K\downarrow$, $K\uparrow$, surface temperature, and air temperature and humidity. Observations were taken from the shore of a small island near the centre of Lake Tekapo. $L\downarrow$ was calculated using air temperature measured at 2 m and Eq. (2.11) and $L\uparrow$ was calculated using surface radiative temperature and Eq. (2.12). Q^* values used in the energy balance data were measured directly at the MEB7 and MEB11 sites.

Surface radiation budget

Hourly observations of surface radiation fluxes are presented in Figure 5.13a. Patches of cumulus cloud reduced $K\downarrow$ in the afternoon. Although the method used to determine $L\downarrow$ would underestimate values in cloudy conditions, the cloud coverage at these times was too small a fraction of the sky to impact significantly on $L\downarrow$. More than any of the land surfaces, the radiation budget of the lake surface was dominated by $K\downarrow$ (Figure 5.13c). The reason for this was the very low overall albedo and the low L^* loss due to the consistent and relatively similar temperatures of the air and water. The largest impact on the diurnal trace of Q^*, other than $K\downarrow$, comes from the diurnal variability of albedo (Figure 5.13b). This had a large diurnal range (~0.28), which equates to a range of 86 W m^{-2} using mean $K\downarrow$.

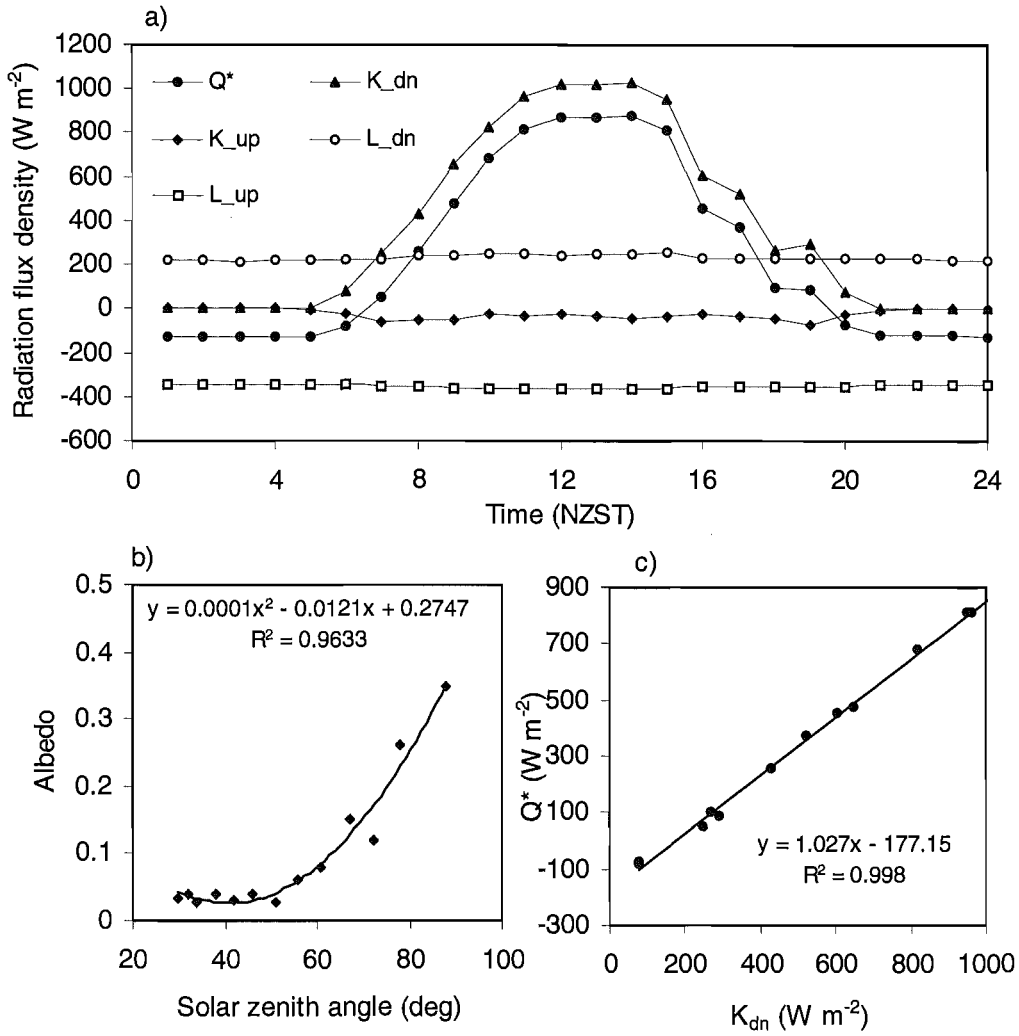

Figure 5.13 Mean hourly surface radiation budget components (a) and relationships between albedo and solar zenith angle (b) and Q^* and $K\downarrow$ (c) over the lake surface, December 7, 1997.

Surface energy balance

The diurnal plot of energy balance components and meteorological parameters for MEB7 on February 8 1999 (the same day presented for the nearby short-tussock surface) is presented in Figure 5.14. As with the water surface energy balance studies noted previously, most available energy in the diurnal cycle was stored in the lake volume (ΔQs), while Q_H was typically small and negative. Q_E also provided only a small sink for surplus energy although it increased through the day until 2100 NZST. The diurnal pattern of energy fluxes demonstrates that ΔQs is closely associated with Q^*, while Q_H and Q_E follow patterns more closely associated with diurnal airflow (Figure 5.14c). The meteorological data depict nocturnal drainage flow followed by a lake breeze shortly after sunrise with incursion of a channelled down valley flow from late afternoon. Q_E began to increase with the onset of the lake breeze and then doubled in magnitude during the afternoon northerly flow. It increased slightly in response to the cool, moist air advection in the lake breeze, but increased further in response to warm, dry air advection in the northerly flow. Despite this difference, Q_E appeared to respond positively to wind speed, irrespective of advected air mass properties.

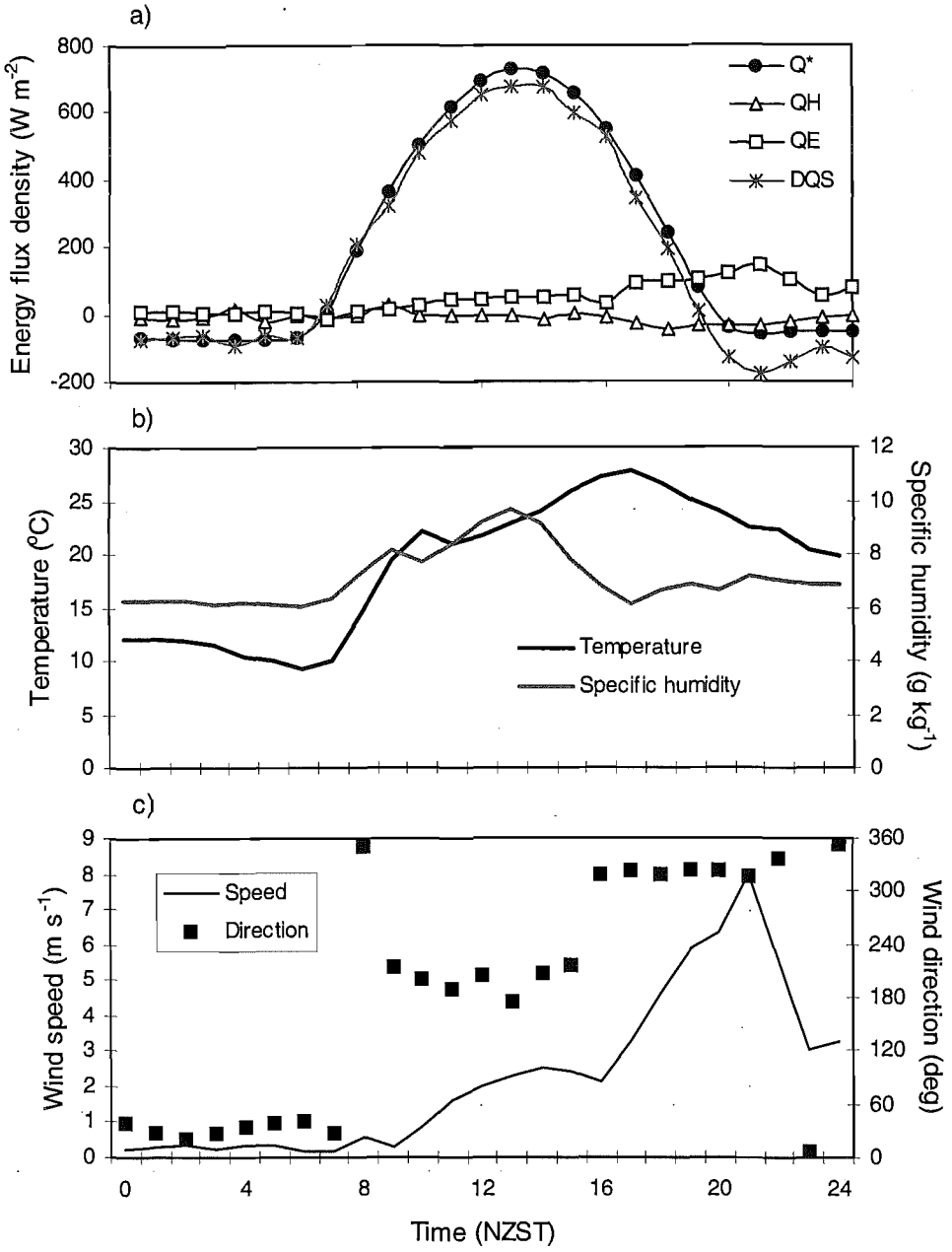

Figure 5.14 Mean hourly surface energy balance components (a) temperature and specific humidity (b) and wind speed and direction (c) at MEB7, February 8, 1999, where DQS is the change in energy stored in the lake body, calculated as a residual.

Considering the relationship noted above and the peak in Q_E after sunset, it is not surprising that neither Q_H nor Q_E showed any statistically significant relationship to Q^* (Figure 5.15). Conversely, Q_G was found to depend almost entirely on Q^*. In contrast, the relationship between Q_E and wind speed is statistically strong, and even Q_H shows reasonable dependence on wind speed. These results show that over the water surface, turbulent fluxes cannot operate effectively without wind. This is because of the lack of surface heat source for thermally generated turbulence, so turbulent transport is reliant on mechanical processes. At low wind speed, turbulent transport remains small because of the very short roughness length of the smooth lake surface. Once small waves develop, the roughness length of the surface increases rapidly as does turbulent transport. Since the temperature gradient in the surface layer is small and even negative, especially during the day, Q_H was similarly small or negative. In contrast, a significant

humidity gradient is likely to exist at all times and it is simply a matter of providing the transport mechanism in order for evaporation to occur. Furthermore, energy is constantly available since at night, the large supply of energy stored in the lake during the day can be used for evaporation. The relationship illustrated in Figure 5.15e, when calculated for all observed wind speeds near the lake, speculates that evaporation rates of up to 775 W m^{-2} could occur during the strongest northwest winds observed during the summer (35 ms^{-1}). In fact, during such events, lake water was observed to be lifted several tens of metres into the air above the lake surface by large turbulent eddies.

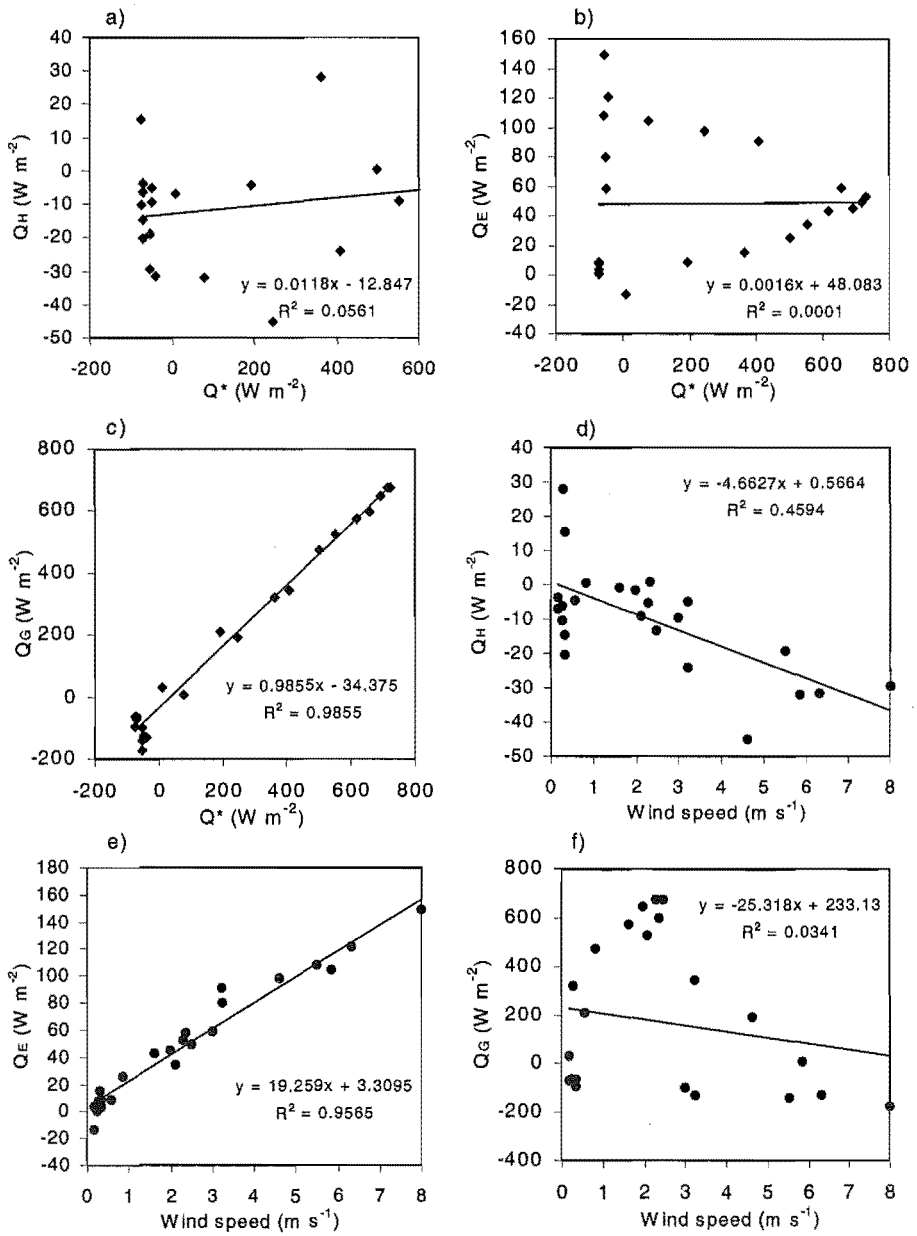

Figure 5.15 Relationship between mean hourly Q^*, wind speed and energy balance components at MEB7, February 8, 1999.

Lake surface mean statistics

The mean statistics for the case presented above, as well as the two sites and the overall lake surface class is presented in Table 5.7. The values of Q_H were very consistent between sites and days, while the partitioning between Q_E and ΔQ_S differed somewhat more, probably as a function of wind speed. For example, the MEB11 site was located

directly west of Tekapo Saddle and was therefore exposed to the strong easterly airflow in the afternoon, when the highest Q_E values were recorded. Because of this, significant spatial variability over the lake surface is likely. Based on the observations presented here, this variability is likely to represent at least 7% of Q^* for Q_E and 14% for ΔQ_S. Further variability is likely to occur as a function of advection. MEB7 and MEB11 were both located on the lake edge. Therefore, in order to obtain a "lake" footprint for source data, only onshore winds could be used. Because of this, airmass parameters were influenced to a large extent by the lake climate. If a station was located a sufficient distance offshore to measure lake surface fluxes during offshore flow, it is expected that Q_E fluxes would be larger and Q_H more strongly negative during the day than observed here due to warm, dry air advection from the land surface. A study designed to examine the influence of this advection found variability up to 100% between stations at either side of a subtropical lake with hot and dry air advection across the lake surface (Assouline and Mahrer 1996). In general, the value for Q_E was small compared with other lake surfaces (e.g. Burba *et al.* 1999, Assouline and Mahrer 1996). This is likely to be a function of the significantly warmer surface temperatures of the lakes in those studies. For example, Sun *et al.* (1997) found a consistent increase in Q_E over a lake surface warming from spring to autumn.

Table 5.7 Mean statistics for energy balance observations over the lake surface.

	Q^* (MJ m^{-2} dy^{-1})	Q_H/Q^*	Q_E/Q^*	$\Delta Qs/Q^*$	*n* (days)
MEB7 8-2-99	18.1	-0.05	0.23	0.82	1
MEB7 mean	18.1	-0.02	0.11	0.92	5
MEB11 mean	20.2	-0.07	0.36	0.71	1
Class mean	18.5	-0.03	0.24	0.79	6
Class σ	2.67	0.03	0.07	0.14	6

5.5 Comparing energy balances of surface cover classes

The five classes of surface cover that dominate the surface area of the Tekapo catchment have been examined with regard to surface radiation and energy balance behaviour during anticyclonic summer days. The purpose of this section is to pool these findings in an intercomparative assessment of the range of energy flux densities associated with heterogeneity of surface cover. This is assessed with regard to firstly, surface radiation budgets and secondly, surface energy balances.

5.5.1 Surface radiation budgets

All other things being equal, the difference in surface radiation budgets between different surface types relates to the radiative properties of each type, including absorption, reflection and emission. In this study, the influence of topographical differences between sites exists, although where possible, horizontal, open areas were selected for this comparison. Furthermore, different days are compared, thereby incurring errors associated with small differences in meteorology, and solar paths between days. However, these problems are small enough that the radiative differences between surfaces are evident.

Figure 5.16 presents comparative daily totals of radiation flux densities observed in the five cases presented earlier, as well as some ratios that help to normalise the comparison between cases. The effect of different days and topography can be observed in the $K\downarrow$ values, which would be equal in an ideal study of the role of surface cover.

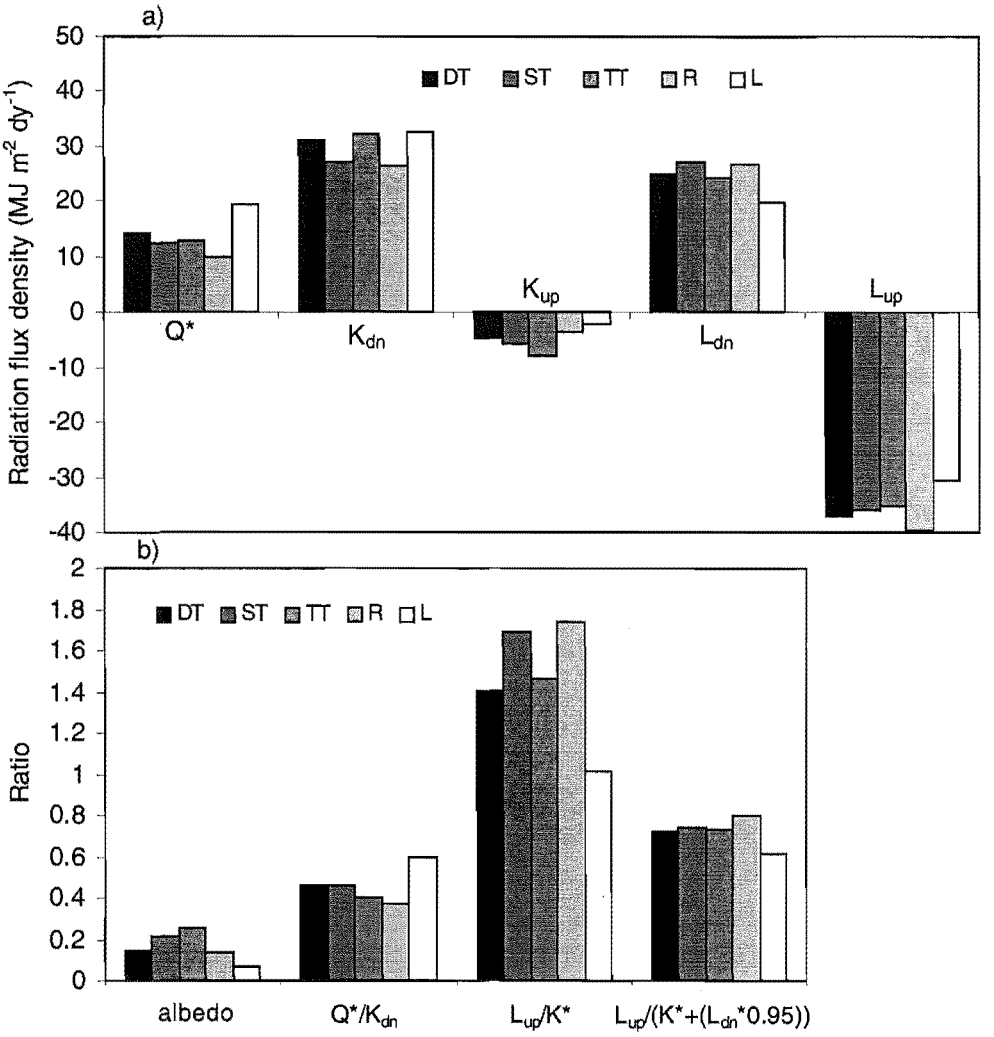

Figure 5.16 Mean daily totals of radiation budget components (a) and ratios of components (b) for five surface types during summer anticyclonic days; DT = degraded tussock; ST = short tussock; TT = tall tussock; R = rock surface; L = lake surface.

All cases but the lake surface were recorded within a 10-day period, making differences due to solar paths minimal. The lake case was recorded closer to the summer solstice, but $K\downarrow$ was reduced by some patches of afternoon cloud, cancelling some of this gain. Several sites were influenced by topography. A slight northerly aspect at the tall tussock site enhanced $K\downarrow$ values, while early sunsets at the rock surface and short tussock sites diminished $K\downarrow$ values. $L\downarrow$ was similarly affected by topography, with the highest values occurring at the rock surface and short tussock sites, which had the smallest sky view factor. The cooler air over the lake surface produced the lowest $L\downarrow$ of the surface classes. The variability of surface temperature between classes is evident in the $L\uparrow$ values. The rock surface reached the highest values, while the density of vegetation can be seen to have a negative influence on surface heating and the cool lake surface (~12°C) emitted the lowest magnitude of radiative energy. The range of $L\uparrow$ over the five classes was 9.2 MJ m^{-2} dy^{-1}, which equates to 26% of the mean.

Albedo values were lowest over the water surface, followed by rock and degraded tussock (Figure 5.16b). Highest mean albedos were recorded over tall tussock, followed by short tussock. Although the colour of these two classes was quite similar, tall tussock provided a denser canopy than short tussock, which presented more sub-canopy groundcover and soil to incoming radiation. The range in mean albedos was 0.19, which equates to a range in $K\uparrow$ of 6.0 MJ m^{-2} dy^{-1} or 20% of mean $K\downarrow$. However, the influence of albedo on Q^* is often countered by the fact that typically, the more $K\downarrow$ that is absorbed (lower albedo), the more surface heating occurs and the greater the loss from $L\uparrow$. Normalising the effect of albedo by the ratio $L\uparrow/K^*$ allows us to evaluate the ability of the surface to re-emit absorbed shortwave radiation in the thermal waveband. The rock surface clearly dominated in this ratio, with significantly low water surface emission of $L\uparrow$. This is because much of $K\downarrow$ is transmitted down into the water column before being absorbed, convective and advective transport results in significant mixing and water has a large heat capacity. Furthermore, the water volume is continually supplied by cold glacial melt water from the catchment headwaters, maintaining a cool surface temperature (~10 °C) and consequently relatively low L↑. Short tussock was also high in this ratio, although it is notable that this surface also received the largest $L\downarrow$ contribution. To account for $L\downarrow$, the ratio of $L\uparrow$ to all radiation absorbed at the surface was used; $L\uparrow/(K^*+L\downarrow\varepsilon)$, where ε was approximated by 0.95. With this ratio, the vegetated surfaces merged closer together, while the lake surface showed a larger net gain and the rock surface a smaller net gain of radiation in the 24 hour period. The pattern of this ratio therefore, is inverse to the pattern of Q^* in Figure 5.16a, since it shows the ability of the surface to re-emit the energy it has gained.

The variation of daily total Q^* over the five surface classes illustrates the importance of both albedo and the ratio of emitted longwave to absorbed shortwave radiation. For example, since the lake surface was lowest in both these ratios, Q^* was the highest (by an average of 36%). This pattern also reflects, to a small extent, the importance of topography. The loss of $K\downarrow$ due to topographic shading was compensated to some extent by higher $L\downarrow$ values, since the surrounding terrain was warmer than the clear atmosphere. The impact of topography on the radiation balance is evaluated in considerably more depth in the following chapter. The range in Q^* associated primarily with surface cover was 9.6 MJ m^{-2} dy^{-1}, which amounts to 70% of the all-class mean.

A comparison of the extent of diurnal albedo variability among the five surfaces is provided in Figure 5.17. All surfaces showed a positive relationship between solar zenith angle and albedo. The largest range occurred at the water surface, and the smallest occurred over degraded tussock, although the range at the rock surface was only marginally greater than degraded tussock. These findings are important to this study because they represent not just a range of albedo by day, but also a range of albedo by space. The large variation in slope angle and aspect that exists in the Tekapo catchment means that a range of albedo of these magnitudes exists over the catchment surface at any given time. Furthermore, the effective zenith angle to a sloping surface can be reduced to zero when the incident angle of $K\downarrow$ is normal to the slope, thereby increasing the range of albedo across the terrain. The exception to this rule occurs with the water surface, which also has the largest range. For all other surfaces, the potential impact of topographically controlled variability in albedo is even greater than the range in albedo implies. This is because, during the hours when albedo changes most dramatically over horizontal surfaces, $K\downarrow$ is typically small, reducing the actual range of $K\uparrow$. However, over complex terrain, the range of albedo can be applied at all times,

including when $K\downarrow$ is at a maximum, thereby significantly increasing the role of the albedo/solar angle relationship on the surface radiation budget.

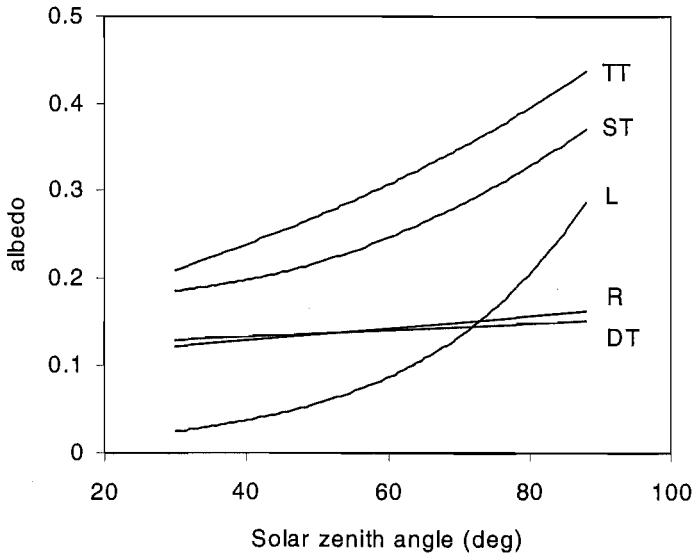

Figure 5.17 Relationship between solar zenith angle and albedo for five surface types during summer anticyclonic days; DT = degraded tussock; ST = short tussock; TT = tall tussock; R = rock surface; L = lake surface.

5.5.2 Surface energy balance

The previous section has illustrated the importance of surface cover on the radiation budget and the range in Q^* that results. This section compares the five classes with respect to the mean diurnal partitioning of Q^* among the three major energy balance components. Figure 5.18 illustrates the mean energy partitioning of the five surface classes. In each of the four land surfaces, Q_H dominated the daily Q^* surplus, illustrating the general dryness of the local climate. Of the four surfaces, the largest magnitudes of Q_H were transported into the atmosphere over rock and degraded tussock surfaces. A positive relationship existed between Q_E and vegetation size and density. Furthermore, longer-term soil moisture data show a positive relationship between vegetation size and density and soil moisture content (Table 5.8). Since soil moisture varied considerably throughout the year, the standard deviation of the proportion of these values to the mean for all vegetated surfaces was used to assess the consistency of these differences. When compared with the mean ratios, the standard deviation values suggest that these differences were representative throughout the study period.

There appear to be two inter-related reasons for the relationships between soil moisture, vegetation and Q_E. Firstly, the smaller and less dense the vegetation is, the less water is able to be conserved in the soil/plant system. Data presented in Table 4.5 shows that little rainfall becomes available for evaporation at the degraded tussock site, probably because of low plant density and lack of rooting zone. Under tall tussock, soil development is likely to be significantly better, allowing greater soil moisture retention. Therefore, it can be expected that, during very dry conditions, such as occurred in the Tekapo catchment during this observation period, moisture will be severely depleted at the less densely vegetated surfaces and consequently, Q_E would be lower. Secondly, the relationship between soil moisture and vegetation in the catchment also reflects hydrological controls on ecosystem location. For example, the dry, frost-heaved,

shallow and stony soils, with sparse tussock vegetation (degraded tussock), exists in the driest areas of the catchment. Although other factors are likely to have significant influence, such as rabbit infestation, burning or grazing of livestock, many of these are inter-related and tussock is more likely to become marginalised where moisture stress is highest, despite their high conservation of moisture. Tall tussock appears to exist at higher elevations and toward the main divide, which corresponds with higher rainfall. However, this also partly describes a zone with a relatively high frequency of soil disturbance by rapid and dynamic geomorphological processes. Since tall tussock species in high density provide a significant resistance to evaporation, their development provides a positive feedback for soil moisture.

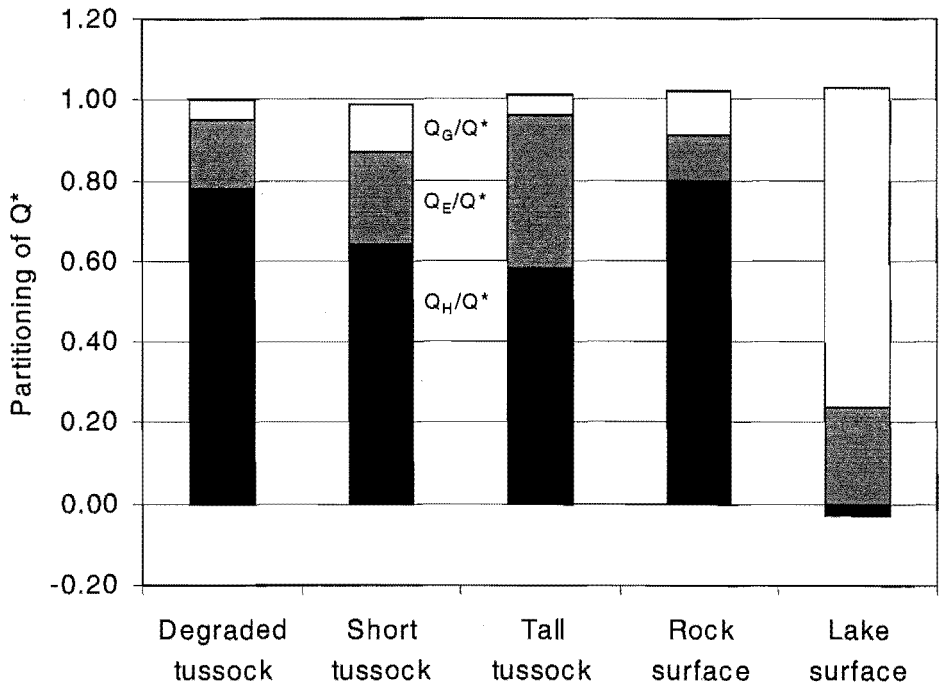

Figure 5.18 Mean daily energy partitioning of Q^* between energy balance components for five surface types during summer anticyclonic days.

By comparison to the land surfaces, the lake surface transported most daily surplus surface radiation into the lake volume, a small amount was lost to evaporation, and Q_H provided a small contribution to daily available energy due to warmer air overlying the cool lake surface.

Table 5.8 Mean soil moisture content for each vegetated surface class, as well as mean and standard deviation of the ratio of soil moisture for each class to the mean of the three classes, from a record representing 17 samples each from 11 sites, obtained intermittently between November 1997 and April 1999.

n=17	Soil moisture content (%volume)	Soil moisture content as proportion of mean for vegetated surfaces	Standard deviation of proportion of mean soil moisture content
Degraded tussock	11.24	0.56	0.17
Short tussock	20.32	1.05	0.20
Tall tussock	24.01	1.39	0.21

In order to compare the dominant control on energy component magnitudes, Table 5.9 presents r^2 values for linear regression between energy components and Q^* and wind speed, as well as multiple regression using both Q^* and wind speed. These results differ from those presented with the case studies because they include all available 30-minute data for each surface class. The three vegetated surfaces show strong relationships between Q^* and Q_H. For degraded and short tussock the relationship is strengthened marginally with the addition of wind speed in multiple regression. The same three classes show a positive relationship between vegetation size and dependence of Q_E on Q^*. This is thought to be the result of plants controlling moisture levels in the soil and due to stomatal control of evapotranspiration. Similarly, Q_G was controlled most strongly by Q^* over the vegetated surfaces, with degraded tussock proving the weakest because of the diurnal asymmetry between Q_H and Q_G at this site. Indeed, although the relationship with wind speed is not significant, it is the only vegetated surface to improve by any margin in multiple regression.

Table 5.9 Comparison of linear relationships (r^2 values) between energy balance components and Q^* and u respectively, as well as multiple regression (mult) using both Q^* and u, based on 30 minute mean data (see Table 5.1 for specific dates and times).

Q_H	Q^*	u	mult	n
Degraded tussock	0.977	0.073	0.982	179
Short tussock	0.949	0.018	0.950	545
Tall tussock	0.974	0.006	0.974	96
Rock	0.836	0.458	0.919	237
Lake	0.013	0.324	0.365	280
Q_E				
Degraded tussock	0.476	0.017	0.550	179
Short tussock	0.615	0.003	0.616	545
Tall tussock	0.969	0.012	0.969	96
Rock	0.526	0.110	0.577	237
Lake	0.085	0.568	0.572	280
Q_G				
Degraded tussock	0.870	0.005	0.884	179
Short tussock	0.948	0.008	0.949	545
Tall tussock	0.943	0.013	0.943	96
Rock	0.952	0.045	0.957	237
Lake	0.958	0.003	0.968	280

The energy balances of rock surface and degraded tussock appear to behave similarly. The relationship between all three fluxes and Q^* is significant, with Q_E being the weakest. Furthermore, wind speed showed some control on the fluxes and Q_H and Q_E correlations were particularly improved with incorporation of wind in multiple regression. Conversely, the lake surface showed a very weak relationship between Q^* and the turbulent fluxes, which were more strongly controlled by wind speed. This was particularly the case for Q_E, which on some days showed a very strong relationship with wind speed, as was shown for February 8, 1999 in Figure 5.15

5.5.3 The effect of soil moisture

In the previous section, a link was suggested between plant type, size and soil moisture. Furthermore, the link between soil moisture and the Bowen ratio (β) was considered for different times at a single site in Chapter Four, establishing a strong negative logarithmic relationship. This section considers this relationship from a spatial perspective, although as with the temporal study, relatively few concurrent data were available. Figure 5.19 illustrates the relationship between β (ratio of daily flux totals) and soil moisture content for five days over different vegetated surfaces.

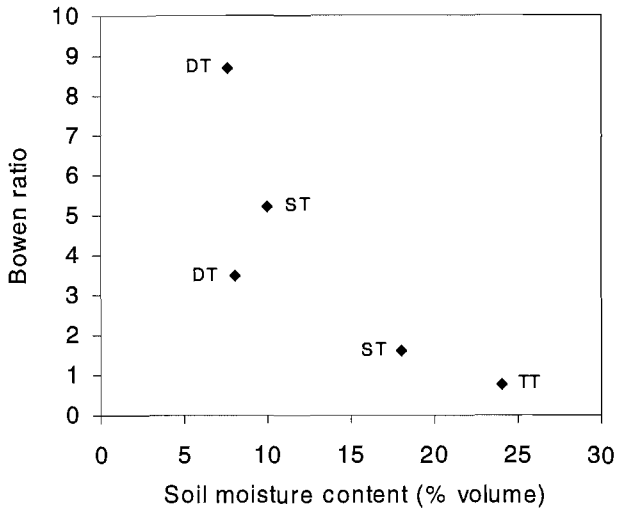

Figure 5.19 Relationship between volumetric soil moisture content and daily integrated β for five surface types during summer anticyclonic days; DT = degraded tussock; ST = short tussock; TT = tall tussock.

A negative logarithmic trend was derived from these data as with the earlier temporal study (Figure 4.15). However, the coefficient of determination is lower due to the smaller sample size of the data representing different locations. Nevertheless, a similar trend is observed in both spatial and temporal controls of β by soil moisture content. Furthermore, the data set that includes the three vegetation types is not as steep as the data set that includes just degraded tussock. This result suggests that short and tall tussock surfaces limit evaporative loss more significantly than degraded tussock given the same soil moisture levels. This is consistent with Campbell's (1989) finding that tussock grasses play a significant role on water conservation through stomatal resistance.

5.6 Summary

The purpose of this chapter was to evaluate the magnitude of spatial variability in surface energy and radiative exchanges that result primarily from heterogeneity of surface cover. Diurnal surface radiation budgets and energy balances were examined during anticyclonic summer conditions over the five most dominant surface types in the Tekapo catchment; degraded tussock, short tussock, tall tussock, rock and lake surfaces.

The lake surface recorded the highest daily total Q^* values of the five surface types, the rock surface recorded the lowest, and the three vegetated surfaces recorded very similar flux densities. Although some variability was associated with topographical differences

between the sites, the main influences were the radiative properties of the surface. In particular, mean diurnal albedo and the ratio between $L\uparrow$ and absorbed allwave radiation accounted for the differences observed in daily radiation budgets. Diurnal changes in albedo were found to correlate closely to solar zenith angle, with large variability in this relationship between different surfaces. The lake surface showed the largest range, although both short and tall tussock had significant ranges, while degraded tussock and rock surfaces varied minimally. In all cases, the relationship between Q* and $K\downarrow$ was statistically significant. Overall, a large range in Q^* was observed, illustrating the importance of these radiative properties for the surface energy budget.

The partitioning of Q^* into Q_H, Q_E and Q_G was also found to vary significantly due to properties of the surface cover. The highest β was observed over the rock surface with decreasing β found over degraded tussock, short tussock and long tussock respectively. A positive relationship was established between plant species, soil moisture and evapotranspiration, illustrating both the hydrological controls on species location and the ability of tussock species to conserve water through stomatal control. By contrast, the lake surface partitioned most available energy into storage in the lake, with small Q_E and slightly negative Q_H. A relationship was established between soil moisture content and β over five vegetated surfaces that was similar to the relationship observed for degraded tussock at different times, although a lack of data impedes the confidence in this finding. The regression gradient was found to be lower when it included the short and tall tussock surfaces, suggesting they had some control on limiting potential Q_E through stomatal resistance. Statistical analyses of the relationship between energy components and Q^* and wind speed revealed the strong dependence of energy components on Q^* over short and tall tussock species. Degraded tussock and rock surfaces showed weaker dependence on Q^* with some (albeit small) relationship with wind speed. This reflected the importance of wind speed for turbulent transfer over surfaces with short roughness lengths, small moisture supplies and lack of physiological controls of vegetation. In contrast, the lake surface showed virtually no relationship between turbulent fluxes and Q^*, while a significant relationship existed with wind speed. Conversely, ΔQs was found to depend almost entirely on Q^* over the water surface.

These results show that surface cover yields considerable control over the magnitude of surface energy exchanges in heterogeneous terrain. The variability associated with surface cover is controlled by the radiative properties of the surface as well as its control over soil moisture, its heat capacity and roughness length. Location was of secondary importance to the surface energy balance, playing a role through advection, both in terms of turbulent transfer (wind speed) and airmass characteristics (temperature and humidity).

Chapter Six:

Spatial modelling of surface radiation components

6.1 Introduction

This chapter considers the spatial controls on the surface radiation budget in the Tekapo catchment for clear-sky conditions, based on mathematical modelling of surface radiative fluxes. The purpose is to examine the relative strengths of the parameters that control spatial variability of surface fluxes in the Tekapo catchment. To this end, sensitivity analyses are presented for each of the dominant controls, including elevation, slope characteristics, shading effects and the radiative properties of the surface. Results are presented from simulations of diurnal fluxes during a mid-summer day in clear-sky, anticyclonic conditions. Initially, the chapter provides an overview of the modelling procedures used in this study and the data used to initialise simulations. The following sections consider shortwave, longwave and net radiation components respectively. Sensitivity analyses are presented for the role of dominant parameters in the spatial variability of these components including elevation, slope properties, leaf area and topographic shading. This is concluded by an evaluation of model performance and discussion of the role of topographic complexity on both the spatial mean and variability of radiative fluxes.

6.2 Model overview

The surface radiation model presented in this chapter was generated from SRAD (Gallant 1997), a FORTRAN based program that determines solar irradiance and fluxes of longwave radiation over a surface generated by a digital elevation model (DEM). Potential incident solar radiation is calculated as a function of latitude, slope angle and aspect, topographic shading, time of year and hour angle based on the formulae of Kondratyev (1977), which were discussed in Section 2.2.1. Temperatures are extrapolated across the surface from observations at a single station using a method based on Running *et al.* (1987), Running (1991) and Running and Thornton (1996).

This method corrects for temperature changes with elevation via a lapse rate, slope aspect effects via a shortwave radiation ratio, and vegetation effects via a leaf area index (*LAI*). Outgoing longwave radiation is calculated from surface temperature and incoming longwave irradiance is calculated from air temperature and the fraction of sky visible at each grid point (sky view factor, *v*). Net radiation is then calculated for each grid point by:

$$Q^* = K\downarrow(\alpha - 1) + L\downarrow - L\uparrow \qquad (6.1)$$

where α is albedo. The DEM, *LAI* and α values are all input as georeferenced surface grids in order to describe the spatial variability of topographic and surface properties. The procedures used to calculate individual fluxes and the input parameters are discussed in more detail in subsequent sections. Methods used in SRAD and its applications are also discussed by Moore *et al.* (1993), Wilson *et al.* (1996), Gallant (1997), Wilson and Gallant (2000).

Model runs were conducted for February 12, 1999. This day was selected because clear skies and weak synoptic pressure gradients produced strong diurnal heating and cooling and locally generated thermal circulations. This day was also an intensive observation day during the Lake Tekapo Experiment (LTEX), so maximum data were available for initialising the model and evaluating its performance.

6.2.1 Topographic modelling

A DEM was generated for the Tekapo catchment with 100 m grid point spacing from 20 m interval contour data and hydrological information for lake levels. From the DEM, slope angle and aspect are calculated in SRAD with a central finite difference scheme (Wilson and Gallant 2000). The DEM and slope angles for the study area are illustrated in Figure 3.2 and the spatial distribution of slope aspect is shown in Figure 6.1. Since the major terrain features run approximately from north to south, there is a large area of east and west-facing slopes and a much larger area of south than north-facing slopes. A larger area of west than east-facing slopes also exists due to the expansive gentle slopes that bound the east of the catchment.

The distribution of grid points over the ranges of elevation, slope angle and slope aspect are provided in Table 6.1. The distribution of elevation and slope angle areas show a very similar pattern. Despite a large range in both parameters, approximately half of the area is in the lowest 400 m (500 to 900 masl), with a slope angle of less than 10°. There is a rapid but fairly constant decrease in the areas of higher elevation and slope angle classes.

The one-dimensional horizon algorithm of Dozier *et al.* (1981) is used to estimate the fraction of the sky hemisphere visible at each grid point. This algorithm constructs profiles across the DEM and determines the horizon angle for each grid point in a discrete number of directions. For this study, 16 divisions of the horizon were used to calculate the sky view factor. The information derived from this process was also used to calculate shading effects from surrounding terrain at discrete time intervals during the diurnal cycle.

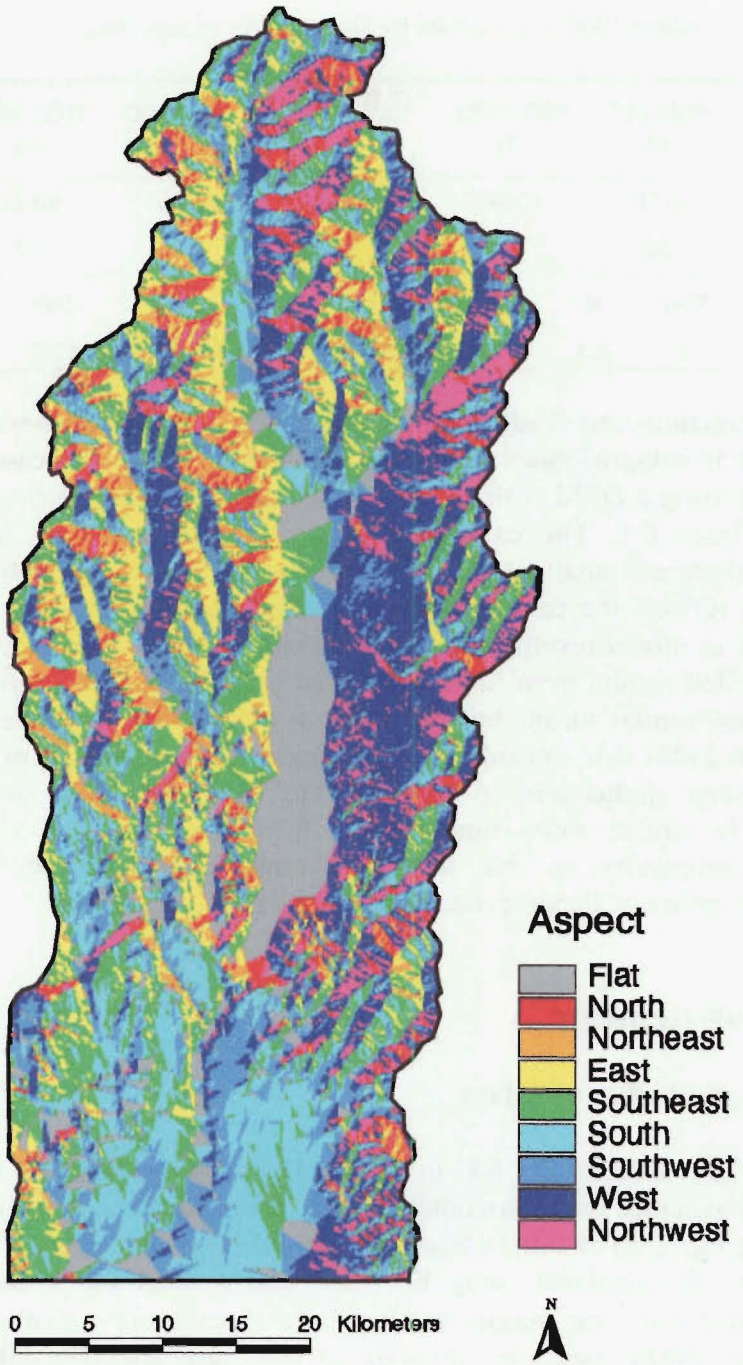

Figure 6.1 Map of slope aspect divisions in the Tekapo catchment, derived from a 100 m resolution DEM, where 'flat' is classified by slope angles of less than 1°.

The accuracy of DEMs has been found to vary considerably, although Stocks and Heywood (1994) concluded that the standard error is of the order of half the contour interval. The importance of this error is dependent on the purpose of the DEM. Wadge (1988) suggested that, compared with applications such as slope stability assessment, where slope angle is a critical model parameter, slope energy balance models are less sensitive to individual grid point values. However, while this may be true for the cosine law of illumination (Eq. 2.6), strongly non-linear effects such as the casting distance of a shadow will yield significantly greater error.

Table 6.1 Areal distribution of elevation, slope angle and slope aspect in the Tekapo catchment, where 'flat' is classified by slope angles of less than 1°.

Elevation (masl)	500-900	900-1300	1300-1700	1700-2100	2100-2500	2500<
Area (%)	45	19	18	14	03	001
Slope angle (°)	0-10	10-20	20-30	30-40	40-50	50<
Area (%)	50	14	16	17	03	002

Slope aspect	Flat	N	NE	E	SE	S	SW	W	NW
Area (%)	9	2.1	2.2	6.6	12.8	16.7	17.7	14.8	18.1

Both sky view fractions and shading parameters produce errors near domain boundaries since no terrain is acknowledged outside of these limits. For this reason, simulations were conducted using a DEM with an area 44% larger than the Tekapo catchment area portrayed in Figure 6.1. The calculated values for the catchment area were then extracted for subsequent analysis and presentation. The spatial resolution selected for this application reflects the compromise between identifying landscape elements at a scale influential to model results and computational expense. McKenney *et al.* (1999) compared modelled results from SRAD using 20 m and 100 m resolution DEMs. The outputs displayed similar means but the range of estimates was greater for the 20 m DEM. They concluded that, considering computational expense, 100 m resolution was sufficient for many applications in their 900 km^2 study area. The study area in the present study is almost three times larger than this, but also contains greater topographical complexity so that a larger compromise must be made between computational expense and appropriate representation of the surface.

6.3 Shortwave radiation

6.3.1 Incident shortwave radiation

The procedure for calculating $K\downarrow$ in clear skies follows several steps. Initially, extraterrestrial irradiance on a horizontal surface just outside the Earth's atmosphere is calculated using Eq. (2.2) and (2.3). Secondly, irradiance on a horizontal surface at each DEM grid point is calculated using Eq. (2.4) and a local transmission coefficient (discussed shortly). For zenith angles greater than 60°, values of optical path lengths are taken from List (1968) since the curvature of the Earth unrealistically inflates path lengths at angles greater than this (Kondratyev 1977). The portion of direct beam irradiance (K_S) transformed into diffuse beam (K_D) radiation in the atmosphere is calculated using Eq. (2.5). This is then divided into circumsolar and isotropic portions using a circumsolar coefficient after Linacre (1992). Isotropic K_D is modified by the sky view factor for each grid point (Eq. 2.8), while circumsolar K_D and K_S are calculated for sloping surfaces using Eq. (2.6) and (2.7). The grid points with and without shading at each interval are then determined and circumsolar K_D and K_S are removed from shaded grid points. The contribution of reflected shortwave radiation (K_r) arriving at each grid point is also determined using:

$$K_r = (K_{dirh} + K_{difh})(1 - v)\alpha \qquad (6.2)$$

where K_{dirh} and K_{difh} are direct and diffuse beam irradiance respectively and v is the sky view factor. This series of calculations is repeated for each of the DEM grid points at 12-minute intervals from sunrise to sunset.

The diurnal mean modelled $K\downarrow$ for February 12 over the catchment surface is presented in Figure 6.2. There is a large range of values (450 W m^{-2}), although the standard deviation is only 10% of this due to the large distribution of grid points near the mean (299 W m^{-2}). Highest flux densities can be found on high altitude, north-facing slopes of moderate angle, while smallest fluxes occur on steeper south-facing slopes.

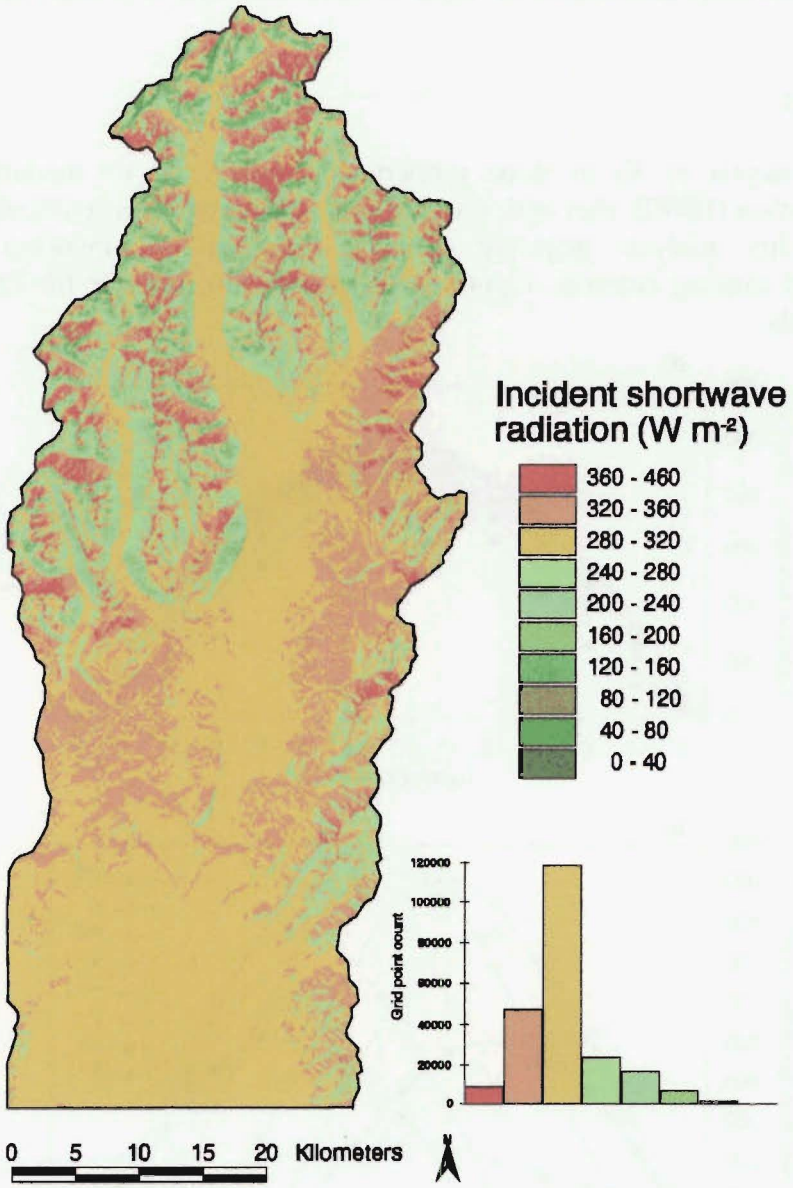

Figure 6.2 Map of modelled $K\downarrow$ in the Tekapo catchment for February 12, 1999, including a histogram of grid point values.

The distribution of flux densities shows that approximately 50% of grid points fall within a narrow range (280-320 W m^{-2}) due to the equally large distribution of nearly flat grid points over the study area (Table 6.1). Qualitatively, Figure 6.2 illustrates the importance of slope properties, elevation and topographic shading on $K\downarrow$. The relative importance of these controls is quantified in the following sections.

Elevation controls

Since optical transmissivity increases with elevation due to reduced path length and atmospheric aerosols, an optical transmissivity lapse rate must be defined for the model domain. The lapse rate used in this study was 0.0008 m^{-1} after Gates (1980), and the reference transmissivity value was taken from the mean (pre-Pinatubo) values recorded at the Mt John observatory and reduced to sea level via the lapse rate. Estimated prior to the calculation of slope effects, the range in elevation in the Tekapo catchment generates a spatial range in mean $K\downarrow$ of 85 W m^{-2} but a standard deviation of only 18.2 W m^{-2} since elevation distribution in terms of catchment area is strongly skewed toward lower values.

Slope effects

Sensitivity analysis of K_S to slope properties is conducted by modelling K_S at a reference location (BREB site) with the range of slope properties found throughout the catchment. This analysis therefore, isolates slope effects, ignoring elevational, locational and shading controls. Figure 6.3 illustrates this analysis for February 12 at hourly intervals.

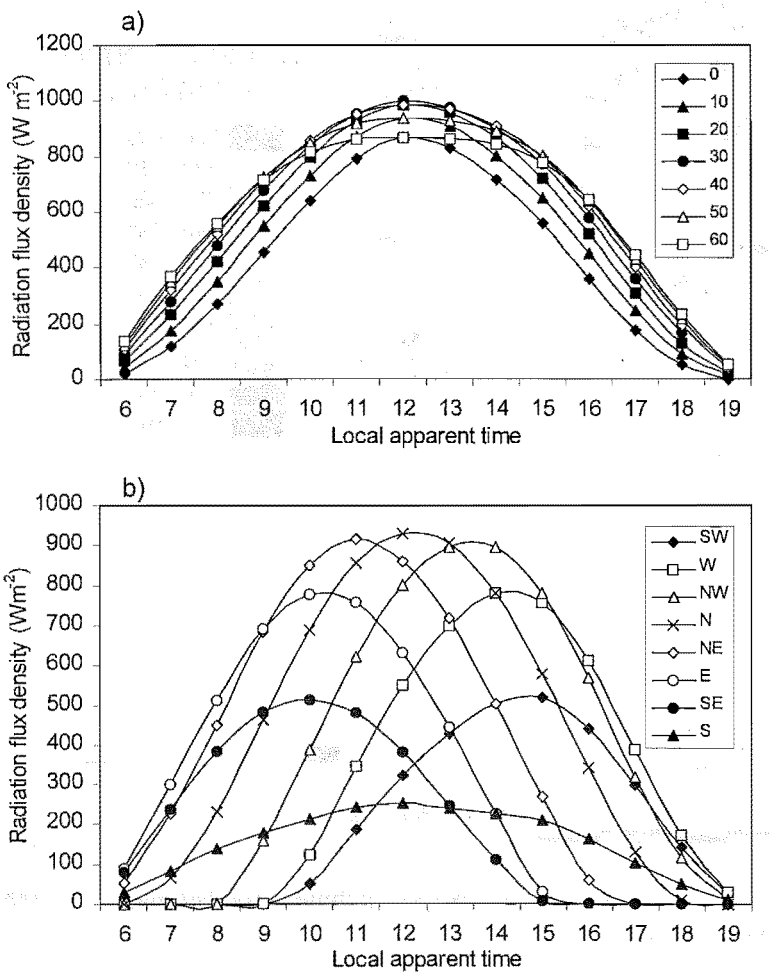

Figure 6.3 Modelled hourly direct beam $K\downarrow$ for a single grid point in the Tekapo catchment for February 12, 1999 showing sensitivity to a) slope angle where aspect is always sunward and b) slope aspect where angle is always 45°.

Figure 6.3a compares hourly daylight flux densities from slope angles of 0 to 60° while considering an aspect always to be facing toward the sun. For most of the day (at higher zenith angles) irradiance generally increases with an increase of slope angle. This is least true during the middle of the day when the zenith angle reaches its diurnal minimum of 30°. However, direct beam radiation reaching the surface is greatest in the middle of the day when the optical path length is smallest. Accounting for this by averaging hourly values over the daylight period, the optimum slope angle for maximum K_S is 45°. This is consistent with Oke (1987) for a northern hemisphere mid-latitude site. The range in values remains fairly constant with a daylight mean range of 195 W m^{-2}, or 33% of the daylight mean irradiance value. The optimum slope angle of 45° was then used as a constant to evaluate the effect of slope aspect (Figure 6.3b). The range in values as a function of aspect is large throughout the day and integrated over daylight hours is 274 W m^{-2} (91% of the mean). Of the two parameters then, slope aspect has a greater control on K_S at the surface than slope angle, although both generate considerable variability in the overall radiation budget.

Figure 6.4 illustrates the combined controls of surface aspect and slope angle when averaged over the daylight period of February 12. In this case, surface irradiance is optimised when north facing with a slope angle of 26°. This reduces rapidly towards the south and higher slope angles (with an overall spatial range of 410 W m^{-2}).

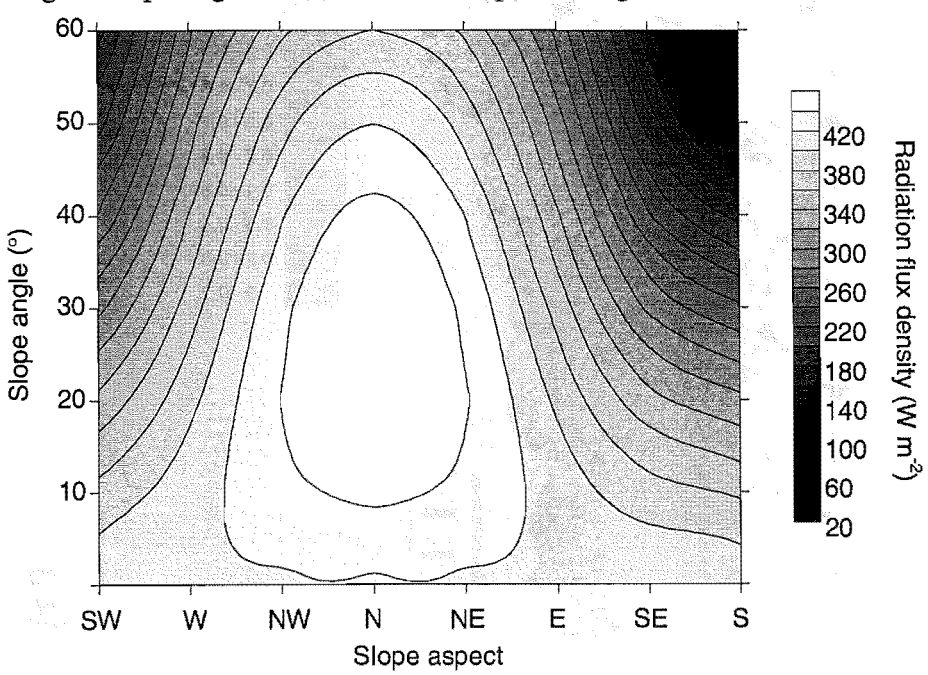

Figure 6.4 Modelled diurnal mean direct beam $K\downarrow$ for a single grid point in the Tekapo catchment for February 12, 1999 showing sensitivity to both slope angle and aspect.

In order to ascertain the spatial distribution of slope influence on $K\downarrow$, a shortwave radiation ratio (S) can be established for each grid point by:

$$S = \frac{K_{ts}}{K_{th}} \tag{6.3}$$

where K_{ts} and K_{th} are total $K\downarrow$ on sloping and horizontal sites, respectively. Generating S for the catchment allows the influence of slope properties to be assessed independently of elevation controls. Figure 6.5 maps S over the catchment surface. A relatively large range exists throughout the catchment with values both greater and less

than unity. However, the vast majority of values are clustered close to unity since the distribution of slope angles is skewed toward smaller values (Table 6.1). The fact that this finding is very similar to that of $K\downarrow$ overall (Figure 6.2), illustrates the strong control of slope properties. Furthermore, a relationship appears to exist whereby an increase in topographic complexity results in an overall decline in S and an increase in its spatial range. This hypothesis is tested more rigorously in Section 6.7.

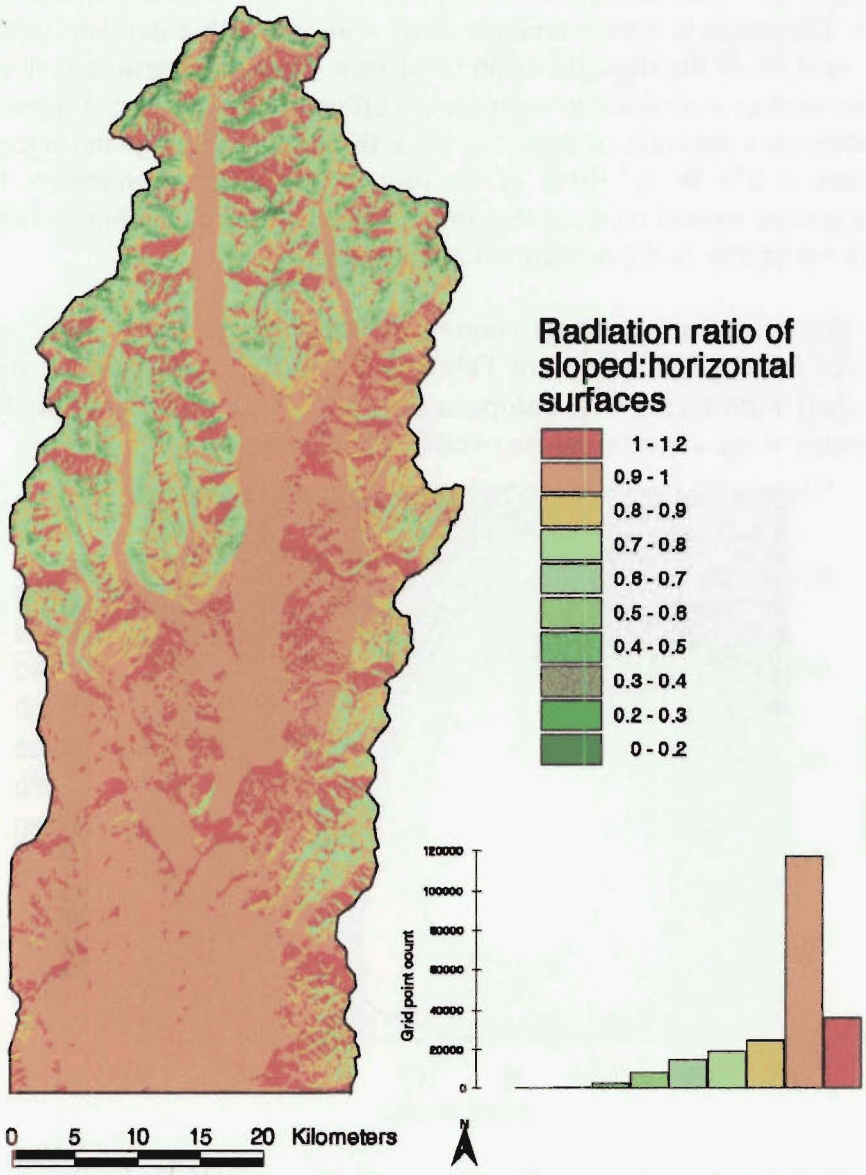

Figure 6.5 Map of modelled radiation ratio (S) in the Tekapo catchment for February 12, 1999.

Shading effects

Figure 6.6 illustrates the extent of shading from surrounding terrain at five times of the day (February 12). In the early morning and late afternoon, a large proportion of the surface area is influenced by shading. In the middle of the day, mid-morning and mid-afternoon, the coverage of shading is significantly reduced due to the lower zenith angle of the sun and due to the approximate north-south orientation of the main valley systems. The shaded area is also smaller in the late afternoon than early morning, due to

the smaller spatial extent of high terrain on the western side of the catchment. At all hours, shading is most extensive in the steeper and higher terrain to the north.

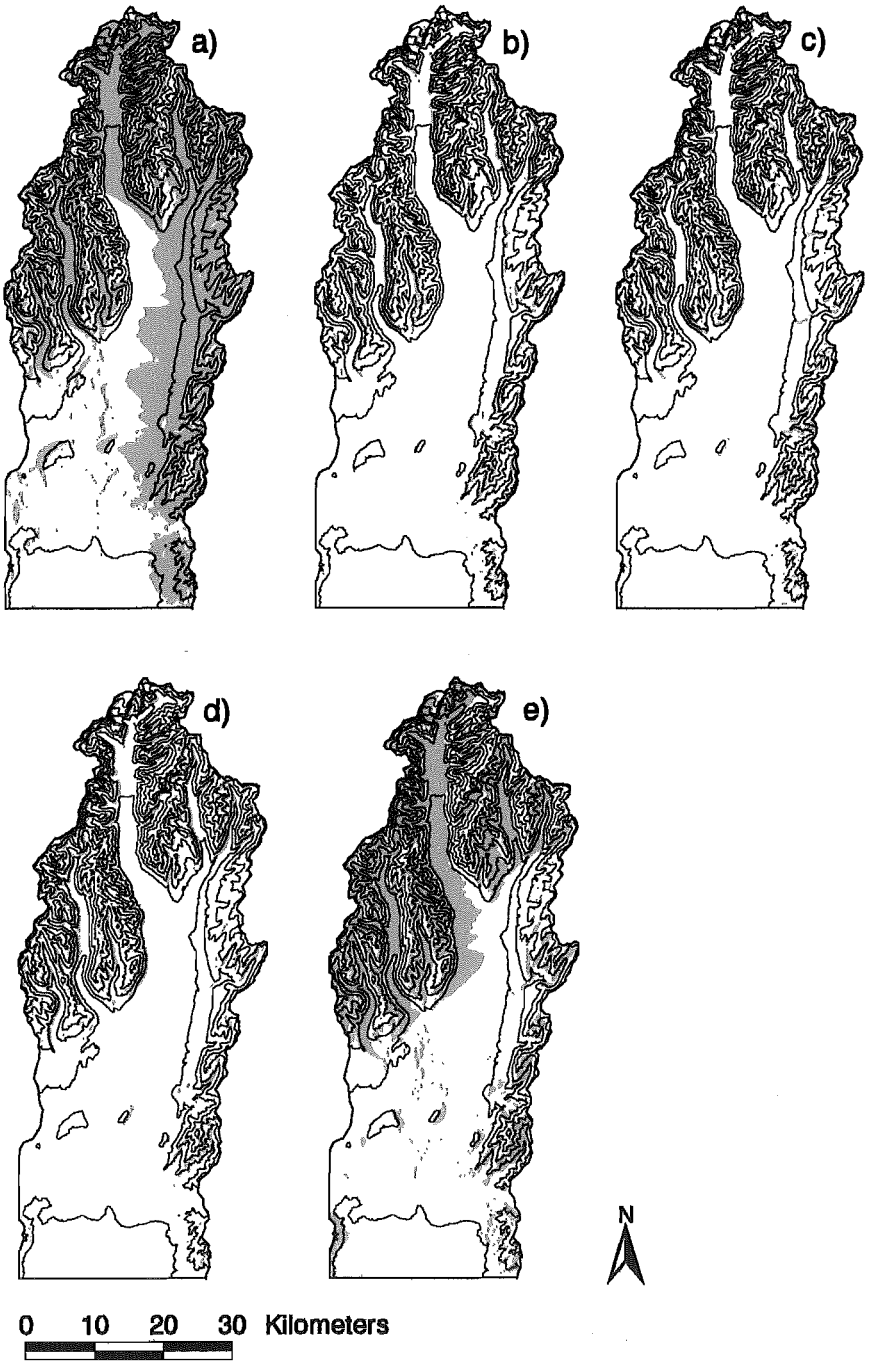

Figure 6.6 Series of maps showing modelled terrain shadows in the Tekapo catchment for a) 0600, b) 0900, c)1200, d) 1500 and e) 1800 NZST for February 12, 1999.

Figure 6.6 illustrates the strong controls of both topographic complexity and orientation on shading. The reduction in $K\downarrow$ associated with shadowing ($K_{(shad)}$) can be estimated by:

$$K_{(shad)} = \overline{K}_{ts} - \left[\overline{K}_{ts} \left(1 - \frac{A_{(shad)}}{A_{(tot)}} \right) + \overline{K}_{ts} 0.1 \frac{A_{(shad)}}{A_{(tot)}} \right] \qquad (6.4)$$

where $A_{(shad)}$ is the 3-D area of the catchment in shadow, $A_{(tot)}$ is the total 3-D catchment area, $K_{ts} \times 0.1$ approximates the isotropic K_D portion of $K\downarrow$ on shaded slopes and the overbar for K_{ts} indicates the spatial mean. Applying Eq. (6.4) to three-hourly shadow maps therefore, illustrates a relatively small diurnal mean reduction in $K\downarrow$ by shadowing, since the increase in shaded area corresponds with a decrease in $K\downarrow$ due to the increase in optical path length (Table 6.2). Subsequently, the spatially and temporally averaged diurnal reduction in $K\downarrow$ as a function of shadowing is only 45.2 W m^{-2}, about 10 % of mean $K\downarrow$. However, the influence of shading at any given time is potentially very large when shaded slopes are adjacent to non-shaded and sunward-oriented slopes. Again, increased topographic complexity appears to result in an overall decrease in $K\downarrow$ and an increase in the range of $K\downarrow$ as a function of shadowing.

Table 6.2 Calculating the reduction of $K\downarrow$ associated with shading in the Tekapo catchment for February 12, 1999.

Time (LAT)	0600	0900	1200	1500	1800	Mean
$\frac{A_{(shad)}}{A_{(tot)}}$	0.43	0.094	0.092	0.092	0.29	0.20
$\overline{K}_{ts}$ (W m^{-2})	68.2	641.3	887.			

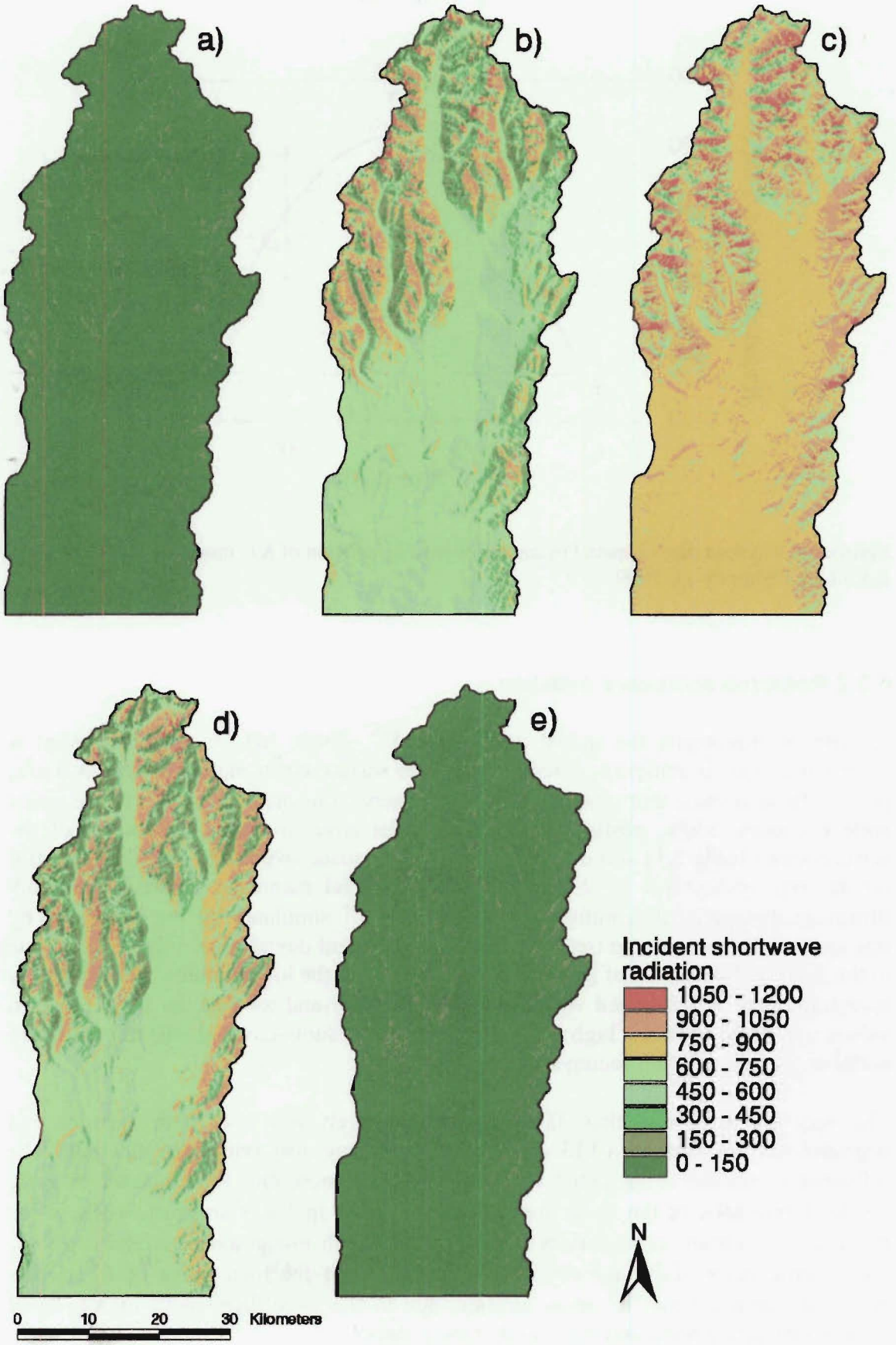

Figure 6.7 Series of maps showing modelled $K\downarrow$ in the Tekapo catchment at three-hourly intervals for the daylight hours of February 12, 1999.

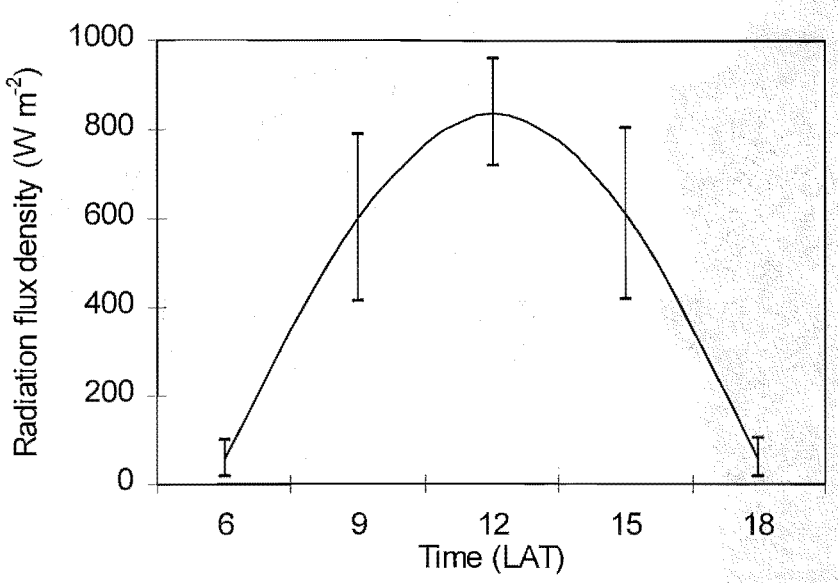

Figure 6.8 Daylight plot of spatial mean and standard deviation of $K\downarrow$, modelled for the Tekapo catchment, February 12, 1999.

6.3.2 Reflected shortwave radiation

In order to investigate the spatial controls on $K\uparrow$, albedo (α) for each grid point is ascertained. This is achieved by reclassifying the surface cover map to assign each grid point with an α value that was determined by observations made over each of the major surface classes. Since, pasture and conifer forest cover a negligible portion of the surface area (Table 3.1) and observations were not made over these surfaces, the grid points were reclassified as tall tussock for all model parameterisations. Figure 6.9 illustrates the spatial distribution of mean diurnal $K\uparrow$ simulated for the catchment by this method. Despite a large range in values, the standard deviation is only 33 Wm^{-2} due to the skewed distribution of grid points heavily toward the lower values. The secondary histogram peak is associated with the high α of snow and ice and the large range in values generated between high altitude, north-facing snow-covered surfaces and lake surfaces, as well as south-facing rock surfaces.

The very low α of the lakes (0.07) and the relatively low α of both the rock and degraded tussock surfaces (0.13, 0.14 respectively) are also evident in this map. The influence of surface α on spatial variability of $K\uparrow$ is more clearly delineated over the gentler topography of the basin area, where the range in $K\downarrow$ is smallest, while in the mountainous terrain, variability is associated with both topographic variability of $K\downarrow$ and heterogeneity of surface cover. For example, half the total range of $K\uparrow$ occurs within the area covered by snow and ice, due to the large differences of $K\downarrow$ found between moderate north and steep south facing slopes.

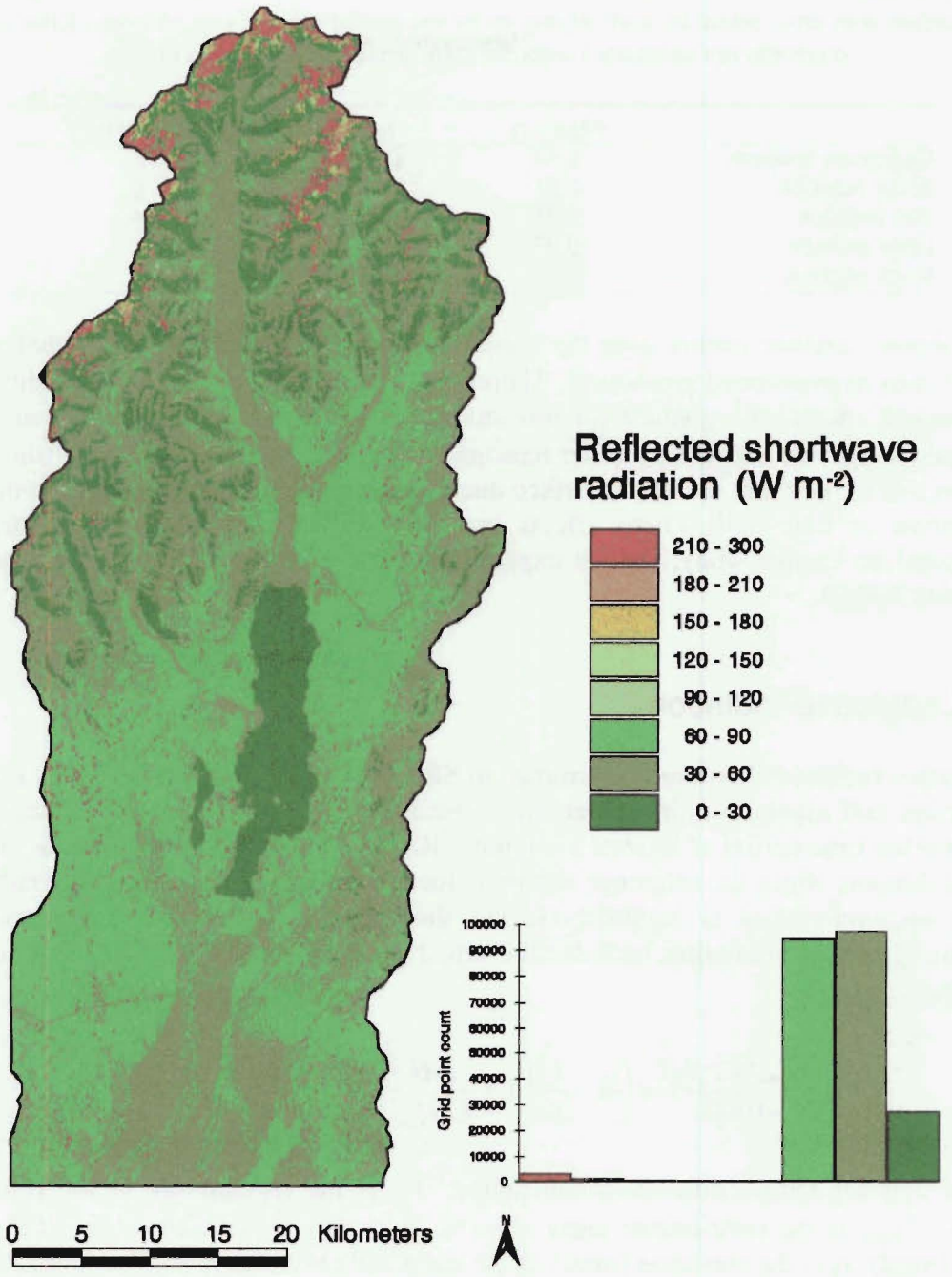

Figure 6.9 Map of modelled $K\uparrow$ in the Tekapo catchment for February 12, 1999, including a histogram of grid point values.

Error assessment

It was shown in Section 5.5.1 that α varied significantly as a function of incident angle for many of the surfaces observed. In order to accurately simulate $K\uparrow$, differential α determined by the incident angle of K_S would need to be established for the unique slope properties at each grid point and at each time step. Due to the computational expense of this procedure, diurnal mean α is assigned for each class except water. Since, all water grid points are horizontal, different α could be assigned for different time steps. The potential error associated with using diurnal mean α for the other surface classes is assessed in Table 6.3

Table 6.3 Daylight mean and standard deviation of albedo (σ_α) for five surfaces and a proxy for a maximum σ of error found by multiplying σ_α by the spatial mean $K\downarrow$ at mid-day. Lake surface σ error is not calculated since this was accounted for in the model.

	Mean α	σ_α	σ error (W m^{-2})
Degraded tussock	0.14	0.01	3.3
Short tussock	0.21	0.05	16.0
Tall tussock	0.25	0.08	23.4
Lake surface	0.07	0.10	~
Rock surface	0.13	0.02	4.5

The largest variance occurs over the water surface, although this is accounted for in model runs as mentioned previously. Therefore, α variability associated with short and tall tussock species are greatest for this study, but still incur errors of less than 10%. Diurnal changes in α occur for other reasons, such as change in roughness of the snow surface due to melt and the water surface due to wind, as well as the presence of dew on vegetation or bare soil. These effects are more difficult to quantify and are not accounted for in this study, but are expected to have a small influence on the surface radiation budget.

6.4 Longwave radiation

Longwave radiative fluxes are determined in SRAD in the following way. First, average minimum and maximum air temperatures, mean surface temperatures and their lapse rates for the time period of interest are input. SRAD extrapolates these values across the model domain. Since the reference station is located on horizontal terrain, the radiation effect on temperature is included via the shortwave radiation ratio (S) introduced previously. The formulation includes the effect of a leaf area index (LAI) on surface irradiance:

$$T = T_b - \frac{T_{lapse}(z - z_b)}{1000} + \left(S - \frac{1}{S}\right)\left(1 - \frac{LAI}{LAI_{\max}}\right) \qquad (6.5)$$

where T is air temperature at screen height, T_b is the temperature at the reference station, T_{lapse} is the temperature lapse rate (°C m^{-1} $\times 10^3$), z is the elevation of the grid point (masl), z_b is the elevation (masl) of the temperature reference station, and LAI_{max} is the maximum leaf area. Longwave radiation fluxes are subsequently determined from the surface and air temperature using Eq. (2.11) and (2.12) so that $L\uparrow$ is a function of surface temperature and the reflected portion of $L\downarrow$, while $L\downarrow$ is a function of air temperature and atmospheric emissivity (Eq 2.13) modified by the sky view factor (v) and $L\uparrow$. The result of these calculations for February 12, 1999 is presented in Figure 6.10. The spatial distribution of L^* clearly resembles elevation since the lapse rates of surface and air temperature are not the same. L^* generally decreases with elevation since the mean diurnal surface temperature lapse is lower that of air temperature. This is enhanced by the generally larger v found at higher elevations, since lower $L\downarrow$ occurs when v is larger. In approximate proportion with the distribution of elevation, the distribution of L^* is skewed toward the lower values. The effect of the sky view factor is also revealed by relatively higher values occurring on valley floors and on steep valley sidewalls.

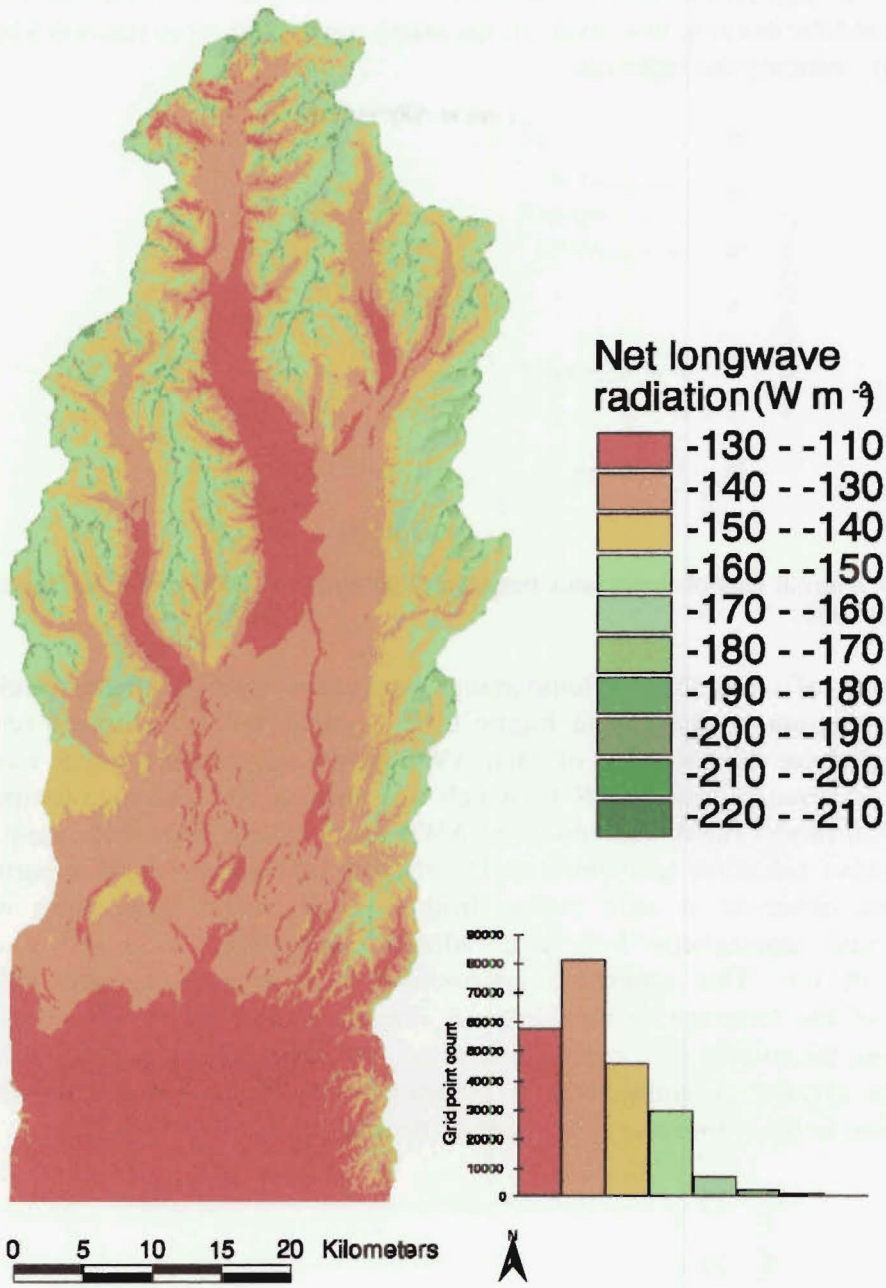

Figure 6.10 Map of modelled L^* in the Tekapo catchment for February 12, 1999, including a histogram of grid point values.

Error assessment

Accuracy of longwave components is clearly dependent on the spatial representativeness of input data. Mean hourly air temperature lapse rates from three pairs of AWS with large elevation differences were used to define the lapse rate for the study area on February 12, 1999. These are plotted in Figure 6.11. The first pair was located in the north of the catchment, situated on the valley floor (AWS1) and on a ridge near the alpine divide (AWS0) (see Figure 3.1 for locations). The second pair was located to the south of the study area on the basin floor (AWS16) and on the top of nearby Mt John (AWS15). The third pair used was AWS16 and AWS0 since they represented the greatest extreme in both elevation and climatological location in the AWS network. The three lapse rates show similar diurnal patterns and magnitudes,

although with significant hourly variability. For example, the influence of cold air advection into the basin at low levels in the afternoon is evident in the AWS16-AWS15 pair, greatly reducing the lapse rate.

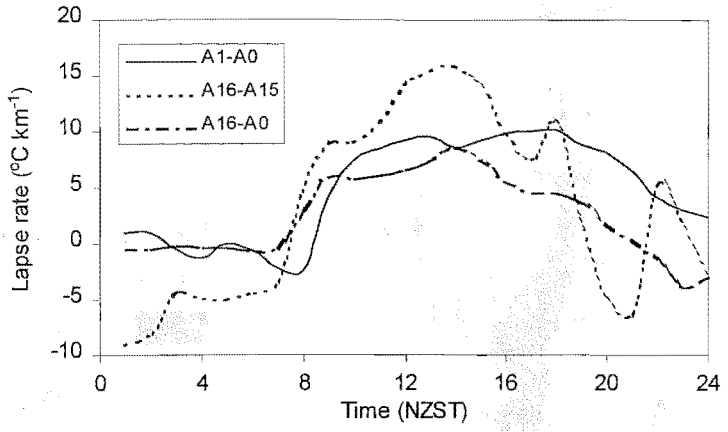

Figure 6.11 Diurnal plot of lapse rates between three pairs of AWS in the Tekapo catchment, February 12, 1999.

The influence of variability of temperature lapse rates throughout the catchment on longwave radiation is assessed in Figure 6.12. A mean hourly reference temperature was calculated for the elevation of each AWS by the mean hourly lapse rate and the reference temperature from AWS16 (which was used as the reference temperature in SRAD for all model runs). The observed AWS temperatures were then compared with their respective reference temperatures. Hourly standard deviations of departure of air temperatures observed at each station from their reference temperature were then converted into atmospheric longwave radiation using Eq. (2.12) and a clear sky emissivity of 0.6. This procedure approximates the error associated with spatial variability of the temperature lapse rate. A diurnal pattern occurs where temperature lapses during the middle of the day show greater variability than at night and therefore contains the greatest potential error. In magnitude however, error associated with the use of a mean hourly lapse rate is very small (diurnal mean = 9.4 W m^{-2}).

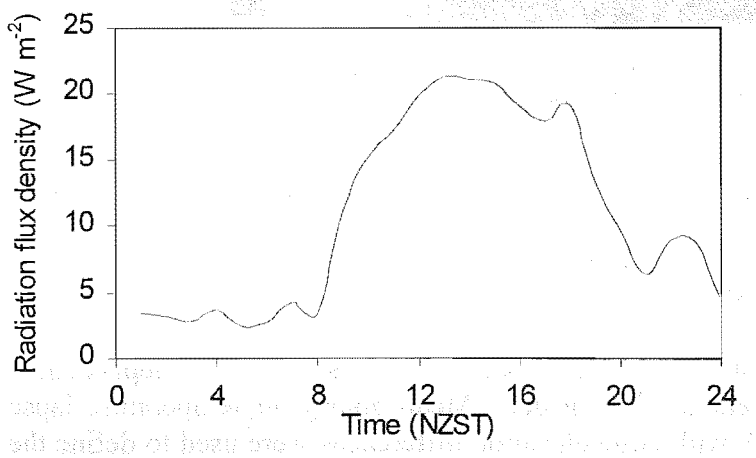

Figure 6.12 Diurnal plot of $L\downarrow$, calculated from the standard deviation of recorded temperature departure from that determined by the mean lapse for all AWS in the Tekapo catchment, February 12, 1999.

The *LAI* is approximated for each surface cover class based on results from surface cover observations and assigned to grid points by surface cover classification in the same way that albedo is. For each surface, *LAI* was approximated from 100×100 m

quadrat surveys of surface cover, where percentage of non-vegetated surface was estimated. Clearly, for rock, water and snow/ice surfaces *LAI* is zero, while for tall, short and degraded tussock, approximations of 0.9, 0.6 and 0.4 respectively, were used. Sensitivity analysis of *LAI* influence on temperature for varying *S* values is provided in Figure 6.13. The range of *S* values used is 0.5 to 2.0, or from half to double the shortwave radiation received on a horizontal surface. Air temperature has a range of 3° C over this range of *S*. At approximately 20° C, with a clear-sky atmospheric emissivity of 0.6, the difference in $L\downarrow$ associated with this range of temperature is only 10.6 W m^{-2} or 4%. Therefore, error in the approximation of *LAI* used in this application is unlikely to yield significant error in L^*.

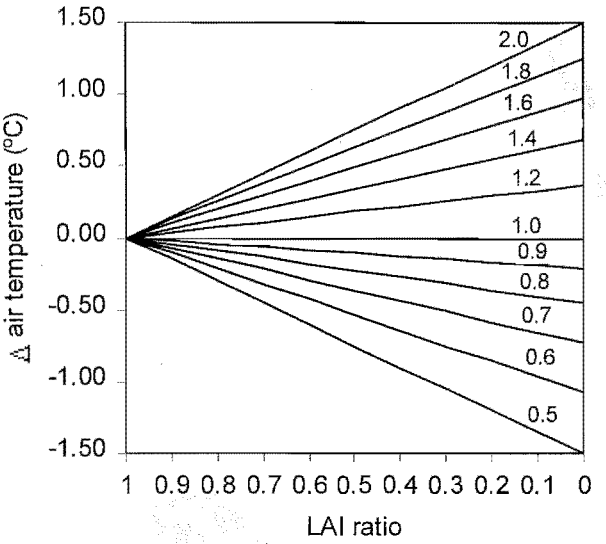

Figure 6.13 Sensitivity analysis of the control on air temperature (at 20 °C) of *LAI* at 11 different levels of *S* ranging from 0.5 to 2.0.

An additional source of error exists from the assumptions involved in extrapolating temperatures beyond the elevations of the AWSs from which the lapses were derived. This error is probably small during the day when the boundary layer extends at least to ridge height. The inversions observed in the valley atmosphere at night, however, may be significantly shallower and confined within the valley atmosphere below ridge level. In the model, the temperature inversion is extended to the upper limits of the model domain, thereby overestimating temperature at ridge tops. Thus L^* is probably lower over the ridge tops and mountain peaks in reality than is predicted by the model. Overestimation of air temperature by 5° C when the correct tempe-rature was 0° C and emissivity 0.6 would generate an error in L^* of +14.5 W m^{-2} (8%). Furthermore, since this occurs at the highest elevations, this error is restricted to a small distribution of grid points (Table 6.1).

*Hourly variability of L**

The spatial distribution of L^* for February 12 at three-hourly intervals, is provided in Figure 6.14. When evaluated on a single scale incorporating both the spatial and diurnal ranges, considerably less detail is evident in each map.

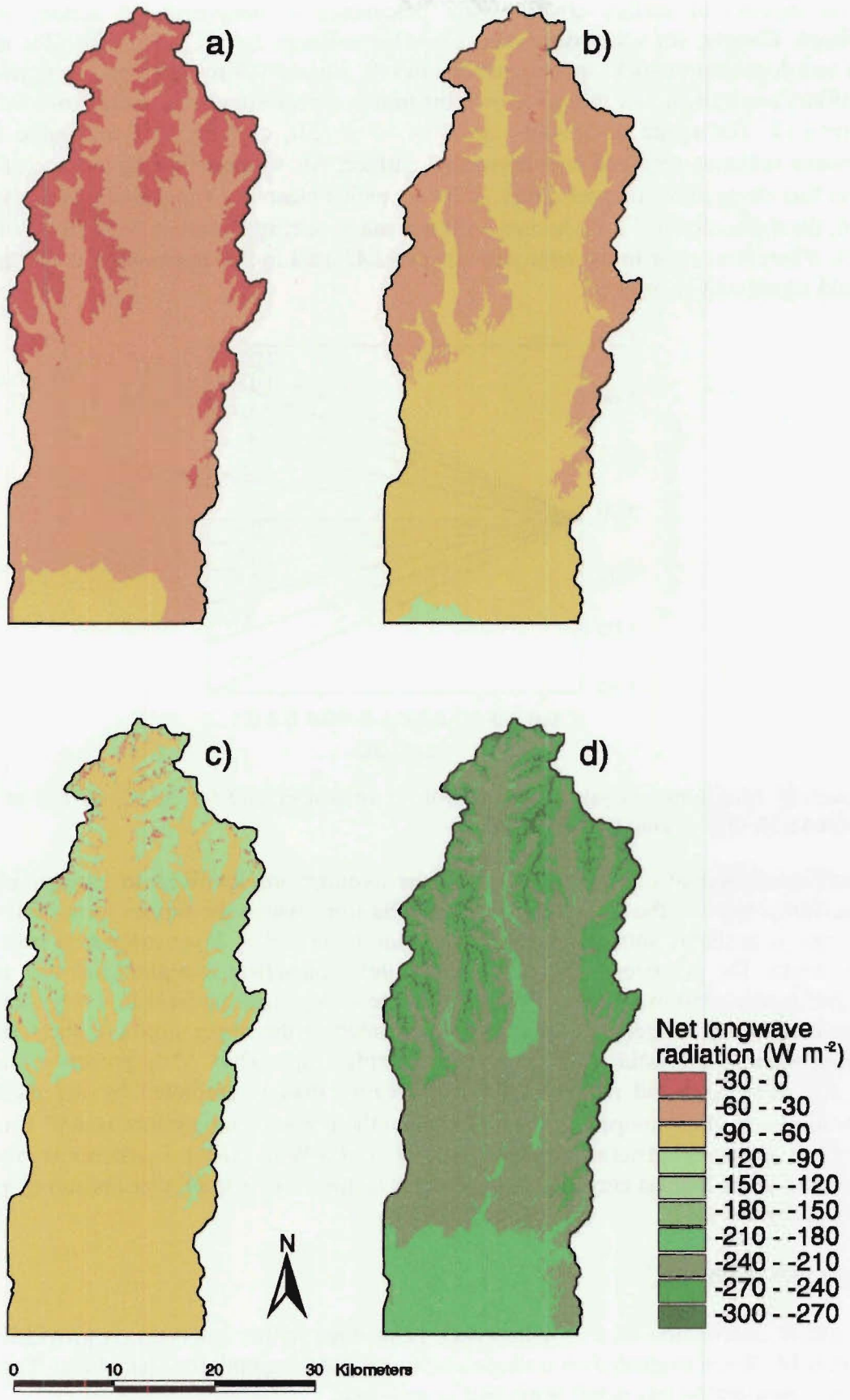

Figure 6.14 Series of maps showing modelled L^* in the Tekapo catchment at a) 0300, b) 0600, c) 0900, d) 1200, e) 1500, f) 1800, g) 2100, h) 2400 LAT, February 12, 1999.

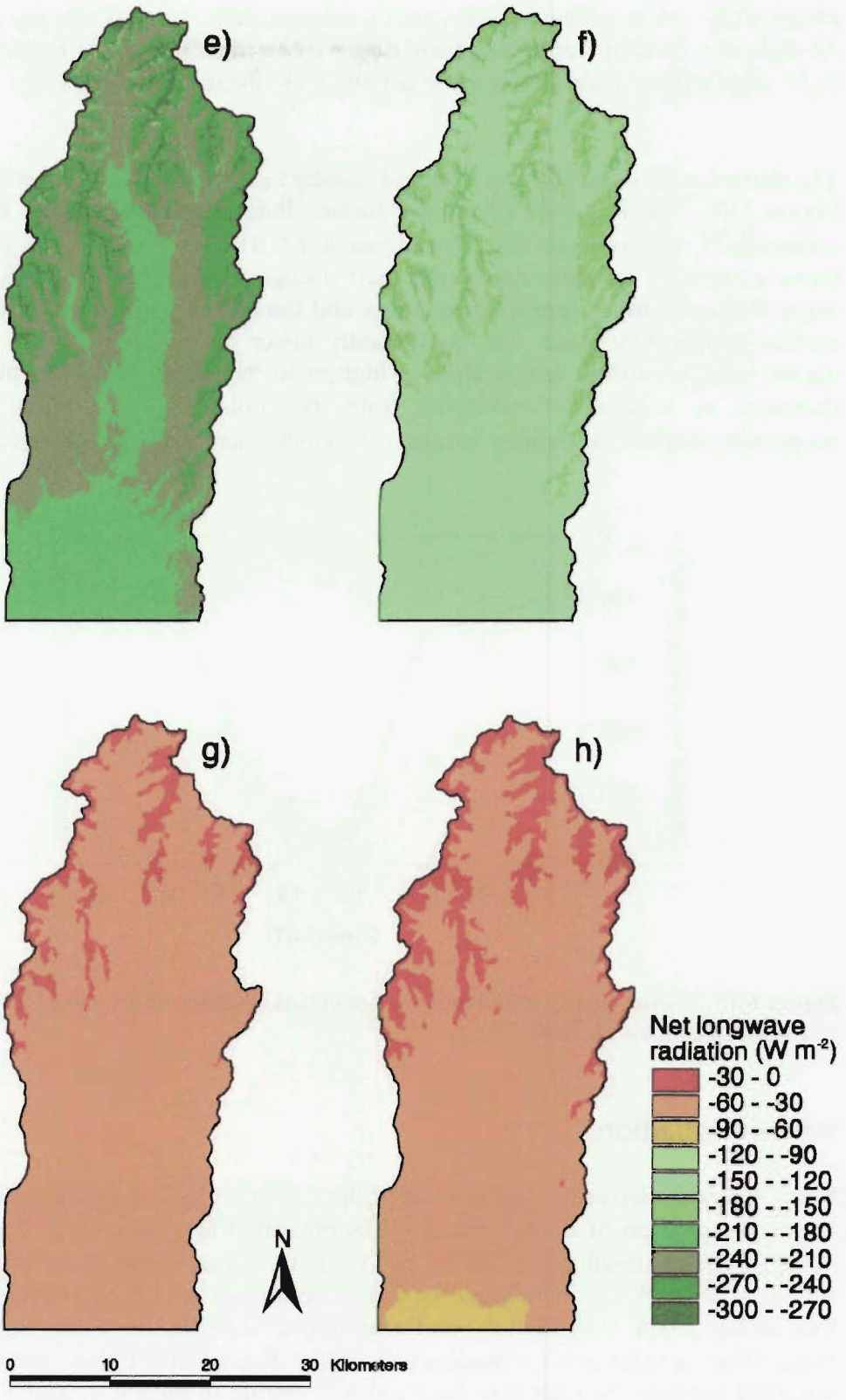

Figure 6.14 continued.

The diurnal trend is most strongly a function of the response of surface temperature to solar radiation and the transport of heat from the surface to produce the lapse in air temperature, which changes considerably through the course of the day (Figure 6.11). At night the air temperature inversion observed by all station pairs leads to an increase in L^* with height, while during lapse conditions in the day, L^* also lapses.

The diurnal plot of the spatial mean and standard deviation of L^* values is presented in Figure 6.15. The influence of greater surface than air heating during daylight hours increases $L\uparrow$ relative to $L\downarrow$ thereby decreasing L^*. The variability is also greatest during these hours since the lapse rates are at their strongest. The relatively low values at night occur because surface temperature is low and the air temperature inversion offsets the surface temperature lapse. The significantly lower L^* in the afternoon than morning occurs because surface temperature is highest in the afternoon, while air temperature decreases as a result of advection from the cool easterly intrusion. Overall, the magnitude of spatial variability is relatively small when compared with $K\downarrow$.

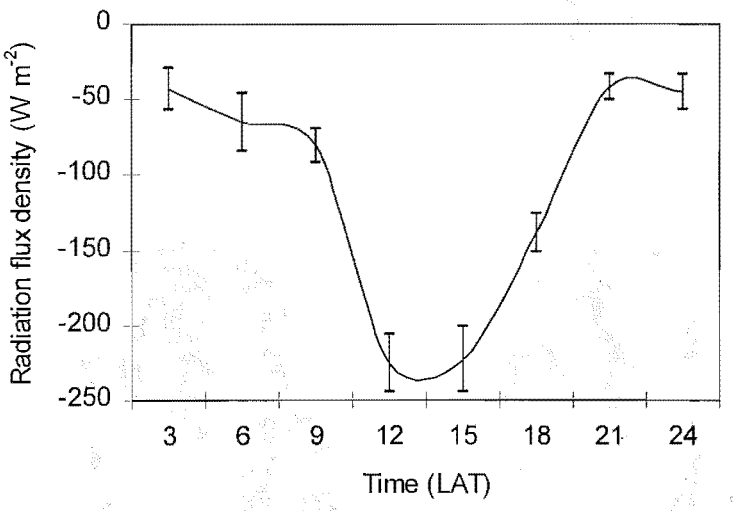

Figure 6.15 Diurnal plot of spatial mean and standard deviation of L^*, modelled for the Tekapo catchment, February 12, 1999.

6.5 Net radiation

Net radiation is derived as the balance of the four individual radiation components. The spatial distribution of diurnal mean Q^* is presented in Figure 6.16. The total spatial range in mean diurnal Q^* is 278 W m^{-2}, while the mean is 149 W m^{-2} and the standard deviation is 49 W m^{-2}. The range in values occurs between high altitude, north-facing rock surfaces with very high Q^* and south-facing ice surfaces where a Q^* loss occurs. Since these surfaces cover a small proportion of the catchment, the distribution of Q^* is weighted towards the relatively homogeneous terrain to the south where values of 165 W m^{-2} +/- 10% are found. In general, the north facing slopes and water surfaces yield the higher Q^* values, while south-facing slopes and snow surfaces yield the lowest. The large, gently sloped basin area also receives above average Q^*, while the east and west facing slopes, particularly steeper slopes, receive moderate to low magnitudes of Q^*.

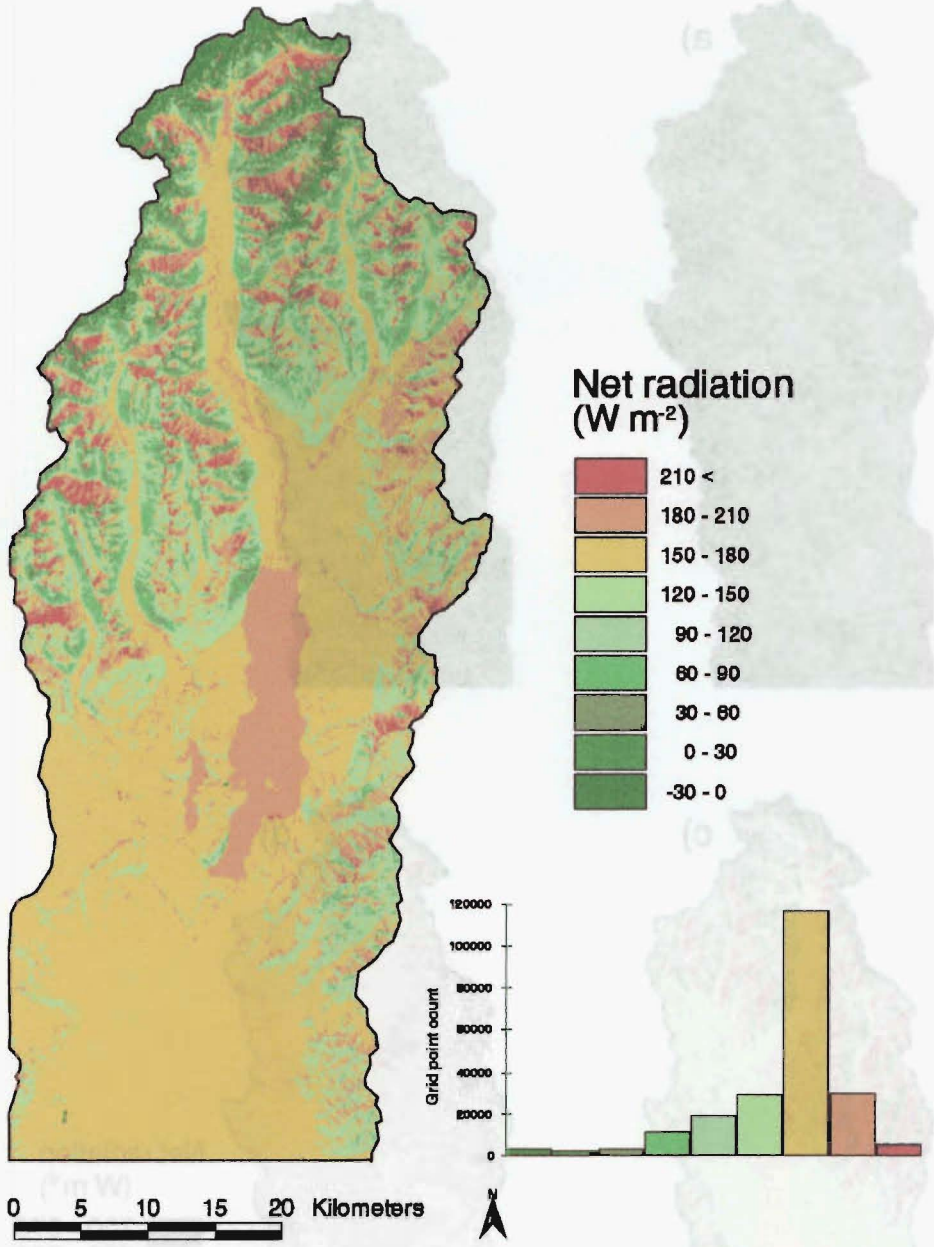

Figure 6.16 Map of modelled Q^* in the Tekapo catchment for February 12, 1999, including a histogram of grid point values.

6.5.1 Hourly variability

When all radiation fluxes are summed and plotted at three-hourly intervals for February 12, 1999 (Figure 6.17), the relative importance of L^* is barely perceptible, even when it dominates the radiation budget at night. Instead, slope properties and albedo appear to dominate the spatial controls on Q^*, while solar angles and path length dominate the temporal variability.

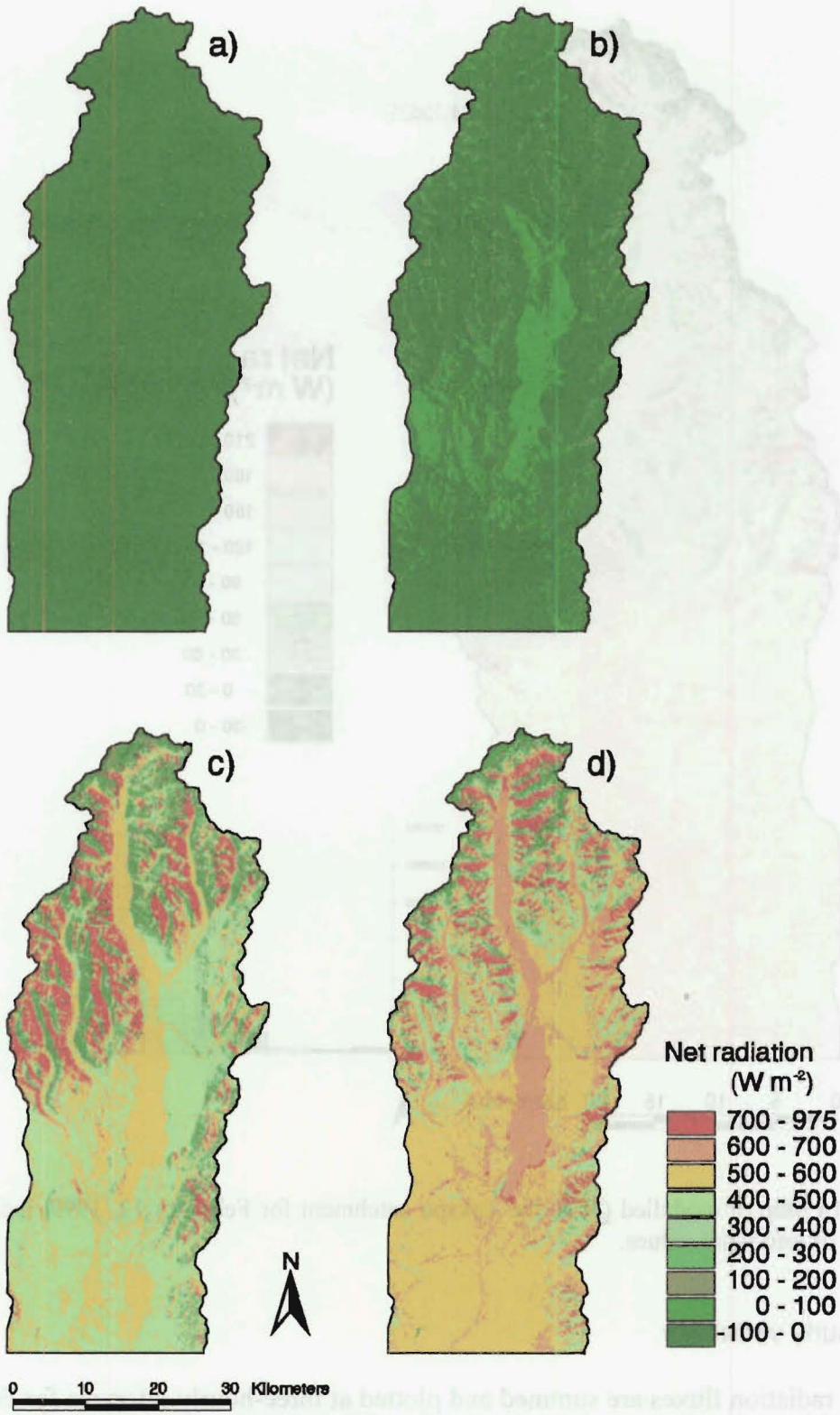

Figure 6.17 Series of maps showing modelled Q^* in the Tekapo catchment at a) 0300, b) 0600, c) 0900, d) 1200, e) 1500, f) 1800, g) 2100, h) 2400 LAT, February 12, 1999.

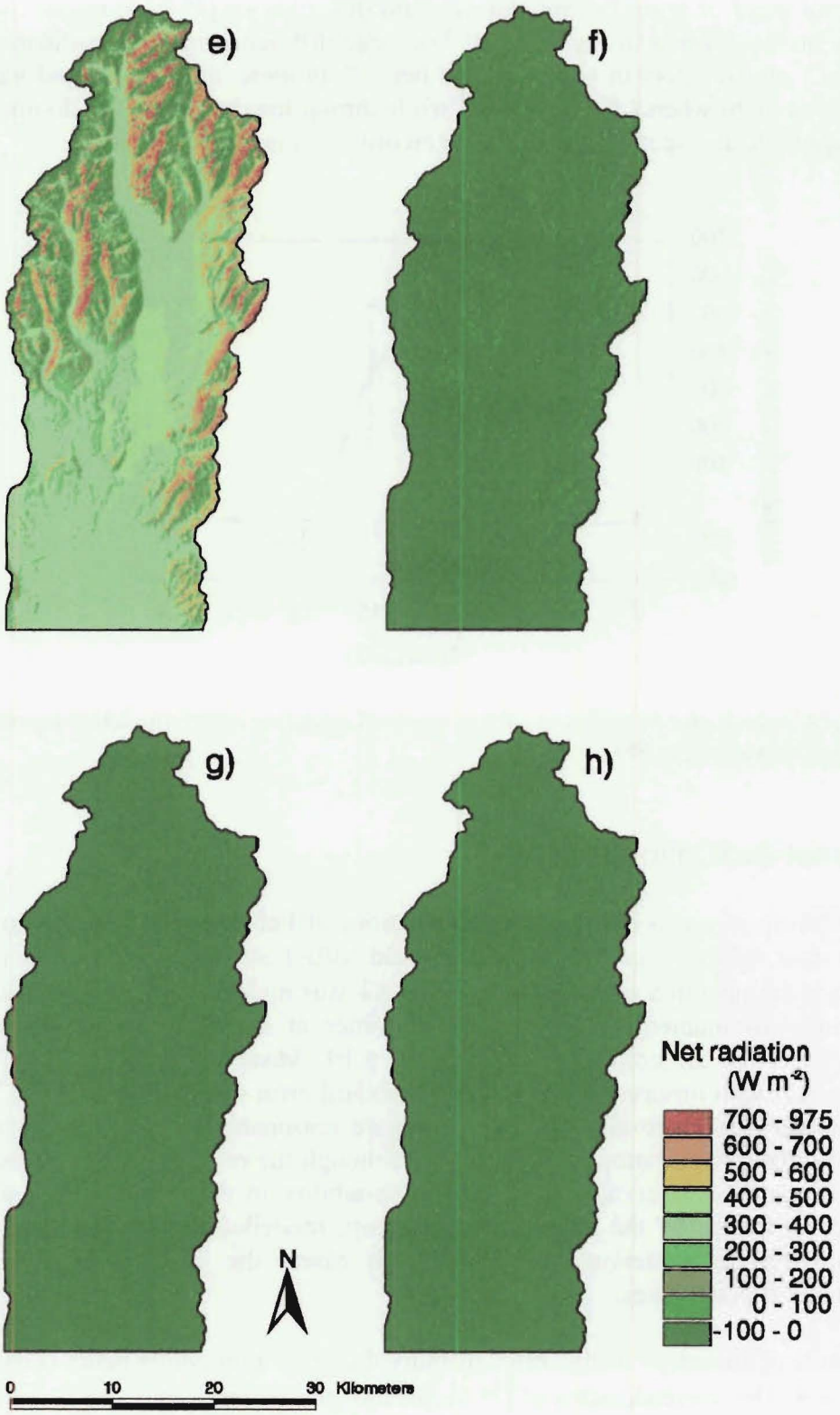

Figure 6.17 continued.

The diurnal trend of spatial mean and standard deviation of Q^* from model output for the study area is plotted in Figure 6.18. The large difference in the significance of the role that L^* and K^* play in Q^* is evident here. Both mean magnitudes and variability are lowest at night when L^* controls Q^*, while during the day, when K^* dominates, the mean magnitude and spatial variability are an order of magnitude greater.

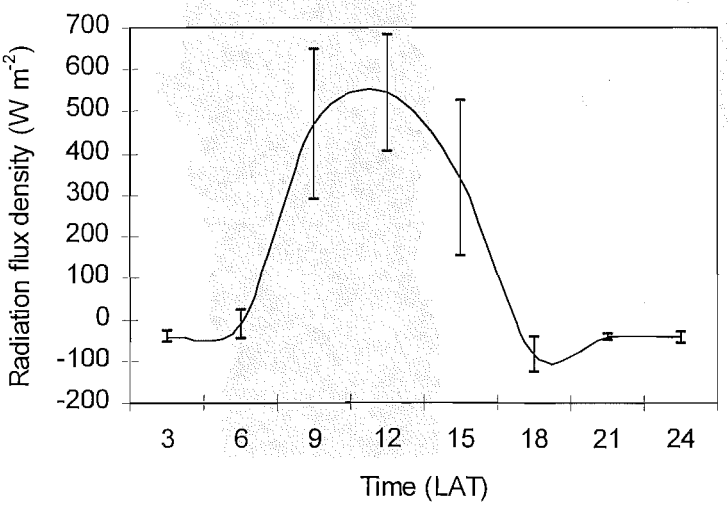

Figure 6.18 Diurnal plot of spatial mean and standard deviation of Q^*, modelled for the Tekapo catchment, February 12, 1999.

6.6 Model evaluation

Model performance was evaluated for simulations of February 12, 1999 by comparing model output with data collected at BREB and MEB1 sites where complete radiation budget stations operated and at AWS1 where $K\downarrow$ was measured. The mean diurnal and three-hourly instantaneous radiation flux densities at these sites are plotted against model output for all components in Figure 6.19. Mean daily fluxes are found to compare well with observed fluxes, with a standard error of estimation of 32.7 W m^{-2}. Instantaneous fluxes are also found to compare reasonably well with observed data (standard error of estimation = 39.3 W m^{-2}), although the relationship is a little weaker at this shorter time interval. The increased variability in three-hourly data would be partly accounted for by the fact that instantaneous modelled fluxes are compared with 15-minute average observed fluxes. In both cases, the model tends to slightly overestimate flux densities.

The relative contribution to this error of individual radiation components is considered in Table 6.4. The overestimation of Q^* occurs as a consequence of overestimation of $L\downarrow$ and $K\downarrow$ and smaller underestimation of $K\uparrow$ and $L\uparrow$. The reason for the overestimation of $K\downarrow$ is most likely to result from overestimation of optical transmissivity for this particular day (since this parameter was derived from a long term mean). The overestimation of $L\downarrow$ is not surprising since it is calculated based on air temperature measured at screen level. Accurate modelling of $L\downarrow$ should include integrated temperatures through the atmospheric column, which would yield somewhat smaller $L\downarrow$ due to the general decrease of temperature with height in the troposphere.

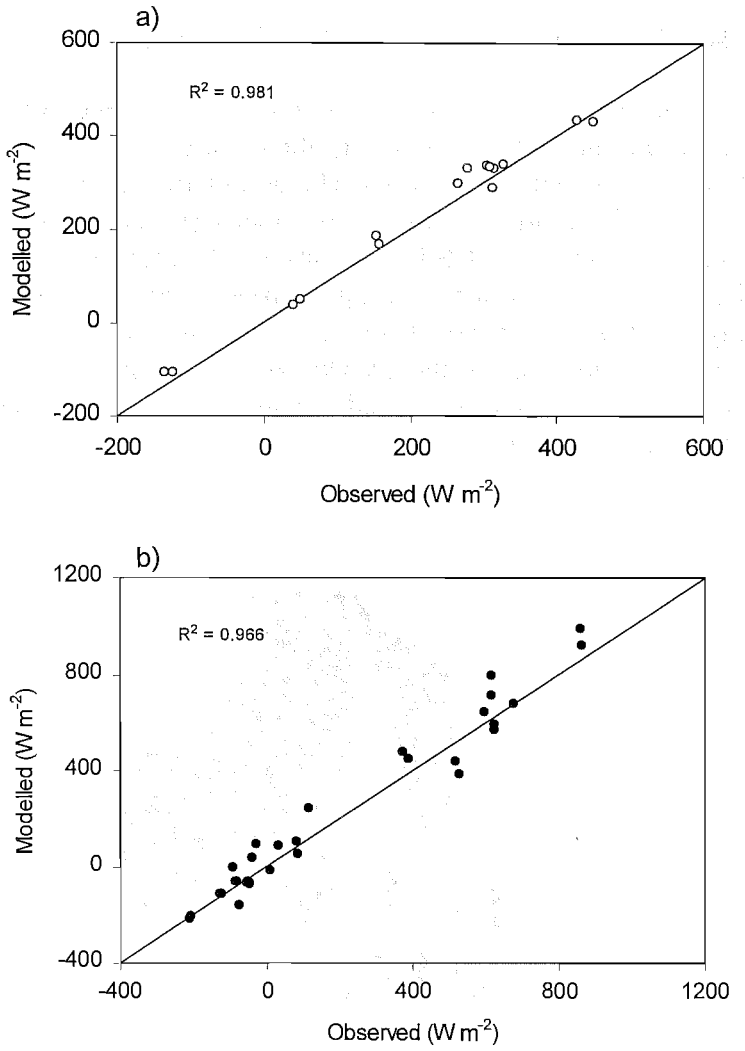

Figure 6.19 Scatter plots comparing modelled with observed radiation components from a) daily mean and b) three-hourly instantaneous fluxes on February 12, 1999.

In conclusion, the model provided good estimates of radiative fluxes particularly over longer time intervals (i.e. over a day). However, confidence in the model is tempered by the small dataset used for verification and the relatively small range in topographic properties in the observational dataset.

Table 6.4 Breakdown of mean radiation budget components observed and modelled (W m^{-2}) at three sites for February 12, 1999 and the difference between modelled and observed data as a percentage of observed data.

	Q*	K↓	K↑	L↓	L↑
observed	155.6	313.6	45.1	296.4	439.6
modelled	177.7	338.1	44.1	331.9	435.9
%difference	14.2	7.8	-2.1	12.0	-0.9

6.7 Assessing the role of topographic complexity

A comparative assessment of the role of topographic complexity on the surface radiation budget is produced by comparing three catchment sub-areas (CS) with significantly different topographic properties. The boundaries for each CS were selected qualitatively based on elevation and slope angle maps (Figure 3.2). Presented in the form of slope angle maps, the three CS boundaries are illustrated in Figure 6.20. CS1 is the section of the catchment closest to the alpine divide and represents steeply incised alpine topography. CS2 is comprised of the eastern ranges and lake basin area, with moderate slope angles and CS3 is the Mackenzie Basin section of the catchment comprised of an expansive, gently sloped basin surface with some low Roche Moutonnee features (such as Mt John).

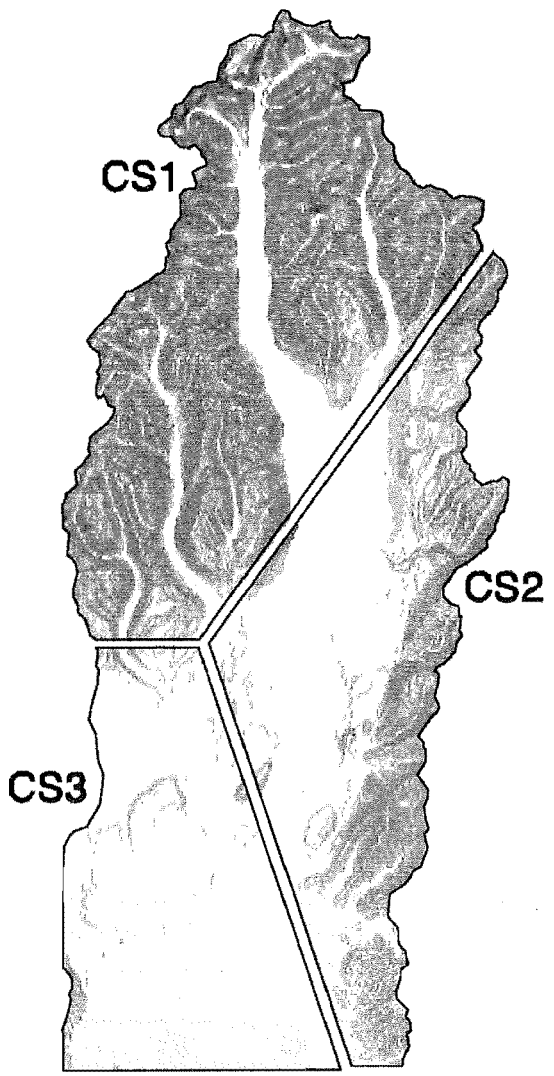

Figure 6.20 Three catchment sub-areas selected for comparison of topographic complexity (shading indicates slope angle).

The descriptive spatial statistics for topographical properties (elevation, slope angle), radiation ratios and radiation flux densities for each CS are provided in Table 6.5. From CS1 to CS3 a drop occurs in elevation and slope angles, as well as the variability in

both properties. This describes three distinct categories of topographic complexity from extremely complex to simple. The importance of slope properties on $K\downarrow$ for each CS is assessed through S (the ratio of $K\downarrow$ on sloping to horizontal surfaces), which increases between CS1 and CS3, illustrating overall reduction in $K\downarrow$ found in complex terrain as a function of slope angle. Variability also increases with topographic complexity. Mean albedo is similar in each CS although variability is double in CS1 compared to CS2 and CS3. In the breakdown of radiation components, mean $K\downarrow$ is significantly reduced in the more complex terrain, while spatial variability is greatly increased. Mean L^* also decreases in more complex topography (although negligibly) suggesting that the stronger lapse in air compared to surface temperature outweighs the control of sky view factors. Variability is also greater in more complex terrain, although the inter-CS differences for L^* are negligible compared with K^*. Since shortwave radiation has been found to dominate the radiation budget and mean albedo is similar in each CS, the difference in mean Q^* between each CS most strongly resembles that of $K\downarrow$. Overall, radiation absorption at the surface decreases in more complex terrain, while spatial variability increases.

Table 6.5 Descriptive spatial statistics for topographical properties and radiative fluxes in three Tekapo catchment sub-areas.

	Mean			Standard deviation		
	CS1	CS2	CS3	CS1	CS2	CS3
Elevation (m)	1489	1035	707	438	381	148
Slope angle (°)	24	11	3	13	11	4
S	0.82	0.95	0.99	0.18	0.09	0.02
Albedo	0.19	0.18	0.20	0.14	0.07	0.06
K↓ (W m^{-2})	281	312	314	60	27	8
L* (W m^{-2})	-99	-98	-96	5	4	2
Q* (W m^{-2})	131	163	162	58	28	15

A comparison of mean and standard deviation Q^* between the three CS for hourly data from simulations of February 12, 1999 are plotted in Figure 6.21. The reduction in Q^* at CS1 occurs throughout the day except during nocturnal hours when its higher elevation is influenced by the nocturnal temperature inversion. However, this is negligible when compared to the reduction of Q^* during the daytime. The generally west-facing property of many slopes increases the mean Q^* for CS2 compared with CS1 in the afternoon, which is also lower than both CS1 and CS3 in the morning. The difference in spatial variability of Q^* between each CS is substantial (Figure 6.21b) where peak standard deviations differ by 200 W m^{-2}. The three CS show a similar pattern whereby greatest spatial variability occurs in mid-morning and afternoon (reflecting the importance of aspect). CS2 deviates slightly from this pattern with greater afternoon variability in accordance with greater mean values.

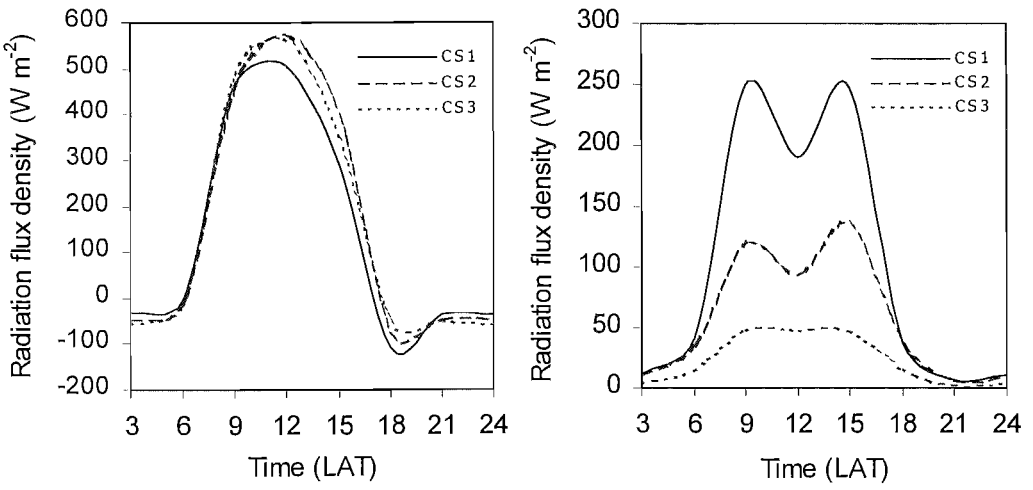

Figure 6.21 Diurnal plots comparing modelled hourly a) mean and b) standard deviation of Q^* for three catchment sub-areas on February 12, 1999.

6.8 Summary

This chapter has investigated the causes for spatial variability in surface radiative fluxes as an important contribution to the surface energy balance of the Tekapo catchment. Spatial modelling of radiation flux components was utilised for this purpose using SRAD. The model compares well with observations, with closer agreement found for daily mean than instantaneous fluxes. Overestimation of both incoming radiative components and much smaller underestimation of outgoing components results in an overestimation of Q^* by 14%. Of the radiation components, $K\downarrow$ contributes most significantly to the radiation budget both in terms of the mean and variability of flux magnitudes. The variability in $K\downarrow$ is associated most strongly with slope aspect, secondly with slope angle, thirdly with shading and finally with elevation. $K\uparrow$ also varied considerably as a function of both the variability found in $K\downarrow$ and albedo. By contrast longwave radiation fluxes contributed little variability to the spatial distribution of Q^*. Net radiation was governed most strongly by elevation with radiation ratios and leaf area indices having relatively small control. Diurnal variability was assessed for each component. Again $K\downarrow$ dominated in diurnal changes, with greatest spatial variability occurring in mid morning and afternoon due to the approximately north-south orientation of the dominant topography.

The role of topographic complexity in the spatial distribution of fluxes was investigated by considering three sub-areas of the study area that contain strongly contrasting topographical properties. The increase in topographic complexity yielded a decrease in Q^* but a large increase in spatial variability. This was governed most significantly by $K\downarrow$. Other components yielded similar averages between topographically different areas although spatial variability in all fluxes was significantly increased with greater complexity.

Chapter Seven:

Mapping spatial variability of turbulent surface energy fluxes

7.1 Introduction

The purpose of this chapter is to investigate the spatial variability of sensible and latent heat fluxes on clear-sky mid-summer days in the Tekapo catchment. The information used in this investigation is the amalgamation of data presented in the previous two chapters, and manipulated in a GIS environment. In Chapter Five, observations of surface energy balances were documented for five surface types in the Tekapo catchment using nine observation sites. This showed that each surface type produced a distinct energy balance that was coherent between sites of the same surface class. Chapter Six focussed on modelling Q^* over the entire catchment surface, accounting for topographic and surface radiative characteristics. With knowledge of the spatial pattern of Q^*, energy partitioning over each surface type and surface classification over the catchment surface, it is possible to construct energy flux density maps for Q_H and Q_E over the catchment for the times when this information applies. A schematic overview of the process of map generation can be reviewed in Figure 3.6. The data derived from this process provide the focus for this chapter. Initially the methods used in constructing energy flux maps are described, and assumptions inherent in the technique are discussed. Secondly, sensible and latent heat flux maps are analysed respectively. Finally, the implications for the controls on spatial variability of surface energy fluxes in complex terrain are discussed, with reference to the role of surface complexity.

7.2 Surface energy flux map construction

Surface energy flux maps are constructed using GIS tools to amalgamate the information presented in previous chapters. The surface energy balance equation as it is

typically written (Eq. 2.14 or 2.15), implies that energy imbalances are generated by the radiation budget and compensated for by heat fluxes. Indeed, this is often the case and observational data presented for the Tekapo catchment shows that the three heat flux components are most often of the same sign as each other and opposite that of Q^* (relative to the direction of energy flow). Subsequently, in order to compare flux magnitudes between different locations or times, they are often non-dimensionalised by the ratio of energy flux density to radiation flux density (*e.g.* Q_H/Q^*). Furthermore, observations presented in Chapter Five showed that, for most surfaces, Q_H and Q_E were strongly correlated to Q^*. Based on this assumption, the GISs constructed to describe spatial patterns of Q_H and Q_E, use the relationships:

$$Q_{H(\mathrm{mod})} = Q^*_{(\mathrm{mod})} \left(\frac{Q_H}{Q^*} \right)_{(obs)} \tag{7.1}$$

and

$$Q_{E(\mathrm{mod})} = Q^*_{(\mathrm{mod})} \left(\frac{Q_E}{Q^*} \right)_{(obs)} \tag{7.2}$$

where $Q_{H(mod)}$ and $Q_{E(mod)}$ refer to the turbulent flux values predicted for each grid point of the spatial model of the Tekapo catchment, $Q^*_{(mod)}$ (W m^{-2}) is the modelled value of Q^* (W m^{-2}) for each grid point (from Chapter Six) and the ratios suffixed by $_{(obs)}$ are the mean ratios found for the particular surface type of each grid point. This method therefore, accounts for the topographic and surface controls on Q^* and the controls of surface type on energy partitioning.

As mentioned in the previous chapter, surface parameters used in this model were reclassified to replace oversown pasture and conifer trees with tall tussock. The actual impact this has on spatial variability is minor due to the negligible surface area of these surface classes. Furthermore, tall tussock is likely to be the most micrometeorologically similar surface of the remaining classes to both pasture and conifers due to their rather similar stomatal behaviour (Kelliher *et al.* 1993).

Observations of surface energy partitioning were not made over snow and ice surfaces in this study. Therefore, the energy partitioning over snow and ice is parameterised based on previous observational studies. The energy fluxes over glacier surfaces in the Southern Alps of New Zealand have been the subject of several studies (Ishikawa *et al.* 1992, Prowse and Owens 1982, Owens *et al.* 1984, Morris 1997, Hay and Fitzharris 1987). They illustrate strong temporal variability in association with both seasonal and synoptic controls.

During summer anticyclonic conditions, turbulent fluxes are relatively small due to low wind speeds operating over low surface roughness. Furthermore, Q_G is assumed to be negligible since the ice surface and subsurface temperatures were almost always at the melting point, so that energy provided to the surface was utilised predominantly for melt (Q_M). In these conditions, since turbulent fluxes are small, melt is most strongly driven by Q^*. For the present study, data were taken from Hay and Fitzharris (1987) since their study site (the Ivory Glacier, elevation 1400-1800m) best represented the region considered in this study. The daily mean ratios of energy partitioning reported by Hay and Fitzharris are presented in Table 7.1. Diurnal variability was reported in terms of daytime and nighttime averages only since this division represented the most significant change over the diurnal cycle.

Table 7.1 Net radiation partitioning during summer anticyclonic conditions on the Ivory Glacier (Hay and Fitzharris 1987).

	Diurnal mean	Daytime mean	Nighttime mean
Q^* (MJ m^{-2} dy^{-1})	11.4	11.48	-0.51
Q_H/Q^*	-0.11	-0.06	0.82
Q_E/Q^*	-0.05	-0.04	0.27
Q_M/Q^*	1.16	1.1	0

The mean energy partitioning ratios used in constructing the spatial models of Q_H and Q_E for all surfaces over the diurnal cycle are provided in Table 7.2. As discussed earlier, the first five surface classes are derived from data collected on clear sky days in mid-summer 1999 and the sixth class is determined from the work of Hay and Fitzharris (1987). The mean values for three-hourly flux analysis can be found in Appendix D.

Table 7.2 Energy partitioning ratios employed in the spatial model of turbulent fluxes and the coefficients of determination for the relationship between turbulent fluxes and Q^*.

	Q_H/Q^*	Q_E/Q^*	R^2 Q_H-Q^*	R^2 Q_E-Q^*
Degraded tussock	0.78	0.17	0.98	0.48
Short tussock	0.64	0.23	0.95	0.62
Tall tussock	0.58	0.38	0.97	0.97
Rock surface	0.80	0.11	0.84	0.53
Lake surface	-0.03	0.24	0.01	0.09
Snow/ice	-0.11	-0.05	~	~

7.2.1 Model assumptions and sources for error

As with most procedures to estimate spatial patterns of variables that can only be directly evaluated at point locations, there are several assumptions with the approach used in the present study. Firstly, the modelling of Q^* for the catchment surface is a critical component of the modelled turbulent fluxes. The estimated error of Q^* modelling was found to be on the order of 14%, although this was based on a limited number of observational comparisons. Secondly, the observed ratios of Q_H/Q^* and Q_E/Q^* incorporate measurement errors. These inaccuracies include instrumental error, as well as error associated with the spatial comparison of data collected non-concurrently. The assumptions and sources for error in the measurement and comparison of turbulent fluxes can be reviewed in Section 3.4.4. System calibrations and tests showed that reasonable accuracy could be expected from observed fluxes and that comparisons of fluxes observed from different systems are also sufficiently accurate to characterise the micrometeorological behaviour of different surface types. Thirdly and most importantly, this method assumes that the ratios observed at point locations in the Tekapo catchment apply to all grid points classified with the same surface types. This assumption has three sources of weakness. The first is that the grid point may be misrepresented by the surface classification procedure used in this study (Appendix A). Furthermore, grid points with mixed surface properties are classified into

the closest spectral class but may be closer to another class with regard to properties critical to energy partitioning. The second weakness is that not all surface types are strongly correlated to Q^*. This is particularly true for the lake water surface, which was found to correlate more strongly with wind speed (Table 5.9). However, the coefficients of determination for the relationship between turbulent fluxes and Q^* should be considered indicative only, with regard to the accuracy of the modelling method employed here. For example, the hysteresis effect that results from differences in morning and afternoon flux densities due to other factors, such as wind speed or changes in surface moisture concentrations, are partly accounted for in this model since only energy ratios observed during the explicit time period considered in the model are used. Furthermore, the influence of wind speed on turbulent fluxes is partly accounted for by the fact that wind speed is found to increase generally at all locations in the afternoon, and this increase is accounted for as a function of time of day. In this way, the model is driven directly by observations as opposed to statistical descriptors. Nevertheless, it is important to consider the factors that generate spatial variability in surface energy flux partitioning that are not accounted for explicitly by surface type. The three most important parameters were found in observational data to be soil moisture, wind speed and advection and these are discussed briefly in the following paragraphs.

Soil moisture was found to vary spatially by 179% throughout the catchment over the summer of 1998/99 and a negative relationship was found between the Bowen ratio and soil moisture (Figure 4.15 and 5.19). Spatial variability in soil moisture is extremely difficult to predict in complex terrain, since it is a function of many processes and conditions including precipitation, soil properties, topographical drainage patterns and evaporation, which all show strong spatial heterogeneity themselves. However, a significant relationship was also found between vegetation type and soil moisture (Table 5.8). Because of this, surface cover classification partly accounts for the spatial variability in turbulent fluxes associated with spatial variability in soil moisture content.

The relationship between energy partitioning and wind speed was quantified through linear regression between individual fluxes and wind speed for data recorded at each energy balance observation site (Table 5.9). This showed that, of the five surfaces, only the lake water surface showed any relationship. The standard deviation of 10-minute average wind speed recorded at the stations around the lake (AWS8,12,13,14), averaged over the diurnal cycle of February 12 1999 was 1.0 m s^{-1} with a maximum of 2.6 m s^{-1}at 1530 NZST and a minimum of 0.2 m s^{-1} at 0900 NZST. Using the equation for the relationship between wind speed and Q_E:

$$Q_E = 5.9u + 40.1 \qquad (7.4)$$

the mean standard deviation of Q_E for February 12 by this proxy is 6 W m^{-2} with a diurnal maximum of 14.8 W m^{-2}. Using the equation for the relationship between wind speed and Q_H:

$$Q_H = -2.3u - 4.5 \qquad (7.5)$$

the mean standard deviation of Q_H for February 12 is 2.3 W m^{-2}. It can be concluded that, even though wind speed is not explicitly considered in the present model, the error associated with its spatial variability is unlikely to yield significant error in prediction of heat fluxes.

The influence of advection was not quantified from the observational data set since this would require a transect of observations perpendicular to the mean wind across a homogeneous surface and this was not included in the observational programme. However, qualitative assessment was made of the influence of advection and, while it was recognisable in diurnal traces, the magnitude of its influence was small compared with the influence of Q^* or surface type. The most significant occurrence of advection in this data set was found to occur as a consequence of the intrusion of cool moist air from the east in association with a regional scale plain-basin wind. Due to the large scale of this wind system, it is likely that point observations of its mean diurnal influence would be representative of the study area, although larger error is likely from hourly observations due to the different times of onset, cessation and maximum magnitude throughout the catchment.

7.3 Sensible heat flux

This section presents model output of sensible heat flux (Q_H) mapped over the Tekapo catchment surface for February 12 1999, including both diurnal mean and three-hourly instantaneous fluxes. The first is generated from both diurnal mean modelled Q^* and observed energy flux ratios. Three-hourly output is constructed from instantaneous Q^* output and the 30 minute average energy flux ratio most closely associated to the time of interest. For example, 0300 LAT Q_H map includes 0300 LAT instantaneous Q^* and the average energy flux ratio from 0230 to 0300 LAT.

The spatial distribution of diurnal mean Q_H modelled for February 12, 1999 is presented in Figure 7.1. The influence of Q^* is significant and can be qualitatively assessed by comparing this figure to Figure 6.16. Because of this influence, high flux densities are found on north facing slopes with lower densities on south, east and west-facing slopes. The influence of surface properties is also clearly critical and can be assessed by comparing this figure with Figure 3.4. From this influence, the lake surfaces, which are associated with the highest Q^* values contain among the lowest Q_H values. Other important surface cover influences include the very high flux densities found over rock surfaces and also the degraded tussock surface, which is most strongly evident in the south of the study area. The difference between tall and short tussock species is not so easily delineated at the scale used in this graphic, illustrating the relative lack of importance of the boundaries between these species on the spatial distribution of Q_H. The grid points are normally distributed with most falling between 60 and 150 W m^{-2}. A significant peak also occurs at the low end of flux density due to the negative Q_H/Q^* found over lake and snow/ice surfaces.

The spatial distribution of Q_H at three-hourly intervals is presented in Figure 7.2. During the night, when Q^* is negative, only the rock surface shows positive Q_H values due to the continuation of lapse conditions over the warm surface from daytime heating and the large heat capacity of the substrate material. During daylight hours, the solar path is clearly important to the spatial variability of Q_H since it dominates the radiation balance and Q_H/Q^* is high. Q_H over the snow/ice surface remains slightly negative throughout the day, while the lake surfaces fluctuate close to zero. The vegetated surfaces respond more closely to Q^*, peaking at mid-day, and the increase in Q_H over degraded tussock is clearly evident from mid-morning to mid-afternoon, when Q^* is large.

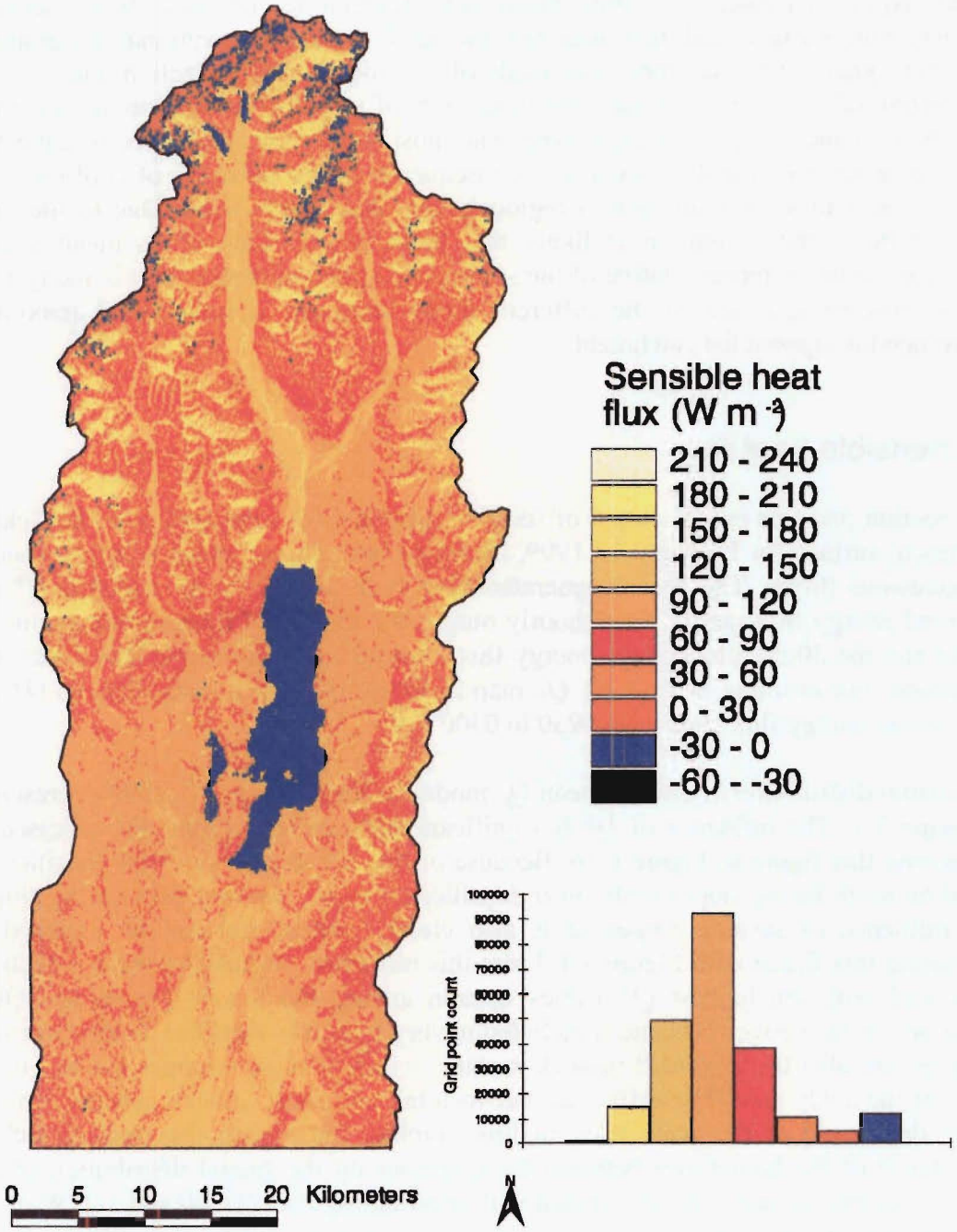

Figure 7.1 Map of modelled Q_H in the Tekapo catchment for February 12, 1999, including a histogram of grid point values.

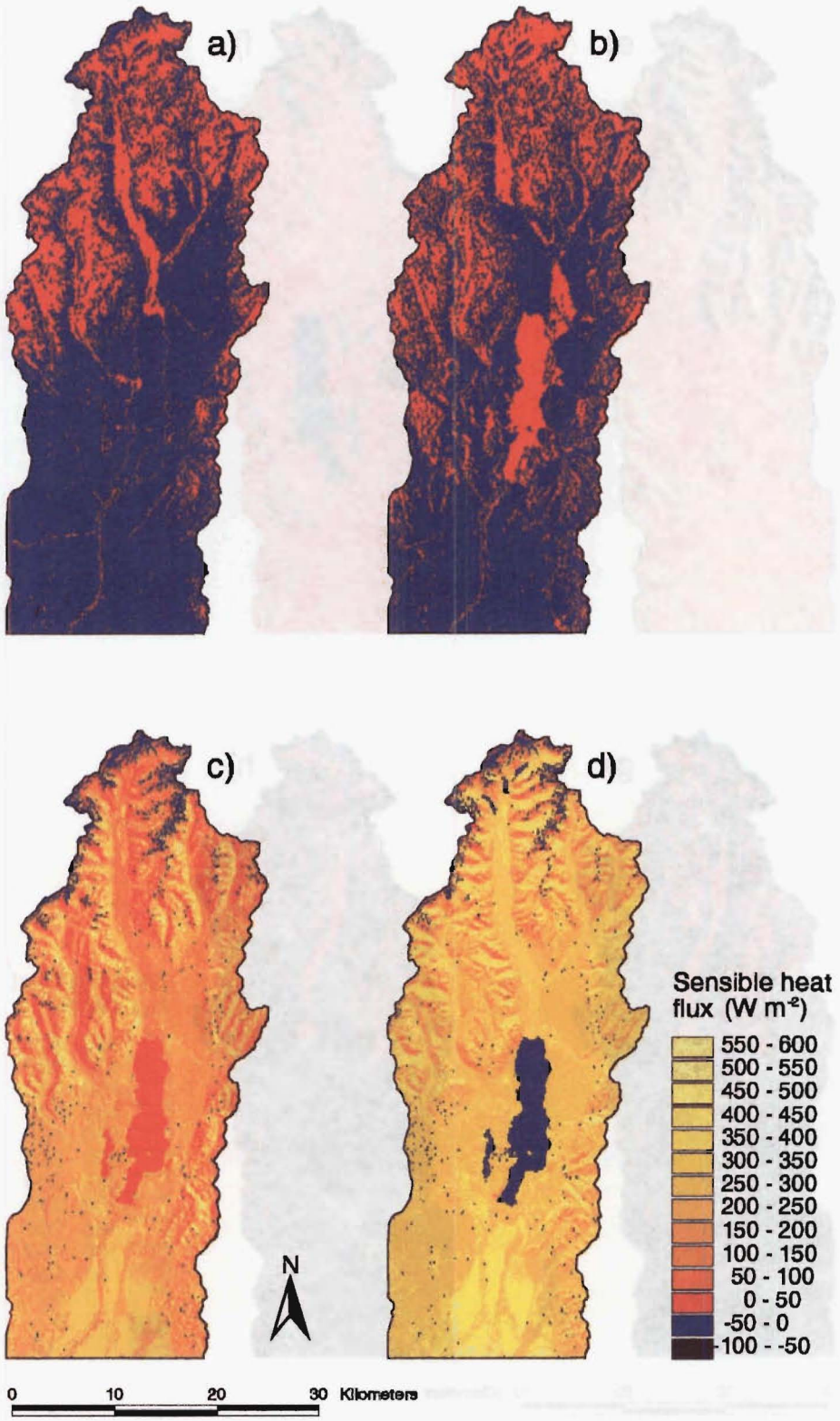

Figure 7.2 Series of maps showing modelled Q_H in the Tekapo catchment at a) 0300, b) 0600, c) 0900, d) 1200, e) 1500, f) 1800, g) 2100 and h) 2400 LAT, February 12, 1999.

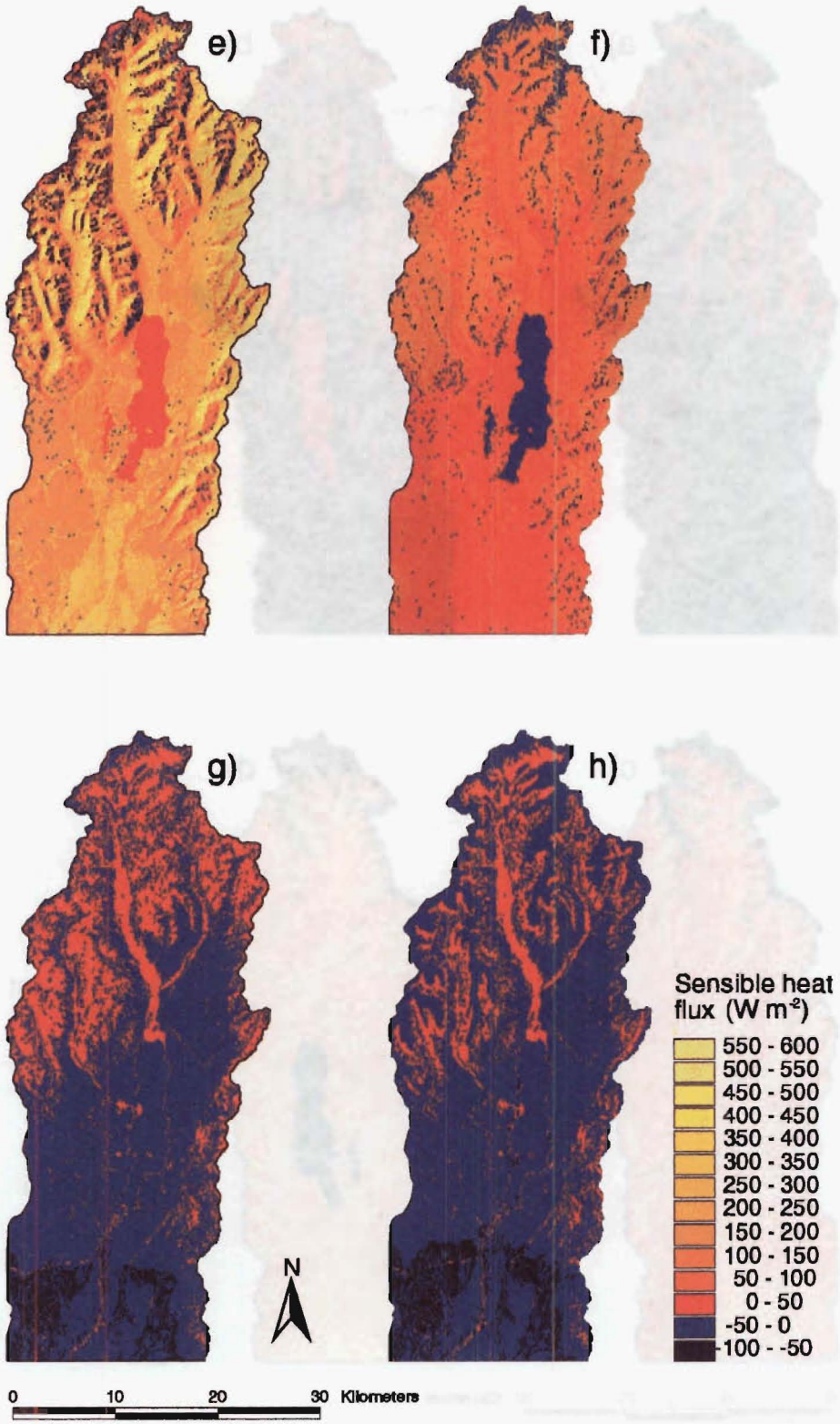

Figure 7.2 continued.

7.3.1 Hourly variability of Q_H

The spatial mean and standard deviation of Q_H at three-hourly intervals is presented in Figure 7.3. Q_H follows a similar pattern to Q^*, peaking at mid-day. The main difference is that Q_H continues to be relatively high through the afternoon in a pattern similar to that observed for the BREB site (Figure 5.2). This pattern probably illustrates the role of cool, moist air advection into the catchment in the afternoon, thereby enhancing Q_H over many surfaces as well as diminishing Q_E in the afternoon due to the depletion of available moisture for evaporation. Spatial variability of Q_H is high throughout daylight hours when mean magnitudes are also high and the spatial variability of Q^* is high. The largest variability appears to occur in mid-afternoon due to the large Q^* variability (Figure 6.21b) at this time, as well as an increase in Q_H/Q^* over some of the surface classes during these hours, particularly rock and degraded tussock.

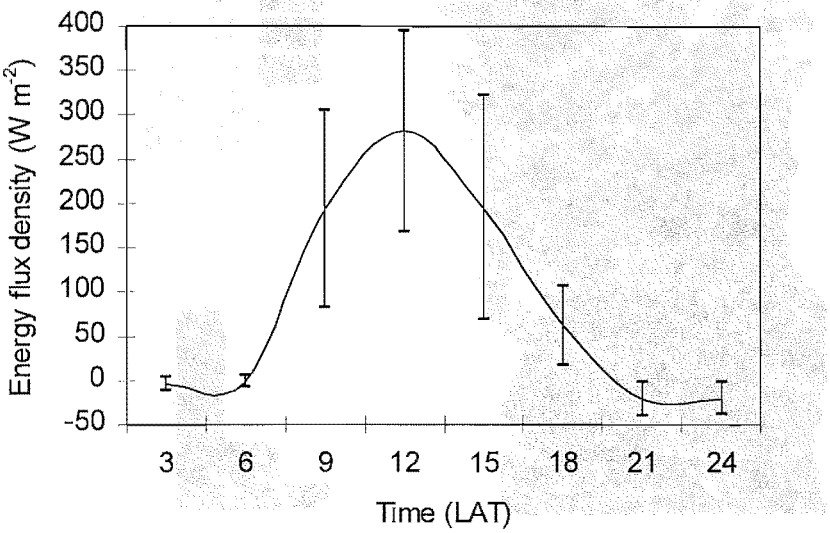

Figure 7.3 Diurnal plot of the spatial mean and standard deviation of Q_H , modelled for the Tekapo catchment, February 12, 1999.

7.4 Latent heat flux

Latent heat flux (Q_E) is examined in this section using the same time frames for analysis as Q_H. Diurnal mean Q_E mapped over the catchment surface for February 12 1999 is presented in Figure 7.4. The range in magnitude and peak distribution of Q_E is significantly lower than Q_H. This was established in Chapter Five when the Bowen ratio for all surfaces except water was found to be greater than one. Negative values are only evident over snow/ice grid points, although the large area of rock surface records negligible flux densities. The largest Q_E values are found over the areas of tall tussock that correspond with highest Q^* values. As with Q_H, Q_E values are fairly normally distributed, but have the peak distribution of grid points occurring between 40 and 60 W m^{-2}.

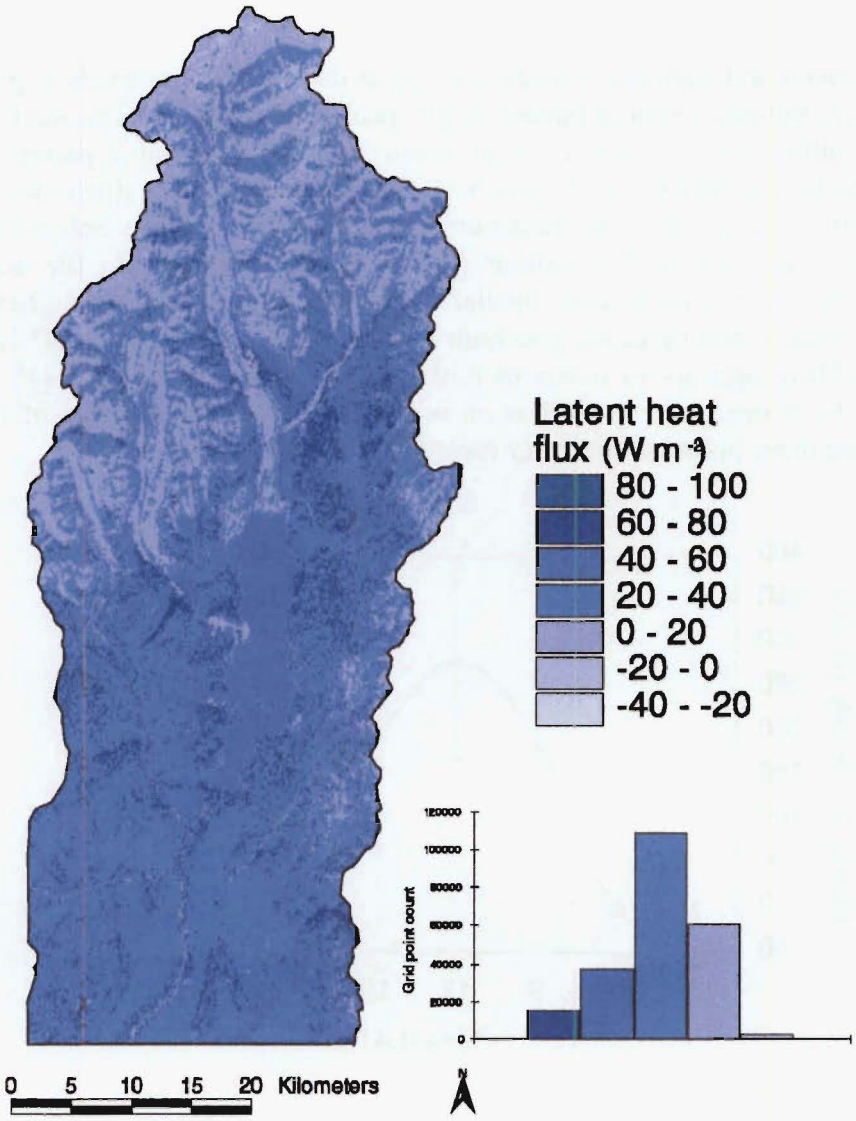

Figure 7.4 Map of modelled Q_E in the Tekapo catchment for February 12, 1999, including a histogram of grid point values.

7.4.1 Evapotranspiration

The spatial variability of evapotranspiration (ET) is determined from Q_E using:

$$ET = \frac{Q_E}{L_v} \tag{7.6}$$

where L_v is the latent heat of vaporisation (MJ kg^{-1}). Thus ET is calculated as kg m^{-2} dy^{-1} which, since 1 kg water = 0.001 m^{-3} = 1 mm m^{-2}, equates to mm dy^{-1}. Since L_v varies as a function of air temperature, and air temperature varies throughout the catchment, L_v is determined from diurnal mean T_a (°C) modelled in SRAD (see Section 6.4 for details) using the polynomial relation determined from data presented in Oke (1987, p392):

$$L_v = T_a^2 \times 10^{-5} - 0.0026T_a + 2.5009 \tag{7.7}$$

ET modelled over the catchment surface for February 12, 1999 is presented in Figure 7.5. The spatial pattern of *ET* differs very little from Q_E since the diurnal mean temperature range in the catchment (9.6 °C) equates to a range in L_v of 0.025 MJ kg^{-1}, which is only 0.01 mm *ET*, using the diurnal and spatial mean Q_E (32 W m^{-2}). A range of 3.6 mm exists over the catchment surface, with a mean of 1.1 mm and a standard deviation of 0.55 mm.

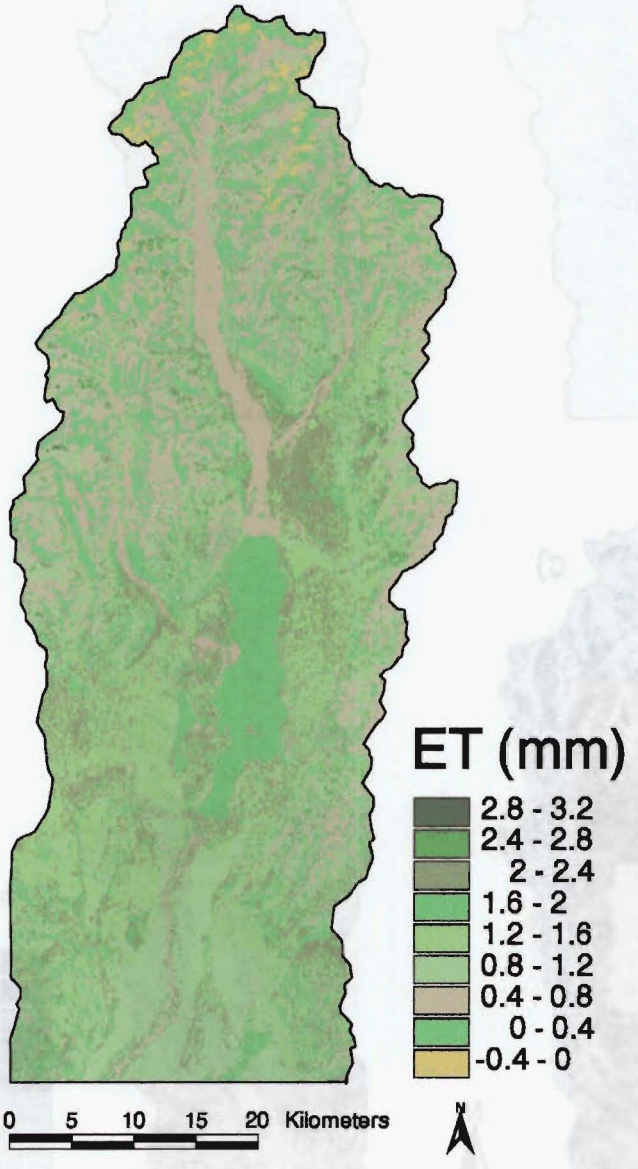

Figure 7.5 Map of modelled evapotranspiration in the Tekapo catchment for February 12, 1999.

7.4.2 Hourly variability of Q_E

The spatial pattern of Q_E modelled over the catchment surface at three-hourly intervals is presented in Figure 7.6. Large diurnal variability is evident in the plots, with very low or negative fluxes found during the night.

Figure 7.6 Series of maps showing modelled Q_E in the Tekapo catchment at a) 0300, b) 0600, c) 0900, d) 1200, e) 1500, f) 1800, g) 2100 and h) 2400 LAT, February 12, 1999.

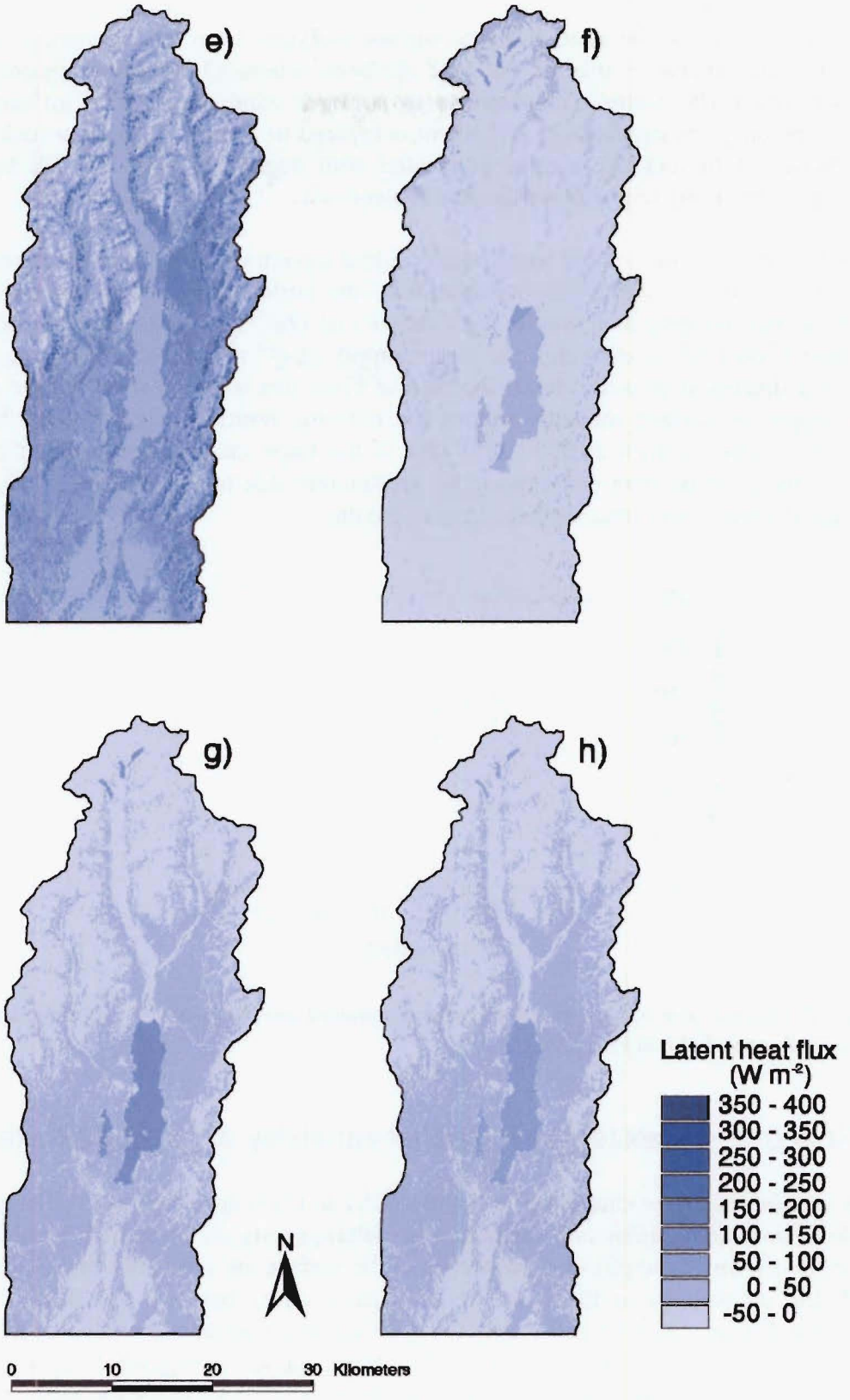

Figure 7.6 continued.

Fluxes over all land surfaces appear to be stronger in the morning than afternoon daylight hours, due to the availability of surface moisture from dew formation during the night. The reverse is true of the lake surfaces, where Q_E increases through the afternoon and early evening in response to stronger wind speed. The influence of surface type on Q_E is particularly prominent compared to Q^* and Q_H. In particular, the three classes of tussock are clearly delineated with degraded, short and tall tussock recording increasingly larger flux densities respectively.

The plot of three-hourly spatial mean and standard deviation of Q_E over the catchment surface in Figure 7.7 shows the importance of the larger fluxes occurring over land surfaces in the morning as a whole. This shows that Q_E/Q^* was sufficiently greater at 0900 than 1200 LAT to outweigh the larger supply of Q^* at 1200 LAT. As suggested above and discussed in more depth in Chapter Five, this was found to be due to the larger supply of surface moisture during the morning hours for evaporation. Spatial variability is also greatest at 0900 LAT due to the large mean magnitudes. It is also higher in the evening than early morning, presumably due to the increase in Q_E over water and decrease over land surfaces later in the day.

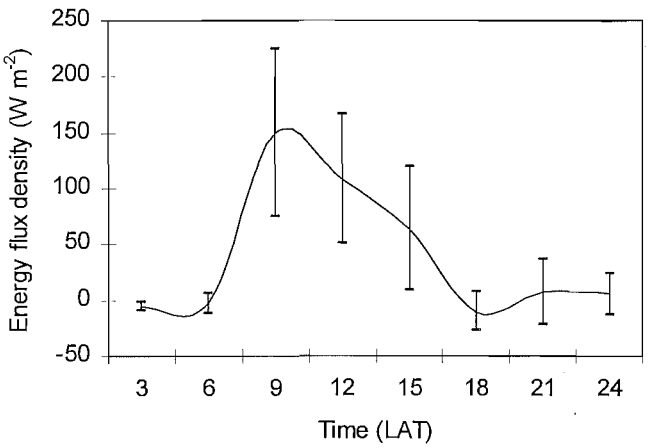

Figure 7.7 Diurnal plot of the spatial mean and standard deviation of Q_E , modelled for the Tekapo catchment, February 12, 1999.

7.5 Role of complex terrain in spatial variability of turbulent fluxes

In this section, the three catchment sub-areas (CS1 to CS3) are employed to investigate the role of both topographic and surface cover heterogeneity on the spatial variability of surface fluxes. Since the physical properties of the surface are critical to the partitioning of Q^*, the differences in the make-up of surface cover between the three CS are provided in Figure 7.8. CS1 is the only CS with snow/ice surfaces and also contains by far the largest proportion of rock surface. The three classes of vegetated surface are of similar size, although small by comparison to the rock surface, while the water surface area is negligible. By comparison, the bulk of water surface (Lakes Tekapo and Alexandrina) exists in the lake basin area (CS2), which is also dominated by tall and short tussock species. A considerably larger proportion of degraded tussock exists in the dryer Mackenzie Basin area (CS3), which is also dominated by short tussock and, to a much smaller extent, tall tussock. Both rock and water surfaces are negligible in CS3.

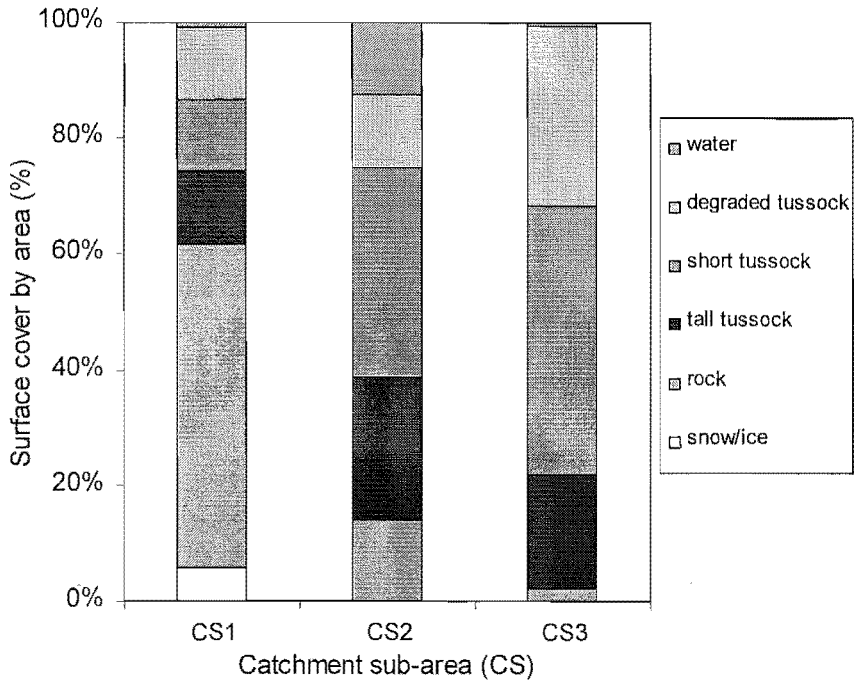

Figure 7.8 Proportional surface area covered by each surface class for three catchment sub-areas.

These findings provide evidence of the relationship between surface cover, topographic properties, precipitation and geomorphological processes as discussed in Chapter Three. In the steeper, higher, wetter terrain of CS1, snowfall is more prevalent, and erosion rates are extremely high. Because of this, soil development, and subsequently vegetation, is less spatially prevalent, with over half the surface area dominated by rock surface. In the dry, flat terrain to the south, the landscape is dominated by tussock grassland with a large proportion of degraded tussock. In between (CS2), where topographic complexity and precipitation are intermediate of the other two areas, the surface is dominated by vegetation with the highest proportion of tall tussock of the three areas and significantly smaller coverage of degraded tussock. Furthermore, relic erosional features have been subsequently filled with runoff from the mountains, forming the largest area of lake surface of the three CS.

7.5.1 Mean diurnal turbulent fluxes

The relative spatial mean and standard deviation of energy transfer from Q^* to turbulent fluxes for the three CS is provided in Table 7.3. Firstly, Q^* values have been reproduced from the previous chapter (Table 6.6). Secondly, spatial statistics for energy flux ratios and densities of both Q_H and Q_E are calculated for each CS. The spatial mean and standard deviation of turbulent fluxes are therefore found as a function of the spatial statistics for Q^* and surface cover, and the role of surface composition on energy partitioning. Therefore, it is not just spatial heterogeneity of either Q^* or surface cover that generates high spatial variability of turbulent fluxes, but the level of contrast of energy partitioning that occurs between different surfaces in a given area. Consequently, despite significantly lower spatial variability of Q^* in CS2 than CS1, the variability of Q_H is similar due to a higher variability in Q_H/Q^*. Despite the fact that surface cover heterogeneity is more complex in CS1 than CS2, the reason for the large

variability is due to the distinctive micrometeorological contrast between the land surfaces and the large area of water surface.

Table 7.3 Descriptive spatial statistics for energy partitioning in three Tekapo catchment sub-areas. Ratios are derived by integrating all catchment subarea gridpoints, not from the catchment subarea mean values.

	Mean			Standard deviation		
	CS1	CS2	CS3	CS1	CS2	CS3
Q^* (W m^{-2})	131	163	162	58	28	15
Q_H/Q^*	0.69	0.58	0.67	0.22	0.24	0.09
Q_H (W m^{-2})	97	92	110	46	43	19
Q_E/Q^*	0.16	0.24	0.22	0.11	0.09	0.08
Q_E (W m^{-2})	22	40	38	16	14	12
β	5.3	3.0	3.2	2.4	2.2	1.3

With regard to mean Q_H/Q^*, the large areas of rock surface in CS1 and degraded tussock in CS3 produce the largest spatial means. However, the significantly lower mean Q^* in the more topographically complex CS1 offsets this potential and CS3 consequently has a significantly higher mean Q_H. The largest magnitude of mean Q_E occurs in CS2, the sub-area which contains the largest areas of water, tall tussock and short tussock, which have the highest Q_E/Q^* ratios. This is closely followed by CS3, with a significant drop to CS1, which is dominated by rock surface with low Q_E/Q^* and also contains a significant portion of snow and ice which has a negative Q_E/Q^*. The spatial variability of Q_E is similar in the three CS due to the small differences in variability of Q_E/Q^* which decrease from CS1 to CS3 as a consequence of the same trend in both Q^* and Q_E/Q^*.

The Bowen ratio (β) is also calculated for the three CS. Both the mean and spatial variability of β are largest in CS1. The mean value is in response to the large area of rock surface, and the spatial variability due to the heterogeneity of surface cover. However, CS2 shows spatial variability in β almost as large as CS1, illustrating the importance of the micrometeorological contrast in surface types, despite a more homogeneous surface cover. CS2 also records the lowest β for the same reasons, as it shows the lowest Q_H and highest Q_E as discussed previously.

7.5.2 Comparisons of diurnal variability

Plots of the three-hourly spatial mean and standard deviation for both Q_H and Q_E in each of the three CS are presented in Figure 7.9. Firstly, it is clear that the difference between Q_H and Q_E in all three CS is significantly larger than the inter-CS differences of either Q_H or Q_E. This shows that, despite the large range in energy partitioning found in each CS, spatial averaging merges the three CS to a large degree. This has important implications for spatial modeling and suggests that, even in complex terrain, spatial averages of surface energy fluxes at the sub-grid scale may yield appropriate approximations for applications in hydrological, biological and atmospheric models. The diurnal patterns of the individual CSs show similar trends to each other as well as to the catchment means (compare Figure 7.9a with 7.3 and Figure 7.9b with 7.7). The larger afternoon Q_H over the warm rock surface is also evident in the CS1 trace compared with CS2 and CS3.

The spatial variability of turbulent fluxes in the three CS shows considerable complexity. In both Q_H and Q_E cases, the magnitude of variability appropriately follows the magnitude of mean fluxes. However, CS1 is likely to be influenced by Q^* significantly to allow the reduction of variability found at midday as with Q^* (Figure 6.21). CS2 shows higher variability in Q_H in the afternoon than morning, probably due to the relatively high Q_H over tussock surfaces in the afternoon contrasting with the drop to negative values over the lake surface at this time. With Q_E, CS2 also shows a midday decrease as the tussock surfaces showed higher Q_E in the morning, while the lake surface showed higher Q_E in the afternoon and evening. The sharp reduction in Q_E over the rock surface in the afternoon, also appears to dramatically reduce the spatial variability in the flux of Q_E in CS1.

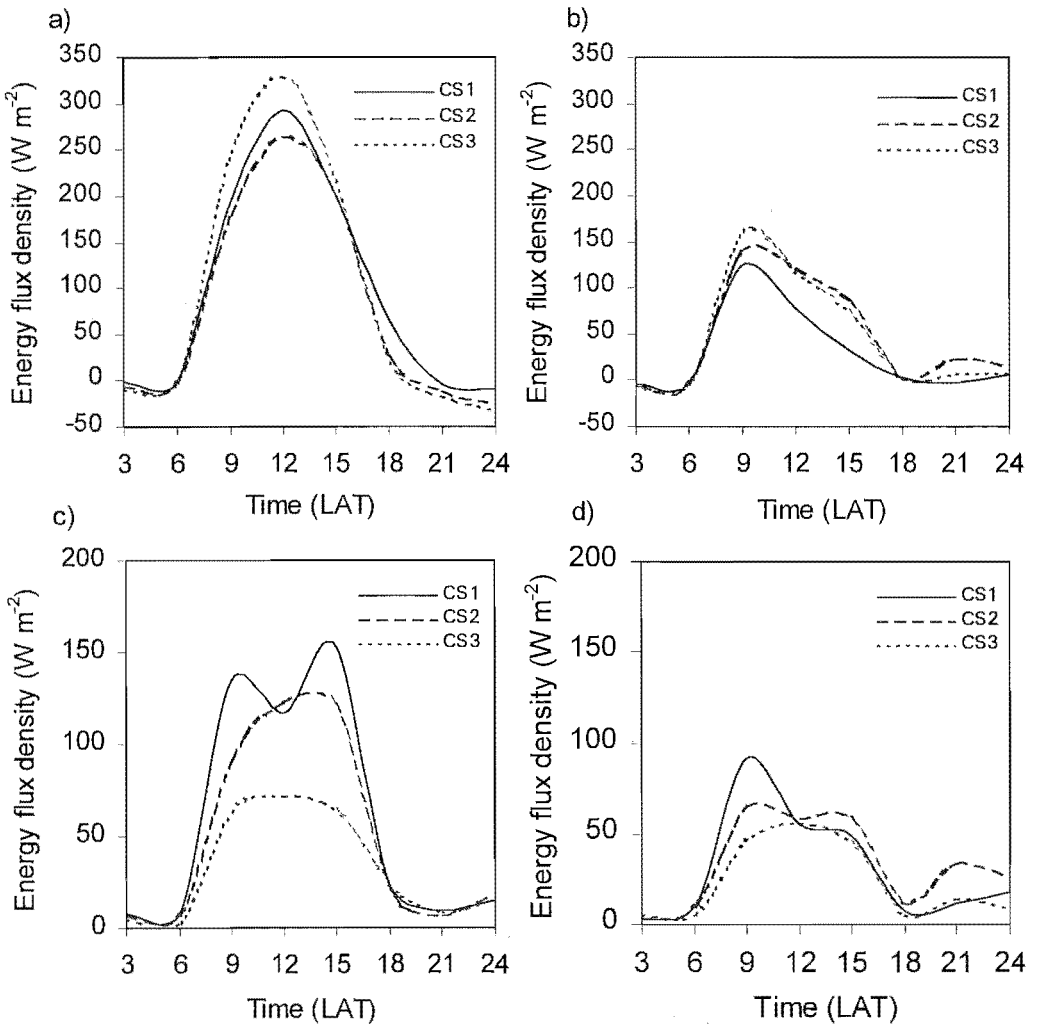

Figure 7.9 Diurnal plots comparing modelled hourly mean a) Q_H and b) Q_E, and standard deviation of c) Q_H and d) Q_E for three catchment sub-areas on February 12, 1999.

In conclusion, both topographic complexity and surface heterogeneity play a large role in spatial variability of turbulent fluxes. The extent of the role depends on, not just the complexity of the landscape, but the contrast of micrometeorological characteristics between surface types within a particular area. Despite this, spatial averages of the fluxes were found to be surprisingly consistent over three areas of strongly contrasting topographical complexity and surface heterogeneity.

7.6 Summary

This chapter has served to investigate the spatial variability of Q_H and Q_E for a clear-sky mid-summer day in the Tekapo catchment. Turbulent heat flux maps were constructed using the results from the previous two chapters. Modelled Q^* from Chapter Six was used in conjunction with turbulent flux densities, non-dimensionalised with reference to Q^*, that were observed over each of the major surface classes of the catchment. The model was constructed in a GIS environment. Since energy partitioning information was restricted to surface types, the model assumes other spatially varying micrometeorological parameters were negligible. The most important of these were found to be soil moisture, wind speed and advection, although these controls were found to be either partially linked with, or significantly less important than, surface type.

Maps and spatial statistics of diurnal mean and three-hourly instantaneous fluxes of Q_H and Q_E, as well as evapotranspiration, were then presented. Significant spatial variability was found to be linked relatively equally between spatial variability of Q^* and surface heterogeneity. With regard to the latter, the micrometeorological differences between surface types were found to be as important as the complexity of surface heterogeneity in generating spatial variability of turbulent fluxes. Despite this, spatial averages for three strongly contrasting topographical sub-areas were relatively consistent, providing confidence in the use of spatial averaging for sub-grid areas of numerical models.

Chapter Eight:

Conclusions

8.1 Introduction

The purpose of this chapter is to summarise the main findings of this study and to discuss their implications in the context of boundary layer meteorological research. In order to achieve this objective, this chapter first revisits the original research goals and discusses the extent to which they have been realised. This is followed by a brief overview of the main findings and a discussion of their implications as well as their limitations. Finally, the chapter concludes with suggestions for future research and the ways by which some of these limitations may be overcome. In this way, the chapter hopes to place the current findings within the framework of both past and future efforts to ascertain the spatial and temporal controls on surface energy exchanges in complex terrain.

8.2 Re-examining research objectives

It was proposed in Chapter One, that one of the most important issues facing mesoscale modelling and atmospheric energy budget studies in complex terrain is addressing the complicated pattern of energy fluxes that occur at the boundary of the Earth's surface. Until these processes are captured in appropriate spatial and temporal resolution, many boundary layer characteristics and phenomena in complex terrain cannot be fully understood. This study was designed to improve understanding of the characteristics and mechanisms of spatial and temporal variability in surface energy fluxes within a large alpine catchment. More specifically, the objectives were to:

1. Evaluate temporal variability of the magnitude of surface radiation and energy fluxes in response to seasonal and synoptic controls.

2. Evaluate spatial variability of the magnitude of surface radiation and energy fluxes within a complex alpine catchment during clear-sky summer days and determine the major controlling factors with regard to topographic characteristics and physical properties of the surface.

3. Map the spatial pattern of surface radiation and energy fluxes throughout the catchment on a scale appropriate to the complexity of the landscape, and evaluate the role of surface complexity on their spatial variability.

Following the theoretical and environmental background provided in the early chapters, each of these objectives was examined in turn from Chapters Four to Chapter Seven. The extent to which these objectives were met is discussed below with respect to each of the principle objectives.

The temporal controls of surface energy fluxes at single sites have been the subject of numerous studies, although these have tended to focus on relatively flat and homogenous terrain. A Bowen ratio energy balance system and radiation sensors measured energy and radiative exchanges at a single location in the MacKenzie Basin for a period of fourteen months. This yielded a unique dataset that provided an update to earlier work in the Southern Alps (Greenland 1973), and included discussion of the reasons for similarities and differences between the two studies. It also allowed comparison between fluxes observed in this particular setting with observations made in mountainous settings at other locations (*e.g.* Whiteman *et al.* 1989, Kalthoff *et al.* 1999, Hennemuth and Kohler 1984, Saunders and Baily 1996). The influence of multiple scales of airflow and airmass characteristics that are representative of mountainous regions were evident at this location.

The second objective was to determine the spatial variability of surface fluxes, and this was carried out using observational data collected at one fixed Bowen ratio station and three mobile eddy covariance stations. Data were obtained for clear-sky summer days at nine locations. Observations were made over the five dominant surface classes in the catchment. From this dataset, energy balances could be derived for each surface class, providing a unique opportunity to assess the spatial variability associated with heterogeneity of surface properties within a relatively small, yet complex area. The observational data illustrated a large range in surface fluxes related to radiative, thermal, hydrological and vegetative properties of the surface. However, while many of the mechanisms responsible for differences in surface radiation and energy balances could be inferred from these data, quantification of the role of many processes was not possible due to the small size of the dataset, and the fact that simultaneous observation of multiple surfaces was limited by the number of energy balance stations available. The dataset was further limited by the inherent difficulties in making energy balance observations in complex terrain. Nevertheless, characteristic energy balances could be derived for each surface class, thereby providing a classification of surface-driven energy balances that could be applied in a spatial model to the entire catchment.

The aim of investigating temporal variability in surface energy fluxes was also to provide a temporal context for the observed spatial variability of surface fluxes (which were made over a relatively short time frame). Consequently, it can be concluded that the large spatial variability of surface fluxes found in Chapters Five through Seven would probably be reduced in winter when lower overall radiation budgets were found together with a more stable surface layer and higher surface moisture values. This is also true of cloudy periods, which were found to occur most commonly during cyclonic northwest and southwest synoptic situations. During anticyclonic conditions, cloud was found to be least prevalent, and the multitude of small to regional scale airflow

produced the largest range of fluxes over the diurnal cycle. It is likely that calm anticyclonic conditions would also produce the greatest spatial variability in surface energy fluxes, since these conditions allow the greatest expression of surface microclimate.

The second and third objectives were also addressed through surface radiation budget modelling of the entire catchment surface at a spatial resolution of 100 m. Evaluation of model performance through point measurements yielded good confidence in the predicted results. Sensitivity analyses illustrated the influence of various terrain properties on the spatial variability of surface radiation fluxes. Furthermore, the results of sensitivity analyses provide valuable information for application to other mountainous regions. Currently, it is not possible to provide this level of detail in mesoscale atmospheric models and most do not include algorithms for processes such as shadowing, sky view factor and separate consideration of diffuse and direct beam shortwave radiation. These attributes all proved to be significant controls of spatial variability of the surface radiation budget.

The final objective was to produce maps of the individual energy budget components over the entire catchment surface. The results from this are strongly dependent on the radiation budget model output and the accuracy and spatial representation of point energy balance measurements. As noted above, the radiation model showed good agreement with observations. Furthermore, observations of surface energy budget partitioning showed significantly smaller differences within each surface class, than between differing surface classes, giving some confidence in the assumptions on which the modelling of surface energy balances over the entire catchment was based. However, theoretical constraints on the measurement of surface fluxes in complex terrain meant that observations were restricted to reasonably simple topographic settings, which may not be representative of more complex parts of the catchment. Furthermore, variability was found in surface fluxes in response to different levels of soil moisture and to advection, particularly of cool, moist air. The dataset used to describe these differences was not sufficient for complete quantification of the role of these spatially varying properties. However, it was noted that a significant relationship existed between soil moisture and vegetation species, so some of the variability in soil moisture was accounted for by surface classification of the energy budget. Another limitation of this approach is the dependence of energy balance components on net radiation. This was found to be realistic for most surfaces except the water surface, which was more strongly correlated with wind speed. However, this too is indirectly accounted for in the model by producing independent simulations for each hour of the day. In this way, the diurnal pattern of wind speed and its influence on energy partitioning was included in the model.

It is concluded that the aims of this research were met successfully and yielded valuable information on the temporal and spatial variability of surface energetics in an alpine catchment. However, several assumptions and limitations are inherent in the approach taken to realise these objectives. These will be discussed further in section 8.4 with the purpose of developing potential improvements for future research, thus building on the findings of this study.

8.3 Summary of main findings

This section provides a summary of the major results of this research. The order in which these results are outlined follows the structure of the four chapters (Chapter Four through Seven) in which research findings were presented.

In Chapter Four, the seasonal and synoptic controls of surface fluxes were examined. Initially, radiation flux densities were considered. The seasonal range in Q^* was found to be 14.2 MJ m^{-2} dy^{-1}, which resulted primarily from variability in K^* (21.1 MJ m^{-2} dy^{-1}) and secondly from L^* (6.3 MJ m^{-2} dy^{-1}). Day to day variability for both Q* and K* values were approximately equal to seasonal ranges, while L^* produced significantly greater ranges due to synoptic influences (10.6 MJ m^{-2} dy^{-1}). This variability was seen to be most significantly a function of cloudiness. Cloudiness was found to vary significantly from one end of the study area to the other as a function of topography and proximity to the alpine divide. This produced ranges in $K\downarrow$ at the headwaters of the catchment of 35.4 MJ m^{-2} dy^{-1} compared with 33.0 MJ m^{-2} dy^{-1} in the lower basin area. Furthermore, the former site had a 20% lower mean annual $K\downarrow$ resulting from the generally greater cloud cover, as well as topographic shading. Modelling $K\downarrow$ for clear-sky days agreed closely with observed values. The seasonal impact of $K_S\downarrow$ was modelled for the range of sloping surfaces found within the study area, with the mean annual flux densities for all slopes having a range of 17.3 MJ m^{-2} dy^{-1} and a maximum of 28.8 MJ m^{-2} dy^{-1}. The largest range associated with slope at any one time was found during the equinox when a range of 20.3 MJ m^{-2} dy^{-1} was found between south-facing 60° slopes to north-facing 40° slopes. This was reduced slightly at the summer equinox (18.7 MJ m^{-2} dy^{-1}), but was significantly less at the winter equinox (11.2 MJ m^{-2} dy^{-1}) due to shorter daylight periods during the diurnal cycle.

The partitioning of net radiation among energy budget components for degraded tussock also showed considerable differences between summer and winter and under different synoptic situations. The most extreme variability was found in the partitioning between Q_H and Q_E, which was found to vary significantly between summer and winter. Daily Bowen ratio (β) values ranged from 6.85 during the 1997/98 summer to –0.13 for the 1998 winter and 9.38 for the 1998/99 summer. A reasonably consistent logarithmic relationship was found between β and soil moisture content for all data, irrespective of season or synoptic situation. The daily net loss of Q_H from the atmosphere to the surface in winter was found to be the result of very strong nocturnal surface layer temperature inversions and the dominance of Q_E in the transfer of energy during daylight hours.

Lowest β values were found during northwest airflow and southwest airflow. The lower β during northwest flow was found to be a function of the relatively warm and dry air advection that occurs during these conditions. The lower β associated with southwest flow in summer was considered to result from the potential for soil moisture to be higher following the passage of a front, often associated with this synoptic situation. In winter, southwest flow produced higher β values, which were thought to be a result of cold air advection and the propensity for frost formation, which resulted in a significant release of Q_E by night. Overall, the largest impact on surface energy fluxes over time was found to result from synoptic controls on the magnitude of net radiation. The second strongest variability resulted from seasonal control on the partitioning of turbulent fluxes.

Observations of surface radiation and energy fluxes at different locations during the same time period also revealed a significant range in flux densities. Within the catchment, the lake surface recorded the highest daily total Q^* values of the five surface types, rock surfaces recorded the lowest and the three vegetated surfaces recorded very similar flux densities. Although some variability was associated with topographical differences between sites, the main influence was the radiative properties of the surface. In particular, mean diurnal albedo and the ratio between $L\uparrow$ and absorbed allwave radiation accounted for the differences observed in daily radiation budgets. Diurnal changes in albedo were found to relate closely to solar zenith angle, with large variability in this relationship between different surfaces. The lake surface showed the largest diurnal range, although both short and tall tussock had significant ranges, while degraded tussock and rock surfaces varied minimally. For all surfaces, the relationship between Q* and $K\downarrow$ was statistically significant. Overall, a large range in Q^* was observed, illustrating the importance of these radiative properties for the surface energy budget.

The partitioning of Q^* into Q_H, Q_E and Q_G was also found to vary significantly due to properties of the surface cover. The highest β was observed over the rock surface with decreasing β found over degraded tussock, short tussock and tall tussock respectively. A relationship was established between plant species, soil moisture and evapotranspiration, illustrating both the hydrological controls on species location and the ability of tussock species to conserve water through stomatal control. By contrast, the lake surface utilised most available energy for heat storage in the lake volume, with small Q_E and slightly negative Q_H. The relationship established between soil moisture content and β over five vegetated surfaces was similar to the relationship observed for degraded tussock at different times, although significantly fewer data reduced the confidence in this finding. Statistical analyses of the relationship between energy components and Q^* and wind speed revealed the strong dependence of energy components on Q^* over short and tall tussock species. Degraded tussock and rock surfaces showed weaker dependence on Q^* with some (albeit small) relationship with wind speed. This reflected the importance of wind speed for turbulent transfer over surfaces with short roughness lengths, small moisture supplies and lack of physiological controls of vegetation. In contrast, the lake surface showed virtually no relationship between turbulent fluxes and Q^*, while a significant relationship existed with wind speed. Conversely, ΔQ_S was found to depend almost entirely on Q^* over the water surface.

The sixth chapter investigated the causes for spatial variability in surface radiation fluxes in the Tekapo catchment. Modelling of radiation flux components was utilised for this purpose using SRAD, a topographically based mathematical model. Output from the model compared well with observations, with closer agreement found for daily mean than instantaneous fluxes. Overestimation of both incoming radiative components and much smaller underestimation of outgoing components resulted in a net overestimation of Q^* by 14%. Of the radiation components, $K\downarrow$ contributed most significantly to the radiation budget both in terms of the mean and variability of flux magnitudes. The variability in $K\downarrow$ was associated most strongly with slope aspect, secondly with slope angle, thirdly with shading, and finally with elevation. $K\uparrow$ also varied considerably as a function of both the variablility found in $K\downarrow$ and albedo. By contrast, longwave radiation fluxes contributed little variability to the spatial distribution of Q^*. L^* was governed most strongly by elevation with sky view factor, radiation ratios and leaf area indices having relatively smaller control. Diurnal

variability was assessed for each radiation component. Again, $K\downarrow$ dominated the diurnal radiation cycle, with greatest spatial variability occurring in mid morning and afternoon due to the approximately north-south orientation of the dominant topography.

The role of topographic complexity on the spatial distribution of fluxes was investigated by comparing three sub-areas of the Tekapo catchment that showed strongly contrasting topographical properties. Increase in topographic complexity was associated with decrease in mean Q^*, but a large increase in spatial variability. This influence was governed primarily by $K\downarrow$. Other components yielded similar averages between topographically different areas, although spatial variability in all fluxes was significantly increased with greater complexity.

The final chapter served to investigate the spatial variability of Q_H and Q_E for a clear-sky mid-summer day in the Tekapo catchment. Turbulent sensible and latent heat flux maps were constructed using the results from the previous two chapters. Modelled Q^* was used in conjunction with observed turbulent flux densities non-dimensionalised by Q^*. Since energy partitioning information was restricted to surface types, the model assumed other spatially varying micrometeorological controls were negligible. The most important of these was found in observations to be soil moisture, wind speed and advection, although these controls were found to be either partially linked with, or significantly less important than, surface type.

Maps and spatial statistics of diurnal mean and three-hourly instantaneous fluxes of Q_H and Q_E, as well as evapotranspiration, showed that large ranges in surface energy flux density exist at any given time, although these are greatest near mid-day. This spatial variability was found to be linked relatively equally between spatial variability of Q^* and surface heterogeneity. With regard to the latter, the contrast in energy partitioning between surface types was found to be as important as the spatial heterogeneity of surface cover in generating spatial variability of turbulent fluxes. Therefore, it is not just surface heterogeneity that is important in generating spatial variability of surface fluxes, but the magnitude of micrometeorological difference between surface types. Despite the large ranges in flux densities found throughout the catchment, spatial averages for three strongly contrasting topographical sub-areas were relatively consistent, providing some confidence for the use of spatial averaging for sub-grid areas of numerical models.

These results show that topography and surface cover yield considerable control over the magnitude of surface energy fluxes in complex terrain. The variability associated with surface cover is controlled by the radiative properties of the surface, as well as its hydrological properties, its heat capacity and roughness length. Of secondary importance to spatial variability of the surface energy balance, location played a role through advection, both in terms of turbulent transfer (wind speed) and airmass characteristics (temperature and humidity). Overlying air mass properties were also found to be important for seasonal and synoptic controls on the temporal variability of surface fluxes.

8.4 Limitations and future research

Several areas for future research could be instigated as a result of this research. Firstly, while many mechanisms responsible for both temporal and spatial controls of surface energy fluxes could be inferred, many could not be quantified with sufficient

confidence due to the small size of the dataset. In order to make statistically significant conclusions about the controls exerted by synoptic patterns and seasonal trends, longer term data would be required. For example, significant variations were noted between two summer seasons, possibly corresponding to large differences in the Southern Oscillation Index, making characterisation of seasonal patterns difficult. A similar conclusion can be drawn about observations of spatial variability in surface energy fluxes. By using point measurement, a compromise was drawn between quality of data and spatial coverage. Many of these problems would be overcome using a larger dataset with greater spatial density of observation sites. For example, the effect of slope properties on surface energy fluxes might be more readily assessed by making observations in a small valley with homogeneous surface cover. However, this would not remove the spatial variability of properties such as soil moisture and its links with the type and density of vegetation. In this way, as well as through geomorphological controls, topography and surface cover are not mutually exclusive landscape characteristics. Thus, observations made over such a surface would not produce results that could be applied to the reality of much of the Earth's surface.

In order to accurately observe the spatial patterns of fluxes over the entire catchment, new measurement systems, currently unavailable, would be required. Thus, until observational instrumentation can be developed to overcome many of the difficulties of measuring surface fluxes in complex terrain, the nature of fluxes in mountains cannot be fully accounted for. The source for such measurements will most likely come from remote sensing, although significant progress is required with regard to the matching of spatial and temporal resolution, as well as accuracy in quantification of near-surface properties and fluxes of scalars from irradiance values.

While the surface radiation budget model used in this study showed good agreement with observations, the observational dataset used for evaluation was limited by its spatial coverage. Thus, the radiation fluxes modelled for very steep or high terrain were not rigorously tested. Despite its sophistication compared with past surface radiation models, several improvements could be made with SRAD to better represent the physics of radiative transfer at the surface. The model currently derives incoming longwave radiation for clear sky days as a function of near surface air temperature. The reason for this is to be able to apply the model to regions where only basic meteorological parameters at a single site are measured. However, were atmospheric soundings available, longwave flux could be calculated with greater accuracy from integration of temperature and humidity through the atmospheric column. It was shown from observations that for most surfaces, albedo varied significantly throughout the day as a function of solar zenith angle. Since non-horizontal topography generates spatial variability in the effective zenith angle, a more accurate spatial model of albedo would need to account for the specific solar incident angle for each grid point at each time step. Further improvement could come from dealing with the anisotropy of incident solar radiation received from reflection from surrounding terrain. This question has been ignored in previous studies, due to its comparatively small importance relative to the level of complexity and computational expense of the model. However, an empirical model could be readily developed from an array of pyranometers, which could be applied to topographical models relatively inexpensively by adjusting the incoming reflected component by an amount dependent on slope aspect and time of day.

Since the energy partition model was generated from observations, the accuracy of the spatial modelling of energy balance components could not be adequately evaluated. The accuracy of this model therefore, is strongly dependent on the spatial representation of a

number of point measurements. The validity of the assumption of spatial representation was discussed at some length at the outset of Chapter Seven. This pointed to sources of invalidity associated with instrument error, assumptions in the surface classification and spatial variability in soil moisture and advective effects. These points were analysed using observational evidence and theory, and it was concluded that the generalisation of these point measurements to the entire catchment was likely to be reasonable, particularly using diurnal means, although this cannot be rigorously tested. Furthermore, while the differences between surface types were clearly larger than the differences found within individual surface classes, observations were restricted to locations with reasonably simple slope and surface properties due to limitations of the measurement technique. Clearly, much of the catchment surface cannot be so simply characterised. A useful direction for future research on this problem would be to utilise surface energy balance schemes in mesoscale atmospheric models. This would be particularly useful in analysing the influence of horizontal advection on surface energy fluxes as well as the role of convergence and divergence in generating vertical advection. Inclusion of hydrological model output of the spatial variability of soil moisture levels due to soil, radiative and topographic properties of the surface would also be useful. However, each of these modelling techniques have their own set of significant limitations and assumptions, and do not provide solutions in themselves. Furthermore, they are equally limited by the accuracy of surface cover classification and the spatial representation of input data. It is likely that the future success of modelling surface energy fluxes in complex terrain relies on the integration of multiple techniques and the collaborative expertise of hydrological, biological and atmospheric scientists.

This thesis has presented research on the temporal and spatial variability of surface energy fluxes in a complex alpine setting. It has provided an observational dataset of time series and space series of fluxes in a large catchment in the Southern Alps of New Zealand. The variability of fluxes was also modelled to determine the role of various components of the landscape, as well as seasonal and synoptic controls. It is hoped that future research can build on the evidence, methodologies and hypotheses generated by this research. In particular, it is envisioned that future observations in other mountain settings will help determine the extent to which the findings of this study can be applied generally to areas of complex terrain.

References

Abareshi, B. and Schuepp, P.H., 1997: Sensible heat flux estimation over the FIFE site by neural networks. *J. Atmos Sci*, **55,** 1185-1197.

Acs, F. and Hantel, M., 1998: The land surface flux model PROGSURF. *Global Planet. Change*, **19**, 19-34.

Adams, J., 1980: Contemporary uplift and erosion in the Southern Alps, New Zealand: Summary. *Bull. Geol. Soc. America,* Part I, **91**, 2-4.

Asai, T., and Mitsumoto S., 1978: Effects of an inclined land surface on the land and sea breeze circulation: A numerical experiment. *J. Meteor. Soc. Japan*, **56** (6), 559-570.

Assouline, S. and Mahrer, Y. 1996: Spatial and temporal variability in microclimate and evaporation over Lake Kinneret: Experimental evaluation. *J. Appl. Meteor.* **35**, 1076-1084.

Atkinson, B.W., 1981: *Mesoscale Atmospheric Circulations,* Academic Press, London, 495pp.

Australian Bureau of Meteorology, December 20, 2000: http://www.bom.gov.au/climate/glossary/soi.shtml

Avissar, R., and. Pielke R.A, 1989: A parameterization of heterogeneous land surfaces for atmospheric numerical models and its impact on regional meteorology. *Mon. Wea. Rev.*, **117**, 2113-2136.

Bader, D.C., and Whiteman, C.D. 1989: Numerical simulation of cross-valley plume dispersion during the morning transition period. *J. Appl. Meteor.*, **28**, 652-664.

Banta, R., and Pantley K.C., 1987: Soil moisture and ridge height effects on katabatic flow simulations. *Fourth Conference on Mountain Meteorology,* 139-145. Amer. Meteor. Soc., Boston, Massachusetts.

Banta, R., and Cotton W.R., 1981: An analysis of the structure of local wind systems in a broad mountain basin. *J. Appl. Meteor.*, **20**, 1255-1266.

Barr, S. and Orgill, M.M. 1989: Influence of external meteorology on nocturnal valley drainage winds. *J. Appl. Meteor.*, **28**, 497-517.

Barr, A.G., King, K.M., Gillespie, T.J., den Hartog, G. and Neumann, H.H. 1994: A comparison of bowen ratio and eddy correlation sensible and latent heat flux measurements above deciduous forest. *Bound.-Lay. Meteor.* , **71**, 21-41.

Barry, R.G., 1992: *Mountain Weather And Climate* (2nd edition). Methuen and Co., Ltd., London, 313 pp.

Barry, R.G., and C. C. Van Wie, 1974: Topo- and microclimatology in Alpine areas. *Arctic and Alpine Environments,* J.D. Ives and R.G. Barry (Eds), London, Methuen, 73-83.

Bemmelen, W., van. 1922: Land and sea breeze in Batavia. *Beitr. Physik. Atmos.,* **10**, 167-177.

Best, M.J., 1998: A model to predict surface temperatures. *Boundary-Layer Meteorology*, **88**, 279-306.

Beyrich, F., Sieghard, H.R. and Weisensee, U. 2000: The LITFASS-98 experiment: Fluxes over a heterogeneous land surface. *Amer. Meteor. Soc. 14th Symposium on Boundary Layer and Turbulence*, 9-10.

Bink, N.J. 1996: The ratio of eddy diffusivities for heat and water vapour under conditions of local advection. *Phys. Chem. Earth,* **21**, 119-122.

Boyer, D. and Feldhake, C.M., 1994: Identification of thermally homogeneous subunits in a steep application pasture. *Journal of Applied Meteorology*, **33,** 1200-1209.

Bowen, I.S., 1926: The ratio of heat losses by conduction and by evaporation from any water surface. *Phys. Rev.*, **27**, 779-789.

Brenstrum, E., 1989: Canterbury's damaging nor'wester. *New Zealand Geographic*, **1**, 110-111.

Brown, R.D. and Fitzharris, B., 1993: The reflectance of snow tussock. *Weather and Climate.,* **13**, 3-9.

Brühl, C., and Zdunkowski W., 1983: An approximate calculation method for parallel and diffuse solar irradiances on inclined surfaces in the presence of obstructing mountains or buildings. *Arch. Meteor. Geophys. Bioclim., Ser. B,* **32**, 111-129.

Brutsaert, W. and Kusta, W.P. 1987: Surface water vapour and momentum fluxes under unstable conditions from a rugged-complex area. *J. Atmos. Sci.,* **44**, 421-431.

Budkyo, M.I. 1958: The heat balance of the earth's surface (translated by N.A.Stepanova) US Department of Commerce, Washington.

Burba GG, Verma SB, Kim J, 1999: Energy fluxes of an open water area in a mid-latitude prairie wetland, *Bound Lay Meteor*, **91**, 495-504.

Campbell, D.I., 1989: Energy balance and transpiration from tussock grassland in New Zealand. *Bound. Lay. Meteor.* **46**, 133-152.

Campbell, D.I. and Murray, D.L., 1990: Water balance of snow tussock grassland in New Zealand. *J. Hydrology,* **118**, 229-245.

Carlson, J.D., and Foster M.R., 1986: Numerical study of some neutrally and unstably stratified boundary-layer flows over a valley at moderate Richardson number. *J. Climate Appl. Meteor.,* **25**, 203-213.

Ching, J.K.S., Clarke, J.F., Godowitch, J.M., 1983: Modulation of heat flux by different scales of advection in an urban environment. *Bound. Lay. Meteor.,* **25**, 171-191.

Clements, W. E., and Nappo, C.J., 1983: Observations of a drainage flow event on a high-altitude simple slope. *J. Clim. Appl. Meteor.*, **22**, 331-335.

Clements, W.E., Archuleta J.A., and Hoard, D.E., 1989: Mean structure of the nocturnal drainage flow in a deep valley. *J. Appl. Meteor.*, **28**, 457-462.

Conklin, P.S., Knoerr, K.R., Schneider, T.W., Baker, B. 1988: A wind tunnel test of probe shadow effects on a sonic anemometer at two orientations. *Amer. Meteor. Soc. 8th Symposium on turbulence and diffusion*, San Diego, Calif., 108-111.

Daggupaty, S.M., Tangilara, R.S. and Sahota, H. 1994: A mesoscale model for inhomogeneous terrain. In Gryning, S.V. and Millan, M.M. (eds) *Air pollution modelling and its application.* Plenum Press.

Defant, F., 1951: Local Winds. In: *Compendium of Meteorology,* T.M. Malone (Ed.), Boston, Amer. Meteor. Soc., 655-672.

de Ridder, K., 1997: Radiative transfer in the IAGL land surface model. *J. Appl. Meteor.***36** 12-21

de Ridder, K. and Schayes, G., 1997: The IAGL land surface model. *J. Appl. Meteor.***36** 167-182

de Wekker,S.F.J, Zhong, S, Fast,F.D, and Whiteman, D.C., 1998: A numerical study of the thermally driven plain-to-basin wind over idealized basin topographies, *J. Appl. Meteor.,* **37,** 606-622.

Doran, J.C., and Gryning S.E., 1987: Wind and temperature structure over a land-water-land area. *J. Climate Appl. Meteor.*, **26** (8), 973-979.

Doran, J.C., Wesely M. L., McMillen R. T., and Neff W. D, 1989: Measurements of turbulrnt heat and momentum fluxes in a mountain valley. *J. Appl. Meteor.*, **28**, 438-444.

Doran, J.C., Horst T.W., and. Whiteman C. D., 1990: The development and structure of nocturnal slope winds in a simple valley. *Bound.-Layer Meteor.*, **52**, 41-68.

Doran, J.C., Shaw W.J., and Hubbe J.M., 1995: Boundary layer characteristics over areas of inhomogeneous surface fluxes. *J. Appl. Meteor.*, **34**, 559-571.

Doran, J.C., Abbott S, Archuleta J, Bian X, Chow J, Coulter RL, de Wekker SFJ, Edgerton S, Elliott S, Fernandez A, Fast JD, Hubbe JM, King C, Langley D, Leach J, Lee JT, Martin TJ, Martinez D, Martinez JL, Mercado G, Mora V, Mulhearn M, Pena JL, Petty R, Porch W, Russell C, Salas R, Shannon JD, Shaw WJ, Sosa G, Tellier L, Templeman B, Watson JG, White R, Whiteman CD, Wolfe D 1998: The IMADA-AVER boundary-layer experiment in the Mexico City area. *Bull. Amer. Meteor. Soc.,* **79,** 2497-2508.

Dozier, J., Bruno, J. and Downey, P., 1981: A faster solution to the horizon problem. *Computers and Geosciences,* **7**, 145-151.

Dubayah, R and Rich, P.M., 1995: Topographic solar radiation models for GIS. *Int. J. Geographical Information Systems,* **9**, 405-419.

Dubayah, R. and Loechel, S., 1997: Modeling topographic solar radiation using GOES data. *Journal of Applied Meteorology.* **36**, 141-154.

Duguay, C.R., 1995: An approach to the estimation of Surface net radiation in mountain areas using remote sensing and digital terrain data. *Theor. Appl. Cimatol.*,**52, 55-68.**

Eckman, R. M. Dobosy R.J., and. Rao K.S, 1992: Spatial variability of the wind over moderately complex terrain. Preprint Volume, *Tenth Symposium on Turbulence and Diffusion*, Sept. 29-Oct. 2, 1992, Portland, Oregon, 84-87.

Espie, P.R. 1997: Tekapo Scientific Reserve: ecological restoration. *Conservation advisory science notes: 149.* Dept. Conservation, 30pp.

Famiglietti, J.S. and Wood, E.F., 1994a: Multiscale modeling of spatially variable water and energy balance processes. *Water Resources Research,* **30**, 3061-3078.

Famiglietti, J.S. and Wood, E.F., 1994b: Application of multiscale water and energy balance models on a tall grass prairie. *Water resources research,* 3079-3093.

Famiglietti, J.S. and Wood, E.F., 1995: Effects of spatial variability and scale on areally averaged evapotranspiration. *Water Resources Research,* **31,** 699-712.

Fleming, P.M., 1987: Notes on a radiation index for use in studies of aspect effects on radiation climate. Unpub. Manuscript, CSIRO, Div. Water Resources, Canberra, Australia.

Forbes, M.C., Banks, T., Sullivan, D.F., Dodd, R.F., Gilmore, A.C. and Kilmarton, P.M. 1995: Mount Pinatubo and atmospheric extinction at Mount John University Observatory, 1987-94. *The Observatory,* **155**, 29-30.

Frech, M. and Jochum, A., 1998: The evaluation of flux aggregation methods using aircraft measurments in the surface layer. *Agricultural and Forest Meteorology.*

Freytag, C., 1985: MERKUR-Results: Aspects of the temperature field and the energy budget in a large Alpine valley during mountain and valley wind. *Contrib. Atmos. Phys.*, **58**, 458-476.

Fritschen, L.J. and Qian, P., 1990: Net radiation, sensible and latent heat flux densities on slopes computed by he energy balance method. *Boundary-Layer Meteorology* **53** 163-171.

Fritschen, L. J., and Qian P. Variation in energy balance components from six sites in a native prairie for three years. Submitted to J. Geophys.

Gallant J.C., 1997: Modeling solar radiation in forests of southeastern Australia. International Congress on Modeling and Simulation (MOD-SIM97), Hobart, Tasmania

Garr, G.E. and Fitzharris, B.B. 1991: A climate classification of New Zealand based on numerical techniques. *New Zealand Geographer,* **47**, 60-71.

Gash, J.H.C. 1986: A note on estimating the effect of a limited fetch on micrometeorological evaporation measurements. *Bound. Lay. Meteor.,* **35**, 409-414.

Gates, D.M. 1980: *Biophysical Ecology.* Springer-Verlag, New York, 611pp.

Geiger, R., 1965: *The Climate Near the Ground, rev. ed.* Cambridge, Harvard University Press, 611 pp. [Translated by Scripta Technica, Inc. from the 4th German edition, 1961].

Goodin, W. R., and Isard, S.A., 1989: Magnitude and sources of variation in albedo within an alpine tundra. *Theor. Appl. Climatology.* **40**, 50-60.

Gordon, D. 1986. The Southern Oscillation and New Zealand weather. *Mon. Wea. Rev.,* **114**, 371-387.

Greenland, D., 1973: The surface energy budget and synoptic weather in the Chilton Valley, New Zealand Southern Alps. *New Zealand Geographer,* **29**, 1-15.

Greenland, D., and Clothier B. 1975: A study of radiation in the New Zealand Southern Alps. *Geografiska Annaler, Ser. A,* **3-4**, 143-151.

Griffiths, G.A. and McSaveney, M.J., 1983: Distribution of mean annual precipitation across some steepland regions of New Zealand. *New Zealand J. Sci.* **26**, 197-209.

Gudiksen, P.H. and Shearer, D.L. 1989: The dispersion of atmospheric tracers in nocturnal drainage flows. *J. Appl. Meteor.,* **28**, 602-608.

Guilloteau, E., 1998: Optimized computation of transfer coefficients in surface layer with different momentum and heat roughness lengths, *Boundary-Layer Meteorology* **87** 147-160.

Hacker, J. M., 1982: Preliminary results of the Alpine experiment DISKUS. *Aero Review,* **10/82**, 44-49.

Halbsguth G., Kerschgens, M. J., Kraus H,. Meindl, G., and Schaller E., 1984: Energy fluxes in an Alpine valley. *Arch. Meteor. Geophys. Bioclimatol., Ser. A,* **33**, 11-20.

Hasager, C.B. and Jensen, N.O., 1999: Surface-flux aggregation in heterogeneous terrain. *Q.J.R. Meteorol. Soc.,* **125**, 2075-2102.

Hastenrath, S. 1997: Measurements of solar radiation and Estimation of Optical Depth in the High Andes of Peru. *Meteor. Atmos. Phys.,* **64** 51-59.

Hay, J.E. and Fitzharris, B.B., 1987: The Synoptic climatology of ablation on a New Zealand Glacier. *Journal of Climatology,* **8**, 201-215.

Hennemuth, B., 1985: Temperature field and energy budget of a small Alpine valley. *Contrib. Atmos. Phys.*, **58**, 545-559.

Hennemuth, B., 1986: Thermal asymmetry and cross-valley circulation in a small Alpine valley. *Bound.-Layer Meteor.*, **36**, 371-394.

Hennemuth, B., 1987: Heating of a small alpine valley. *Meteorol. Atmos. Phys,* **36**, 287-296.

Hennemuth, B., and H. Schmidt, 1985: Wind phenomena in the Dischma Valley during DISKUS. *Arch. Meteor. Geophys. Bioclimatol., Ser. B*, **35**, 361-387.

Hennemuth, B., and U. Köhler, 1984: Estimation of the energy balance of the Dischma Valley. *Arch. Meteor. Geophys. Bioclimatol., Ser. B*, **34**, 97-119.

Hogstrom,U. 1996: Review of some basic characteristics of the atmospheric surface layer. *Bound.-Lay. Meteor.* **78**, 215-246

Horst, T.W. and Weil, J.C. 1992: Footprint estimation for scalar flux measurements in the atmospheric surface layer. *Bound. Lay. Meteor.,* **59**,279-296.

Horst, T. W., and J. C. Doran, 1988: The turbulence structure of nocturnal slope flow. *J. Atmos. Sci.*, **45**, 605-616.

Humes, K.S., Kustas, W.P. and Goodrich, D.C., 1997: Spatially distributed sensible heat flux over a semiarid watershed. Part I: Use of radiometric surface temperatures and a spatially uniform resistance. *J. Appl. Meteor.* **36:,** 281-301.

Hunt, J. C. and Richards, K.J., 1984.Stratified airflow over one or two hills. *Bound. Lay. Meteor.* **30**. 223-259.

Hunt, J. C.R., W.H. Snyder, and R.E. Lawson, Jr., 1978: Flow structure and turbulent diffusion around a three-dimensional hill. Fluid Modeling Study on Effects of Stratification Part 1. Flow Structures. EPA-600/4-78-041. U.S. EPA, Environmental Sciences Research Laboratory, Research Triangle Park, North Carolina. 84 pp.

Huntingford, C., Blyth, E.M., Wood, N., Hewer, F.E., and Grant, A., 1998: The effect of orography on evaporation. *Bound. Lay. Meteor.,* **86**, 487-504.

Idso, S.B., 1981: A set of equations for full spectrum and 8-14 μm and 10.5-12.5 μm thermal radiation from cloudless skies. *Water Resources Res.,* **17**, 295-304.

Isard, S.A., 1987: The effect of slope-aspect on turbulent transfer in an alpine fellfield: Niwot Ridge, Front Range, Colorado. *Physical Geography,* **8**, 133-147.

Ishikawa, N. Owens, I.F., and Sturman, A.P., 1992: Heat Balance Characteristics during fine periods on the lower parts of the Franz Josef Glacier, South Westland, New Zealand. *International Journal of Climatology,* **12**, 397-410.

Jarvis, P.G. and McNaughton, K.G. 1986: Stomatal control of transpiration: scaling up from leaf to region. *Adv. Ecological Res.*, **15**, 1-49

Kalma, J.D., 1989: A comparison of expressions for the aerodynamic resistance to sensible heat transfer. *CSIRO Technical Memorandum*, 89/6.

Kalthoff, N., Fiedler, F., Kohler, M., Kolle, O., Mayer, H. and Wenzel, A., 1999: Analysis of energy balance components as a function of orography and land use and comparison of results with the distribution of variables influencing local climate. *Theor. Appl. Climatology,* **62**, 65-84.

Kelliher, F.M., Leuning, R., Schulze, E.-D. 1993: Evaporation and canopy charactersitics of coniferous forests and grasslands. *Oecologia,* **95**, 153-163.

Kessler, A. and Jaeger, L. 1999: Long-term changes in net radiation and its components above a pine forest and a grass surface in Germany. *Int. J. Climatol.,*. **19, 211-226.**

Kolle, O. 1997: Long-term comparison of energy flux calculation methods over an agricultural field. *Phys. Chem. Earth,* **21**, 111-117

Kondo, H., 1990: A numerical experiment of the "extended sea breeze" over the Kanto Plain. *J. Meteor. Soc. Japan*, **68**, 419-434.

Konzelmann, T. Calanca, P., Muller, G., Menzel, L. and Lang, H., 1997: Energy balance and evapotranspiration in a high mountain area during summer. *J. Appl. Meteor.*, **36**, 966-973.

Kondratyev, K.Y, 1969: *Radiation in the atmosphere.* International Geophysics series, Academic Press, New York, 912pp.

Kondratyev, K.Y., 1977: Radiation regime of inclined surfaces. Technical Note No. 152, WMO No. 467, World Meteorological Society, Geneva, Switzerland.

Kossmann, M., Vogtlin, R, Corsmeier, U, Vogel, B., Fiedler, F., Binder, H.-J., Kalthoff, N. and Beyrich, F. 1998: Aspects of the convective boundary layer structure over complex terrain. *Contrib. Envir.,* **32,** 1323-1348.

Kumar, L., Skidmore, A.K. and Knowles, E, 1997: Modelling topographic variation in solar radiation in a GIS environment. *Int. J. Geographical Information Science,* **11,** 475-497.

Kuwagata, T., Kondo, J. and Sumioka, M. 1993: Thermal effect of the sea breeze on the structure of the boundary layer and the heat budget over land. *Bound. Lay. Meteor.* **67,** 119-144.

Lamb, P.J. 1970: An investigation of the Canterbury Nor'wester. *Unpublished M.A. Thesis*, University of Canterbury, New Zealand.

Lamb, P.J. 1974: The Nor'wester's advance across the Canterbury Plains, New Zealand. *New Zealand J. Sci.* **17**, 375-380.

Lang, A.R.G., McNaughton, K.G., Chen Fazu, Bradley, E.F. and Ohtaki, E. 1983: Inequalities of eddy transfer coefficients for vertical transport of sensible and latent heats during advective inversions. *Bound-Lay. Meteor.*, **25**, 25-41.

Laymon, C., Quattrochi, D., Malek, E., Hipps, L., Boettinger J., and McCurdy, G., 1998: Remotely-sensed regional-scale evapotranspiration of a semi-arid Great Basin desert and its relationship to geomorphology, soils, and vegetation. *Geomorphology, 21, 329-349.*

Leclerk, M.Y. and Thurtell, G.W. 1990: Footprint predictions of scalar fluxes using a markovian Analysis. *Bound Lay. Meteor.*, **52**, 247-258.

LeDrew, E. F., and G. Weller, 1978: A comparison of the radiation and energy balance during the growing season for arctic and alpine tundra. *Arct. Alp. Res.*, **10**, 665-678.

Lee, H.N., 1997: Improvement of surface flux calculations in the atmospheric surface layer. *Journal of Applied Meteorology,* **36,** 1416-1423.

Lee, I. Y., Coulter R. L., Park H. M., and Oh J.-H., 1995: Numerical simulation of nocturnal drainage flow properties in a rugged canyon. *Bound.-Layer Meteor.*, **72**, 305-321.

Leone, J. M., Jr., and Lee R. L., 1989: Numerical simulation of drainage flow in Brush Creek Valley, Colorado. *J. Appl. Meteor.*, **28**, 530-542.

Lhomme, J.P., Monteny, B., 1993: Estimates of convectives fluxes over sparse canopy from infrared temperature. In Bolle, H.J., Feddes R.A. and Kalma J.D. (eds), *Exchange processes at the Land Surface for a Range of Space and Time Scales,* (Proceedings of the Yokohama Symposium, July 1993) IAHS Publication **NO. 212,** 437-443.

Liang, Xu, Wood, E.F., Lettenmaier, D.P., Lohmann, D., Boone, A., Chang, S., Chen, F., Dai, Y., Desborough, C., Dickinson, R.E., Duan, Q., Ek, M., Gusev, Y.M., Habets, F., Irannejad, P., Koster, R., Mitchell, K.E., Nasonova, O.N., Noilhan, J., Schaake, J., Schlosser, A., Shao, Y., Shmakin, A.B., Verseghy, D., Warrach, K., Wetzel, P., Xue, Y., Yang, Z. and Zeng, Q., 1998: The project for intercomparison of land-surface parameterization, schemes (PILPS) phase 2 (c): red--Arkansas River basin experiment: 2. Spatial and temporal analysis of energy fluxes. *Global and Planetary Change*, **19**, 137-159.

Linacre, E.T., 1992: Data-sparse estimation of lake evaporation, using a simplified penman equation. *Ag. For. Meteor.* **64**, 237-256.

Liu, B.Y.H., Jordan, and R.C., 1963: A rational procedure for predicting the long-term average performance of flat-plate solar-energy collectors. *Solar Energy*, **7**, 53-74.

List, R.J. (ed.), 1968. *Smithsonian Meteorological Tables,* 6th rev. ed. Washington, D.C. Smithsonian Institute, 352 pp.

Lohmann, D., Lettenmaier, D., Liang, X., Wood, E.F. Boone, A., Chang, S., Chen, F., Dai, Y., Desborough, C., Dickinson, R.E., Duan, Q., Ek, M., Gusev, Y.M., Habets, F., Irannejad, P., Koster, R., Mitchell, K.E., Nasonova, O.N., Noilhan, J., Schaake, J., Schlosser, A., Shao, Y., Shmakin, A.B., Verseghy, D., Warrach, K., Wetzel, P., Xue, Y., Yang, Z. and Zeng, Q., 1998: The project for intercomparison of land-surface parameterization, schemes (PILPS) phase 2 (c): red--Arkansas River basin experiment: 3. Spatial and temporal analysis of water fluxes. *Global and Planetary Change*, **19**, 161-179.

Lowe, P.R., 1977: An approximating polynomial for the computation of saturation vapor pressure. *J. Appl. Meteor.*, **16** (1), 100-103. **[442]**

Lowry, W.P., 1980: Clear-sky direct-beam solar radiation versus altitude: A proposal for standard soundings. *J. Appl. Meteor.*, **19**, 1323-1327.

Lyons, T.J., Smith, R.C.G. and Xinmei, H., 1996: The impact of clearing for agriculture on the surface energy budget. *Int. J. Climatology,* **16**, 551-558.

Mahrt, L., 1982: Momentum balance of gravity flows. *J. Atmos. Sci.*, **39**, 2701-2711

Mahrt, L., 1996: The bulk aerodynamic formulation over heterogeneous surfaces. *Bound. Lay. Meteor.* ,**78**,87-119.

Maki, M. and Harimaya, T. 1988: The effect of advection and accumulation of downslope cold air on nocturnal cooling in basins. *J. Meteor. Soc. Japan*, **66** (4), 581-597.

Marks, D., and Dozier J., 1979: A clear-sky longwave radiation model for remote Alpine areas. *Arch. Meteor. Geophys. Bioclimatol., Ser. B*, **27**, 159-187.

Massman, W. J., 1992: Correcting errors associated with soil heat flux measurements and estimating soil thermal properties from soil temperature and heat flux plate data. *Agric. Forest Meteor.*, **59**, 249-266.

Massman, W.J., Fox, D.G., Zeller, K.F. and Lukens, D. 1990: Verifying eddy correlation measurements of dry deposition: A study of the energy balance components of the Pawnee Grassland. *Research Pap. RM-288,* U.S. Dept. Agric. Fort Collins CO. 14pp.

McCauley, M.P. and Sturman, A.P. 1999: A study of orographic blocking and barrier wind development upstream of the Southern Alps, New Zealand. *Meteor. Atmos. Phys.,* **70**, 121-131.

McCutchan, M.H., and Fox, D.G., 1986: Effect of elevation and aspect on wind, temperature and humidity *J. Clim. Appl. Meteor.*, **25**, 1996-2013.

McGowan, H.A., Owens, I.F., and Sturman, A.P, 1995: Thermal and dynamic characteristics of alpine lake breezes, Lake Tekapo, New Zealand. *Bound. Lay. Meteor.,* **76**, 3-24.

McGowan, H.A., Owens, I.F., and Sturman, A.P, 1996: Aeolian dust transport and deposition by foehn winds in an alpine environment, Lake Tekapo, New Zealand. *Geomorphology* **15**, 135-146.

McGowan, H.A. and Sturman, A.P. 1996. Interacting multi-scale wind systems within an alpine basin, Lake Tekapo, New Zealand. *Meteor. Atmos. Phys.* **20**, 1-13.

McKee, T.B., and. O'Neal, R.D. 1989: The role of valley geometry and energy budget in the formation of nocturnal valley winds. *J. Appl. Meteor.*, **28**, 445-456.

McKendry, I.G., A.P. Sturman, and I.F. Owens, 1987: The Canterbury Plains north-easterly. *Weather and Climate,* **7**, 61-74.

McKendry, P.J. and O'Connor, K.F. 1990: The ecology of Tussock Grasslands for Production and Protection. *Unpublished Report for Dept. Conservation.* Centre for Resource Management, Lincoln University and University of Canterbury161pp.

McKenny D.W., Mackey B.G., and Zavitz B.L., 1999: Calibration and sensitivity analysis of a spatially distributed solar radiation model. International Journal of Geographical Infromation Science, **57**: 329-55

McKeown, W. and Leighton, R., 1999: Mapping heat flux, *Journal of Atmospheric and Oceanic Technology*, **16,** 80-91.

McNaughton, K.G. and Laubach, J. 1998: Unsteadiness as a cause of non-equality of eddy diffusivities for heat and vapour at the base of an advective inversion. *Bound.-Lay. Meteor*, **88**, 479-504.

McNeill ,D.D. and Shuttleworth, W.J. 1975: Comparitive Measurements of the energy fluxes over a pine forest. *Bound-Lay Meteor.,* **9**, 297-313

Mikami, M., Toya,T., and Yasuda, N. 1996: An analytical method for the determination of the roughness parameters over complex regions, *Boundary-Layer Meteorology* **79** 23-33.

Mitsuta,Y. and Tamagawa, I. 1993: Evaporation at Desert Station in HEIFE, Proc., International Symposium on HEIFE, Kyoto, Japan, 8-11, Nov., pp.379-390.

Monteith, J.L., Szeicz, G. and Waggoner, P.E. 1965: The measurement and control of stomatal resistance in the field. *J. Appl. Ecol.,* **2**, 345-355.

Monteith, J.L., and Unsworth, M.H. 1990: *Principals of Environmental Physics,* 2nd Ed. Edward Arnold, London, 291pp.

Moore, I.D., Norton, T.W. and Williams, J.E., 1993: Modelling environmental heterogeneity in forested landscapes. *J. Hydrology,* **150**, 717-747.

Moran, R.J. 1971: Soil heat flow investigations in the Chilton Valley. *Unpublished MA thesis,* Department of Geography, University of Canterbury.

Morris, A.L., 1997: *Synoptic influences on ablation, energy exchange and local winds, Brewster Glacier, South Westland, New Zealand* Unpublished Masters Thesis in Geography, Department of Geography, University of Canterbury, Christchurch, New Zealand.

Motha, R.P., Verma, S.B. and Rosenberg, N.J. 1979: Exchange coefficients under sensible heat advection determined by eddy correlation. *Agric. Meteor.*, **20**, 273-280. New York.

Müller, H., and Whiteman, C.D., 1988: Breakup of a nocturnal temperature inversion in the Dischma Valley during DISKUS. *J. Climate Appl. Meteor.*, **27**,188-194.

New Zealand Meteorological Service, 1986: Summaries of climatalogical observations to 1980. *New Zealand Meterological Service Miscellaneous Publication,* **177**, 172pp

Noat, O. and Mahrer, Y., 1989: Modeling microclimate environments: A verification study. *Boundary-Layer Meteorology,* **46,** 333-354.

Nunez, M., 1980: The calculation of solar and net radiation in mountainous terrain. *Journal of Biogeography*, **7**, 173-186.

Oke, T. R., 1987: *Boundary Layer Climates (2nd ed.)* New York, John Wiley and Sons, 435 pp.

Oliver, H.R., 1992: Studies of surface energy balance of sloping terrain. *International Journal of Climatology*, **12**, 55-68.

Orgill, M. M., and Schreck R. I., 1985: An overview of the ASCOT multi-laboratory field experiments in relation to drainage winds and ambient flow. *Bull. Amer. Meteor. Soc.*, **66**, 1263-1277.

Orlanski, L. 1975: A rational subdivision of scales for atmospheric processes. *Bull. Amer. Meteor. Soc.*, **56**, 527-530.

Orvis, K.H., 1997: Insulation landscape of Great Smoky Mountain National Park. *Proceed of the AAG 93rd Annual meeting, Fort Worth Texas, USA.*

Oue, H., Tagashira, Otsuki H., 1993: The microclimate role of agricultural land use in moderating the thermal environment. In Bolle, H.J., Feddes R.A. and Kalma J.D. (eds), *Exchange processes at the Land Surface for a Range of Space and Time Scales,* (Proceedings of the Yokohama Symposium, July 1993) IAHS Publication **NO. 212**, 527-533.

Owens, I.F., Marcus, M.G. and Moore, R.D., 1984: Temporal variations of Energy transfers over the lower part of the Franz Josef Glacier. *Geography for the 1980s,*

Parish, T.R. and Bromwich, D.H. 1990: Numerical simulation of the katabatic wind circulation over the Antarctic Continent. *Antarctic Journal of the USA,* **15**, 262-262.

Parlow, E., 1995: Progress in environmental remote sensing research and applications. *Proceedings of the 15th Earsel Symposium Basel, Switzerland.*

Pielke, R.A., Dalu, G. A., Lee, T.J., Rodriguez, E., Eastman, J., Kittle, T.G.F., 1993: Mesoscale parameterization of heat fluxes due to landscape variability for use in general circulation models. In Bolle, H.J., Feddes R.A. and Kalma J.D. (eds), *Exchange processes at the Land Surface for a Range of Space and Time Scales,* (Proceedings of the Yokohama Symposium, July 1993) IAHS Publication **NO. 212,** 331-342.

Peixoto, J.P. and Oort 1992: *Physics of Climate*. Springer-Verlag, New York. Pp560.

Plesko, N., and Sinik N., 1978: The energy balance in the mountains of Croatia. *Arb. Zentralanst. Meteor. Geodyn.* (Vienna), **31**, 9/1-9/16.

Pluss, C. and Mazzoni, R. 1994: The role of turbulent heat fluxes in the energy-balance of high alpine snow cover.,*Nordic Hydr.,* **25** 25-38.

Polcher, J., McAvaney, B., Viterbo,P., Gaertner, M.-A., Hahmann, A., Mahfouf, J.-F., Noilhan, J., Phillips, T., Pitman, A., Schlosser, C.A., Schulz, J.-P., Timbal, B., Vereghy, D., Xue, Y., 1998: A proposal for a general interface between land surface schemes and general circulation models. *Global and Planetary Change,* **19,** 263-278.

Prowse, T.D. and Owens, I.F., 1982: Energy balance over melting snow, Craigieburn Range, New Zealand. *Journal of Hydrology (N.Z.)*, **21**, 133-147.

Raupach, M.R. and Finnegan, J.J., 1997: The influence of topography on meteorological variables and surface-atmosphere interactions. *J. Hydrology.,***190**, 182-213.

Raupach, M.R., 1993: The averaging of surface flux BPdensities in heterogeneous landscapes. In Bolle, H.J., Feddes R.A. and Kalma J.D. (eds), *Exchange processes at the Land Surface for a Range of Space and Time Scales,* (Proceedings of the Yokohama Symposium, July 1993) IAHS Publication **NO. 212,** 343-355.

Revell, M.J., Purnell, D. and Lauren, M.K. 1996: Requirements for large-eddy simulation of surface wind gusts in a mountain valley. *Bound. Lay. Meteor.*, **80**, 333-353.

Rott, H., 1979: Vergleichende Untersuchungen der Energiebilanz im Hochgebirge. [Comparative studies of the energy balance in the high mountains]. *Arch. Meteor. Geophys. Bioclimatol., Ser. A*, **28**, 211-232.

Running, S.W., Nemani, R.R. and Hungerford, R.D., 1987: Extrapolation of synoptic meteorological data to mountainous terrain and its use for simulating forest evapotranspiration and photosynthesis. *Canadian J. For. Res.,***17**, 472-483.

Running, S.W. 1991: Computer simulation of regional evapotranspiration by integrating landscape biophysical attributes with satellite data. In *Land Surface*

Evaporation: Measurement and Parameterisation, eds T.J. Schmugg and J. Andre, Springer-Verlag, London, 359-369

Running, S.W. and Thornton, P.E. 1996: Generating daily surfaces of temperature and precipitation over complex topography. In *GIS and Environmental Modeling: Progrss and Research Issues,* eds M.F. Goodchild, L.T. Steyaert, B.O. Parks *et al.* GIS world Inc., Ft. Collins, 93-98.

Ryan, A.P. 1984: *Flying Weather: Manual of New Zealand Aviation Climatology* New Zealand Meteorological Service, Wellington New Zealand, 120pp.

Saunders, I.R. and Baily, W.G. 1996: The physical climatology of alpine tundra, Scout Mountain, British Columbia, Canada. *Mount. Res. Develop.,* **16**, 51-64.

Saunders, I.R., Bowers, J.D., Huo, Z., Bailey, W.G. Verseghy, D., 1999a: Simulation of alpine tundra surface microclimates using the Canadian Land Surface Scheme I: albedo and net radiation modelling. *Int. J. Climatology,* **19**, 913-926.

Saunders, I.R., Bowers, J.D., Huo, Z., Bailey, W.G. Verseghy, D., 1999b: Simulation of alpine tundra surface microclimates using the Canadian Land Surface Scheme II: Energy balance and surface microclimatology. *Int. J. Climatology,* **19**, 1131-1141.

Scheaffer, J.D., and E.R. Reiter, 1987: Measurements of surface energy budgets in the Rocky Mountains of Colorado. *J. Geophys. Res.*, **92**, 4145-4162.

Schmid, H.P. 1994: Source areas for scalars and scalar fluxes. *Bound. Lay. Meteor.* **67**, 293-318.

Schneider, C., Parlow, E and Scherer, D., 1996: GIS-based modeling of the energy balance of Tarfala Valley, Sweden using Landsat-TM data. *Progress in Environmental Remote Sensing Research and Applications,* ed E. Parlow, Balkema, Rotterdam.

Spronken-Smith, R.A., Oke, T.R. and Lowry, W.P., 2000: Advection and the surface energy balance across an irrigated urban park. *Int. J. Clim.,* **20**, 1033-1047.

Spronken-Smith, R.A., Oke, T.R. and Lowry, W.P. 2000: Advection and the surface energy balance across an irrigated urban park. *Int. J. Climatology,* **20**, 1033-1047.

Stannard, D.I., Rosenberry, D.O. 1991: A comparison of short-term measurement of lake evaporation using eddy correlation and energy budget methods. *J.Hydrology,* **122** 12-22.

Steinacker, R. 1984: Area-height distribution of a valley and its relation to the valley wind. *Contrib. Atmos. Phys.*, **57**, 64-71.

Steven, M.D., and Unsworth N.H., 1980: Shade-ring corrections for pyranometer measurements of diffuse solar radiation from cloudless skies. *Quart. J. Roy. Meteor. Soc.*, **106**, 865-872.

Stocks, A.M. and Heywood, D.I., 1994: Terrain modelling for mountains. In, Price, M.F. and Heywood, D.I. *Mountain Environments and Geographic Information Systems*, Taylor and Francis, London.

Stull, R. B., 1988: *An Introduction to Boundary Layer Meteorology.* Kluwer Academic Publishers, Boston, 666 pp.

Sturman, A.P., Trewinnard, A. and Gormon, P. 1984: A study of atmospheric circulation over the South Island of New Zealand (1961-1980). *Weather and Climate,* **4**, 53-62.

Sturman, A.P., 1987: Thermal influences on airflow in mountainous terrain. *Prog. Phys. Geog.,* **11,** 183-206.

Sturman, A.P. and Tapper, N.J., 1996: *The weather and climate of Australia and New Zealand.* Oxford University Press, Melbourne, Australia, 476pp.

Sugita, M., Kayane, I, and Hiyama, T., 1993: IGBP/BAHC field experiment to address scale problems in land-surface parameterization. In Bolle, H.J., Feddes R.A. and Kalma J.D. (eds), *Exchange processes at the Land Surface for a Range of Space and Time Scales,* (Proceedings of the Yokohama Symposium, July 1993) IAHS Publication **NO. 212,** 389-396.

Sun, J. and Mahrt, L., 1994: Spatial distribution of surface fluxes estimated from remotely sensed variables. *American Meteorological Society,* **33**, 1341-1353.

Sun, J., Lenshow, D.H., Mahrt, L., Crawford, T.L., Davis, K.J., Oncley, S.P., Macpherson, J.I., Wang, Q., Dobosy, R.J. and Desjardins, R.L. 1997: Lake induced atmospheric circulations during BOREAS. *J. Geophys. Res.*,**102**, 29,155-29,166.

Sutton, O.G., 1953: *Micrometeorology*, McGraw-Hill Book Company, Inc. New York, 333 pp.

Swinbank, W.C. 1951. The measurement of vertical transfer of heat and water vapor by eddies in the lower atmosphere. *J. Meteor.* **8**, 135-145.

Tabony, R.C., 1985. The variation of surface temperature with altitude. *Met. Mag.* **114** 37-48.

Tangirala, R.S, Rao K.S., and Hosker R.P., Jr., 1992: A puff model simulation of tracer concentrations in the nocturnal drainage flow in a deep valley. *Atmos. Env.,* **26A**, 299-309.

Tanner, B.D., and Greene J. P, 1989: Measurement of sensible heat and water vapor fluxes using eddy correlation methods. *Final report, CSI contract DAA09-87-D-0038 to U.S. Army Dugway Proving Grounds.* Salt Lake City, UT, 17pp.

Tanner, C. B., 1976: Measurement of evaporation. *Irrigation of Agricultural Lands,* R.M. Hagan, H.R. Haise, and T.W. Edminster (Eds.), **11**, pp. 534-574.

Tapper, N.J. 1988: Surface energy balance studies in Austarlia's seasonally wet tropics: results from AMEX Phase I and II. *Aust. Meteor. Mag.* **36**, 61-68.

Thompson, M.A., Campbell, D.I., Spronken-Smith, R.A., 1999: Evaporation from natural and modified raised peat bogs in New Zealand. *Agricultural and Forest Meteorology* **95**, 85-98.

Tinarelli, G., Anfossi, D., Brusasca,G. Ferrero, E., Giostra, U., Morselli, M.G., Tampieri, F., Trombetti, F. 1994: Lagrangian model simulation of 3-D concentration distribution in complex terrain. In Gryning, S.V. and Millan, M.M. (eds) *Air pollution modelling and its application.* Plenum Press, New York.

Tyson, P. D., 1969: Air pollution fumigation conditions associated with the dissipation of the mountain wind and onset of the valley wind over Pietermaritzburg. *S. Afr. Geogr. J.*, **51**, 99-105.

van den Assem, S., 1997: *Dispersion of Air Pollution in the Christchurch Area.* Unpublished PhD Thesis in Environmental Science, Department of Geography, University of Canterbury, Christchurch, New Zealand.

Vergeiner, I., and Dreiseitl E., 1987: Valley winds and slope winds-observations and elementary thoughts. *Meteor. Atmos. Phys.*, **36**, 264-286.

Verhoef A., Allen, S.J. and Lloyd, C.R., 1999: Seasonal variation of surface energy balance over two Sahelian surfaces. *Int. J. Climatology,* **19,** 1267-1277.

Wadge, G. 1988: The potential of GIS modelling of gravity flows and slope instabilities, *Int. J. GIS.,* **2**, 143-152.

Wagner, A., 1938: Theorie und Beobachtung der periodischen Gebirgswinde. [Theory and observation of periodic mountain winds]. *Gerlands Beitr. Geophys.* (Leipzig), **52**, 408-449. [English translation: Whiteman, C.D., and Dreiseitl E., 1984: Alpine Meteorology: Translations of Classic Contributions by Wagner A., Ekhart E. and Defant F. PNL-5141 / ASCOT-84-3. Pacific Northwest Laboratory, Richland, Washington, 121 pp].

Wang, J., Gao, Y., Hu, Y., Shen, Z, Yasushi, M., Sahasi, K., 1993: An overview of the HEIFE experiment in the People's Rupublic of China. In Bolle, H.J., Feddes R.A. and Kalma J.D. (eds), *Exchange processes at the Land Surface for a Range of Space and Time Scales,* (Proceedings of the Yokohama Symposium, July 1993) IAHS Publication **NO. 212,** 397-403.

Watts, I.E.M., 1947: The relations of N.Z. weather and climate: an analysis of the westerlies. *New Zealand Geographer,* 3 115-129.

Webb, E.K., Pearman, G.I. Leunig, R., 1980: Correction of flux measurements for density effects due to heat and vapour transfer. *Quart. J. Roy. Meteo. Soc.,* **106**, 85-100.

Webb, T.H. 1992: Soils of the upper Waitaki Basin, South Island, New Zealand. *D.S.I.R. Land Resources Scientific Report,* **3,** 100pp

Wenzel, A., Kalthoff, N and Fiedler, F, 1997: On the variation of the energy balance components with orography in the Rhine Valley. *Theor. Appl. Climatology,* **57**, 1-9.

Whitehouse, I.E. and Pearce, A.J. 1992: Shaping the mountains of New Zealand. In Soons, J.M. and Selby, M.J (eds) *Landforms of New Zealand (2nd ed),* Longman Paul, Auckland, New Zealand, 531pp.

Whiteman, C.D., 1982: Breakup of temperature inversions in deep mountain valleys: part 1. observations. *J. Appl. Meteor.,* **21**, 270-289.

Whiteman, C.D., 1989: Morning transition tracer experiments in a deep narrow valley. *J. Appl. Meteor.*, **28**, 626-635.

Whiteman, C.D., 1990: "Observations of thermally developed wind systems in mountainous terrain." Chapter 2 in Atmospheric Processes Over Complex Terrain, (W. Blumen, Ed.), *Meteor. Monogr.,* **23** (no. 45), Amer. Meteor. Soc., Boston, Massachusetts, 5-42.

Whiteman, C.D., and Allwine K.J., 1986: Extraterrestrial solar radiation on inclined surfaces. *Environ. Software*, **1**, 164-169.

Whiteman, C.D., Allwine K.J., Orgill M.M., Fritschen L.J., and Simpson J.R., 1989a: Deep valley radiation and surface energy budget microclimates. I. Radiation. *J. Appl. Meteor.*, **28**, 414-426.

Whiteman, C D., Allwine K.J., Orgill M.M., Fritschen L.J., and Simpson J.R., 1989b: Deep valley radiation and surface energy budget microclimates. II. Energy budget. *J. Appl. Meteor.*, **28**, 427-437.

Whiteman, C.D., and Dreiseitl E., 1984: Alpine meteorology: translations of classic contributions by A. Wagner, E. Ekhart and F. Defant. PNL-5141 / ASCOT-84-3. Pacific Northwest Laboratory, Richland, Washington, 121 pp.

Whiteman, C.D. and Mckee, T.B. 1982: Breakup of temperature inversions in deep mountain valleys: Part II. Thermodynamic model. *J. Appl. Meteor.*, **21**, 290-302.

Wilson J.P., Inskeep W.P., Wraith J. M., and Snyder R D, 1996: GIS-based solute transport modeling applications: scale effects of soil and climate data input. Journal of Environmental Quality, **25**: 445-53

Wilson, J.P. and Gallant, J.C., 2000: Secondary attributes. In Wilson, J.P. and Gallant, J.C (eds) *Terrain Analysis: Principles and Applications.* John Wiley and sons, New York, 87-131.

Wood, E.F., Lettenmaier, D.P., Liang, X., Lohmann, D., Boone, A.B., Chang, S., Chen, F., Dai, Y., Dickinson, R.E., Duan, Q., Ek, M., Gusev, Y.M., Habets, F., Irannejad, P., Koster, R., Mitchel, K.E., Nasonova, O.N., Noilhan, J., Schaake, J., Schlosser, A., Shao, Y., Shmakin, A.B., Verseghy, D., Warrach, K., Wetzel, K., Xue, Y., Yang, Z., Zeng, Q., 1998: The project for intercomparison of land-surface parameterization schemes (PILPS) phase 2 (c) red--Arkansas River basin experiment: 1. Experiment description and summary intercomparisons. *Global and planetary change.* **19**, 115-135.

Yoshino, M.M, 1966: Some aspects of air temperature climate of the high mountains in Japan. *Jap. Progr. Climat.,* 21-7.

Yoshino, M.M. 1975: Climate in a small area: An introduction to local meteorology, Tokyo, University of Tokyo Press.

Appendix A: Surface cover classification scheme

The area and extent of six main classes of surface type were mapped using supervised classification of a mosaic of Indian Remote Sensing Satellite (IRS-1C) images, captured during February 1997. The surface types classified for this study were snow and ice, bare rock, water, tall tussock, short tussock, degraded tussock, cultivated grasses and conifer forest. The images contained three spectral layers, two in the visible region (0.52-0.59 μm and 0.62-0.68 μm) and one in the near infrared (0.77-0.86 μm). Data from these spectral bands have a pixel resolution of 23.5 m. The images were orthorectified and cloudless coverage was extracted and mosaiced with contrast matching between adjacent tiles. From the complete image, supervised classification was conducted in the Erdas Imagine software suite, using the following procedure.

Initially, feature space images of each pair of spectral layers were mapped to explore the spectral ranges of various surface classes. Secondly, points in the landscape of known surface type were used as seeding tools to find all spectrally related pixels in the study area. The relationship to the spectral signature of seed pixels was defined by standard deviations from the seed signature. The number of standard deviations used varied between classes depending on the spectral uniqueness of each class. For example, the snow and ice class of pixels was contained in a relatively narrow spectral band, so that the classification procedure was performed with a narrow range of deviation from the seed pixel. By comparison, the lake surfaces required a looser relationship with the seed pixel in order to account for spectral variance associated with spatial variability of turbidity.

In several cases, the spectral variability for classes was so large that broadening the spectral deviation to accept all appropriate pixels lead to an unacceptable level of overlap between classes. In order to remove this problem, the process outlined above was repeated for each of the selected surface classes for up to 8 sub-class points. The purpose of generating these sub-classes was to cover the variability of spectral signatures found within individual classes. The variability was due to factors such as different illumination angles, and shaded compared with non-shaded surfaces. Classification was then applied throughout the entire image with nonconforming pixels classified into the nearest class using *mahalanobis distance*. Finally, the sub-classes were amalgamated, to produce the eight surface classes listed above.

The accuracy of this procedure is reliant on decisions based on subjective and intuitive analysis. Firstly, ground truths were evaluated using maps, photos and local knowledge. Fortunately, the homogeneity and well-defined spectral boundaries of many of the selected surface classes limited the error associated with this approach. However, accuracy in the division between short and tall tussock would be the most compromised of class divisions with some probability of dense short tussock being classed as tall tussock, and sparse tall tussock being classed as short tussock. Secondly, the images obtained for classification in this study had already undergone contrast matching between tiles to smooth the mosaiced image. This means that an unknown selection of pixels was altered by an unknown amount. Although this was not documented, it is expected that this was minimal. Finally, decisions about the number of sub-classes and deviation from the seed pixel spectral signatures were based on information from the feature space images and local knowledge, combined with trial and error in order to

obtain realistic class boundaries (based on maps, aerial photos and local knowledge). Nevertheless, subjective evaluation of the accuracy of this procedure revealed close agreement between the classified image and information from other sources.

Appendix B: Synoptic circulation statistics

Table B.1 presents monthly mean synoptic circulation percentage frequencies for the South Island of New Zealand for the period December 1997 to February 1999. Using subjective classification of daily mean sea level pressure charts for the New Zealand region, circulations are classified into anticyclone (ANT), cyclonic northwesterly (CNW), cyclonic southwesterly (CSW) and other (OTH).

Table B.1 Monthly mean synoptic circulation percentage frequencies for the South Island of New Zealand, December 1997 to February 1999.

	ANT	CNW	CSW	OTH
December (1997)	35	26	19	19
January (1998)	45	19	26	10
February	54	32	14	0
March	45	23	19	13
April	67	20	13	0
May	52	6	10	32
June	60	10	27	3
July	58	23	6	13
August	55	16	19	10
September	50	33	17	0
October	13	32	45	10
November	63	7	10	20
December	48	16	26	10
January (1999)	68	10	16	6
February	58	16	16	10
Mean (1998)	51	20	19	10

Appendix C: Comparison of ground heat flux techniques

Data from 27 hours of 15-minute averages of Q_G, determined using the two techniques discussed in Section 3.4.3 are plotted in Figure C.1. For the 'storage' method, two flux plates were inserted at 8 cm, with 2 temperature probes each at 2 and 6 cm. Soil moisture content and bulk density were determined using the method outlined in Section 3.4.5. In the 'non-storage' method, six flux plates were inserted 1 cm below the

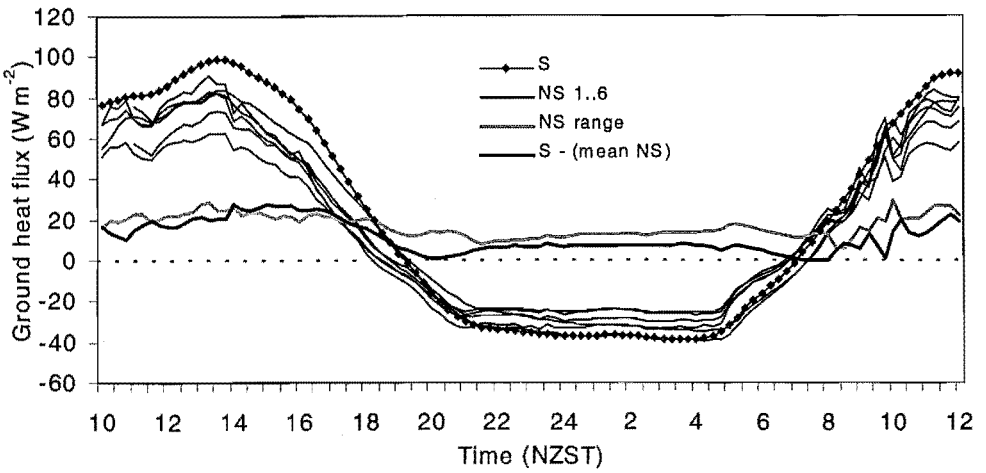

surface.

Figure C.1 Q_G estimated by the storage method (diamonds) and non-storage method (thin black lines), range of non-storage values (thick grey lines) and difference between storage values and mean non-storage values (thick black lines) for October 23/24 1998.

The storage technique can be seen to slightly exaggerate flux magnitudes when compared to the non-storage technique. This difference may be a function of the storage in the thin layer above the non-storage sensors. It may also result from over-estimation by the storage technique due to temperature sensors being arranged too close to the surface for a true bulk average or from soils being drier than estimated. However, when comparing the range of values derived from the six non-storage sites with the departures of the storage from the mean non-storage values, it is clear that differences in values between the sites that use the same technique are of the same magnitude as differences between the two techniques. This is likely to result from subtle differences between sites or the amount of disturbance that took place when inserting the sensors. It is also notable that the non-storage technique showed more detail in the diurnal cycle, although the main features were captured by both techniques. Finally, the magnitudes involved (<25 Wm^{-2}) are relatively insignificant as a component of the total energy budget.

Appendix D: Three-hourly mean energy partition ratios

Three-hourly energy partitioning ratios for a) Q_H/Q^* and b) Q_E/Q^* used as parameters in turbulent flux model (Chapter Seven) are provided in Table D.1.

Table D.1 Three-hourly energy partition ratios for a) Q_H/Q^* and b) Q_E/Q^*, where DT is degraded tussock, ST is short tussock, TT is tall tussock, R is rock surfaces, L is lake surfaces and S/I is snow and ice.

a) Q_H/Q^*

	DT	ST	TT	R	L	S/I
0300 LAT	0.14	0.13	0.30	-0.15	0.14	0.82
0600 LAT	0.14	0.13	-1.31	-0.19	0.28	-0.06
0900 LAT	0.65	0.46	0.41	0.46	0.08	-0.06
1200 LAT	0.71	0.54	0.49	0.75	-0.002	-0.06
1500 LAT	0.81	0.53	0.53	0.85	0.001	-0.06
1800 LAT	0.96	0.71	0.34	0.97	-0.18	-0.06
2100 LAT	0.27	0.97	0.72	-0.07	0.54	0.82
2400 LAT	0.24	0.88	0.58	-0.02	0.1	0.82

b) Q_H/Q^*

	DT	ST	TT	R	L	S/I
0300 LAT	0.005	0.21	0.12	0.17	-0.01	0.27
0600 LAT	0.02	0.22	4.9	0.21	-0.12	-0.04
0900 LAT	0.21	0.37	0.45	0.28	0.04	-0.04
1200 LAT	0.09	0.23	0.38	0.16	0.07	-0.04
1500 LAT	0.06	0.24	0.43	0.08	0.09	-0.04
1800 LAT	0.01	0.19	-0.62	0.07	0.40	-0.04
2100 LAT	0.13	-0.27	-0.35	0.29	-2.7	0.27
2400 LAT	0.06	-0.23	-0.15	0.17	-1.6	0.27